Alma Mater Studiorum
– Università degli Studi di Bologna –

Dipartimento di Ingegneria Energetica Nucleare
e del Controllo Ambientale

Dottorato di Ricerca in Ingegneria Energetica Nucleare e del Controllo Ambientale

– Ciclo XIX –

Settore Scientifico Disciplinare: ING-IND 18

Simulation of Gas Breakdown and Plasma Dynamics in Plasma Focus Devices

Dottorando:
Michele Frignani

Relatore:
Chiar.mo Prof. Marco Sumini

Coordinatore:
Chiar.mo Prof. Alessandro Cocchi

Esame finale anno 2007

A tutta la mia famiglia
ed al piccolo Andrea

CONTENTS

Preface

Forty years of experiments demonstrated the ability of Plasma Focus (PF) devices to produce nuclear fusion reactions in magnetically pinched plasmas. Notwithstanding the relative simplicity of the device and the wide literature on the subject, many questions are still open both on the device design and on the understanding of the physical processes characterizing the plasma formation, evolution a confinement.

The design of a device is a complex procedure based on multiple step of refinement to reach the optimized working conditions. A first rough definition of the main electrical parameters is essentially based on experimental observations and macroscopic considerations. Few basic rules reveals themselves quite effective for small devices (for bank energies up to few kJ), but fail for more powerful devices. Moreover, an experimental optimization of the working parameters would represent a hard work, not always leading to the best performances. Computer simulations can aid in this task providing a low cost and rapid tool to tune the geometrical and electrical parameters of the device.

The plasma dynamics equations have been collected in a simplified model and coupled with the equivalent electric circuit equations in a highly non-linear problem. The developed code allows to obtain the timing of the plasma dynamics and of the electric circuit discharge, together with many other quantities of interest, like the sheath axial velocity, known to be related with the sheath stability during the radial collapse. The code has been fully tested simulating the PF device, operated at the Nuclear Engineering Laboratory of Montecuccolino for neutron production from D-D fusion reactions. The good agreement between experimental results and numerical analysis has confirmed the reliability of the model.

Recent experimental activities both in the U.S. and in Italy have unquestionably shown the occurrence of reactions whose cross sections have either high energy threshold levels or too small values at the projectile energy predicted by theoretical models. In particular, the attention has been drawn to the short-lived radioisotopes breeding for medical applications. The machine shall be both highly energetic and highly repetitive, to accomplish the proposed task: a 150 kJ Mather type PF with repetition frequency of 1 Hz working in the MAcurrent range has been designed. The developed code has been used for the electrodes optimization of the device, and an iterative procedure of successive refinement has lead to a final solution quite

different from the starting trial. Moreover, the high complexity of the machine has required the design of a collector to connect the coaxial cables coming from the capacitor bank with the electrodes. Particular attention has been drawn in maintaining the collector inductance in the range fixed in the preliminary design; other problems related to the insulation effectiveness, the electrodynamic forces and the flexibility of the central core have been fully analyzed and solved.

The developed macroscopic code gives an accurate description of the current sheath evolution and of the characteristic time of the discharge but is not a proper tool to investigate in depth the physical phenomena. Also on this subject, the strength of computer simulations is of help; in the past, many fluid codes were developed and good results matching the physics of the macroscopic motion of the current sheath were obtained. However, when the energy distribution function of the charged species deviates from the assumed Maxwell-Boltzmann one, the fluid codes fail: a microscopic approach, through fully kinetic models is needed.

In particular, a Particle-In-Cell Monte-Carlo-Collisional (PIC-MCC) code has been developed to simulate the first stage of the gas breakdown in a PF device, which is known to be a highly non-stationary phenomenon, far from the thermal equilibrium. The very high multiplication rate of charged particles makes similar simulations computationally expensive: innovative numerical techniques have been developed and applied to control the number of simulation particles with a limited loss of precision and an high improvement in performances. The interest on similar numerical techniques is growing in the field of electrically bounded plasma dynamics, due to the recent expansion of industrial applications of plasma discharges for materials processing.

The developed code have allowed to show the deviation of the electron energy distribution function from the Maxwellian one. Comparisons with hydrodynamic codes show a faster breakdown development than the expected one; the results confirm those obtained with similar kinetic simulations in hydrogen and the prominent role played by the photo-electric effect in the first stage of the discharge evolution. A sensitivity study on the PF working parameters (filling gas type and pressure, electrodes geometry, external voltage ramp, insulator configuration, ...) has been performed.

The dealt subjects can be naturally divided into two parts. After a brief introduction to the research activity (Chapter 1), aimed to define the current work placing the the international scenery, a first part is devoted to the macroscopic simulation oriented to the PF design. In particular, the basic rule of thumb generally applied in PF preliminary design are discussed in Chapter 2. A full description of the implemented model and developed code for the electrodes optimization follows in Chapter 3. The simulation tool has been tested on an existing machine and applied to the design of new high energetic and repetitive one (Chapter 4), today under preliminary test; a detailed description of the collector design and of the theoretical and experimental evaluation of its electrical parameters closes the first part through Chapter 5. A second part, fully dedicated to the microscopic simulations of the electrical breakdown, then opens. The breakdown basis and many aspects of the underlying physics are treated in Chapter 6, with particular attention to the PF breakdown peculiarities. The developed numerical model and the code description fully occupies Chapter 7, while the following Chapter 8 is entirely devoted to the

description of the innovative numerical techniques for the control of the simulation particle number. Chapter 9 closes the second part with a detailed description of the microscopic simulation results and a sensitivity analysis on few working parameters.

CHAPTER 1

Introduction to the research activity

Abstract. The main subject of the present research activity is centered on the simulation and design of Plasma Focus devices. A brief introduction on the historical background and on the actual state of art will be presented showing how the present work takes place in the international context.

1.1 The Dense Plasma Focus

A *Dense Plasma Focus* (DPF) is a device that can generate, accelerate and pinch a plasma by electromagnetic forces. The short-lived pinched plasma is sufficiently hot and dense to enhance nuclear fusion reactions, even with high threshold energies, which make it a multi-radiation source. Since the whole discharge lasts few tens of microseconds, the DPF works in pulsed mode and can be efficiently operated in a repetitive regime.

The device was independently developed in the early 1960s by J. W. Mather [1] (USA) and by N. V. Filippov [2] (ex-URSS) in two configuration, which mainly differs in the macroscopic direction of motion of the accelerated plasma (axial and radial respectively).

1.1.1 The device

In its best known "Mather" version, the PF is composed of two coaxial cylindrical electrodes, closed and electrically insulated at one end and open at the other, as depicted in Figure 1.1.

The electrodes assembly is contained in a vacuum chamber filled with a mixture of low atomic number gases, at a pressure typically ranging from 0.5 to 10 Torr. If operated (as usual) in the so called direct polarity, the inner electrode (IE), the anode, is connected through a fast switch (spark-gap) to the high voltage source of an external capacitor bank, while the outer electrode (OE), the cathode, is grounded. As soon as the switch is closed, the energy E_C stored in the capacitor bank is released through the electrodes in a time that is generally of microsecond order. A voltage of typically tens of kilovolts, impressed between the electrodes, produces an electrical field strongly enhanced by the insulator sleeve that separate the electrodes; here, an electrical overvolted discharge rapidly develops into a sheath of plasma, which evolves axially along the electrode assembly under the effect of a $J \times B$ force density, until it collapses at the open end of the system where it is pinched. The pinch has a duration of a few tens of nanoseconds, and coincides temporally with a sudden, sharp drop in the total current signal, caused by a decrease in plasma conductivity due to strong confinement. Although only charge of the order of a Coulomb are involved, they are released in microsecond times, so that peak currents flowing through the plasma can be of the order of MegaAmpere. Electrodes radiuses and lengths are usually not greater than few tens centimeters; this means that radial currents between two coaxial electrodes can be accelerated to velocities of the order of 10 cm/µs, obtaining a very effective method to transform potential energy into kinetic energy.

As first approximation, the electrical behavior of the device can be easily understood by studying its equivalent lumped circuit, depicted in Figure 1.2. Neglecting the problems of impedance mismatch, transmission lines delay and not-ideal switch conditions, the external circuit consists in a capacitor bank C_0, charged at a voltage V_0, connected to the device through an ideal switch; the line presents a total resistance R_0 and a total inductance L_0. During the sheath dynamics, the plasma inductance L_p and its resistance R_p vary in time. The plasma resistance can be usually neglected with respect to the external one.

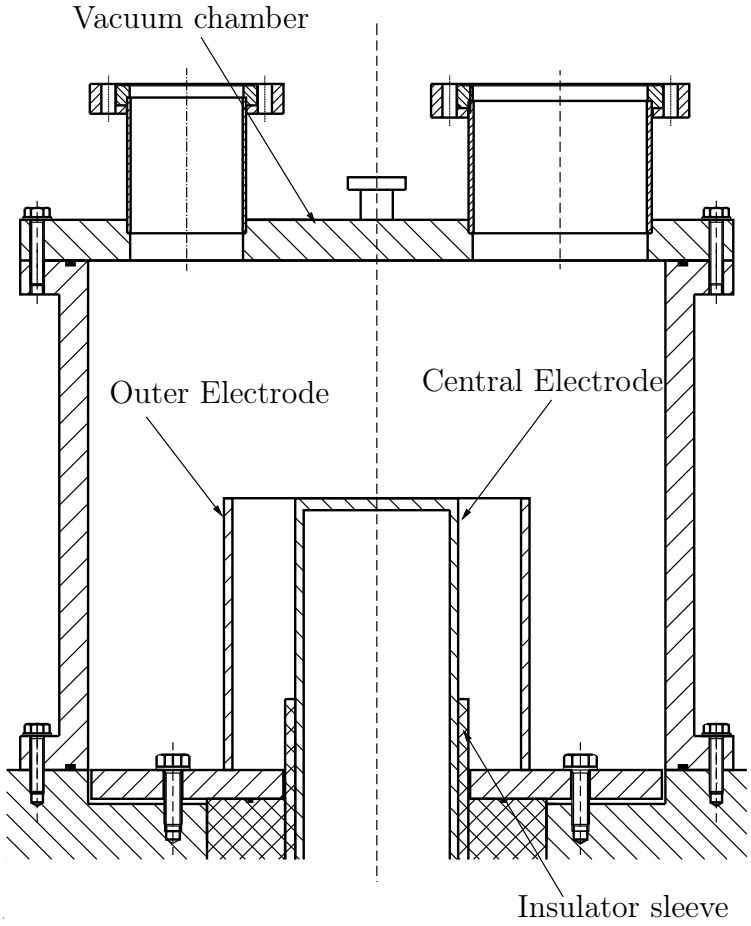

Figure 1.1: General scheme of a PF device in the Mather-type configuration.

Neglecting the plasma resistance $R_{\mathrm{p}}(t)$, the equation describing the lumped RLC circuit is [3]

$$\frac{\mathrm{d}}{\mathrm{d}t}((L_0 + L_p(t))I) + R_0 I = V_0 - \frac{1}{C_0}\int_0^t I(t')\ \mathrm{d}t'\,; \tag{1.1}$$

assuming also L_{p} constant in time, the equation can be easily solved by means of Laplace transform. Usually, the PF device equivalent RLC circuit is strongly *underdamped*, that means $R_0 \ll 2\sqrt{L/C_0}$ with $L = L_0 + L_{\mathrm{p}}$ the total inductance. The typical current waveform of a PF device in a short circuit test is, indeed, an exponentially damped sinusoid as obtainable by solving equation (1.1) (see Appendix 5.A for more details):

$$I(t) = \frac{V_0}{\omega L}\exp(-\zeta t)\sin(\omega t)\,, \tag{1.2}$$

where, for typical PFs electrical parameters,

$$\zeta = \frac{R_0}{2L} \qquad \text{and} \qquad \omega \simeq \frac{1}{\sqrt{LC_0}}\,. \tag{1.3}$$

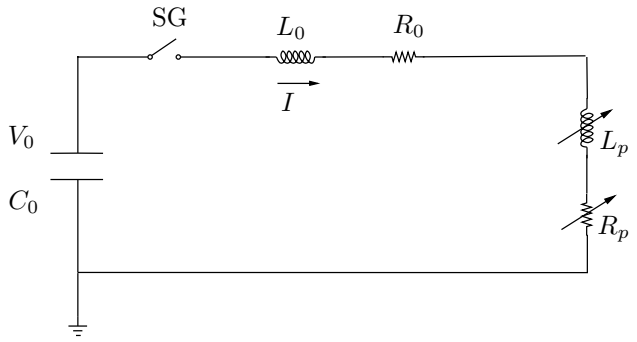

Figure 1.2: Lumped equivalent electrical circuit.

From the capacitor laws, under the simplifying hypothesis $R_0 \ll 2\sqrt{L/C_0}$ (equivalent to $\zeta/\omega \ll 1$), the voltage drop over it is:

$$V(t) = V_0 \exp\left(-\frac{R_0}{2L}t\right) \cos\left(\frac{t}{\sqrt{LC_0}}\right) .$$

A better description of the electrical discharge, during normal operations, can be obtained only by specifying the time-dependence of the inductance $L_\mathrm{p}(t)$ related to the plasma sheath dynamics, as will be better investigated in the first part of the present work.

1.1.2 The discharge phases

The PF dynamics can be ideally separated in four main phases [1, 4, 5] as shown in Figure 1.3.

As soon as the spark-gap is triggered closing the circuit, a discharge develops. The seed electrons present between the electrodes in the vacuum chamber are accelerated by the electric field, strongly enhanced by the presence of the insulator sleeve and by the cathode edge. Once the ionization energy of the background gas is reached, multiple ionization avalanches make the charged particles grow exponentially as predicted by the *Townsend law* for the electrical gas breakdown (*breakdown phase*); the ionized gas develops suddenly in a plasma sheath onto the insulator sleeve. The macroscopic flow of charges connects the electrodes providing a low resistance path for the current flowing from the capacitor bank to the ground of the system.

The current density flowing through the electrodes and the plasma produce a current loop. The magnetic field is, then, confined between the electrodes and the axial-symmetric current sheet (CS); consequently, the magnetic pressure acts as a sort of magnetic piston (MP) and pushes the sheath. As soon as the CS is formed and carries the circuit current, the plasma detaches from the insulator and grows in dimensions; its profile develops in a parabolic shape due to the dependence of the magnetic pressure from the radial position. The sheath is then pushed towards the open end of the electrodes (*rundown phase*). During this phase, the motion of the CS is characterized by a roughly constant axial velocity (about 10^7 cm/s): the sheath sweeps the background neutral gas it meets and grows in density, but also looses part of the plasma in the region where its tail connects to the OE.

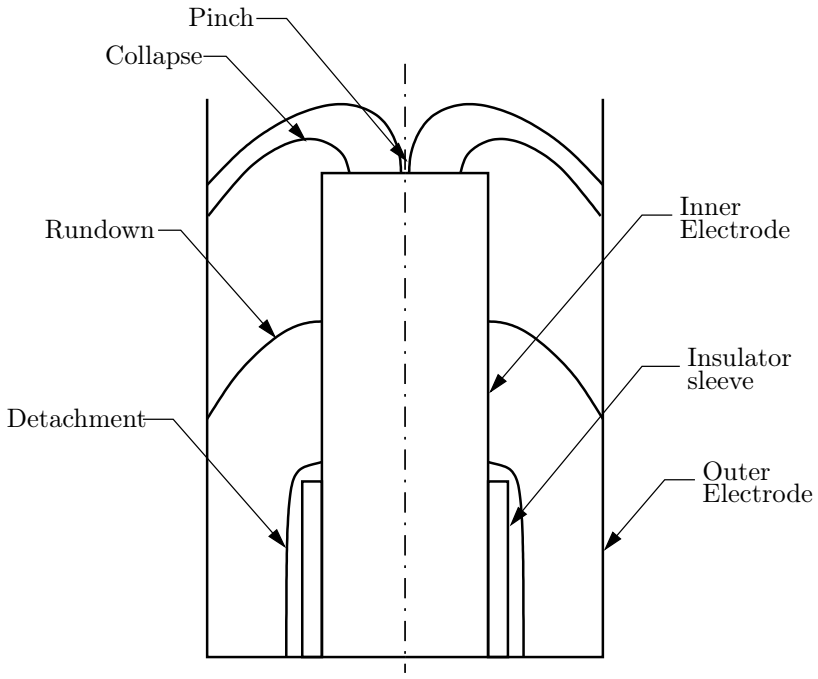

Figure 1.3: Discharge phases.

As the open end of the electrodes is reached, the sheath is driven to collapse towards the symmetry axis (*collapse phase*). The current profile inflates and accelerates; the inductance grows rapidly lowering the peak current. When the axial-symmetric shock-front reaches the symmetry axis, the plasma is radially compressed in a hot and dense focus (*pinch phase*), in which fusion reactions occur depending on the filling gas mixture. To maximize the compression effect of the pinching mechanism, this should occur in time-coincidence with the first maximum of current. The gas trapped in the focus is estimated as about 10% of that originally there. The pinch phase is not yet well understood and multiple theories has been developed to explain experimental results on radiation production and emission.

Since the pinch effect, even being the most efficient way of heating and compressing a plasma, is not a stable magnetic confinement configuration, the short-lived focus suddenly develops Magneto-Hydro-Dynamic (MHD) instability of zero-th and first order and disrupts. Consequently, the current path is broken and the electrical circuit is opened.

It is evident that the dynamics of the sheath is strictly related to the circuit discharge, since the evolution of the plasma modifies the inductance parameter of the equivalent circuit. The maximum of energy conversion is obtained if the coincidence between the peak current and the radial collapse into the focus is reached.

1.1.3 Fields of application

As previously mentioned, PF devices are widely used and studied as multiple radiation sources. Depending on the filling gas mixture, intense bursts of neutrons [6]

and charged particles beams (relativistic electron beams [7] and ion beams [8]), as well as hard and soft X-rays [9, 10] can be obtained. Moreover, the ongoing research aim at demonstrating their potential application as x-ray sources for next generation micro-electronics lithography and surface micro-machining; their properties as pulsed x-ray and neutron source are under investigation for medical applications and security inspection analysis, while intense ion beams are of interest for materials implantation. Other applications include nuclear explosion simulations (i.e. for testing of the electronic equipment) and non-contact discovery and/or inspection of the nuclear materials (fission products) by neutron activation analysis (NAA). In the last years, they have been also studied as possible competitive breeder of short-lived radioisotopes (SLR) [11, 12].

The advantages of PF devices as radiation sources are evident. Their main drawback is related to the repetition frequency, which usually make them less competitive than other devices. Indeed, in order to move their technology from the applied research environment to possible industrial application, PFs need to be operated at high pulse repetition rate in the so called repetitive mode. However at each pulse, or shot, part of the device input energy is converted into thermal loads on the structural components of the machine itself, and this could be a major cause for the PF mechanical failure [13]. Proper cooling systems are therefore to be designed and installed onto PFs to get them operate repetitively. Thermal loads are not only problematic from a macroscopic point of view, given the induced thermal strain and stress, but also from the microscopic point of view of plasma purity: metal particles are ablated by the high temperature plasma from the electrodes and carried by the sheath into the pinch region where nuclear reactions occur.

On the other hand, it is expected that, as well established for neutrons (see Section 1.2.1), larger bank energies could produce higher SLRs yields. However, many scientific and technological issues must be addressed for a high-energy Plasma Focus device, especially if operating at high pulse repetition rates, e.g. 1 Hz [14].

1.2 Experimental evidences

The worldwide experimental activity on PF devices has leaded to many not yet well understood experimental evidences and to interesting empirical laws. In particular, the comparison between many devices, of different power, proves a relation between bank energies and neutron yields; moreover, the breakdown phase seems to have effect on the whole plasma discharge and, especially, on the pinch stage and fusion reactions. Few theories have been developed to explain the anomalous emission from the focus and the possibility of fusion reaction with high energy thresholds.

1.2.1 The scaling law

About forty years of tests on PF devices of different power operated in deuterium, show the existence of proportionality laws relating the neutron yield Y_n to the bank energy E_C or to the peak current I_{max}. In Figure 1.4 experimental data are presented for many worldwide PF facilities.

The first *scaling law* [1, 4]

$$Y_n = 10^6 \cdot E_C^{1.5 \div 2.5} ,$$

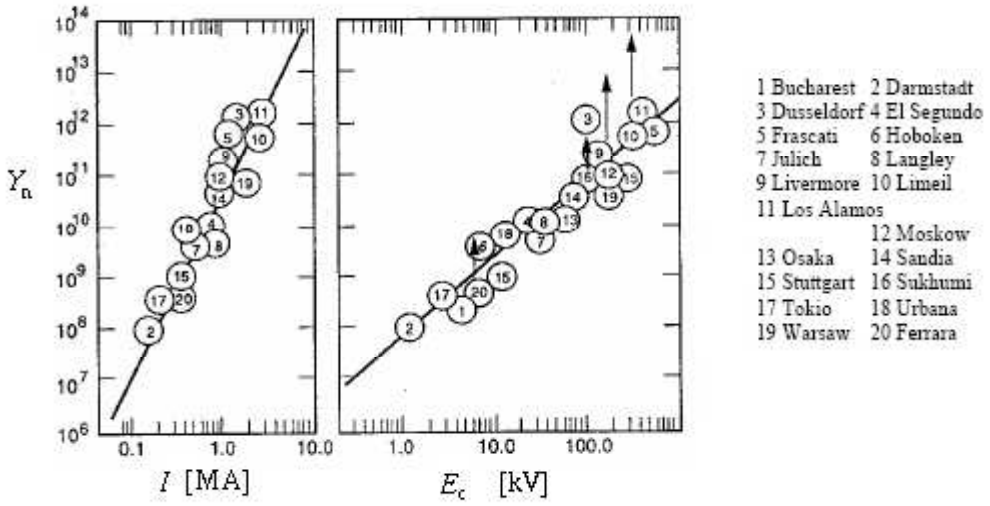

Figure 1.4: Empirical scaling law relating neutron yield and bank energy (on the right) or peak current (on the left).

with E_C measured in kJ, appears to be approximately followed over the whole range of energy on which data are available (i.e. about 1 kJ÷1 MJ). The uncertainty on the energy power depends mainly on the operating parameters of the PF device, which should be optimized in term of external inductances, charging voltage, filling pressure, gas purity ...

From pressure balance pinch relation $B^2/8\pi = nkT$ (with B the magnetic field, n the plasma density, k the Boltzmann constant and T the plasma temperature), the maximum peak current appears to be the real important parameters that could affect the total neutron yield. However, the uncertainties on the proportionality constant and on the power, for an analogous current based scaling law, increase. A typically accepted rule is

$$Y_n = 10 \cdot I_{max}^{3\div4},$$

but it has to be used with even more care since the focus current is not easily deducible from the measured one.

Many theories have been developed to justify the scaling laws, but the main unsolved problem is related to the uncertainty on the fusion mechanism (thermonuclear, beam-target, plasmoids, ...) and on the charged particles energy distribution functions. In few cases, it was observed [1] that small fractions of high-Z contaminants appear to have beneficial effects on the ion average temperature. Highly optimized devices are shown to have a reproducibility of neutron production from the plasma focus discharge within a factor of 0.1.

Recently, a new experimental campaign conducted to show the feasibility of a suitably designed high energetic and repetitive PF as a SLR breeder [12, 14] could produce interesting results to allow the extension of the scaling law to other reaction

products, just like radioisotopes.

1.2.2 The role of the breakdown

It is well-known that the breakdown phase in a PF device is essential for good plasma pinching and high neutron and X-rays emission yields [15, 16, 17]. The geometrical and material insulator parameters are strictly connected with the operating conditions, such as gas filling pressure and maximum applied voltage [18, 19]. Modification of the insulator configuration is almost always needed in PF operation: even though theoretical analyses and numerical simulations provide helpful hints, the insulator optimized design comes mainly from experimental trials and fails, also in connection with *knife-edge* insertion [20]. The physical phenomena related with the electrical breakdown in PF devices are still under investigation, since strictly connected with charge particles interaction with insulator and conductive materials; experiments point out that the insulator surface conditioning is of fundamental importance for a good discharge behavior, confirming the importance of the breakdown development on the overall phenomenon [20].

One possible explanation of the breakdown role on the focus conditions was firstly depicted in [21, 22]. By means of image converter photographs, the production of plasma filaments was clearly shown. Maximum neutron yields were observed to occur under initially fairly uniformly distributed striations around the IE. It was observed that the evolution of the filamentary structure develops into an axial-symmetric sheath with evident radial striations, which are thought to enhance the mechanism of neutron production. At lower operating energies, the filamentary patterns persists on the CS and the filamentary structures form a finite number of intense radial spikes during the rundown and collapse phase; the radial structures were observed to occur in pairs (force-free) and their final annihilation is thought to represent the main ion and electron heating mechanism (magnetic field annihilation) causing higher X-ray and neutron production.

Recently [23], the formation and the role of filaments in pinch type discharges was revisited. It arises that the formation of distinct current filaments are a peculiar feature of high-current pulsed discharges and comes from their earliest stages. Many experimental data from high-speed cameras, soft X-ray pinholes and fast deuterons angular distribution have been analyzed and explained on the basis of filamentary structures.

1.2.3 High energy threshold fusion reactions

As previously stated, the failure of predictive models is primarily due to the lack of a precise knowledge of the energy distribution of the reacting particles during the pinch phase of dense magnetized plasmas. Feeding the up to today available experimental data, as input parameters in the most reliable even complex models, it seems that triggering of certain nuclear reactions should not be allowed.

However, recent experimental activities, both in the US and Italy, have unquestionably shown the occurrence of reactions whose cross sections have either high energy threshold levels or too small values of the projectile energy, as predicted by the above mentioned models. Even considering the high energy tail of the Maxwellian spectrum and an average pinch density of 10^{19} cm^{-3}, the very high yields experimen-

tally observed [24, 25, 12] are not justifiable. These considerations suggest that more complex and yet unidentified reaction mechanisms play a key role in the physical phenomena occurring in the pinch.

A possible solution could be represented by the in-pinch formation of many peculiar and microscopic plasma domains of enhanced nuclear reactivity. These zones, usually referred to as "plasmoids" or "hot spots", are characterized by very high densities (even above solid state values), fairly high temperatures (above 3 keV), small dimensions (20÷300 µm), and magnetic fields sufficiently strong to trap ions with energies of the order of 5 MeV/nucleon. The life-time of these structures is supposed to be in the interval 0.5÷5 ns. If the reactants involved are captured within the plasmoids, the density and temperature conditions are sufficiently high to produce high nuclear reaction rates [26, 27, 28].

The reaction rate is given by

$$RR = \alpha \int_{E_{\min}}^{E_{\max}} \frac{\mathrm{d}\phi}{\mathrm{d}E} \sigma(E) \sqrt{E}\, \mathrm{d}E \,,$$

with $\mathrm{d}\phi/\,\mathrm{d}E$ the projectile energy distribution function and σ the reaction cross section; α is a proportionality constant depending on the target density and on the projectile mass, while $E_{\min}$ is the threshold energy for the considered reaction. Measured yields of high Z-low Z reactants were considered and compared with theoretically estimated values obtained combining the reaction rate with the density of plasma target nuclei and the plasmoid life-time; the results were in good agreement with experimental data for a variety of nuclear fusion reactions with threshold energies in the range 0.3÷4 MeV, when an energy distribution function in the form of

$$\frac{\mathrm{d}\phi}{\mathrm{d}E} \sim E^m \,, \text{ with } m = 2.5 \,,$$

was considered [25].

The filamentary structure of the CS could be a possible explanation of the plasmoids formation in the pinched plasma [23].

1.3 Theoretical and numerical models

PF devices are quite predictable machines thanks to the simplicity of the equivalent circuit and to the empirical scaling law for neutron yield. However, the underneath physics is not yet completely clear. Few simple general considerations and models are here presented.

1.3.1 The plasma scaling

An interesting feature of PFs is that the energy density of the focused plasma is practically a constant over the whole range of devices, independently from their bank energy if optimally designed. The more energetic is the machine the higher is the focus volume, the corresponding lifetime and the outcoming radiation yield. However, the *scalability of plasma phenomena* assures that the plasma dynamics,

Physical property	Scale factor
l, t; L, C	x^1
v; R, V, I	x^0
E, B; σ; n_b	x^{-1}
J, n	x^{-2}

Table 1.1: Scale factors for each physical property in gas discharges plasma similarity transformation.

and the consequent plasma and radiation characteristics, are mainly the same for the smallest and largest PFs.

A first plasma similarity transformation was derived for gas discharges [29, 30], and further applied to plasmas in cosmic astrophysics [31].

Being derived for gas discharges, the scaling applies best to plasmas with a relatively low degree of ionization; the ionization energy of the neutral background gas is an important explanatory scale parameter. Starting from the unchanged physical properties, it's clear that the particles masses, m, are constant and, therefore, invariant; consequently their velocities, v, are fixed. Since the particle charge, q, is a constant, as well as the mass-to-charge ratio, the potentials must not vary if a particles falling through an electric potential, V, gain the same energy. As direct consequences, time and spatial scales (l, t) have to vary proportionally to keep velocities constants; moreover, the electric field, E, scales inversely with the distance. In order to satisfy Faraday's law of induction and Ampere's law, also the magnetic field, B, must scale inversely with the distance. It follows that current density, J, scales with the particle density, n, and therefore that current itself, I, is invariant, since from the Gauss's law, densities must scale with the inverse square of the distance (the same is deducible imposing the constant speed of the Alfvèn wave, which implies that particle densities must scale with the square of the magnetic field). Electrical conductivity, σ, obtained as the ratio between the current density and the electric field, scales inversely with the distance. Finally the neutral gas density, n_b, must scale with the inverse of the length since the electrical conductivity is proportional to the electron density and inversely proportional to the background gas density; therefore the ionization fraction scales with the distance. Other scaling factor of electrical macroscopic properties (inductance L, capacitance C and resistance R) are easily deducible by their definition or by the previous relations.

The commonly used scaling rules are summarized in Table 1.1.

1.3.2 Design parameters: the snowplow model

Notwithstanding the advantages of scalability of the PF parameters, the design of a device is a complex procedure based on multiple steps of refinement.

A first rough definition of the main electrical parameters is essentially based on experimental observations and macroscopic considerations. It's known to exist a lower limit to the operating voltage of a PF device, essentially given by the voltage drop across the focus tube during the axial acceleration phase. This parameter has to be parallelly tuned with the axial speed of the CS. A suitable lower limit is fixed by

the efficiency of the electromagnetic mechanism ($3 \div 4$ cm/µs for deuterium), related to the ionization rate, shock temperature and electrical conductivity. On the other hand, experimental data show focusing problems for too high axial speeds (about 10 cm/µs) due to current spokes development; the instability of the plasma flow has been recently modeled solving the MHD equations on a fixed Eulerian mesh [32]. The consequent operating voltage results in the range of $20 \div 30$ kV. Once chosen a proper bank energy, from the RLC circuit theory, an inductance upper limit arises to keep a sufficiently high current peak. This is one of the main problem to be faced during PF design and optimization; when a current in the regime of the MAis sought-after, many technological problems arise and have to be faced with care.

Once fixed the electrical parameter of the external circuit, a careful design of the electrodes dimensions must follow. Many theoretical and numerical models exist and give good results, but the best results are obtained through the so called *snowplow model*. Under the hypothesis of stationary conditions, the magnetic pressure $p_B = B^2/(2\mu_0)$ is balanced by the kinetic energy of the background gas, given by $p_T = nkT = \rho v^2$, with v axial speed of the CS. Expressing the magnetic field $B(r)$ as a function of the dependent current I, by integration over the inter-electrode gap (from the inner radius r_{int} to the outer one r_{ext}), the axial speed of the sheet is obtained as

$$v = \sqrt{\frac{\mu_0 I^2 \ln\left(\dfrac{r_{\text{ext}}}{r_{\text{int}}}\right)}{4\pi^2 \rho (r_{\text{ext}}^2 - r_{\text{int}}^2)}} \,.$$

Under the hypothesis $r_{\text{ext}}/r_{\text{int}} \lesssim 3$, a series expansion of the logarithm leads to the approximate relation

$$v \simeq \sqrt{\frac{\mu_0 I^2}{8\pi^2 \rho r_{\text{int}}^2}} \,. \tag{1.4}$$

Using the equation of the momentum conservation in the transverse direction [33], it can be shown that steady solutions can only exist if the axial speed of the layer exceeds the minimum velocity given by equation (1.4). It is then easy to remap the v variable on a dimensionless parameter a which is defined in the interval $[0, 1]$:

$$a = \sqrt{\frac{\mu_0 I^2}{8\pi^2 \rho r_{\text{int}}^2 v^2}} \,. \tag{1.5}$$

Comparing literature data, it appears that all focus tube are operated in a range $a \in]0.5, 1[$.

The analytical snowplow model is known to give good results only during the rundown phase. Other theoretical models, like the *slug model* [4], can be used to describe the radial phase to obtain a trial value for the electrodes radiuses. However, even if the one-dimensional snowplow model fails for the collapsing phase, it can be extended to the two-dimensional space (r, z) and numerically implemented, in order to obtain a proper tool for electrodes design optimization.

1.3.3 A microscopic description

As previously stated, the design of a PF device cannot be free from experimental activities and physical understanding of the connected problems. The cited macroscopic models give quite accurate description of the CS profile, as well as of the characteristic time of the discharge, but are not a proper tool for a deep investigation of the physical phenomena.

In the past, many authors developed two-dimensional MHD models to investigate in better details the dynamics of the rundown and collapse phases [34, 35, 36, 37, 38]. Recently [39], an MHD code based on the modified free points method (i.e. a gridless method, very useful for problems involving large deformations) has been developed to solve the full dissipative set of MHD equations with Braginski transport [40]. A continuous refinement of the physical models has allowed to get an increasing accuracy on the dynamics description.

Even if the fluid codes appear to match correctly the physics of the macroscopic motion of the CS, they fail in the description of the breakdown and pinch phase, where Maxwellian assumption of the energy distribution function of charged species lead to misleading results. A microscopic approach, by kinetic models, is then necessary.

The starting point of macroscopic simulations (both from snowplow and MHD models) is the assumption of a well-formed plasma sheath on the insulator sleeve. Moreover, the available experimental data [18, 19] describe the feature of this phase mainly at an advanced temporal stage (hundred of nanoseconds), when the plasma sheath is well-formed and current densities reach values of the order of hundreds of kA/cm^2. Due to the influence of the gas breakdown in the sheath development and in the subsequent phases of the discharge, a more precise description of its generation and evolution in the first stage of the discharge is needed. Up to today, both fluid [41] and kinetic [42] codes have been developed to model the ionization growth in a PF discharge, but many improvements are still needed.

Widely tested numerical methods, like the coupled Particle-In-Cell (PIC) Monte-Carlo-Collisional (MCC) kinetic model [43, 44], can be successfully used for a microscopic description of the transport of the charged particles under strong electric fields. The very high multiplication rate of charged particles makes such simulations quite expensive even on modern computers, unless control techniques are developed and applied to maintain an affordable number of simulation macro-particles. The interest on such numerical techniques is relevant not only for PF application, but even for other fields of plasma physics and dynamics.

One of the most important but hard aspect of similar simulation is the correct modelization of the microscopic collisional events of charged particles with the boundaries of the domain of interest. A deep investigation on the interaction of charged particle with conductive and insulating materials is needed. Experimental data are not always readily available to allow comparisons.

Part I

Macroscopic Simulation and Design Optimization

CHAPTER 2

Introduction to PF design

Abstract. The design and optimization of a PF device is a complex procedure, which involves many connected subjects like the choice of the circuit parameters, the electrode design and the careful choice of auxiliary components. After general considerations on external circuit parameters, the attention will be drawn on the electrodes design; at last, the optimization of a real device will be presented. This brief introduction to the problem will guide the reader through the next sections in the first part of the present work.

2.1 External circuit parameters

The first step in the planning of a PF device is the estimation of the total bank energy and peak current, on the basis of the expected operational capabilities. Since the charging voltage can be chosen in a rather small interval, all the other electrical parameters can be easily deduced.

2.1.1 Charging voltage and bank energy

PF devices usually are operated to very high voltages, extremely higher than those strictly necessary to produce the gas breakdown. Indeed, there is a lower limit on the charging voltage of the capacitor bank due to the inductive voltage drop during the axial acceleration phase. It's quite intuitive that the variable inductance of the equivalent RLC circuit grows during the sheath motion, since the space filled by the magnetic field increases with its axial position (see Section 3.1.4 for more details). The voltage drop related to the inductance component of the circuit is given by the first term $\mathrm{d}(LI)/\,\mathrm{d}t$ of equation (1.1). During the first stages of the discharge, the current grows rapidly but the inductance is mainly due to the external circuit term (constant and of the order of tens of nH). To obtain the maximum compression effect in the focus phase, the acceleration of the CS should end in temporal coincidence with the first maximum of the current, roughly given by equation (1.2) (hundreds of kA); then, it follows that the maximum value of the voltage drop is mainly given by the varying inductance component, which means

$$\frac{\mathrm{d}}{\mathrm{d}t}(L(t)I(t)) = L\frac{\mathrm{d}I}{\mathrm{d}t} + I\frac{\mathrm{d}L}{\mathrm{d}t} \sim I\frac{\mathrm{d}L}{\mathrm{d}t}\,.$$

In this occasion, the CS profile can be considered in first approximation with no curvature, connecting the IE of radius r_{int} with the OE of radius r_{ext}. Simply applying the formula to calculate the inductance between two coaxial cylinders of length, the inductance of the focus tube can be written as

$$L_{\mathrm{p}}(t) = \frac{\mu_0}{2\pi}\ln\left(\frac{r_{\mathrm{ext}}}{r_{\mathrm{int}}}\right) z(t)\,,$$

where $z(t)$ is intended to represent the axial position of the CS along the electrodes. The inductive voltage drop is, then, given by

$$I\frac{\mathrm{d}L}{\mathrm{d}t} = I(t)\frac{\mu_0}{2\pi}\ln\left(\frac{r_{\mathrm{int}}}{r_{\mathrm{ext}}}\right)\frac{\mathrm{d}z}{\mathrm{d}t}\,, \tag{2.1}$$

with $v = \mathrm{d}z/\,\mathrm{d}t$ the macroscopic velocity of the sheath during the rundown.

Typically the radiuses ratio lead to $\ln(r_{\mathrm{int}}/r_{\mathrm{ext}}) \simeq 0.5 \div 1$, while the peak current is $I \simeq 0.5 \div 1$ MA; this gives an inductive voltage drop per axial speed of

$$\frac{1}{v}\,\mathrm{d}V \simeq 10^{-1}\ \mathrm{Vs/m}\,,$$

or, equivalently, about 1 kV per 1 cm/µs.

The range of suitable axis speeds in a PF tube is rather small [4, 45]: the lower limit is fixed by the efficiency of the electromagnetic drive mechanism which is strictly

related to the plasma conductivity, i.e. to the ionization rate (see Appendix 2.A for more details).

Since, usually, the velocity of the CS is taken in the range $3 \div 8$ cm/µs for a PF tube operating in deuterium, the corresponding shock temperature is $2 \div 5 \cdot 10^4$ K. Lowering the axial speed to 1 cm/µs, would reduce the plasma temperature to about $2 \cdot 10^3$ K ($T_2 \sim v_1^2$, see equation (2.9)) and the plasma conductivity ($\sigma \sim v_1^3$, as from equation (2.10)) to too low values, with certainly insufficient ionization for the magnetic drive to be operative.

On the other hand, observations also show that it is difficult to obtain consistent conversion of axial speed into focusing action when the first exceeds 10 cm/µs (if the classical configuration of the electrodes is wanted to be preserved against more exotic ones [45]).

Thus, from equation (2.1), it follows that the inductive tube voltage drop is in the range $3 \div 10$ kV, which is the main reason why most PF work with charging voltages in the range $20 \div 30$ kV.

Once fixed the charging voltage V_0, the wanted bank energy E imposes the total capacity C_0 of the system, being

$$E = \frac{1}{2} C_0 V_0^2 \,. \tag{2.2}$$

2.1.2 Inductance and peak current

As previously stated, a typical PF peak current $I_{\max}$ is in the range $0.2 \div 1$ MA. Referring to the maximum current of the equivalent RLC circuit, as deducible from equation (1.2), one obtains

$$I_{0,\max} \simeq \frac{V_0}{\sqrt{\dfrac{L_0}{C_0}}} \tag{2.3}$$

if only the external inductance L_0 is considered and under the hypothesis of negligible resistance R_0 (perfect sinusoidal current).

From experience, the peak current during focus operation is typically 60% of the maximum ideal current $I_{0,\max}$. It is therefore necessary to design the external circuit parameter in order to obtain a maximum ideal current $I_{0,\max} \sim 1.6 \div 1.7\, I_{\max}$.

By substitution of equation (2.2) into equation (2.3), a first estimation of the maximum external inductance L_0 can be immediately found as

$$L_0 = \frac{2E}{I_{0,\max}^2} \,.$$

Therefore, the external inductance L_0 of a PF device shall be of the order of few tens of nH: obviously, lower is the inductance, greater is the obtainable peak current for a fixed bank energy.

Typical inductances of $30 \div 40$ nH can be achieved without much difficulty. One easy way to both increase bank capacitance and decrease inductance is based on the employment of parallel elements in the external circuit. Nevertheless, a similar choice make all the system management very complex, as will be investigated in more details in Section 2.3.

2.2 Electrodes design

The condition for device optimization is the time coincidence between pinch and maximum current. The electrodes design is therefore a fundamental aspect: the radiuses ratio influences the focus tube inductance, while the total length is related to the maximum current of the external circuit through the sheath axial speed. The snowplow model is of great aid in such a nonlinear task, but few simple considerations help in fixing a starting point.

2.2.1 A first rough solution

As already shown in Section 1.3.2, coupling the expressions of the magnetic and gas pressure, the CS axial speed is given by equation (1.4). Since the velocity is proportional to I, considering the $I(t)$ in time of a typical lumped RLC circuit and neglecting the damping exponential (see equation (1.2)), the CS axial average velocity can be obtained integrating $I(t)$ over the first quarter period and dividing by $\pi/2$:

$$\overline{v} = \sqrt{\frac{\mu_0 \ln\left(\frac{r_{\text{ext}}}{r_{\text{int}}}\right)}{4\pi^2\rho(r_{\text{ext}}^2 - r_{\text{int}}^2)}}\frac{2}{\pi}I_{0,\max}\int_0^{\pi/(2\omega)}\sin(\omega t)\,\mathrm{d}(\omega t) = \sqrt{\frac{\mu_0 \ln\left(\frac{r_{\text{ext}}}{r_{\text{int}}}\right)}{\pi^4\rho(r_{\text{ext}}^2 - r_{\text{int}}^2)}}I_{0,\max}\,, \tag{2.4}$$

where $I_{0,\max}$ is the maximum ideal current.

Assuming the average rundown velocity as the velocity of the whole phenomenon, the CS approaches the end of the electrodes at about

$$t_l = \sqrt{\frac{pi^4(r_{\text{ext}}^2 - r_{\text{int}}^2)}{\mu_0 \ln\left(\frac{r_{\text{ext}}}{r_{\text{int}}}\right)}}\frac{l\rho^{1/2}}{I_{0,\max}}\,, \tag{2.5}$$

where l represents the total length of the electrodes.

On the basis of the external inductance L_0 and capacitance C_0 (as derived in the above section), the period of the sinusoidal current of the equivalent LC circuit (R_0 is here neglected) can be evaluated as

$$T = \frac{2\pi}{\omega} = 2\pi\sqrt{L_0 C_0}\,,$$

ω being approximately given by the second of equations (1.3). The peak current $I_{0,\max}$ is reached at time $t_0 = T/4$, which can be compared with CS axial transit time of equation (2.5), leading to the scaling parameter

$$\frac{t_l}{t_0} = \frac{1}{2\pi\sqrt{L_0 C_0}}\sqrt{\frac{\pi^4\rho(r_{\text{ext}}^2 - r_{\text{int}}^2)}{\mu_0 \ln\left(\frac{r_{\text{ext}}}{r_{\text{int}}}\right)}}\frac{l}{I_{0,\max}} \simeq \frac{2}{\sqrt{L_0 C_0}}\sqrt{\frac{2\pi^2 r_{\text{int}}^2\rho}{\mu_0}}\frac{l}{I_{0,\max}}\,,$$

for $r_{\text{ext}}/r_{\text{int}} \lesssim 3$, as showed in Section 1.3.2. The ratio should lie around the unity to ensure the maximum transfer of external energy into compression strength.

Another important design parameter is the good matching between the external inductance L_0 e the focus tube one L_l

$$\frac{L_l}{L_0} = \frac{1}{L_0}\frac{\mu_0}{2\pi} l \ln\left(\frac{r_{\text{ext}}}{r_{\text{int}}}\right) ;$$

in this case, the approaching of the ratio to 1 ensure a good energy transfer from external circuit to magnetic compression. Deviations from the ideal value of 1 could induce the *current shedding effect*, common to all the type of shock tubes: a portion of the tube current stays behind, near the backwall insulator sleeve, without contributing to the effective current of the plasma sheath (even if measured by diagnostics).

The two scaling parameters represent a sort of *figure of merit* (FOM) for the PF design. Typically an error of $\pm 10\%$ on their value can be assumed.

Practically, the two parameters are not enough to set the electrodes geometry. However, experimental data and other theoretical aspects limit the variability range of few variables. As previously shown, CS axial speed can vary in a rather small range. Moreover, typical operating pressures are of the order of few Torr to improve gas breakdown and maintain reasonable electrodes dimensions. These limits help in determining an initial trial value for length l and radiuses r_{ext} and r_{int}.

One should notice that the proposed solution needs many refinements. Mainly, no information is yet available on the collapse phase, which is the most critical: the peak current is wanted in time-coincidence of the pinch stage, rather than at the end of the axial transit; moreover, during the last stages the inductance of the collapsing sheath rapidly increases modifying the peak value and the inductive voltage drop.

2.2.2 Electrodes optimization

The global problem is clearly non-linear. Depending on the plasma shape and position, the inductance related to the plasma gun changes (from a minimum corresponding to the breakdown to a maximum at the pinch stage) modifying the parameters of the equivalent circuit. Therefore, the current flowing in the plasma sheath is not that of an ideal RLC circuit; it strongly influences the magnetic pressure which drives the sheath in its axial rundown and collapse.

On the basis of the snowplow theory, a more complex model of partial differential coupled equations can be written and numerically solved. To take correctly into account the varying inductance due to the sheath motion, the mathematical model must be based, at least, on a two-dimensional geometrical domain; the hypothesis of perfect axial-symmetry is, indeed, a good approximation. The sheath profile can hence be modeled as a sequence of conical finite elements connected to the electrodes, which closes the electrical circuit. The inductance of the plasma gun depends strictly on the sheath profile and the CS discretization allows a rather simple way to evaluate it. Once known the total inductance of the circuit and the inductive voltage drop due to the sheath advance, the equation (1.1) can be solved to obtain the current flowing in the CS. The magnetic pressure is, then, immediately deduced and each element of the sheath profile can be pushed through the solution of the equation of motion, taking into account both its inertia and the momentum change due to the swept gas.

The model is still rather simple. The breakdown is not modeled and the CS is initially created on the insulator sleeve. Initial and boundary conditions are not yet completely clear, and still need to be investigated. Furthermore, no information is available on the plasma properties in front of the shock. Consequently, no consideration can be made on the pinch stage. Notwithstanding, the model gives good results on the CS timing and its profile shape [46]. The method will be described in detail in Chapter 3 and compared with experimental results in Chapter 4.

Starting from the first trial value obtained as proposed in the above section, a code based on the snowplow model can help to find the best theoretical electrodes configuration. However, adjustments of the electrodes and insulator geometrical parameters, as well as of the filling gas pressure, should be possible on the basis of experimental tests. This means that in the design of a new device, the electrical and mechanical connections of the electrodes to the vacuum chamber must be planned carefully providing a sufficient degree of flexibility. In Chapter 5, the subject will be dealt in greater detail.

2.3 A real device

The above brief description of a PF design procedure is still not complete. The planning of a new real device requires great care on auxiliary device management and connection. In particular, the main goal and challenging technological problems in the design of the PFMA1 (Plasma Focus for Medical Applications 1), a 150 kJ repetitive plasma focus for the production of F^{18}, will be here presented.

2.3.1 The goal and the needs

Experiments in the past five years have demonstrated production of short-lived radioisotopes with a Plasma Focus device, using the so-termed *endogenous mode* [12, 24].

Short lived, positron emitting radioisotopes (SLRs), like F^{18} and O^{15}, gain rapidly growing interest for use in medical diagnostics, i.e. positron emitting tomography (PET). However, severe difficulties are related to short half-life of the radioisotopes and to the localization of the production facility. Only recent studies opened a new perspective for the use of PF devices to produce SLRs. Starting from the results obtained by Brzosko and coworkers [24, 25], a research activity has been planned and started to validate and improve this promising technology. The preliminary results appear consistent, confirming the viability of the technique [11, 12]. Due to the high energy thresholds of few of the tested reactions, the observed results seem to be an evidence of the plasmoids theory, already presented in Section 1.2.3. While in conventional techniques targets are irradiated with charged particle beams generated from outside, in endogenous production both projectile and target are confined in the same region where they react.

Filling the PF chamber with He^3 and O^{16} in gaseous form, the reactions

$$O^{16} + He^3 \rightarrow F^{18} + p$$
$$O^{16} + He^3 \rightarrow O^{15} + He^4$$

can take place. The second reaction branch has a yield 2–3 times smaller.

So far radioisotope activities of only a few micro-curies have been obtained from single discharges in small scale PF machines (capacitor bank energies of approximately 7 kJ). Scaling laws for neutron yield in PF neutron generators are experimentally well established up to 1 MJ of bank energy, as already stated in Section 1.2.1. If similar laws are supposed to hold also for nuclear reactions that produce SLRs, it could be expected that higher activities could be obtained with larger bank energies, about 150 kJ, operating at high pulse repetition rates, e.g. 1 Hz.

The expected production rate is 1 Ci of F^{18} in 2 hours. One major advantage in this use of a PF to breed short-lived radioisotopes is the neutron-free feature of the $O^{16} + He^3$ nuclear reaction (as well as of other similar ones), which reduces considerably the activation of structural elements, clearly very undesirable, and also makes the shielding required for radiation protection far less demanding than for other devices. Moreover, the prompt production makes SLRs available on demand.

Notwithstanding the great advantages of a similar solution, many scientific and technological issues must be addressed for a high-energy PF device to run at one pulse per second [13, 14].

2.3.2 Working parameters

Due to the high demanding bank energy $E = 150$ kJ, it is convenient to work at high charging voltage to reduce the needed total capacitance. Indeed, from the definition of the electrostatic energy by equation (2.2), it follows that at a nominal charging voltage V_0 of 30 kV, in perfect agreement with the design limits described in Section 2.1.1, the required capacitance is $C_0 \simeq 350$ µF.

As previously stated in Section 2.1.2, a total external inductance L_0 of few tens of nH is usually achievable; the PFMA1 being a very large and complex device, the total inductance L_0' (here intended as the sum of the external circuit and focus tube inductances) can be safely estimated of the order of 40 nH. For low resistance value ($R_0 \simeq 1 \div 10$ mΩ), its the damping effect on the RLC discharge can be neglected and the ideal short circuit maximum current $I_{0,\max}$ estimated through equation (2.3) to be of the order of 3 MA.

As stated, the production of F^{18} through in-vacuum endogenous reactions requires a mixture of O^{16} and He^3 as filling gas. Due to the high mass number of the oxygen (in molecular form), its gas pressure must be kept sufficiently low. In order to achieve a sufficient number of reactants in the focus, it's preferable to have working pressures p_{D_2} equivalent to about 10 Torr of deuterium.

The working parameters of the PFMA1 are summarized in Table 2.1.

2.3.3 Challenging problems

A so high capacitance can be reached only employing more capacitors operating simultaneously. In the choice of capacitors for typical PF operation, an important feature is the life expectancy, as a function of the operating voltage, the discharge frequency and the voltage reversal percentage. The severity of working parameters can strongly reduce the capacitor life.

The discharge of the capacitors on the electrodes must take place through a fast switch able to carry large currents, usually of the orders of few hundreds of kA. The fast spark gap (SG) switches are nowadays considered the best choice in the field

Working parameter	Value
Charging voltage (V_0)	30 kV
Bank capacitance (C_0)	350 µF
Total inductance (L'_0)	40 nH
External resistance (R_0)	$1 \div 10$ mΩ
Bank energy (E)	150 kJ
Ideal peak current ($I_{0,\max}$)	3 MA
Discharge frequency (ω)	0.3 MHz
Filling gas (D_2) pressure (p)	13.33 mbar
Repetition frequency (f)	1 Hz

Table 2.1: PFMA1 operational parameters.

of *pulsed power* applications. Another fundamental feature in addition to the high voltage-current operability, is a very low time-jitter[1] in their closure: having to use multiple switches (one for each capacitor, due to the maximum sustainable current limit), the simultaneity of the trigger is of great importance. Other requirements are a good recirculating cooling system, a simple coupling with the capacitor and a sufficiently low inductance (to reduce the magnetic energy losses, proportional to $1/2LI^2$).

Even the connections between elements of the bank must have a low inductance. The elements parallelization is of great advantage also in this situation aiding to reduce both inductance and resistance. The use of coaxial cables for high voltages and currents is a safer and more flexible solution than that of clamped parallel plates.

The connection between the coaxial cables and the focus tube is a very delicate problem, which usually requires the design of an ad-hoc collector.

When the limit of the MA is overcome as maximum current, great care is demanded to minimize the detrimental effect of the magnetic field. The transient diffusion of the magnetic field in conductor materials can explain the well-known *skin-depth effect*; at very high current densities, each electrical connection must be well defined by means of the so called *current gasketing* and sharp edge must be smoothed to avoid current paths with null bending radius which would induce too high magnetic fields, able to vaporize the materials. In a pulsed regime, the eigenfrequencies of the structure could be problematic if comparable with the operational ones, as well as electrodynamic forces could induce too high maximum deformation compromising the vacuum sealing.

On the other hand, highly transient over-voltage spikes impose to design with great care the insulators. Moreover, everywhere a dielectric surface connects a high-voltage element and grounded one, a favorable path for a *surface discharge* is created; its effect represents a loss term in the energy transfer and can seriously damage the insulating material.

All the above mentioned technological problems will be faced in Chapter 5, with a special attention to the issues related to the collector design (inductance and capac-

[1] The jitter is the standard deviation of the breakdown time assumed to have a Gaussian distribution, being based on a stochastic process.

itance, current gasketing, surface tracking, flexibility, electrodynamical forces, ...).

2.A Plasma physics and shock dynamics

To better understand the evaluations on CS dynamics in a PF tube proposed in Section 2.1.1, it's preferable to recall few well-known equations of plasma physics and shock dynamics.

2.A.1 Partial pressures and Saha equations

For a gas at temperature T consisting of multiple species, the partial pressure of the i-th species is given by $p_i = n_i kT$, where n_i is its density and k the Boltzmann constant, or equivalently by

$$p_i = \rho_i R_i T = \rho_i \frac{R_0}{M_i} T \,,$$

with ρ_i mass density, R_i gas constant for the i-th species, R_0 universal gas constant and M_i the molecular weight. Obviously, $p = \sum_i p_i$. When the species are single or multiple ionized particles of the same gas, the total pressure is given by

$$p = \frac{R_0}{M} \rho T \left(1 + \sum_i i\alpha_i \right) = \rho T \chi \,,$$

with α_i as fraction of ionized particles over the total for the i-th ionization degree; the quantity χ is known as the *departure coefficient*.

As well as the *Saha equation* can be written for a single ionized gas

$$\frac{n_\mathrm{i} n_\mathrm{e}}{n} = \frac{Z_\mathrm{i} Z_\mathrm{e}}{Z} \exp\left(-\frac{E_\mathrm{ion}}{kT} \right)$$

with ionization threshold energy E_ion, a system of Saha equations can be obtained recursively for a generic gas with multiple degrees of ionization. The generic equation for the i-th species is

$$\frac{\alpha_i}{\alpha_{i-1}} (1 - \chi) = \frac{2k^{5/2}}{R_0} \left(\frac{2\pi m_\mathrm{e}}{h^2} \right)^{3/2} M \frac{Z_i}{Z_{i-1}} \frac{T^{3/2}}{\rho} \exp\left(\frac{E_i}{kT} \right) , \tag{2.7}$$

m_e being the mass of the electron and h the Plank's constant. The above equation can be easily found from the classic one, remembering that the density of the electrons can be written as $n_\mathrm{e} = n(1 - \chi)$, with $n = \rho R_0 / k$. The electrons partition function Z_e has been explicitly substituted for convenience.

2.A.2 Shock-jump equations

From the *shock-jump theory for strong shocks* [47, 48], in the coordinate system of a 1-D shock front moving in a gaseous non-magnetic system, the following balance

equations can be written

$$\begin{aligned}
&\rho_1 v_1 = \rho_2 v_2 && \text{mass continuity}\\
&\rho_1 v_1^2 = \rho_2 v_2^2 + p_2 && \text{momentum continuity}\\
&\frac{1}{2} v_1^2 = \frac{1}{2} v_2^2 && \text{energy continuity}\\
&p_2 = \rho_2 \frac{R_0}{M} T_2 \chi && \text{thermal–pressure equilibrium}\\
&h_2 = \frac{\gamma}{\gamma - 1} \frac{p_2}{\rho_2} && \text{heat equation}
\end{aligned}$$

where 1 and 2 label the ambient gas properties and the shocked particles ones respectively (with ρ the mass density, p the pressure, v the velocity, h the enthalpy, M the molecular weight and γ the effective specific heat of the gas while R_0 being the universal constant of gases,), the density ratio across the shock can be written as

$$\Gamma = \frac{\rho_2}{\rho_1} = \frac{\gamma + 1}{\gamma - 1},$$

which depends only on the specific heat ratio. The shock temperature is then given by

$$T_2 = \frac{M}{R_0} \frac{\Gamma - 1}{\Gamma^2} \frac{v_1^2}{\chi} \tag{2.9}$$

where χ may be determined by the solution of the system of equations (2.7).

For example, for a fully ionized hydrogen gas ($\gamma = 5/3$, $\chi = 2$), one obtains $T_2 = 1.13 \cdot 10^{-5} v_1^2$ as the temperature of the plasma behind the shock.

2.A.3 The Spitzer resistivity

The plasma temperature is strictly related to the collision frequencies of charged particles on which the plasma conductivity strongly depends. The simple Lorentz gas resistivity, can be corrected to account for the effects of the collision range and for the electron-electron interaction, leading to the *Spitzer resistivity* []:

$$\eta = \sigma^{-1} = 65.3 Z \ln \Lambda T_{\mathrm{e}}^{-3/2}\ \Omega\mathrm{m}\,, \tag{2.10}$$

where $\ln \Lambda$ is known as the *Coulomb logarithm*, related to the ratio between the *Debye length* and the 90° electron-ion impact parameter.

CHAPTER 3

The 2D snowplow numerical code

Abstract. The dynamics of a PF device can be simulated using a so called snowplow model, which solves the coupled equations of the external equivalent circuit and of the plasma sheath motion. The model will be here presented in details describing the set of partial differential coupled equations and the methods adopted to solve them numerically.

3.1 The snowplow model

As already stated in Section 1.3.2 and Section 2.2.2, the snowplow model can be a valuable tool for the study of the PF dynamics and its design optimization, once fixed the external circuit parameters.

The code developed is intended to solve the system of coupled equations for the electrical circuit with time-varying parameters, for the motion of the sheath described as a sequence of conical finite elements in cylindrical geometry and for the continuity of mass to take into account the gas swept and ionized by the plasma sheath. The breakdown phase has been modeled through an energetic balance: it is supposed the discharge occurs on the insulator sleeve with perfect axial symmetry when the internal energy due to the ohmic heating has reached a sufficiently high value to ionize at least the 80% of the mass gas contained in the layer; then, at each time-step, the system of partial differential equations is solved by means of finite forward difference methods: the inductance of the new configuration is updated and, from circuit equation, voltage and current are calculated; once the flowing current is known, the magnetic pressure is immediately deduced; it acts normally on each conical element, which is moved solving the momentum equation and taking into account the effects of inertia; the type of gas and its pressure inside the vacuum chamber make possible to evaluate the portion of it swept by each element in its motion; the sheath is maintained connected to the electrodes imposing the boundary conditions on its end-elements. At each time-step a reshape of the sheath is carried out re-normalizing the length of elements, to keep the segment density per unit length constant along the sheath; moreover, the portion of plasma crossing the electrodes is considered lost, as if it recombined in neutral gas in the turbulent tail in touch with the OE.

When the sheath reaches the axis of symmetry, the code stops, since the snowplow model fails to simulate the shock-wave reflection and microscopic interaction inside the focus. The main aim is to find the proper configuration that gives the time correspondence between maximum current obtained by the circuit discharge and plasma collapse in the pinch.

The code is written in modern Fortran 90 making deep use of its object-oriented features and user-defined variable types [49, 50].

3.1.1 Equivalent circuit

The equivalent electrical circuit of a PF device can be modeled as in Figure 1.2: the bank capacitor C_0, charged at a voltage V_0, is connected to a transmission line with resistance R_0 and inductance L_0 through a fast spark-gap switch; during the sheath dynamics, the plasma inductance L_p and resistance R_p vary in time. After the breakdown, the plasma resistance can be usually neglected with respect to the external one.

Letting R_SG be constant resistance associated to the SG and acting during a switching period τ_SG, the equation describing the lumped RLC circuit is

$$\frac{\mathrm{d}}{\mathrm{d}t}((L_0 + L_\mathrm{p}(t))I) + (R_0 + R_\mathrm{SG}(t) + R_\mathrm{p}(t))I = V_0 - \frac{1}{C_0}\int_0^t I(t')\ \mathrm{d}t' \,;$$

it can be split into two simple coupled differential equation in time as follows

$$\frac{\mathrm{d}}{\mathrm{d}t}(L(t)I) + R(t)I = V_{\mathrm{C}}(t)$$
$$\frac{\mathrm{d}V_{\mathrm{C}}(t)}{\mathrm{d}t} = -\frac{I}{C}$$

where $V_{\mathrm{C}}(t)$ is the varying voltage on the capacitor bank, and, for convenience, it has been assumed $L(t) = L_0 + L_{\mathrm{p}}(t)$ and $R(t) = R_0 + R_{\mathrm{SG}}(t) + R_{\mathrm{p}}(t)$. The initial conditions are

$$I(t=0) = 0$$
$$V_{\mathrm{C}}(t=0) = V_0$$

3.1.2 Equation of motion

The shape of the current sheath is described by the position in the plane (r, z) as function of a local coordinate λ along the profile. In this way, the sheath can be modeled as a sequence of infinitesimal elements[1] $\delta\lambda$ with normal unit vector $\widehat{n}(\lambda)$ located in $\vec{r}(\lambda)$. The plasma sheath has a variable thickness, but is considered negligible by the snowplow model: the dynamics of the sheath, and all the parameters related to it, will be studied as if the ionization front coincides with the magnetic piston which drives the current sheath.

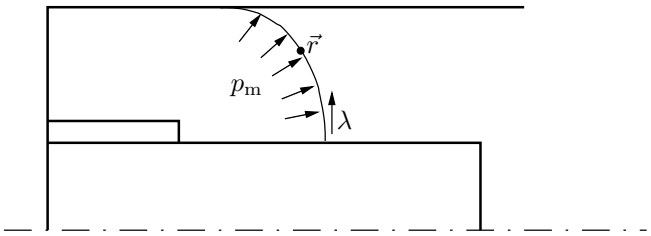

Figure 3.1: Generic plasma sheath profile under the action of magnetic pressure.

Since the mass of each element $\delta\lambda$ changes in time, the momentum equation is

$$\frac{\partial(\delta\vec{p})}{\partial t} = \delta\vec{F}\,, \tag{3.3}$$

where $\delta\vec{p}$ and $\delta\vec{F}$ are referred to an infinitesimal element of length $\delta\lambda$ and are functions of the local coordinate λ and of the time t. The equation is obviously coupled with

$$\frac{\partial\vec{r}}{\partial t} = \vec{v}\,.$$

The force $\vec{F}$ acting on each element of the sheath depends on the current density flowing in it; as the breakdown occurs, the current density $\vec{J}$ flowing in the sheath

[1] The symbol δ will be used to indicate an infinitesimal quantity referred to the infinitesimal element $\delta\lambda$ of the sheath.

interacts with the field of magnetic induction $\vec{B}$ self-induced in the toroidal region of space closed by the current loop. The density of *Lorentz's force* $\vec{J}\times\vec{B}$ per volume unit can be considered as a pressure pushing the sheath away from the insulator (*detachment*) and then towards the end of the electrodes.

In axial symmetry, the magnetic pressure is defined as

$$p_{\mathrm{m}}(r) = \frac{|\vec{B}(r)|^2}{2\mu_0}\,, \tag{3.4}$$

where r is the radial component of vector $\vec{r}(\lambda)$; the field of magnetic induction is related to the current inducing it by the *Biot-Savart's law*:

$$|\vec{B}(r)| = \frac{\mu_0 I}{2\pi r}\,, \tag{3.5}$$

valid on the whole region at the back of the plasma sheath (independently on variable z). Substituting the equation (3.5) into (3.4), it is readily shown that

$$p_{\mathrm{m}}(r) = \frac{\mu_0 I^2}{8\pi^2 r^2} \tag{3.6}$$

is directly proportional to the square of current I and inversely proportional to the square of the distance r from the axis of symmetry.

The magnetic pressure acts normally to each infinitesimal element $\delta\lambda$ of the sheath; the total force on each of them is then

$$\delta\vec{F} = p_{\mathrm{m}}\,\delta S\widehat{n}\,, \tag{3.7}$$

where the infinitesimal surface depends on the radial position of the element by

$$\delta S = 2\pi r\,\delta\lambda\,. \tag{3.8}$$

Substituting the equations (3.6) and (3.8) in (3.7), the generic elementary force is

$$\delta\vec{F} = \frac{\mu_0 I^2}{4\pi r}\,\delta\lambda\widehat{n}\,. \tag{3.9}$$

From the definition of momentum $\vec{p} = m\vec{v}$, the lhs of equation (3.3) can be manipulated in

$$\frac{\partial(\delta\vec{p})}{\partial t} = \frac{\partial(\delta m\vec{v})}{\partial t} = \delta m\frac{\partial\vec{v}}{\partial t} + \vec{v}\frac{\partial(\delta m)}{\partial t}\,;$$

making use of equation (3.9) for the rhs of the same equation, equation (3.3) becomes

$$\frac{\partial\vec{v}}{\partial t} = \frac{1}{\delta m}\left(\frac{\mu_0 I^2}{4\pi r}\,\delta\lambda\widehat{n} - \vec{v}\frac{\partial(\delta m)}{\partial t}\right)\,.$$

The initial condition for position $\vec{r}$ and velocity $\vec{v}$ are

$$\vec{v}(t=0) = 0$$
$$\vec{r}(t=0) = \vec{r}_{\mathrm{ins}}$$

where $\vec{r}_{\mathrm{ins}}$ is a function of (r,z) which defines the boundary of the insulator sleeve.

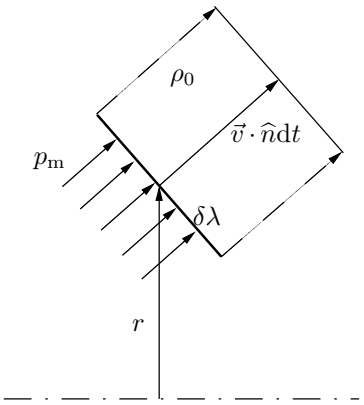

Figure 3.2: Ideal motion of an infinitesimal sheath element $\delta\lambda$ sweeping part of the filling gas.

3.1.3 Mass continuity

The momentum equation contains the variation of mass in time for each sheath element $\delta\lambda$. Its analytical expression can be easily obtained referring to Figure 3.2. In an infinitesimal time interval $\mathrm{d}t$, the sheath element $\delta\lambda$ sweeps the gas contained in a toroidal volume of rectangular section having $\delta\lambda$ and $\vec{v}\cdot\hat{n}\,\mathrm{d}t$ as edges. Since ρ_0 is the mass density of the unperturbed filling gas at the pressure p_0 (considered as an ideal gas), the mass swept is given by

$$\mathrm{d}(\delta m) = \rho_0\,\mathrm{d}(\delta V) = 2\pi\rho_0\, r\,\delta\lambda\,\vec{v}\cdot\hat{n}\;\mathrm{d}t\,,$$

or, better, in the form of a partial difference equation

$$\frac{\partial(\delta m)}{\partial t} = \rho_0\;\mathrm{d}(\delta V) = 2\pi\rho_0\, r\,\delta\lambda\,\vec{v}\cdot\hat{n}\,. \tag{3.11}$$

The equation can be integrated over λ to obtain the variation in time of the total mass of the plasma sheath Λ:

$$\frac{\mathrm{d}m}{\mathrm{d}t} = 2\pi\rho_0\int_\Lambda r\,\vec{v}\cdot\hat{n}\;\mathrm{d}\lambda\,.$$

Assuming s as the initial thickness for the plasma sheath, the condition at $t = 0$ is

$$m(t=0) = m_0 = 2\pi s\int_\Lambda r\rho_0\;\mathrm{d}\lambda\,.$$

3.1.4 Varying inductance

In Section 3.1.1, the inductance of the equivalent circuit was split in a constant term L_0 associated to the external circuit and in a varying contribute $L_\mathrm{p}(t)$ due to the plasma sheath dynamics. This second term can be evaluated making use of the classical formula for the inductance of two coaxial cylinders of radiuses r_int, r_ext and length l, crossed by the same current:

$$L_\mathrm{cyl} = \frac{\mu_0}{2\pi}\,l\,\ln\left(\frac{r_\mathrm{ext}}{r_\mathrm{int}}\right)\,.$$

The formula can be applied to the part of the electrodes already crossed by current sheath, here called *active part*; calling z_{end} the z-coordinate in which the sheath is in contact with the cathode, then the contribution of the active part of the electrodes is given by

$$L_{\text{act}} = \frac{\mu_0}{2\pi} z_{\text{end}} \ln\left(\frac{r_{\text{ext}}}{r_{\text{int}}}\right) .$$

Modeling the current sheath as a sequence of infinitesimal zero-thickness $\delta\lambda$ elements, the equation can be applied to each of them projected along the z-direction, considering another element of the same length, but different radius, crossed by the same current in the opposite direction. During the rundown phase, the generic

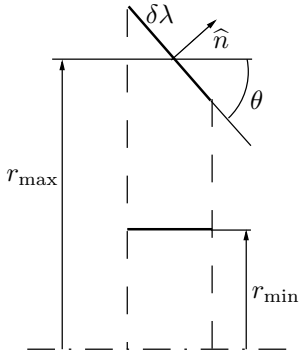

Figure 3.3: Inductance of two coupled infinitesimal elements of current.

element of the sheath can be considered having radius r_{max}, while the second element is located on the inner electrode so that $r_{\text{min}} = r_{\text{int}}$; as soon as the current sheath crosses the end of the electrodes, it can be split into two parts as shown in Figure 3.4: a first part is made by elements $\delta\lambda$ with radius greater than r_{int} and a second funnel-shaped part is made by elements with radius lower than r_{int}. If one supposes that the IE is extended to cross the current sheath, than the inductance can be calculated as the sum of the two contributes.

Each sheath element gives a contribution δL of the form

$$\delta L = \frac{\mu_0}{2\pi} \delta\lambda \cos\theta \ln\left(\frac{r_{\text{max}}}{r_{\text{min}}}\right) ,$$

where θ is the angle between the element $\delta\lambda$ and the z-direction as a function of λ, so that $\delta\lambda\cos\theta = \delta z$ represents the projection of the element along z; r_{min} and r_{max} depend on the position λ on the sheath profile, according to the following piecewise functions of λ

$$r_{\text{max}} = \begin{cases} r(\lambda) & \text{if} \quad r_{\text{int}} \le r(\lambda) < r_{\text{ext}} \\ r_{\text{int}} & \text{if} \quad r(\lambda) < r_{\text{int}} \end{cases}$$

$$r_{\text{min}} = \begin{cases} r_{\text{int}} & \text{if} \quad r_{\text{int}} \le r(\lambda) < r_{\text{ext}} \\ r(\lambda) & \text{if} \quad r(\lambda) < r_{\text{int}} \end{cases}$$

Taking into account the inductance of the active part of the electrodes and in-

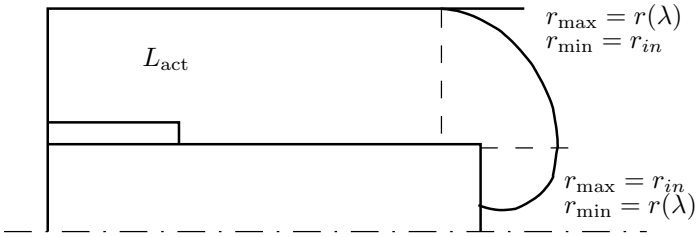

Figure 3.4: Split of inductance calculation.

tegrating the δL contributions over the whole current sheath Λ, the total varying inductance is given by:

$$L_{\text{p}} = L_{\text{act}} + L_{\text{cs}} = \frac{\mu_0}{2\pi}\left(z_{\text{end}} \ln\left(\frac{r_{\text{ext}}}{r_{\text{int}}}\right) + \int_{\Lambda} \cos\theta \ln\left(\frac{r_{\max}}{r_{\min}}\right)\, \mathrm{d}\lambda\right), \qquad (3.12)$$

where the spatial coordinate z_{end}, $r_{\max}$ and $r_{\min}$ are functions of time.

Before breakdown occurs, the inductance of the equivalent circuit is only due to the external one, so the initial condition is given by

$$L(t=0) = L_0\,.$$

3.1.5 Internal energy equation and breakdown model

The breakdown of both the SG and the PF have been modeled through simple macroscopic considerations.

Due to the features of plasma fast switches, the SG is substituted by a constant resistance R_{SG} acting from $t = 0$ to $t = \tau_{\text{SG}}$.

The breakdown model is based on the plasma sheath ohmic heating. Fixed a thickness of the gas layer lying on the insulator sleeve, it mass is deduced by the pressure of the filling gas. Its resistance can be experimentally related to the internal energy of the gas through [51, 52]

$$R_{\text{p}} = R'_{\text{p}}\left(1 - \frac{E}{E_{\text{ion}}}\right),$$

where E is the average internal energy of the layer and E_{ion} is the energy necessary to fully ionize it. The constant R'_{p} is related to the pressure p of the gas and is experimentally given by

$$R'_{\text{p}} = \left(\frac{0.18}{p}\right)^{\frac{1}{3}}$$

with p expressed in mbar. The ionization energy density is about $6.5 \cdot 10^8$ J/kg for diatomic deuterium.

The time variation of the gas layer internal energy is given by the ohmic law:

$$\frac{\mathrm{d}E}{\mathrm{d}t} = R_{\text{p}} I^2 = R'_{\text{p}}\left(1 - \frac{E}{E_{\text{ion}}}\right) I^2\,.$$

when the internal energy reaches the 80% of E_{ion}, the layer is assumed to have developed into a CS, sufficiently conductive to be pushed by the MP.

The sheath internal energy is updated during the whole simulation, but, just after the detachment phase, it results in a plasma resistance completely negligible if compared to the external circuit one. Being a 0-dimensional property of the layer, the internal energy is modified proportionally to the global mass of the CS.

3.1.6 System of coupled equations

From previous sections (3.1.1 to 3.1.4) the following system of coupled equations can be built

$$\frac{\mathrm{d}E}{\mathrm{d}t} = R'_{\text{p}} \left(1 - \frac{E}{E_{\text{ion}}}\right) I^2$$

$$\frac{\mathrm{d}(LI)}{\mathrm{d}t} = V_C - RI$$

$$\frac{\mathrm{d}V_C}{dt} = -\frac{I}{C}$$

$$L = L_0 + \frac{\mu_0}{2\pi} \left(z_{\text{end}} \ln\left(\frac{r_{\text{ext}}}{r_{\text{int}}}\right) + \int_\Lambda \cos\theta \ln\left(\frac{r_{\max}}{r_{\min}}\right) \, \mathrm{d}\lambda \right)$$

$$\frac{\partial \vec{v}}{\partial t} = \frac{1}{\delta m} \left(\frac{\mu_0}{4\pi} \frac{I^2}{r} \, \delta\lambda \widehat{n} - 2\pi\rho_0 r \delta\lambda (\vec{v} \cdot \widehat{n}) \vec{v} \right)$$

$$\frac{\partial \vec{r}}{\partial t} = \vec{v}$$

$$\frac{\partial(\delta m)}{\partial t} = 2\pi\rho_0 r \delta\lambda (\vec{v} \cdot \widehat{n})$$

with initial conditions

$$E(t=0) = 0$$

$$I(t=0) = 0$$

$$L(t=0) = L_0$$

$$V(t=0) = V_C$$

$$\vec{v}(t=0) = 0$$

$$\vec{r}(t=0) = \vec{r}_{\text{ins}}$$

$$m(t=0) = m_0 = 2\pi s \int_\Lambda r\rho_0 \, \mathrm{d}\lambda$$

Moreover, the breakdown conditions reflects on the sheath as

$$\vec{v}(t \le t') = 0$$

$$\vec{r}(t \le t') = \vec{r}_{\text{ins}}$$

with t' given by the condition $E(t') = 0.8E_{\text{ion}}$.

Defining $\vec{r}_{\text{int}}(r,z)$ and $\vec{r}_{\text{ext}}(r,z)$ as the functions describing the boundary of the inner and OE respectively, the boundary conditions are simply given by

$$\vec{r}(\lambda = 0) \in \vec{r}_{\text{int}}$$

$$\vec{r}(\lambda = \lambda_{\text{end}}) \in \vec{r}_{\text{ext}}$$

where $\lambda_{\text{end}}(t)$ represents the last possible value for the local variable λ.

3.2 Numerical model

To solve the system of coupled equations numerically, a proper discretization in time and space is needed. The logical sequence of instructions will be described in details.

The code is entirely written in modern Fortran 90 [49, 50]; the user-defined variable types and the related functions and subroutines allow to have an easy-to-read code.

3.2.1 Time discretization

The obtained differential equations in time can be numerically solved only if discretized over the variable t. The derivatives in time are solved using the Euler method with forward finite differences. The generic equation

$$\frac{\mathrm{d}y}{\mathrm{d}t} = f(y)\,, \tag{3.17}$$

becomes

$$y^{(h+1)} = y^{(h)} + f(y^{(h)})\Delta t\,,$$

where the superscript (h) is used to denote the generic time iteration and Δt is the time-step.

In the most general case, the function f will depend on time variable physical quantities and on the local coordinate along the current sheath. To solve each equation a subroutine based on the Euler method has been employed; it gets as input parameters the rhs of the differential equation in the form of (3.17) and a reference parameter for the segment of the sheath discretization.

The time-step must be small enough to ensure a good accuracy of the method and avoid an excessive growth of the current in a single time-step. It can be chosen starting from simple considerations on a lumped RLC circuit with constant parameters $R = R_0$, $C = C_0$ and $L = L_0 + L_{\mathrm{el}}$ where L_{el} is the inductance of the electrodes as if short-circuited at their open end. Preliminary tests were performed and a time-step was fixed as a function of the lumped RLC time-constant, in order to obtain a relative error less than 3% with respect with the analytical solution.

3.2.2 Space discretization

Only the local variable λ is discretized, since the current sheath is modeled as a sequence of connected finite elements with a fixed density η per unit length. The subscript i will be used to denote the generic i-th segment of the sheath. Each one is defined by the coordinates (r, z) of the two extreme points, called nodes; making use of them, it is possible to define the geometrical characteristics of the segment: length l_i, length Δz_i, Δr_i of the projections on z and r directions, normal direction $\widehat{n}_i$ and mid point $\vec{\overline{r}}_i$.

Making use of the user-defined variables and structures allowed by Fortran 90, the sheath element has been defined as a structure containing all the just mentioned properties of the segment and the physical quantities referred to it, like mass m_i and velocity $\vec{v}_i$. Moreover, the two nodes are defined as pointers (one of them as target) linked to the same node on the adjacent sheath element; in this way the

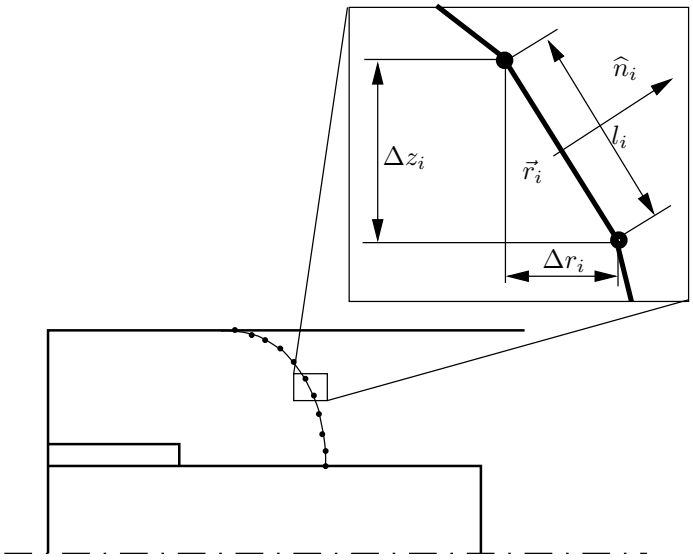

Figure 3.5: Discretization of the current sheath in finite elements.

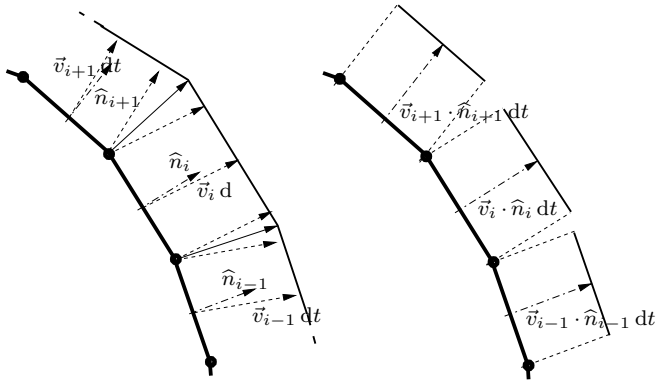

Figure 3.6: Motion and mass sweeping for the generic i-th element.

continuity of the sheath is always preserved, since moving the second node of i-th segment is the same as moving the first of $(i+1)$-th segment. Every-time a node changes, the segment is reinitialized calling a specific subroutine which refers to user-defined functions and operators.

Each equation depending on λ has to be rewritten for the generic i-th segment and solved for i going from 0 to the $(n-1)$-th segment, where n is the total number of segments. At each time-iteration, the sheath is moved calculating the mean velocity between adjacent elements and using it to evaluate the final position of the common node. During its motion, each segment sweeps a portion of gas according to the equation (3.11), where the scalar product is modified in $\vec{v}_i \cdot \hat{n}_i$.

On the extreme nodes, the sheath is bounded to the inner and outer electrodes cutting the part that eventually crosses the OE during the time-step. The corresponding mass is considered lost as if the plasma recombines in neutral gas, interacting with the grounded wall. The boundary conditions and sheath development at the end of the inner electrode is a delicate subject and should be treated using the shock-wave diffraction theory [47, 48]. In the case of closed IE it is known that, when reaching a similar discontinuity, the shock-wave front starts moving downwards at half the velocity in the z-direction. In the case of hollow electrode the correct condition is still under investigation.

The main problem connected with the sheath discretization is related to its motion. While during the rundown phase the sheath approximately conserves its length, entering the collapse phase the sheath starts growing. Moreover during the detachment from the insulator, the discontinuity in curvature makes some elements growing faster than others, depending on the direction of the velocity vector $\vec{v}_i$. At each time iteration the sheath needs to be reshaped with elements of the same length: being η the density of segments per unit length and $l_{\text{tot}}^{(h)}$ the total length of the current sheath, the number of segments is recalculated as $\eta\, l_{\text{tot}}^{(h)}$ and the nodes redistributed on the old elements starting from the inner boundary. Modifying the elements length, also the mass and momentum have to be proportionally redistributed on the new sheath on the basis of conservation principles.

The segment density η must be properly chosen to have a good discretization of the sheath. The best way is to base it on the inter-electrode gap $(r_{\text{ext}} - r_{\text{int}})$, by subdividing it in a fixed number of parts and using the obtained length as the inverse of η. As done for the time-step, this way to choose the discretization parameters is strongly close to a sort of a-dimensionalization of the problem.

3.2.3 Set of numerical equations

After time and space discretization, the system of coupled equation obtained in Section 3.1.6 becomes

$$
\begin{aligned}
E^{(h+1)} &= R'_{\mathrm{p}} \left(1 - \frac{E^{(h)}}{E_{\mathrm{ion}}}\right) (I^{(h)})^2 \Delta t \\
I^{(h+1)} &= \frac{1}{L^{(h+1)}} (L^{(h)} I^{(h)} + (V_C^{(h)} - R I^{(h)}) \Delta t) \\
V_C^{(h+1)} &= V_C^{(h)} - \frac{I^{(h)}}{C} \Delta t \\
L^{(h+1)} &= L_0 + \frac{\mu_0}{2\pi} \left(z_n^{(h+1)} \ln\left(\frac{r_{\mathrm{ext}}}{r_{\mathrm{int}}}\right) + \sum_{i=0}^{n-1} \cos\theta_i^{(h+1)} \ln\left(\frac{r_{i,\max}^{(h+1)}}{r_{i,\min}^{(h+1)}}\right) \right) \\
\vec{v}_i^{(h+1)} &= \vec{v}_i^{(h)} + \frac{1}{m_i^{(h)}} \left(\frac{\mu_0}{4\pi} \frac{(I^{(h)})^2}{r_i^{(h)}} l_i^{(h)} \hat{n}_i^{(h)} - 2\pi\rho_0 r_i^{(h)} l_i^{(h)} (\vec{v}_i^{(h)} \cdot \hat{n}_i^{(h)}) \vec{v}_i^{(h)} \right) \Delta t \\
\vec{r}_i^{(h+1)} &= \vec{r}_i^{(h)} + \vec{v}_i^{(h)} \Delta t \\
m_i^{(h+1)} &= m_i^{(h)} + 2\pi\rho_0 r_i^{(h)} l_i^{(h)} (\vec{v}_i^{(h)} \cdot \hat{n}_i^{(h)})
\end{aligned}
$$

with initial conditions

$$
\begin{aligned}
E^{(h=0)} &= 0 \\
I^{(h=0)} &= 0 \\
L^{(h=0)} &= L_0 \\
V^{(h=0)} &= V_C \\
\vec{v}^{(h=0)} &= 0 \\
\vec{r}^{(h=0)} &= \vec{r}_{\mathrm{ins}} \\
m_i^{(h=0)} &= 2\pi\rho_0 s r_i^{(h=0)} l_i^{(h=0)}
\end{aligned}
$$

Boundary conditions are treated as described in Section 3.2.2.

3.2.4 Flow chart

The sequence of operations followed by the code is summarized in Figure 3.7.

After reading the known parameters from a formatted input file, a sheath is generated with the same profile of the insulator sleeve and a fixed thickness. Calling the general procedure for the reshape, the sheath is split into a proper number of elements according with the fixed segments density η.

The internal energy is updated together with the circuit parameters, until the CS is formed. Then, the inductance L_{p} can be calculated and used as new value to solve the circuit equations calling the Euler routine. Then, the mass continuity equation and the momentum equation are solved for each element of the current sheath; as the nodes coordinates are updated, the segments properties are recalculated. Once finished the iterative cycle over the elements, boundary conditions are applied to the

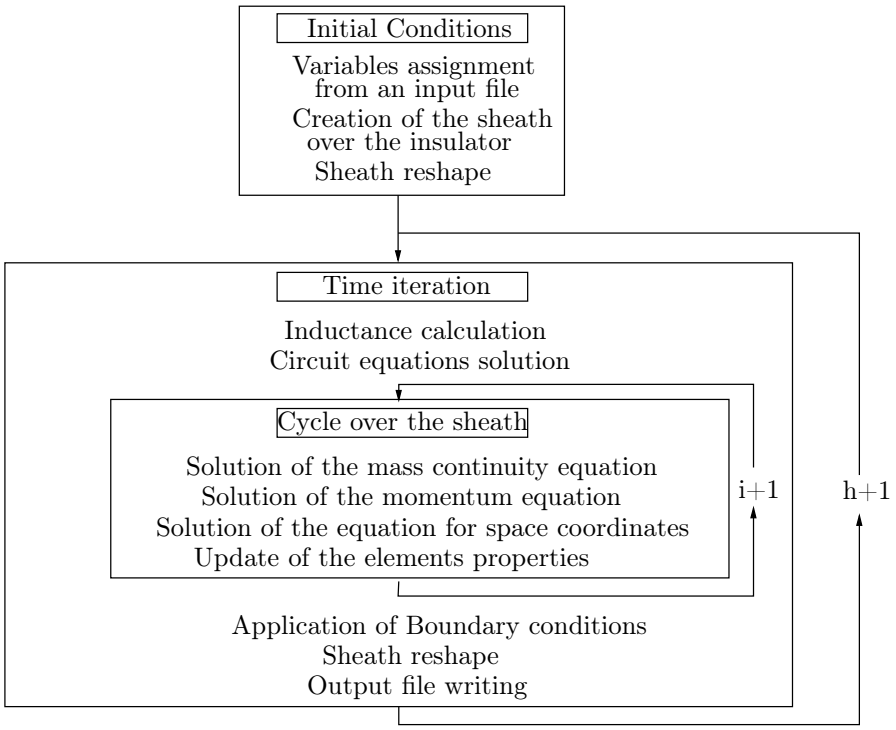

Figure 3.7: Sequence of operation in the numerical code.

first and last node and the new sheath is reshaped. At the end of the time iteration the physical quantities of interest are printed in an output file.

These operations are repeated until the minimum radial coordinate of the sheath elements mid-points reaches a position close to the symmetry axis. The value $r_i = 0$ is not allowed, since it would generate a divergent magnetic pressure.

3.3 Future improvements

The developed code presents some innovative features based essentially on geometry versatility: the IE can be hollow or closed at a specified z-coordinate and the insulator sleeve can have an outer radius equal to the IE one (0-thickness) or even a 0-length and a thickness equal to $r_{\text{ext}} - r_{\text{int}}$. Moreover the graphical user interface improves the speed in the optimization procedure.

Even if simulations are in good agreement with experimental results, several aspects could be improved.

A deep study on the shock wave propagation and reflection should be done to improve the conditions at IE ending edge. Then, another interesting aspect could be the analysis of non conventional electrodes layouts to improve the device performances.

Mass continuity equation is not completely correct, since it is supposed the i-th sheath element moves accordingly to $\vec{v}_i \cdot \widehat{n}_i$ and not to $\vec{v}_i$. Even considering the velocity vector and not its projection, the result wouldn't change much, since the

short time-step in use makes the differences negligible. A more accurate formulation could be obtained evaluating the area of each quadrilateral having two adjacent nodes at iteration h and $h+1$ as vertexes; however this would require the knowledge of the new positions before calculating the swept mass: the new formulation of momentum and mass continuity equation would change becoming strong coupled and requiring an iterative method of subsequent approximation to be solved.

Also external circuit model could be improved. A crucial aspect in the design of the PF external circuit is represented by the problem of impedance mismatch: if the impedance of different branches in series are not equal, then part of the electric power is not transmitted but reflected back producing a decrease in performances and electromagnetic noise in probes signals. A correction factor less than 1 multiplying current I could be introduced to decrease the nominal power transmitted from the bank energy to the PF electrodes. However, the only way to evaluate the needed correction is a proper study of the external circuit components and is not strictly connected with the code optimization.

Looking at the numerical side, some improvements could be useful. The Euler method to solve the system of coupled equations could be substituted by a corrector-predictor one, by a Runge-Kutta higher order method, or by an implicit method implementation. In each case, the main result would be a possible increase of the time-step and a subsequent speed-up of the code, but it seems not so necessary on modern computers.

Another little improvement could touch both the numerical and theoretical side. As mentioned, the time-step Δt and segment density η are chosen on the basis of the external circuit characteristic time and inter-electrode gap respectively. This choice is in some way similar to a dimensionless process on the physical quantities. Numerically speaking, reducing the problem to a dimensionless one can have two different aims: one is the decrease of computations obtained collecting multiplication factors; the other one is that the code could be depurate by fixed parameters that could bring to numerical instabilities for some particular configuration. From the physical point of view, the a-dimensionalization process usually produces dimensionless numbers which characterize the problem under examination. Starting from them, some rule for optimization could be deduced.

Finally, the optimization procedure for the PF design could be made easier if done automatically by the code itself. Defining a range of variability for the input parameters and few behavioral rules, the code could change the device configuration to reach an optimal configuration.

3.A Detailed description of the code

To make the code comprehension, usability and maintenance easier, the structure of directories and the files content are examined in detailed. Moreover, a deep analysis of subroutines and functions is proposed. Finally, a graphical user interface to the program will be presented.

3.A.1 Directories and files

The root of the archive contains the following directories:

– `sources` collects the source files (`.f90`, `.mod`, `.o` and a local `Makefile`);

– `input` contains an example for the input file;

– `output` will contain the output files (one directory for each project title);

– `matlab` collects the matlab script files for the GUI;

Moreover, a `Makefile` is given in the main directory. It refers to the Intel Fortran Compiler for Linux platforms to resolve dependencies between modules (`install` option) and to generate the executable file (`all` option) in the root directory; the options `cleanobj`, `cleanmod` and `cleanall` provide a rapid tool to remove the `.o` object files, the `.mod` files and both of them respectively.

The files dependencies are shown in Figure 3.8; the files contents will be readily described.

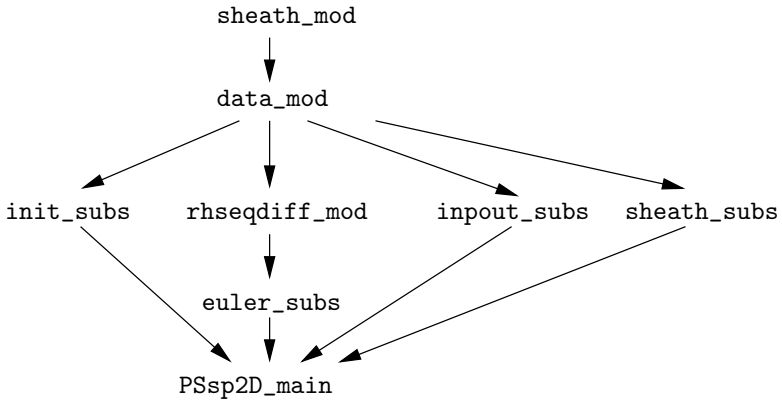

Figure 3.8: Source files dependencies.

3.A.2 Source files and code structure

The modular capabilities of Fortran 90 have been widely used. The source file names end with "`_subs`" if containing subroutines or modules of subroutines, and with "`_mod`" if containing modules with data or user-defined constructors.

`sheath_mod`

The file contains the main module, called `SEGfunction`, used to model the plasma sheath via user-defined variables and extended operators.

First of all, two user-defined structures are used to define a point (`Coord2D`) and a vector (`Vec2D`) in the (r, z) plane of the sheath. In this way the nodes and vectors characteristic of each segment can be declared and each component can be easily referred to. Making use of these two structures, another one, called `Seg2D`, is defined for the generic segment of the sheath. The first two elements (`node1`, `node2`) are two pointers of `Coord2D` type used to define the nodes of the sheath: in this way making the second one to point to the first of the adjacent segment, it is easy to avoid

problems with the sheath continuity and one can refer to the first of the i-th segment as well as to the second of the $(i-1)$-th one. Moreover the structure contains the coordinates of the segment mid-point (`ptoM`, `Coord2D` type), its normal unit vector (`nVEC`, `Coord2D` type), the radial and axial components differences (`rDELTA` and `zDELTA`, `real`) and its total length (`lengthSEG`, `real`); also physical quantities as mass (`mass`, `real`) and momentum (`vVEC`, `Vec2D` type) are associated to the segment. As last, two pointers of `Seg2D` type, named `nextSeg2D`and `prevSeg2D`, point to the previous and next segment along the sheath profile. The properties of the linked lists are here very useful, most of all in the routine of the sheath remapping (see `SheathReshape`).

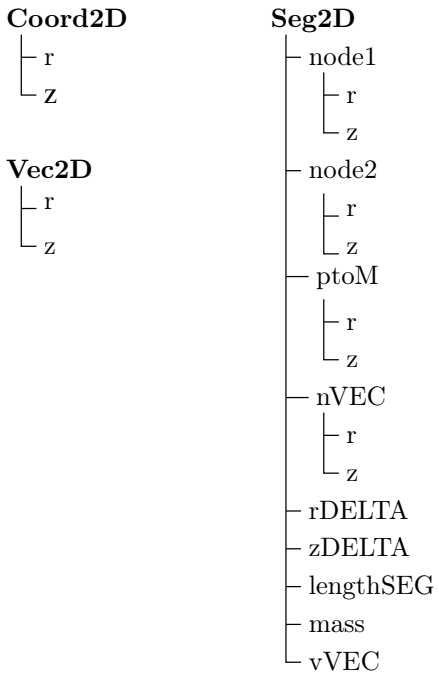

Figure 3.9: User-defined structures for 2D points, vectors and sheath elements.

In the same module, the basic operators are extended to the user defined type `Coord2D` and `Vec2D`. In particular

- `FUNCrDELTA(SEG)`, `FUNCzDELTA(SEG)` act on a `Seg2D` to calculate its `rDELTA` and `zDELTA`;
- `FUNClenghtSEG(SEG)` returns the length of the segment;
- `FUNCptoM(SEG)` returns the (r, z) coordinates of the segment;
- `sumCoord2D(rz1,rz2)` can be used to sum coordinate by coordinate two nodes;
- `FUNCnormal(SEG)` making use of `rDELTA`, `zDELTA` and `lengthSEG` calculates the normal unit vector to the segment `SEG`;
- `sumVec2D(VEC1,VEC2)` sums component by component two 2D vectors;

- `vectorialAVERAGE(SEG1,SEG2)` calculates the vectorial average of the two momentum vectors of `SEG1` and `SEG2`;
- `divVec2Dscalar(VEC1,a)` divides the two `Vec2D` components of `VEC1` by a scalar `a`;
- `prodVec2Dscalar(VEC1,a)` multiplies the two `Vec2D` components of `VEC1` by a scalar `a`;
- `DOTproduct(VEC1,VEC2)` makes the scalar product of two vectors `VEC1` and `VEC2`;
- `CROSSr(SEG,ASCr)` allows to calculate the intersection between a line perpendicular to the z axis and passing for $(0, \texttt{ASCr})$ and the line that contains `SEG`;
- `CROSSz(SEG,ORDz)` the same of `CROSSr` but for the intersection with a line parallel to z axis.

`data_mod`

This source file contains all the module of data definition. In particular,

- `SEGdata` contains the segment identity, the maximum length of each one and the first node of the linked list representing the sheath;
- `SHEATHvec` contains mainly global and temporary variables and parameters related to the sheath;
- `GEOMdata` fixes as global all the geometrical parameters that define the domain;
- `GASdata` contains data of the filling gas and other physical constants of interest;
- `RLCdata` define all the RLC electrical parameters;
- `TIMEstep` contains simulation parameters for the time dependent numerical solution;
- `IOoperation` fixes few indexes for the input/output operations.

The modular definition of the variables allow to call for the proper modules where necessary.

`sheath_subs`

The file contains all the subroutine related to the sheath development and reshape. A brief description will follow for each of them:

- `segSETUP` initializes the generic segment, fed as dummy parameter, through the functions contained in `sheath_mod`;
- `FINDrMIN` identify the minimum radial coordinate of the sheath profile, necessary to stop the simulation;

- `MAPO` is used to initialize the plasma sheath over the insulator sleeve creating two or one segments, depending on the insulator geometry; the subroutine `sheathRESHAPE` will then redistribute the nodes over it;
- `BOUNDARYnodes` imposes the boundary condition of continuity between the sheath and the electrodes; during the sheath motion the first node could detach from the IE while the last usually crosses the OE, so their position must be redefined and the total mass updated;
- `sheathRESHAPE` remap the sheath profile to maintain a fixed segment density and to proportionally preserve the mass between the two profiles; this subroutine acts independently from the geometrical parameters of the domain since the call to `BOUNDARYnodes` has already fixed the boundary conditions;
- `INDUCTANCE` updates the inductance of plasma gun taking into account the contributes of the sheath profile and the swept part of the IE.

`init_subs` and `inpout_subs`

The file `init_subs` contains few subroutines oriented to the check of the input parameters and to the simulation and auxiliary initializations.

- `initFILEinp` checks the existence of the specified input file and stops the program if it is not found;
- `GEOMcheck` checks the compatibility of the geometrical input parameters printing error messages on the stdout in case of inconsistencies;
- `initFILEout` creates the output directories for the project specified in the input file and initializes the units for the output operations;
- `initPARAM` performs few simple conversions and initializes the necessary simulation parameters (density of segments, printing indexes, boundary conditions indexes, ...);
- `initialCOND` fixes the initial conditions for the simulation start up.

The file `inpout_subs` contains two main subroutines, one for the input (`readINP`) and one for the output operations (`printOUT`). The first reads sequentially the file fed in input skipping the lines starting with "!" that are considered as comments. The subroutine `printOUT` prints on the proper files the sheath properties (nodes coordinates, mass, velocity, ... on `sheath.dat`), the circuit parameters (V, I, L, $\mathrm{d}I/\mathrm{d}t$ on `electric.dat`) and the frames for the animation of the sheath profile. Other files (`firstlastnodes.dat` and `sheathvel.dat`) are used for the extreme nodes position and velocities and for the sheath macroscopic velocity along the axial and radial directions.

`rhseqdiff_mod` and `euler_subs`

As described in Section 3.2.3, the euler method allow to write each differential equation in a discrete form in time where the value at the next time instant is given by

the previous one plus an advancing term multiplied by the time-step. Exploiting the simple feature of the method, all the advancing functions of each differential equation of interest are contained in a single file (`rhseqdiff_mod`). The external subroutine contained in `euler_subs`, then, calls the external function passed as dummy parameter and solves the differential equation.

`PFsp2D_main`

The main program follows the flow chart of Figure 3.7. After the check on the input file, it is read and the initialization and control of the geometry and other parameters are performed. The initial conditions are, then, calculated and imposed and the main time cycle is started. The set of differential equations for the circuit is solved for the inductance calculated for the initial sheath profile; iteratively the nodes of the sheath are pushed and the boundary conditions imposed on the extreme nodes, just before the sheath is reshaped to preserve the segment density. All the time dependent variables are printed out. At last, the minimum radial coordinate of the sheath profile is evaluated to stop or continue the time cycle.

3.A.3 Graphical User Interface (GUI)

To improve the code usability and increase the speed for the procedures of input generation and output manipulation, a user-friendly graphical interface was developed exploring the capabilities of the *Matlab UI-tools* in a UNIX environment. In Figure 3.10, the mask for the input parameters is presented.

The interface allows the user to generate a new input file or to load and modify an old one through a generic file selection window (see Figure 3.11); a check on the input parameters is made and a preview of the resulting geometry is created, as shown in Figure 3.12. The execution is performed calling the stand-alone F90 compiled code, giving the chosen file as input or the just created one.

After the execution is terminated, a new interface window, shown in Figure 3.13, is opened. A list of physical quantities is presented and the user can choose which to plot in abscissas and ordinates.

Moreover, a script to generate the sheath profiles in a 2D geometry is accessible. Another script is callable to create a rendered 3D movie of the sheath dynamics (three merged snapshots are presented in Figure 3.17).

By the exam of the obtained results the user can simply go back and modify the input parameters to improve the device performances.

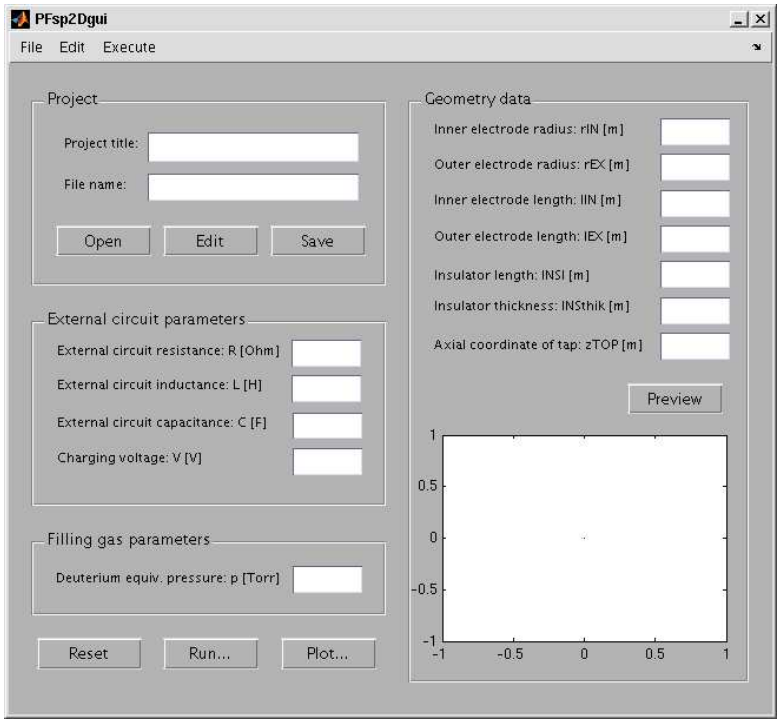

Figure 3.10: Graphical User Interface in the Matlab environment.

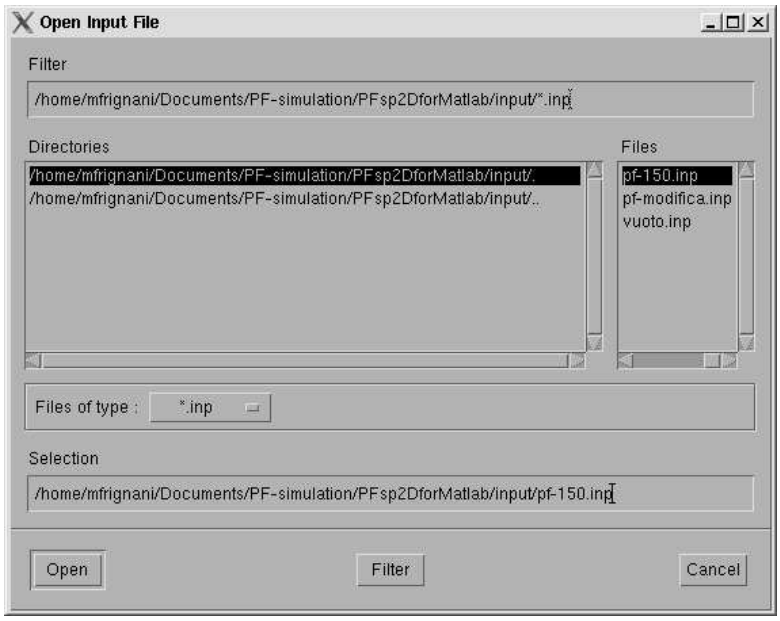

Figure 3.11: Input file selection.

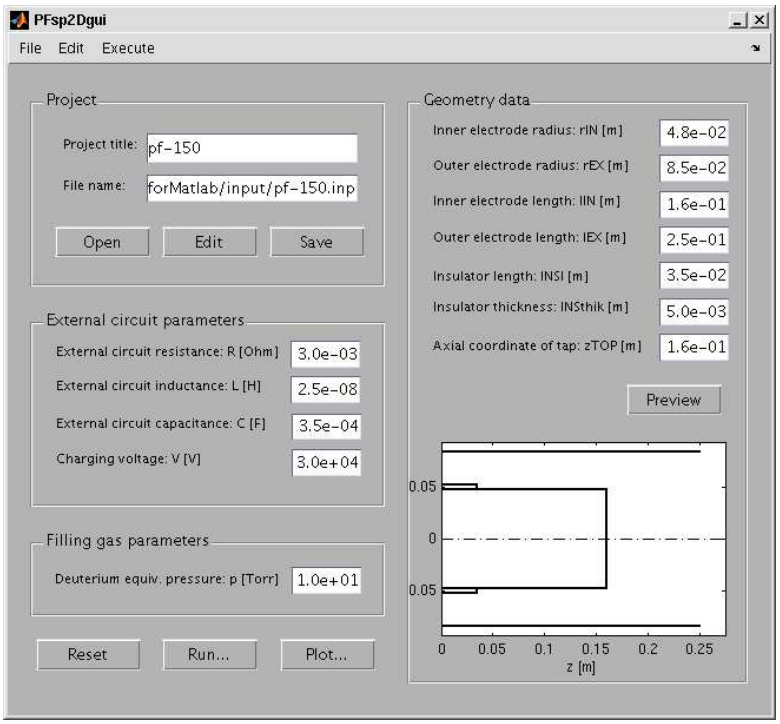

Figure 3.12: Input parameters and geometry preview.

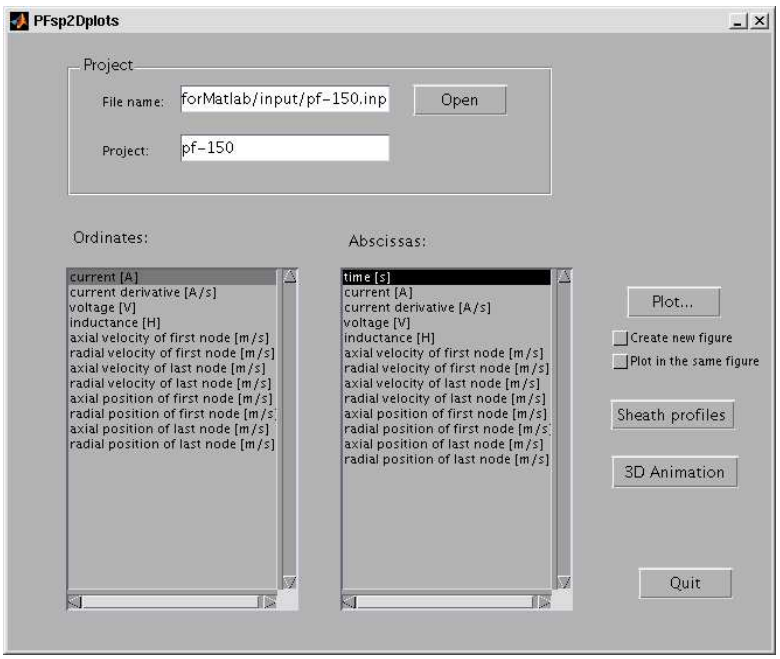

Figure 3.13: Plot utility.

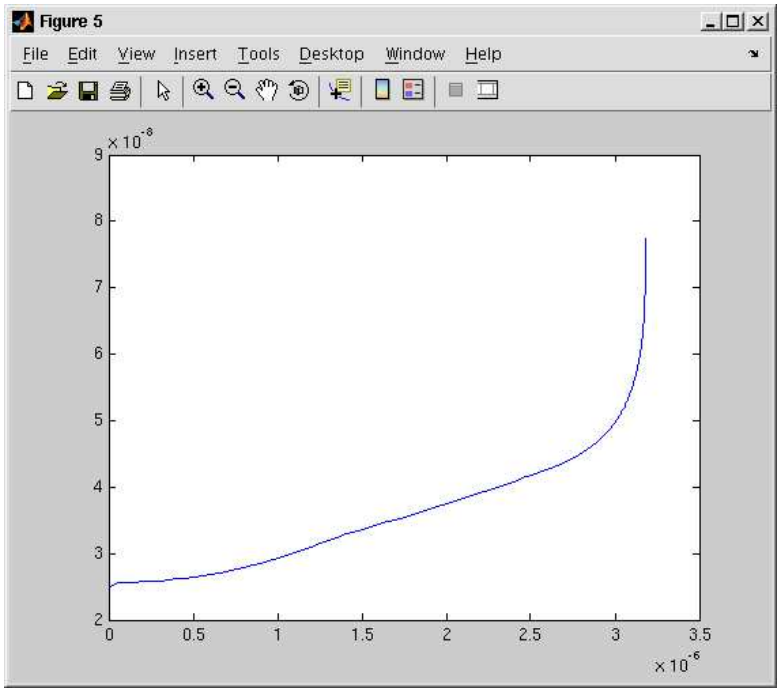

Figure 3.14: Plot of total inductance vs. time.

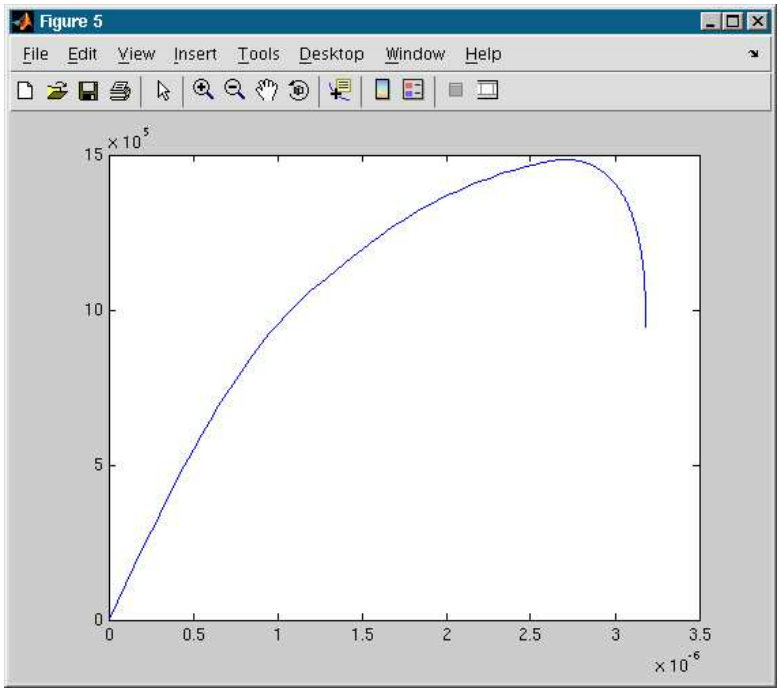

Figure 3.15: Plot of current vs. time.

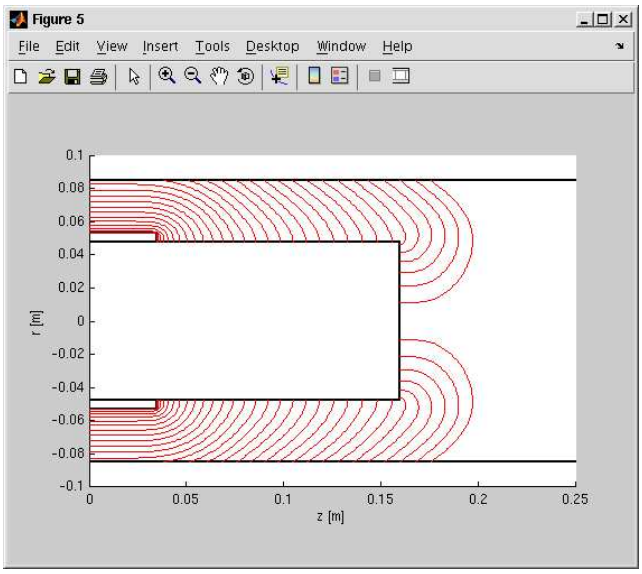

Figure 3.16: Plot of sheath profiles.

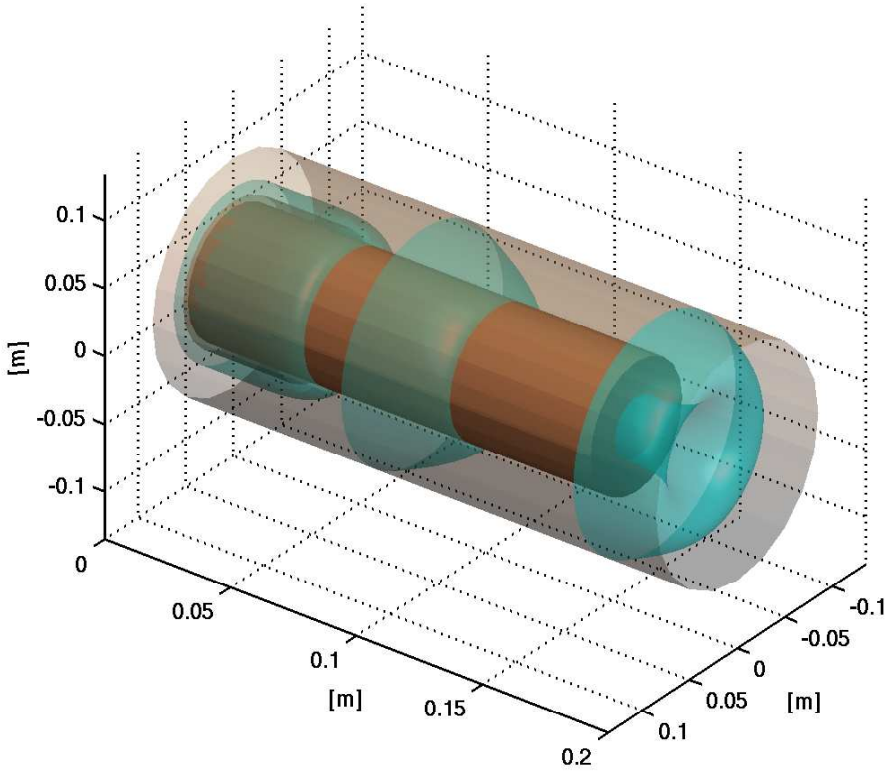

Figure 3.17: 3D profiles of the current sheath at three different temporal stages (detachment, rundown, collapse).

CHAPTER 4

Electrodes design

Abstract. The results of the snowplow model presented in the previous Section are here proposed. First of all, a real device, operated in the facility of the Laboratory of Nuclear Engineering in Montecuccolino, is simulated and the results compared with other theoretical and numerical models and with available experimental data. Then, the design of the PFMA1 electrodes will be presented.

Working parameter	Value
Charging voltage (V_0)	$20 \div 25$ kV
Bank capacitance (C_0)	7.2 µF
Total inductance (L'_0)	91 nH
Electrodes inductance (L_0)	75 nH
External resistance (R_0)	8.67 mΩ
Maximum bank energy (E)	3.24 kJ
Ideal peak current ($I_{0,\max}$)	220 kA
Discharge frequency (ω)	1.2 MHz
Filling gas pressure (p_{D_2})	$1.5 \div 3$ mbar
Repetition frequency (f)	1 Hz
IE external radius (r_{int})	1.2 cm
OE external radius (r_{ext})	2.4 cm
Electrodes length (l)	11.6 cm
Insulator length (l_{ins})	3.4 cm
Insulator thickness (s_{ins})	0.5 cm

Table 4.1: Electrical, operational and geometrical parameters of the PF of Montecuccolino. The inner electrode is hollow and a thickness of 1 mm is assumed for it. According to typical values for SG switches, it has been chosen $R_{\text{SG}} = 0.25\ \Omega$ and $\tau_{\text{SG}} = 5$ ns.

4.1 Test of the snowplow model

The snowplow code is run for a real device in order to better understand the behavior of the PF discharge from the point of view of the plasma sheath and equivalent electrical circuit. The numerical results are then compared with other available models and experimental data.

4.1.1 The Plasma Focus of Montecuccolino

The Montecuccolino PF is a compact Mather type device designed to be a repetitive pulsed source of neutrons from D_2 fusion reactions [53]. Due to the reduced overall dimensions, bank capacitance is quite low and external inductance rather high: massively parallelization was not possible and plates connections not so efficient as coaxial configuration (see Chapter 5 for more details on the subject). The electrical parameters are summarized, as obtained through short circuit tests [54], in Table 4.1 together with other operational parameters of interest and electrodes and insulator dimensions.

The best experimental results on the neutron yield were obtained operating the PF at a charging voltage of 25 kV and a filling deuterium pressure of 2.67 mbar. The hereafter presented results will be referred to these working parameters.

Starting from the current profile in time, the first half quarter of a typical RLC can be immediately identified in Figure 4.1. The maximum current $I_{\max} = 203.2$ kA is obtained at $t_{\max} = 1.1$ µs; however the simulation does not stop at this point, but

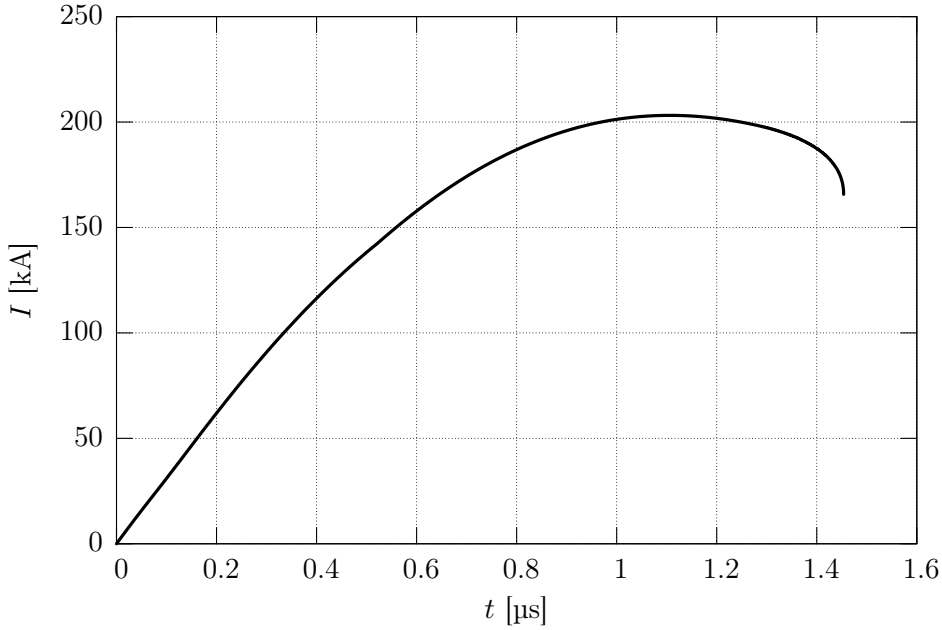

Figure 4.1: Current profile versus time as obtained through the snowplow simulation of the Montecuccolino PF, operating at 25 kV and a filling deuterium pressure of 2.67 mbar

the plasma sheath still advance and collapse introducing an high voltage drop due to the inductance derivative, which is the main cause of the current dip at the end of the waveform.

Dwelling upon the inductance profile (presented in Figure 4.2), it is easy to distinguish the three main phases of the sheath development: the inductance rises strongly during the detachment of the sheath from the insulator; once reached the outer electrode the sheath profile is essentially constant during the whole rundown, thus producing a linear growth of the inductance; finally the collapse phase is characterized by the greater inductance derivative, which induces the higher voltage drop.

Due to the breakdown model, even the overall resistance is time dependent. From Figure 4.3, the three characteristic phases arise evident: in times of the order of few ns, the spark gap switch is closed and its resistance suddenly decreases up to be negligible. A second contribute comes from the plasma resistance, which is lowered through dissipative ohmic heating proportionally to the current I, being related to the internal energy of the plasma. Starting from values of the order of 0.1 Ω, it results almost negligible after less than two hundreds of ns, and only the constant contribute of the external circuit remains.

Other electrical quantities of interest are the voltage on the bank capacitors and the current derivative, reported in Figure 4.4 and 4.5 respectively. As expected, the voltage presents a cos-like behavior. The current derivative, instead, is an experimental data of interest since obtained by not-self-integrated Rogowski coils; here,

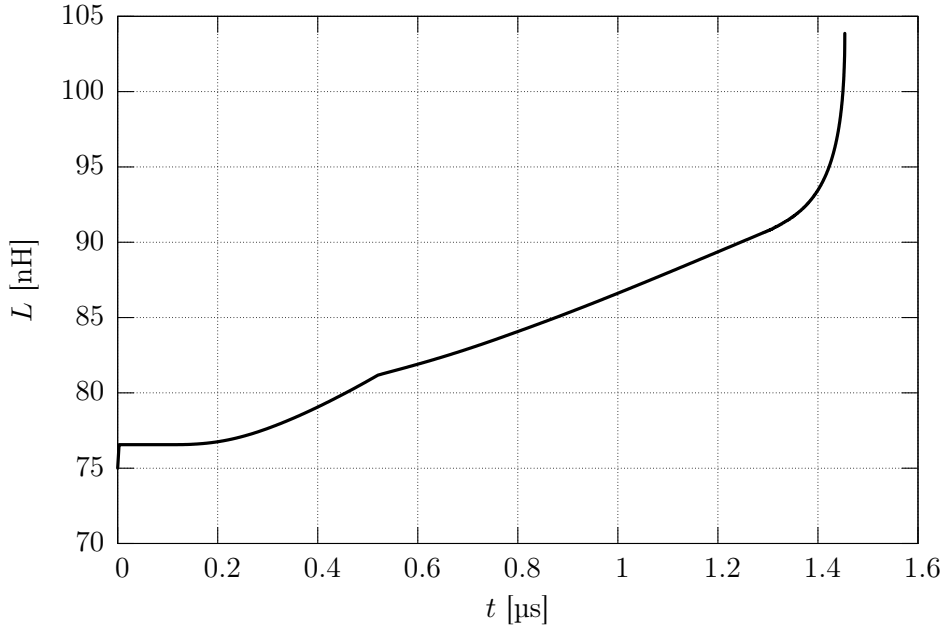

Figure 4.2: Inductance profile of the Montecuccolino PF simulation.

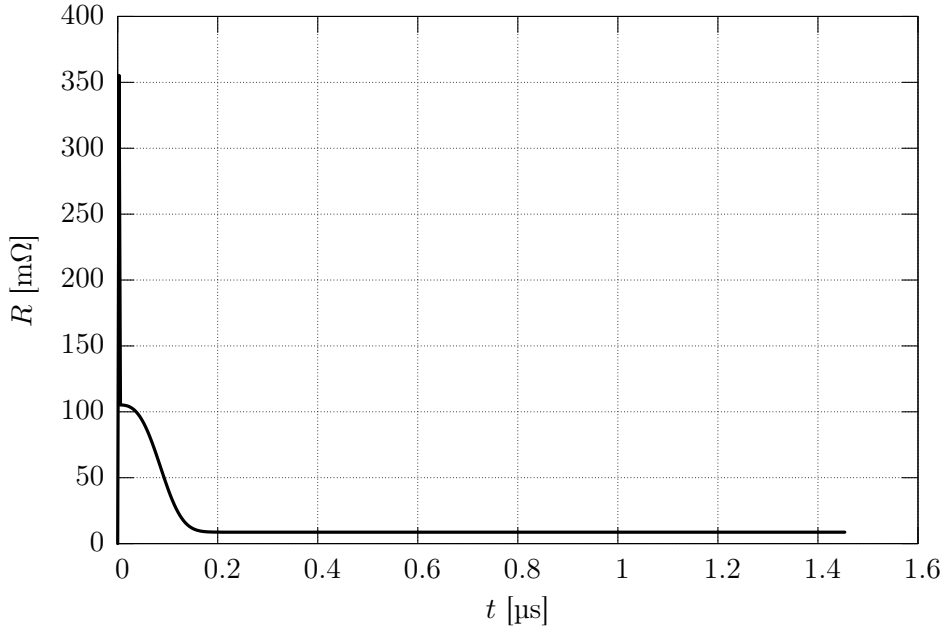

Figure 4.3: Resistance profile of the Montecuccolino PF simulation.

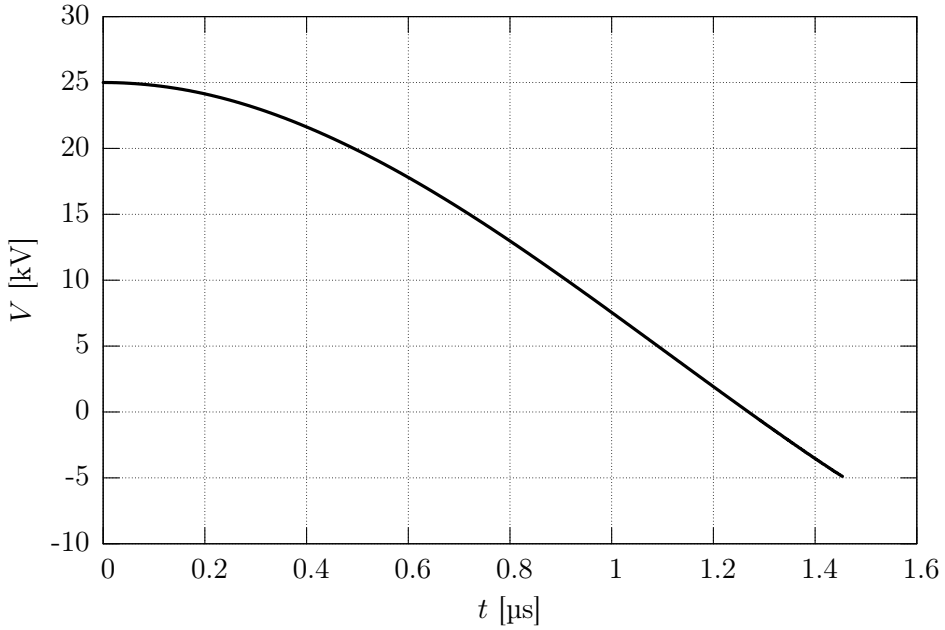

Figure 4.4: Capacitor voltage profile of the Montecuccolino PF simulation.

its sudden drop can be easily related to the observed current dip. Splitting the inductance into a constant contribute L_0 and the time varying one $L_\mathrm{p}(t)$, sum of the inductance of the active length of the electrodes L_act and of that associated with the CS L_cs (see equation (3.12)), it is easy to derive the voltage drop between the closed end of the electrodes, given by

$$V_\mathrm{p} = \frac{\mathrm{d}(L_\mathrm{p} I)}{\mathrm{d}t} = L_\mathrm{p}\frac{\mathrm{d}I}{\mathrm{d}t} + I\frac{\mathrm{d}L_\mathrm{p}}{\mathrm{d}t}\,.$$

It is plotted in Figure 4.6, where a first discontinuity is evident corresponding to that of the inductance derivative corresponding to the end of the detachment phase. Moreover, while in the rundown phase a nearly constant value of V_p is preserved, the collapse determines a drastic voltage drop: the minimum radial coordinate of the sheath rapidly approaches the axis increasing rapidly the inductance, while the current has almost reach its maximum (null derivative). This is the main reason of the modeled current dip shown in Figure 4.1, even if the obtained over-voltage value is rather overestimated, since the CS does not create a pinched plasma column of null radius. When the axial-symmetric plasma layer pushed by the MP collapses, the magnetic field starts diffusing inside the plasma and a shock-wave then induces an expansion [4, 55]. An additional term due to an anomalous resistivity should be considered for the particles trapped in the high magnetic field.

The exact time instant corresponding to the end of the discharge phases is directly given as output from the code: the end of the detachment phase is determined when the last node touches the outer electrode (0.51 µs); the end of the rundown is obtained by the last instant for which the first node radial coordinate is still fixed

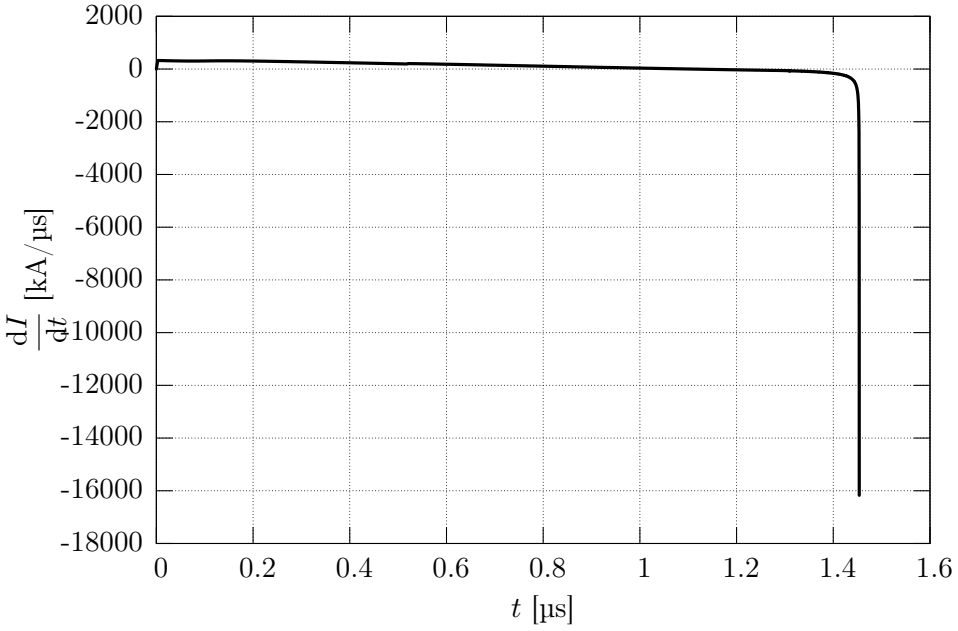

Figure 4.5: Current derivative profile of the Montecuccolino PF simulation.

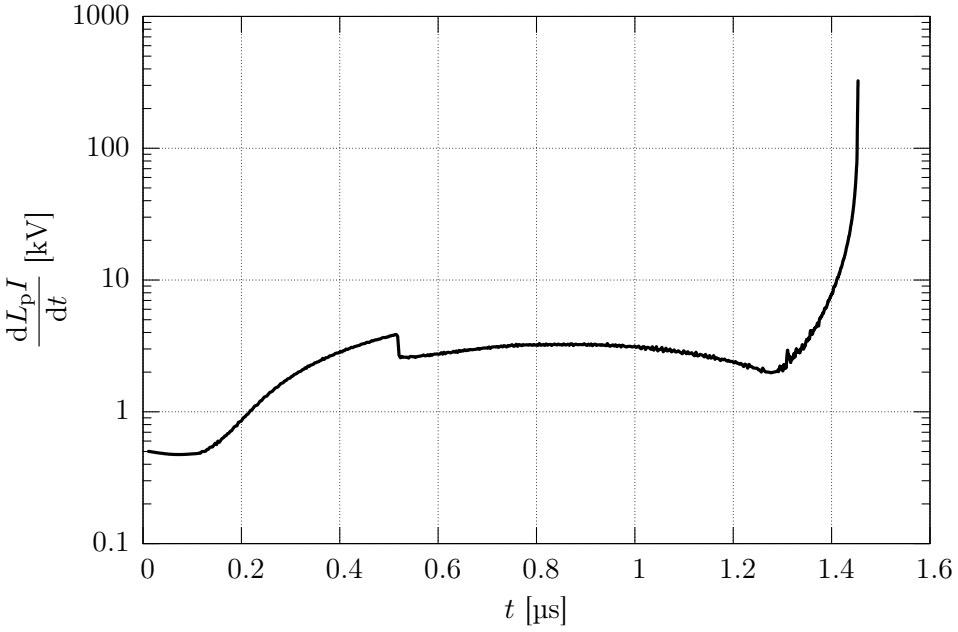

Figure 4.6: Inductive voltage drop profile of the Montecuccolino PF simulation.

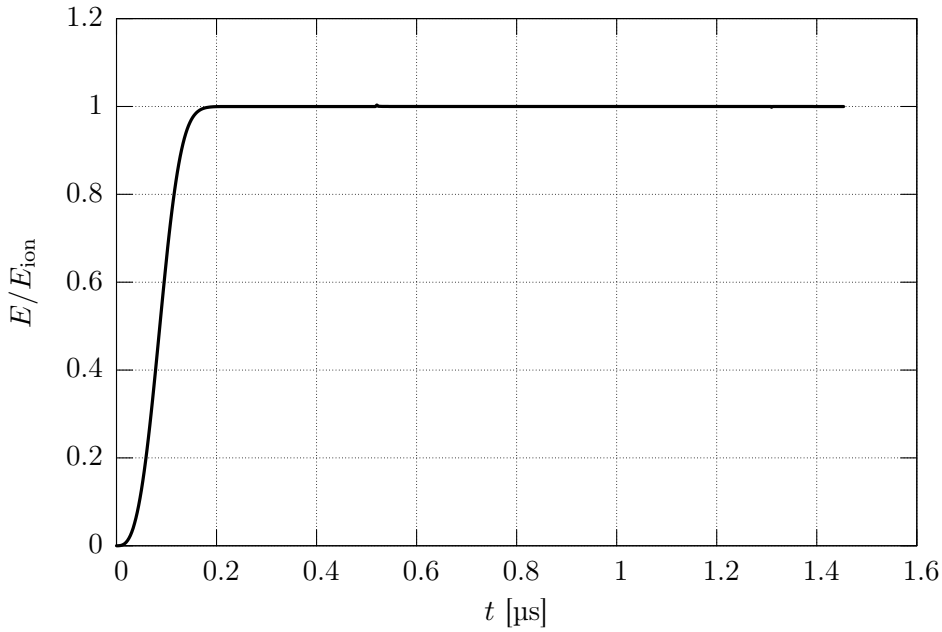

Figure 4.7: Ratio between the internal energy of the plasma layer and the ionization energy of the gas contained in it, as obtained from the Montecuccolino PF simulation.

at r_{int} (1.28 µs); as last, the pinch time corresponds with the end of the simulation, obtained from the comparison of the minimum radial coordinate of the sheath profile with $r = 0$ (1.45 µs). The time instants perfectly match with the derivative changes in the inductance profile. Moreover, it can be noted that the plasma resistance has already reached negligible values at the end of the detachment phase, as confirmed from the ratio between the internal energy and the ionization energy of the layer presented in Figure 4.7. Even the total mass of the CS is strictly related to the discharge phase, since the boundary conditions on its tail strongly influence it. In Figure 4.8, the sudden drop of the sheath total mass is in time coincidence with the detachment phase, where great part of the CS is lost at the impact with the OE.

The event can be better understood looking at the sheath dynamics, reported in Figure 4.9 through its profiles evolution in time. The analysis of the radial and axial position of the first and last node of the sheath, depicted in Figure 4.10 and 4.11, allow to show the imposed boundary conditions. Moreover, it can be noticed that, after an initial transition period, the rundown axial advance of the sheath is almost linear.

The velocities of the first and last nodes of the modeled sheath are reported in Figure 4.12 and 4.13. The sudden changes in their derivative is strictly connected with the different phases the sheath goes through. It can be observed that the radial velocity of the first node reaches the critical value of 10 cm/µs at the end of the rundown. Due to the boundary condition imposed by the shock-wave diffraction theory, it is converted in a strong initial radial velocity (half of the axial one just before the shock jump), going to be strongly enhanced by the MP compression. At

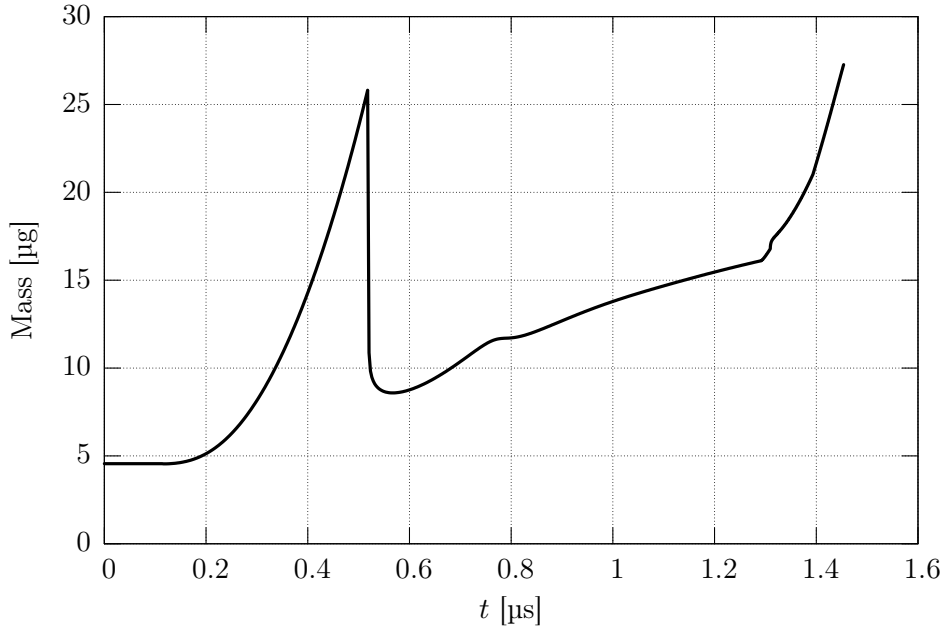

Figure 4.8: Total mass of the plasma layer as obtained from the Montecuccolino PF simulation.

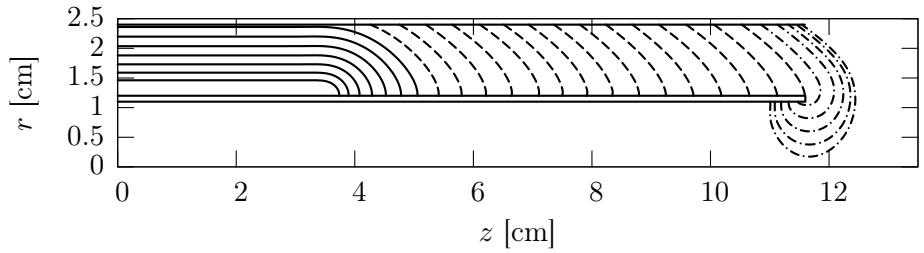

Figure 4.9: Sheath profiles of the Montecuccolino PF simulation. The different discharge phases are denoted with different line types: continuous line for the detachment, dashed for the rundown and dash-dotted for the collapse phase respectively.

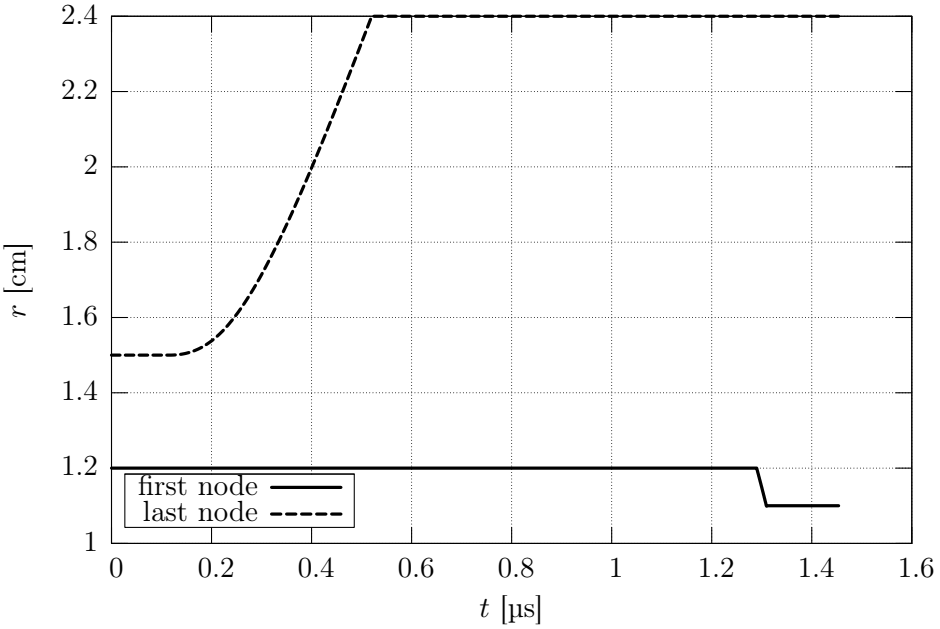

Figure 4.10: Time dependent radial position of the first and last node of the sheath profile as obtained from the Montecuccolino PF simulation.

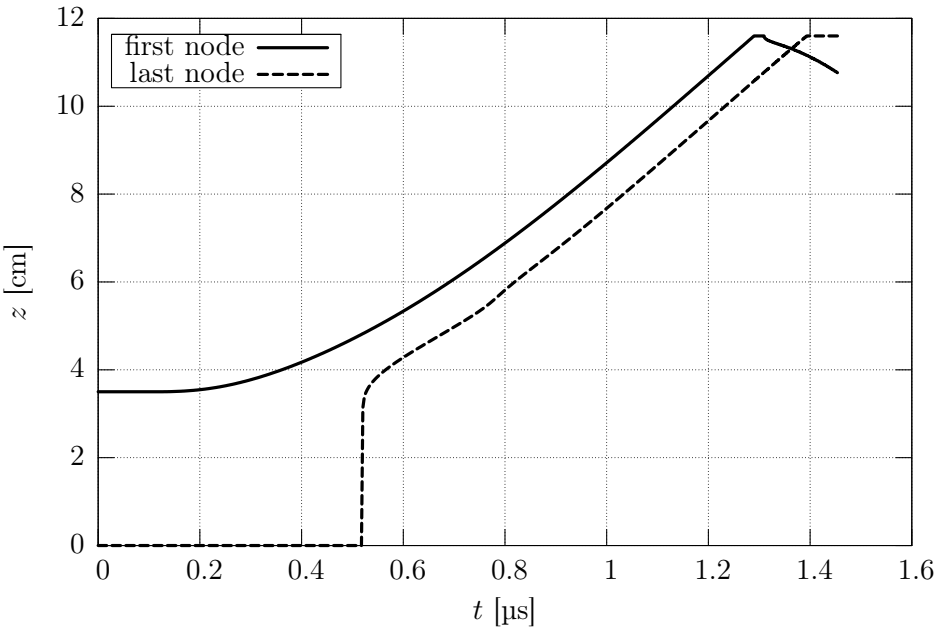

Figure 4.11: Time dependent axial position of the first and last node of the sheath profile as obtained from the Montecuccolino PF simulation.

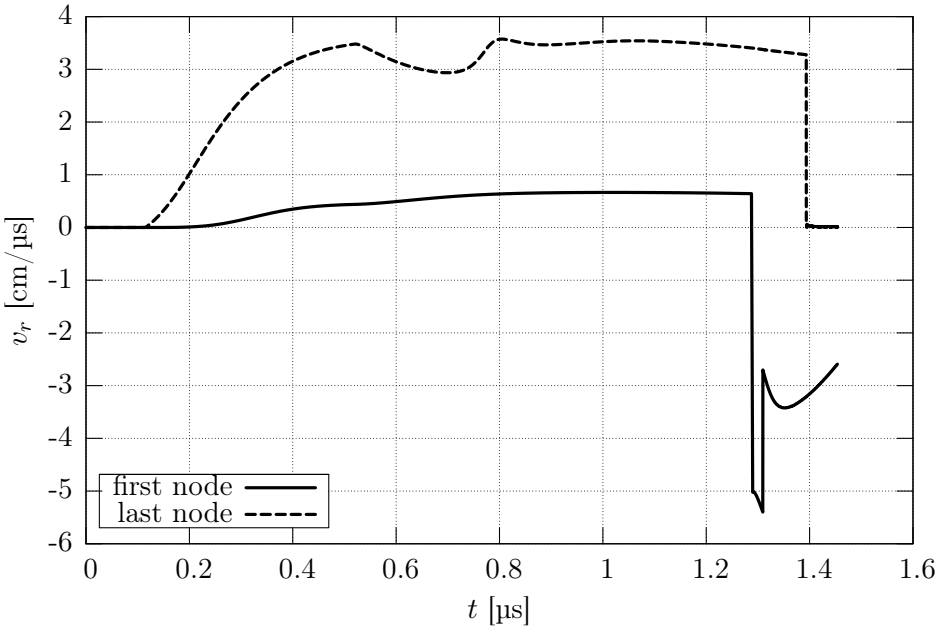

Figure 4.12: Time dependent radial velocity of the first and last node of the sheath profile as obtained from the Montecuccolino PF simulation.

the end of the IE, the two velocity components of the first node of the CS obviously change their signs from positive to negative.

In seek of completeness, the Montecuccolino PF simulation can be exploited to show the different behavior of the CS during the transition from the rundown and collapse phase in presence of a tapped or hollow IE. The time coincidence of the discharge phases is slightly modified by the hollow or tapped IE geometry. In the same way, even the insulator configuration does not modify the discharge behavior: at the end of the rundown, the sheath profile assume the same shape and the macroscopic velocities are preserved. The main difference is represented by the inductance increase in the case of OE of the same length of the IE: the blowing of the sheath near the OE increases the inductance and, consequently, the voltage drop and the current dip at the end of the discharge. In any case, the maximum current differs for a maximum of a 2%, and the pinch instant for a 3%, which are comparable with numerical , as well as experimental, errors. On the other hand, the focus time is strongly influenced by the filling pressure of the working gas, as shown in Figure 4.15. The mass growth of the sheath, sweeping the background gas, reduces its axial velocity increasing the time interval necessary for the rundown and collapse phases.

The charging voltage of the capacitor bank is another working parameter of great importance. While the inductance profile remains unchanged, an increasing voltage implies both an increase of the maximum current and a reduction of the pinch time, evidently, the second being an effect of the first: the current is roughly given by $V_0\sqrt{C_0/L_0'}$ and the magnetic pressure, that drives the CS, behaves proportionally

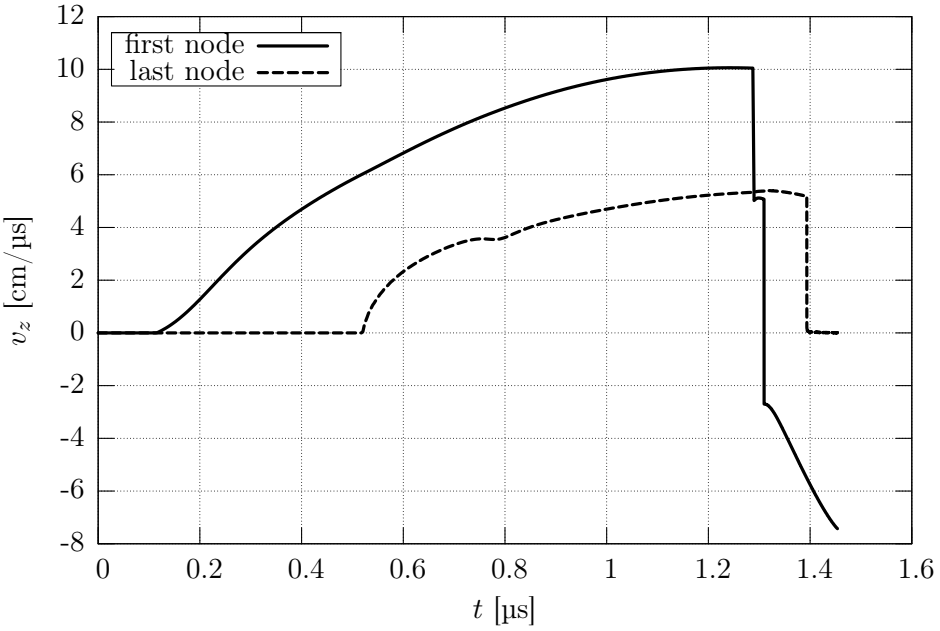

Figure 4.13: Time dependent axial velocity of the first and last node of the sheath profile as obtained from the Montecuccolino PF simulation.

to I^2.

4.1.2 Comparisons with the theoretical model

In Section 1.3.2 a brief description of the theoretical snowplow model was given. It is based on the experimental evidence that all relevant properties of a plasma layer approach stationary state in a short time [56, 57]. Hence, the rundown phase of a coaxial gun like the PF can be described by stationary equations.

As already shown, equation (1.5) represents a FOM of the PF. The parameter a can be roughly evaluated by simple considerations: the peak current of the equivalent RLC circuit is $I_{0,\max} = V_0\sqrt{C_0/L_0'} \simeq 220$ kA; the transit time of the CS over the inner electrode can be evaluated both experimentally or numerically (see Section 4.1.3) and, knowing the IE length, the resultant rundown average velocity $\overline{v}_z$ is about 10 cm/µs (as confirmed even by Figure 4.13). By substitution in equation (1.5), one obtains

$$a = \sqrt{\frac{\mu_0}{8\pi^2\rho r_{\text{int}}^2}}\frac{I_{0,\max}}{\overline{v}_z} = \sqrt{\frac{\mu_0 R_0 T}{8\pi^2 M_{\text{m}}}}\frac{I_{0,\max}}{r_{\text{int}}\overline{v}_z\sqrt{p}} \simeq 1.1\,,$$

being $\sqrt{\mu_0 R_0 T/(8\pi^2 M_{\text{m}})} \simeq 0.01$ m^2(mbar)$^{1/2}$/sA, with R_0 the universal constant of ideal gases, M_{m} the molar mass of the gas; T is expressed in unit of Kand p in mbar. The obtained value is greater than the upper limit theoretically derived, but within a 10% which can be ascribed to rough evaluation of the involved parameters.

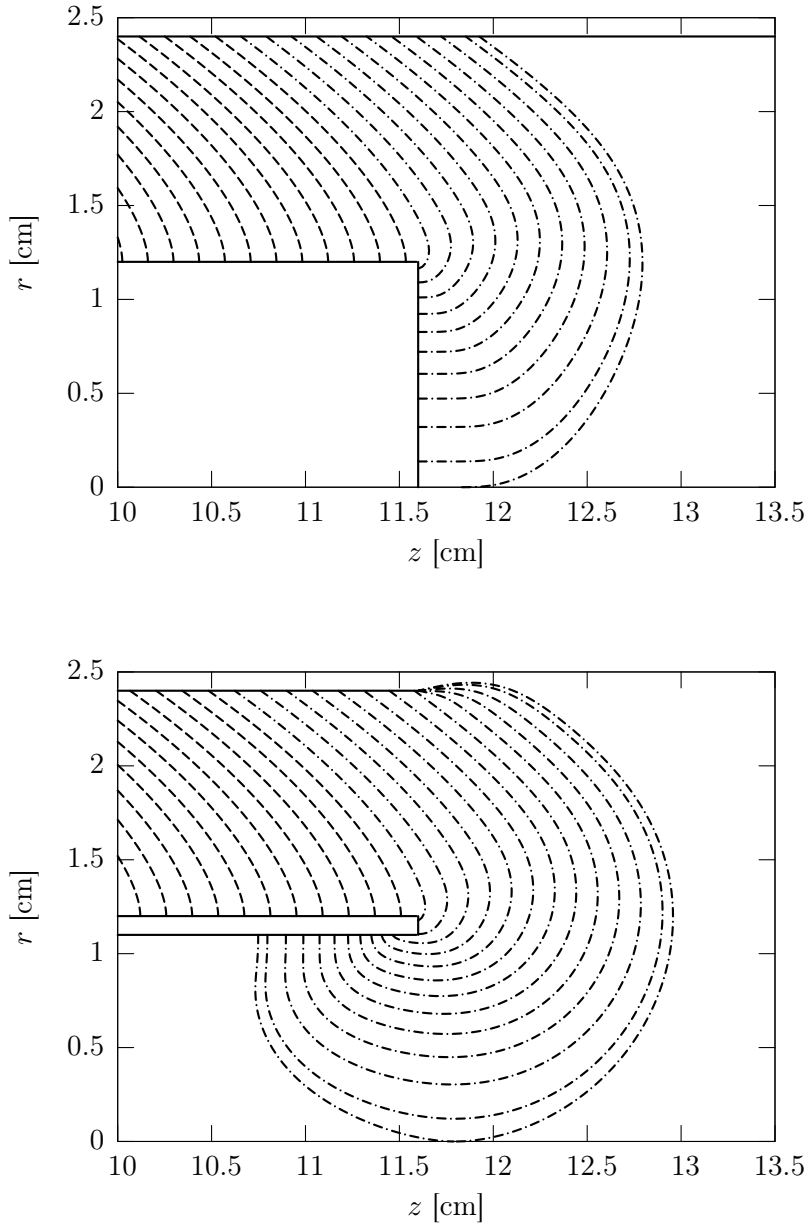

Figure 4.14: Final stages of the sheath profile evolution in the case of a tapped IE (up) and a hollow IE (bottom). In the second case the OE has the same length of the inner one, as the Montecuccolino PF is the case.

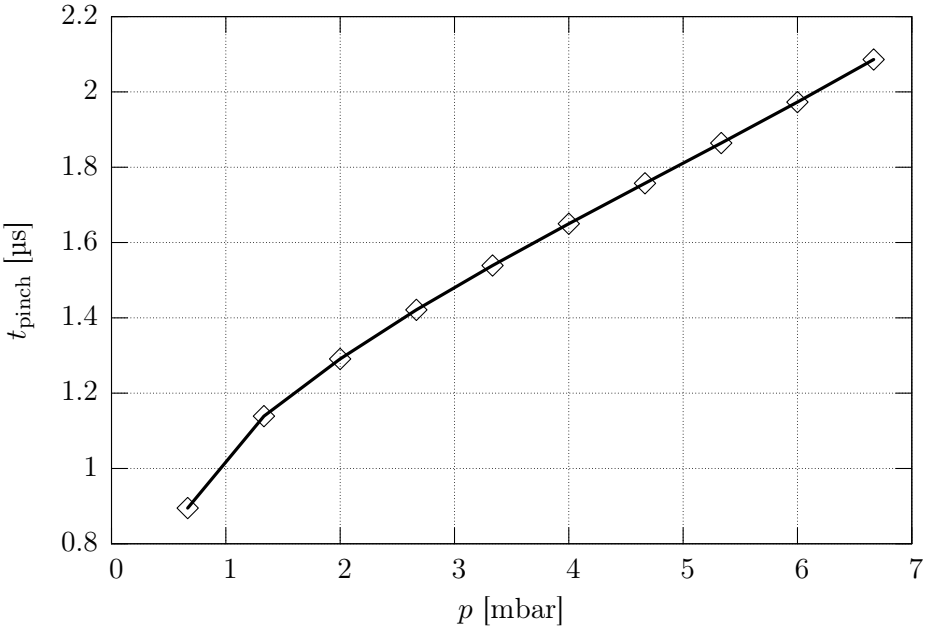

Figure 4.15: Focus time instant vs. working gas pressure, as obtained trough the Montecuccolino PF simulations.

From the snowplow simulations of the device, the parameter a can be evaluated directly through the ratio between the current and the axial velocity of the sheath (in output) scaled by a constant parameter depending on the inner radius dimension and on the filling gas pressure. Considering both the axial velocities of the first and the last node of the CS, the result is shown in Figure 4.16. The line corresponding to the axial velocity of the first node, rapidly lies on a fixed value which perfectly confirms what found from the above rough calculation; the dashed line does not represent a stationary behavior, but this must not surprise since the axial velocity of the CS tail is strongly influenced by the boundary conditions.

The obtained value of a at the end of the rundown, when the stationary state of the CS advance is reached, is about 0.95. Remembering that a should lie in the theoretical interval $[0, 1]$, indicating better performances approaching 1, the obtained value is an index of the optimal performances of the PF of Montecuccolino. Tuning properly the charging voltage and the filling gas pressure, the same result can be achieved in a reasonable range of operability. The increase of the charging voltage implies an increase of the peak current and, to maintain the axial average velocity of the CS under the maximum limit of about 10 cm/µs, the working pressure should be increased too leading to a decrement of the multiplying constant. A further increase of the filling gas pressure would compromise the time coincidence between the peak current of the equivalent RLC circuit and the focus instant, worsening the pinch conditions.

The steady state fluid model for a generic coaxial gun allows also to derive an analytical expression for the profile of the CS $z(r)$; it is found to depend on a and

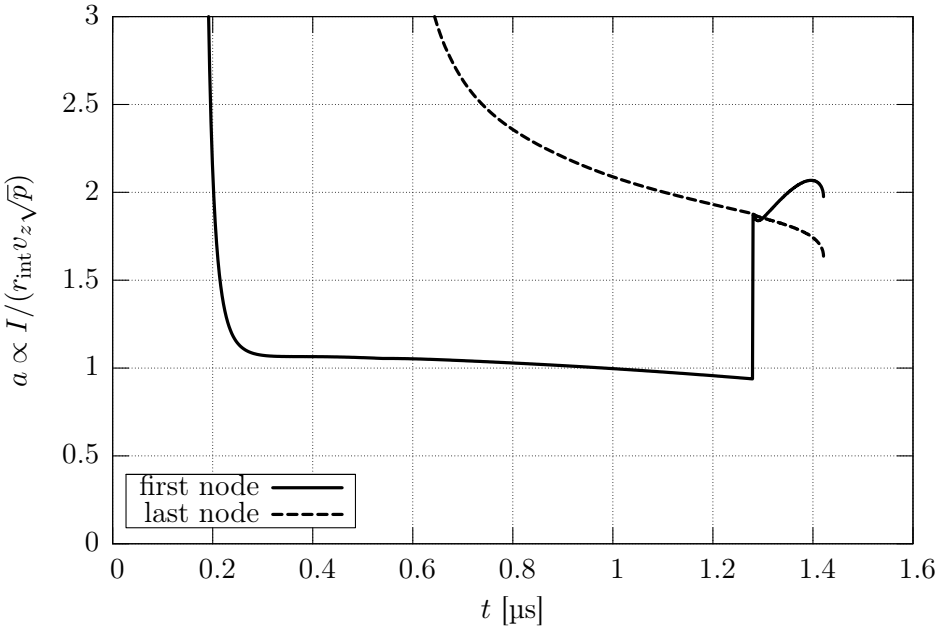

Figure 4.16: Figure of merit of the Montecuccolino PF device as derived from the snowplow theoretical and numerical models.

$r_{\rm int}$ as follows

$$z(r)-z_0 = -\frac{r_{\rm int}}{2a}\left(\frac{r}{r_{\rm int}}\sqrt{\left(\frac{r}{r_{\rm int}}\right)^2 - a^2} - \sqrt{1-a^2} - a^2 - \ln\frac{\dfrac{r}{r_{\rm int}} + \sqrt{\left(\dfrac{r}{r_{\rm int}}\right)^2 - a^2}}{1+\sqrt{1-a^2}}\right), \tag{4.1}$$

where z_0 is the axial coordinate of the sheath attachment to the IE at the considered time instant, while z and r are the 2D coordinates of the profile.

The profile, as obtained from equation (4.1), is plotted in Figure 4.17 together with that obtained from the simulation. The working parameters are those employed in the analysis presented in Section 4.1.1, while a is here assumed equal to unity. The discrepancy between the two profiles would increase reducing a. This is probably due to the slightly different solution of the conservation equation and to the boundary conditions of the numerical model, which modify the sheath shape at each time iteration.

4.1.3 Comparison with experimental and numerical data

The comparison of the numerical data with those of theoretical models seems to confirm the goodness of the implemented code. To dispel all doubts, the comparison with experimental data or other numerical model is necessary.

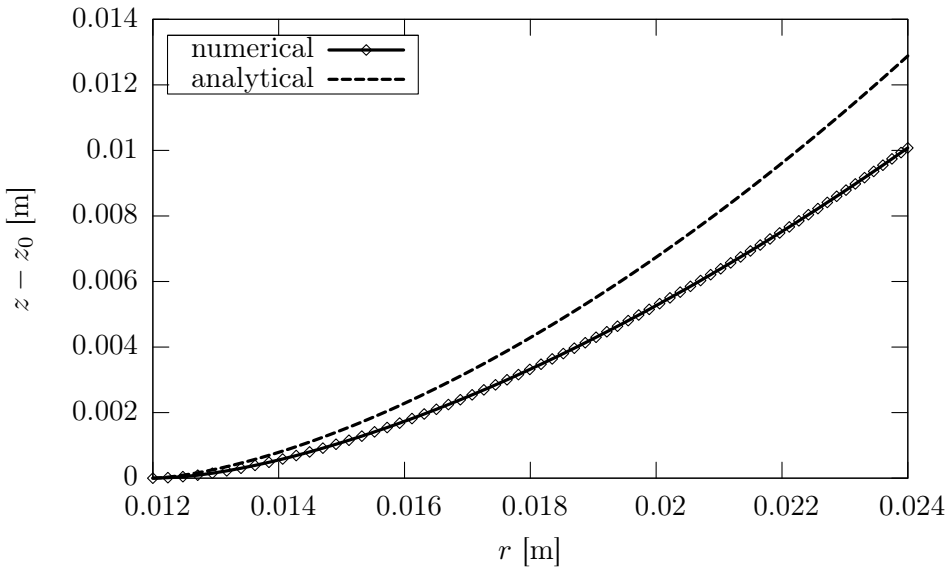

Figure 4.17: Comparison between the analytical profile for $a = 1$ and the numerical one obtained by the 2D snowplow code for the Montecuccolino PF.

The PF device of Montecuccolino is equipped with a Rogowski coil which allows to measure the current of the bank capacitor discharge on the PF load. The signal obtained by a typical measure is plotted in Figure 4.18 and compared with the data of the above described numerical code and with those of a mono-dimensional code based on a combination of a 1D snowplow model for the rundown phase and of a 1D slug model for the collapse phase [4, 55]. Even if the experimental signal is quite noisy, due to a not perfect shielding of the diagnostic apparatus, the dip of the current is quite evident; the pinch occurs at 1.5 µs from the triggering of the discharge. The 1D model seems to fail in predicting both the focus instant and the dip in the current profile; the steeper derivative of the current could derive from a not sufficiently precise calculation of the CS inductance. The 2D model here presented gives better results showing a perfect agreement in the less noisy middle part of the discharge; the focus time is predicted with an error lower than 3% and even the current dip is correctly modeled.

The pinch time instants dependence on filling gas pressure, presented in Figure 4.15, are in good agreement with experimentally observed square-root-like behaviors.

The goodness of PF design, given by the $a \simeq 1$ parameter, is experimentally confirmed by the measured neutron yield of the PF device which correctly matches the one predicted on the basis of the scaling law [53].

Although simplified models for the SG and PF breakdown phases are used, the set of differential equations presented in Chapter 3 leads to accurate results and reproduce the experimental data. The sheath modeling and reshape algorithm and the assumed boundary conditions appear a good choice able to avoid numerical instabilities and to describe the sheath profile with good agreement with theoretical

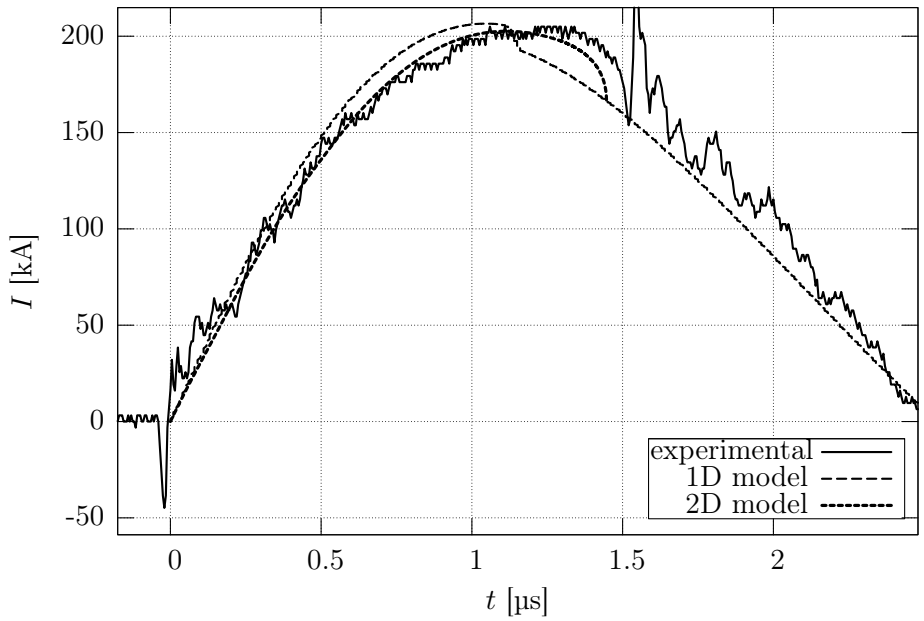

Figure 4.18: Comparison between an experimental current profile as measured by a Rogowski coil and the numerical simulation obtained from a 1D numerical model and the here presented 2D one.

and experimental data from literature [1, 19, 33, 58].

4.2 Design of the PFMA1 electrodes

The 2D snowplow numerical code revealed itself a good tool in the simulation of the macroscopic dynamics of the plasma in a PF device. Its potentialities can be further exploited in the PF design field. In the present Section, the electrodes optimization for the PFMA1 device will be described starting from a rough solution obtained by the parameters presented in Section 2.2.1 and refining it through the code. Due to the approximations of the numerical model, a fine tuning of the electrode dimensions is possible only experimentally.

4.2.1 First trial values

The operational parameters of the PFMA1 device are summarized in Table 2.1 of Section 2.3.2. As presented in the parent Section, they are derived from the needs of the precise task and combined with the technological challenging problems connected with power pulsed devices.

The electrical and working parameters of the device are a good starting point towards the design of the electrodes tube. As previously stated in Section 2.2.1, there are two main conditions to satisfy: the first is the temporal coincidence between the maximum current of the RLC discharge and the focus of the collapsing CS; the

second is the matching between the external device inductance L_0 and the inductance L_l of the focus tube, related to the power transmission between the two components.

When the device is operated at full power, the estimated peak current is $I_{0,\max} = V_0\sqrt{C_0/L_0'} = 2.8$ MA. Following the equation (2.4), the average axial velocity of the CS is

$$\overline{v} \simeq \sqrt{\frac{\mu_0 \ln\left(\frac{r_{\text{ext}}}{r_{\text{int}}}\right)}{\pi^4 \rho (r_{\text{ext}}^2 - r_{\text{int}}^2)}} V_0 \sqrt{\frac{C_0}{L_0'}}\,,$$

depending on the geometrical parameters of the focus tube and on the electrical fixed ones.

The frequency of the discharge is about $\omega = (\sqrt{L_0' C_0})^{-1} = 0.3$ MHz corresponding to a characteristic period of $T = 2\pi/\omega = 4t_0 = 5.9$ µs. Hence, the electrodes length l can be approximately related to the maximum current time instant t_0 by equating this with the averaged transit time of the CS $t_l = l/\overline{v}$:

$$l = \overline{v} t_0 = \sqrt{\frac{\mu_0 \ln\left(\frac{r_{\text{ext}}}{r_{\text{int}}}\right)}{4\pi^2 \rho (r_{\text{ext}}^2 - r_{\text{int}}^2)}} V_0 C_0\,. \tag{4.2}$$

Since a good matching between the inductances of the external circuit L_0 and electrodes L_l is wanted, the total inductance can be written as $L_0' = L_0 + L_l = 2L_0$, deriving $L_l = L_0$. This last condition allows to write a new relation between the total inductance and the geometrical parameters of the focus tube:

$$L_l = \frac{L_0'}{2} = \frac{\mu_0}{2\pi} l \ln\left(\frac{r_{\text{ext}}}{r_{\text{int}}}\right)\,, \tag{4.3}$$

where the formula for the inductance of two coaxial cylinders has been used (see Section 5.2.1 for more details).

Deducing l from the rhs of equation (4.3) and equating it with equation (4.2), the following expression containing all the parameters of interest can be found:

$$\sqrt{\frac{r_{\text{ext}}^2 - r_{\text{int}}^2}{\ln^3\left(\frac{r_{\text{ext}}}{r_{\text{int}}}\right)}} = \left(\frac{\mu_0}{4\pi}\right)^{3/2} \frac{4}{\sqrt{\pi\rho}} V_0 \frac{C_0}{L_0'}\,.$$

In the case of PFMA1, the fixed electrical parameters, collected in Table 2.1, lead to the value of 41 cm for the rhs. Once fixed the radiuses ratio $R_{\text{r}} = r_{\text{ext}}/r_{\text{int}}$ as independent variable, the above equations allow to deduce the IE radius r_{int} and the electrodes length l as functions of R_{r}. In Figure 4.19, the resultant curves are reported in cm for convenience.

The electrical parameters of the PFMA1 lead to quite surprising values of the geometrical dimension of the focus tube. For example, a radiuses ratio $R_{\text{r}} = 1.2$ would give $r_{\text{int}} = 4.8$ cm, $r_{\text{ext}} = 5.8$ cm and $l = 54.9$ cm. In any case, it must be remembered that these values are obtained under idealized hypothesis which could lead to misleading conditions in particular cases. A refinement process based on few basic rules is necessary and the snowplow code will help to reach the task.

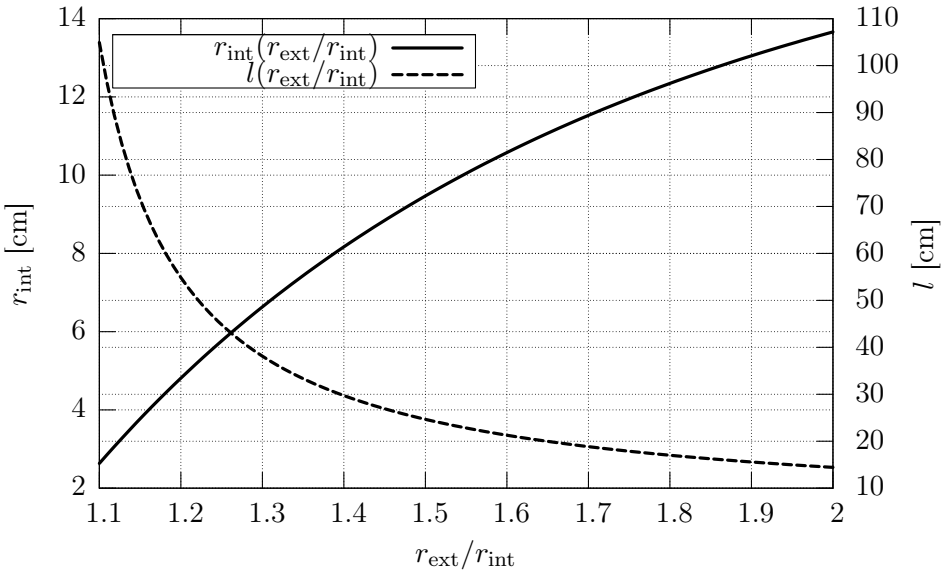

Figure 4.19: IE radius (left axis) and electrodes length (right axis) as functions of the radiuses ratio in the case of PFMA1.

4.2.2 Criteria of refinement

One of the main bond in the design of the PFMA1 core, is the volume reduction of the vacuum chamber, the He^3 component of the filling gas mixture being rather expensive. Due to the refilling needs in repetitive operational mode, a maximum volume of about 30 dm^3 can be accepted. This fixes an upper limit to the OE radius and to the electrodes length, even considering that the plasma sheath inflates during the collapse (see for example Figure 4.9) and could touch the grounded walls of the chamber; the high current would flow through a not properly designed discharge path. In few cases, the vacuum chamber could be directly used as grounded electrode, but this would make too complex the procedure to tune dimensions through experimental tests. On the other hand, the IE must be closed to allow in internal recirculating cooling (see Section 5.3.3).

The snowplow code can be used to evaluate the first trial solution proposed at the end of the above Section. In particular, the attention can be drawn to the current and inductance profiles presented in Figure 4.20 and to the CS first and last node axial velocities of Figure 4.21. As first can be observed that the maximum current of 2.1 MA is obtained at 3.4 µs, which is quite lower than the evaluated quarter period of the equivalent lumped RLC circuit. This can be explained giving a look at the inductance profile: the initial inductance is the half of the constant assumed value for L_0' and grows approximately linearly and slowly, due to the low electrode radiuses ratio; the equivalent inductance of the first quarter of the discharge is about 3/4 the total (obtained about at the end of the rundown). The increasing inductance then reduces the obtainable peak current since it has reached in advance its maximum (minimum derivative). Finally, in the collapsing phase, the inductance further grows

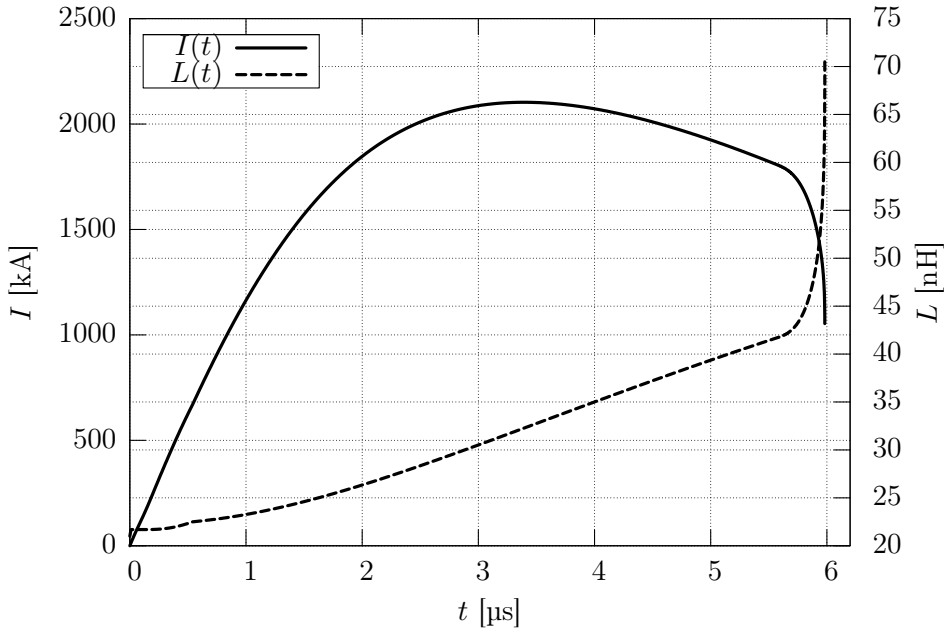

Figure 4.20: Current and inductance profiles for the first trial solution of PFMA1 electrodes design: $r_{\text{int}} = 4.8$ cm, $r_{\text{ext}} = 5.8$ cm and $l = 54.9$ cm.

and the high voltage drop produces a marked current dip.

The axial velocities represented in Figure 4.21 confirm the proportional dependence on $I(t)$. However, the obtained maximum value of about 12 cm/µs is too high if compared with the acceptable range $3 \div 8$ cm/µs, discussed in Section 2.1.1.

Furthermore, even if the low radiuses ratio reduces the electrodes inductance, the little gap (only 1 cm) could be too small to have a good breakdown on the insulator sleeve [18, 19]. Therefore, it would be better to maintain the inner radius and to increase the outer one to avoid an excessive inductance increase during the sheath collapse; on the other hand, even the length should be reduced to keep constant the electrodes inductance and reduce the transit time.

However, the resulting bigger outer radius would increase the varying inductance of the collapsing phase (going with the natural logarithm of the radiuses ratio) and, consequently, the voltage drop. These conditions of high time variability of the equivalent circuit impedance are not negligible, since they were shown to influence both the peak current and the characteristic period, used to evaluate the average axial velocity and the electrodes length respectively.

As deducible, the problem is highly non-linear and the first trial value reveals itself not representative in the case of the PFMA1. An iterative solution going through a trial and fail method based on the above criteria is needed. The result presented in the next Section takes into account also the real external inductance obtained through the collector design, as calculated in Section 5.2.3.

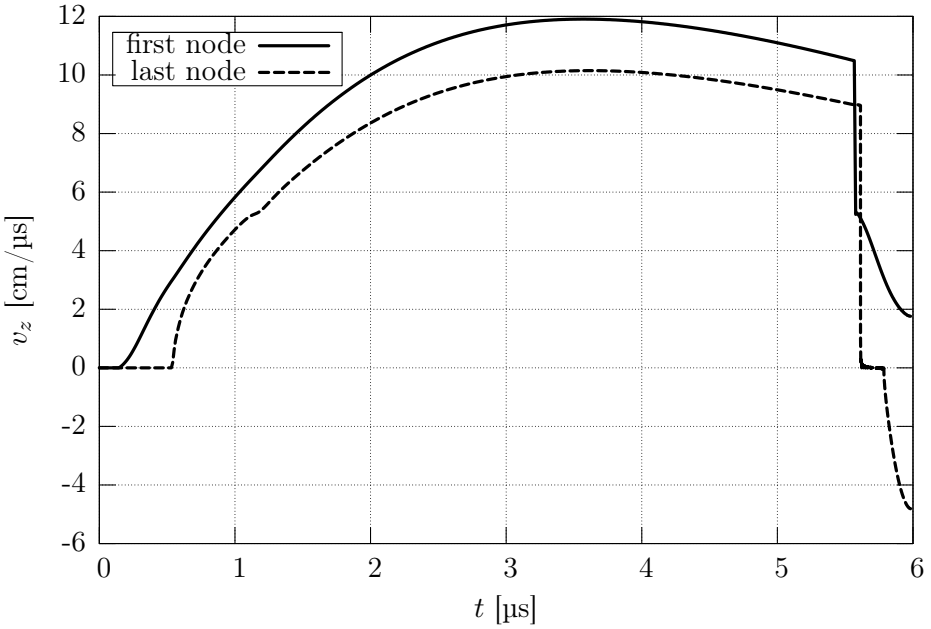

Figure 4.21: Axial velocity of the CS first and last nodes for the first trial solution of PFMA1 electrodes design: $r_{\text{int}} = 4.8$ cm, $r_{\text{ext}} = 5.8$ cm and $l = 54.9$ cm.

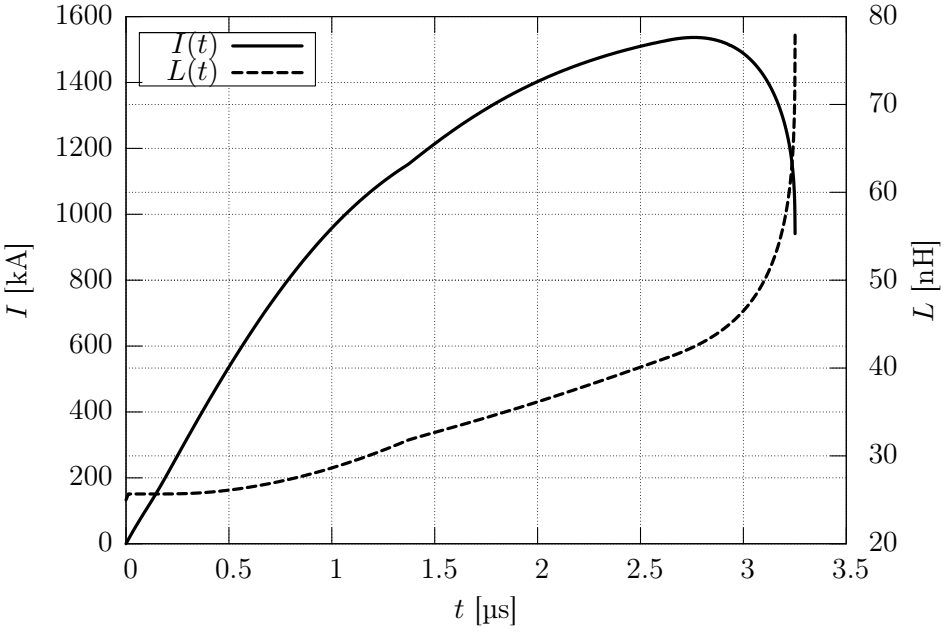

Figure 4.22: Current and inductance profiles for the optimal solution of the PFMA1 electrodes design.

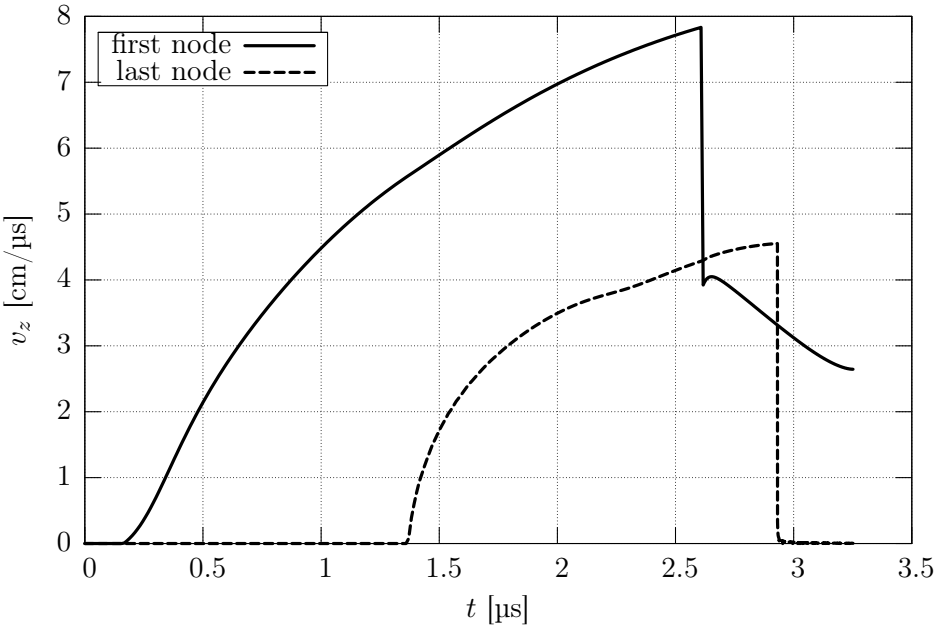

Figure 4.23: Axial velocities of the CS first and last nodes for the optimal solution of the PFMA1 electrodes design.

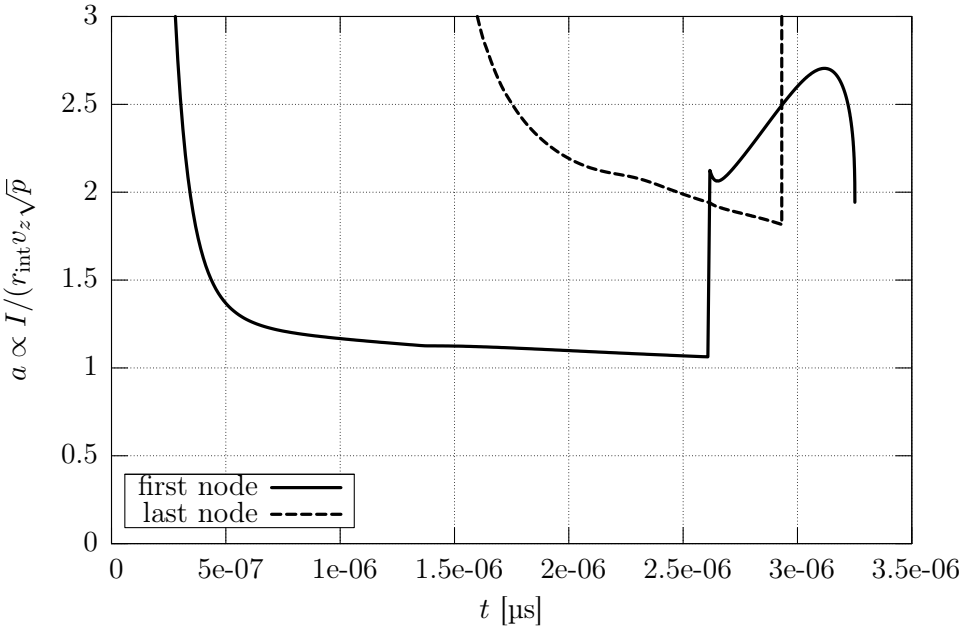

Figure 4.24: Figure of merit of the PFMA1 device as deduced from the snowplow numerical model for the optimized configuration.

4.2.3 Optimized electrodes

The main two problems related to the first trial solution which arose in the previous Section are: the interelectrode gap is too low and leads to a reduced initial inductance modifying the expected peak current value and instant; the electrode length is too high for the equivalent RLC circuit characteristic quarter period with time-dependent parameters.

Testing many configurations varying firstly the length and secondly the interelectrode gap (radiuses ratio), the following optimal geometrical parameters were obtained:

$$\begin{aligned} r_{\text{int}} &= 5 \text{ cm} \\ r_{\text{ext}} &= 8.5 \text{ cm} \\ l &= 16 \text{ cm}\,, \end{aligned}$$

which lead to an electrode inductance $L_l \simeq 17$ nH.

The resulting current and inductance profiles are reported in the double-axis plot of Figure 4.22. As can be easily seen the peak current does not reach the predicted maximum value. This has two main advantages: the current positive derivative has still a not negligible value when the collapse starts and the inductive voltage drop grows rapidly; the maximum current ($I_{0,\max}(t = 2.8\ \mu\text{s}) = 1.54$ MA), flowing in the circuit, is lower than the maximum predicted one reducing the problems connected with both ohmic and plasma-wall-interaction heating, and with electrodynamics forces (see Section 5.3.4 and 5.3.3 respectively). Notwithstanding, the pinch current is still sufficiently high, about 1 MA.

The corresponding maximum sheath axial velocity is consequently lowered to values comparable with the acceptable variability range.

The FOM, defined through equation (1.5) is plotted in Figure 4.24, making use of the current and axial velocities data obtained from the snowplow simulation of the PFMA1 under the assumed operational parameters. As seen for Figure 4.16, the value approaches the theoretical maximum of 1 confirming the proper design of the electrodes.

The electrode length can be even increased of $1 \div 2$ cm leading to a little higher inductance. A more visible plateau in the nearby of the maximum current and axial velocity would be obtained. However, while the peak current would increase up to near 1.6 MA, the focus current wouldn't be modified, with no advantage on the pinch performances.

The obtained length produces a lower inductance with respect to the external one leading to $L_l/L_0 = 0.7$. The value is still acceptable since it allows to maintain a total inductance L_0' of about 44 nH and to keep low the dimensions of the vacuum chamber.

The geometrical parameters of the focus tube will be used in the next Chapter for the design of the PFMA1 collector.

CHAPTER 5

The PFMA1 design

Abstract. Starting from a summary on the choice of the auxiliary components (capacitors, spark gap, coaxial cables, ...), a detailed description of the problems related with the design of a high energetic and repetitive PF working in the MA regime will be given. In particular, the reader attention will be driven towards the inductance minimization, the insulator effectiveness, the electrodynamic forces and the flexibility of the focus tube dimensions.

5.1 The external circuit components

Once fixed the design parameters (bank energy, repetition rate, maximum operating voltage, peak current), a careful choice of the components of the discharging line must be done taking into account all the related technological limitations. Many considerations on the collector and electrodes design will depend on it [14, 59]. The ease of the components coupling is of great importance for the device mounting and maintenance.

The basic principle of parallelization is widely used to increase total capacitance while reducing inductance and resistance.

5.1.1 Operating voltage and bank capacitors

The capacitors choice is related to the maximum operating voltage, to the maximum transfer current, to the ringing frequency and to the acceptable voltage reversal. Since the voltage reversal is as more detrimental as higher the charging voltage, it is convenient to choose a capacitor model with a maximum operating voltage greater than that strictly needed. The number N of capacitors, besides scaling the capacitance of each od them, influences also the maximum current flowing through each DM.

The 350 µF bank capacitance can be achieved through a set of parallelly connected General Atomics 32899, 11 µF capacitors rated at 36 kV and 150 kA. The number $N = 32$ satisfy both the requirement on the total capacitance anche on the maximum sustainable current: $N = C_0/C_{\text{cap}} = 350/11 \simeq 32$ and $I_{\text{cap,max}} = I_{0,\text{max}}/N \simeq 94\,\text{kA} < 150\,\text{kA}$. The equivalent series inductance (ESL) of the capacitors being about 30 nH, the number N is sufficiently high to reduce the total inductance of the whole bank to $L_{\text{cap,tot}} \simeq 0.94$ nH.

The capacitors are also compatible with the discharge repetition frequency of 1 Hz. Their expected life is greater of about 3 million cycles at a charging voltage of 1 Hz and a voltage reversal of about 60% of the charging voltage.

The optimal layout of the capacitor bank is found to be in a circular array of 2.2 m of maximum encumbrance. The chosen arrangement ensures a symmetrical current flux towards the electrodes and, in the meanwhile, it minimizes the pressure exerted on the floor (each capacitor is about 140 kg).

5.1.2 Switches and triggering mode

Due to the high operating voltage and current and to the firing repetition rate, the switch prerequisites are very demanding. To lower the maximum current (detrimental even because of its high time-derivative) and the total inductance per switch, their parallelization is mandatory: each capacitor must be coupled with its own switch.

The drawback of a similar choice lies in the increased complexity of the system under both the electrical and operational viewpoints. As a matter of fact, the coupling of a switch over the single capacitor must be as easy and effective as possible. Moreover, the nominal jitter of the switch closure has to be of 10 ns as maximum. A similar requisite is satisfied only by field-distortion or laser-triggered SG. On the other hand, the recovery time of this kind of switch is of the order of ms which

Component	Inductance (nH)	Capacitance (nF)
Capacitor	30	$11.1 \cdot 10^3$
Spark-Gap	26	–
4 Coaxial cables	100	2

Table 5.1: Electrical properties of the components of each discharge module.

is fully compatible with the required repetition frequency. Nevertheless, the firing frequency induces cooling problems, which become even worse due to the high operating voltage: a circulating system of deionized water is the only solution.

The SG-183 "Montecuccolino type" has been specifically designed for this application by REB3. Each spark gap is directly fitted onto its capacitor with a coupler; the current return path is through a shield canister that couples with the ground ring of the capacitor. SF_6 fills the space between the spark gap and the canister to prevent corona effects and allow to lower the inductance of the device (about 26 nH) reducing the gap between high-voltage and grounded parts. The main cooling is effected circulating deionized water in the switch-capacitor coupler. The dielectric gas is purified dry air that flows at a rate of about 0.33 L/s per switch. Synchronous triggering of the SGs is obtained through a trigger unit based on a trigatron spark gap. Maximum parallel jitter is estimated at 6 ns.

5.1.3 Coaxial cables and connections

The SG-183 is designed to house up to 4 coaxial cables in parallel. Obviously, as already stated multiple times, heavier is the parallelization lower are the maximum current per path and the total inductance; hence, the choice of 4 cable per switch, for a total of 128 discharging lines, is mandatory. The coaxial solution is extremely important since this configuration of the transmission line makes its inductance the lowest achievable. Furthermore the outer conductor of the cable partially screens the electromagnetic noise induced by the current pulsed transition.

The chosen cables are the 2248 from Dielectric Sciences. These are roughly 8–9 AWG, rated for 100 kVDC and 30 kVAC.

The cables fit in the SG-183 shield canister through specifically designed connectors. The inner conductor, instead, is housed in the high voltage (HV) plate of the switch through a special connector based on the multilam technology: a series of thin helical reeds encircle the metal point mounted on the cable and ensure an optimum electrical contact minimizing the resistance.

The same solution has been chosen on the side of the home-designed cable collector.

5.1.4 The discharge module and the auxiliary components

The assembly of each capacitor, its switch and the corresponding four coaxial cables will be hereafter termed as "discharge module" (DM). The main electrical properties of their components are summarized in Table 5.1, as rated by the suppliers. It can be easily shown that the total inductance from the 32 parallel DMs is only $L_{\mathrm{DMs}} \simeq$

5 nH. The corresponding resistance is assumed completely negligible. Clearly, even if optimized to operate at full-power, the modularity of the system allow multiple tests (like the short-circuit ones [59]) discharging a limited number of DMs.

In seek of completeness, few details on the auxiliary components are here reported; even not strictly necessary for what will follow, they make clearer the high complexity of the device.

Two main critical components of the system are the power supply (PS) and its relative distribution box (DB). The first has to charge the whole bank at 30 kV in less than one second and at a repetition frequency of one Hz. It is designed to work in constant current but it can be regulated both in voltage ($1 \div 30$ kV) and current ($1 \div 12$ A). The DB is a complementary oil cooled device through which the charging of the capacitor bank takes place. It performs other two fundamental tasks: it ensures that the capacitors are completely insulated from each other during the discharge and it is intended to protect the PS from the effects of voltage reversal. As previously mentioned, once the capacitors are charged they have to be triggered synchronously to ensure the superposition of the stored energy in the discharge onto the load. This task is fulfilled through 5 m long pulse-forming lines parallelly connected to a trigger unit (TU) based on a trigatron spark gap. Finally, the vacuum system comprises a maglev turbomolecular pump assisted by two oil-free scrolls for the pre-vacuum; an active ion gauge and a capacitance manometer monitor the pressure in the chamber, while a flowmeter is connected to two electronic control valves to adjust the input of gases.

The main electrical diagnostic tools are a fast HV probe, based on a capacitor divider, and a self-integrated Rogowski coil [4]. A proper seat for each probe has to be foreseen in the design of the collector.

5.2 The collector preliminary design

The collector design has to meet two main requirements: to keep a sufficiently low inductance of the external circuit and to realize an effective electrical connection between the DMs and the electrodes. In the present section a preliminary electromechanical design of the collector is presented: from the basic rules for the inductance, resistance and capacitance calculations and the overall available space, an outline of the layout is defined and the related electrical parameters are evaluated.

5.2.1 Few basic rules

The collector design cannot leave the related electrical properties out of consideration. In particular, its inductance strongly influences the performances of the device representing a loss term due to the conversion of the stored energy into a magnetic energy ($W_B = 1/2LI^2$). Also the resistance is related to a waste of energy converted in ohmic heating; it will be shown that this term is completely negligible. Finally, the capacitance is relevant only on the analysis of the pre-breakdown discharge phase: before the sheath formation, the collector behaves like a big charging capacitor and both the voltage derivative on its plates and the overvoltage spike preceding the discharge may induce surface discharges on the dielectric insulators ahead the electrodes.

Due to the axial-symmetry of the whole device (of both the focus tube and the capacitor bank array), the collector will preserve the same property ensuring a good symmetry of the current discharge. This means it will be made of axial-symmetric elements like cylinders or circular plates.

Neglecting the boundary effects, the inductance due to a current flowing in similar geometrical configurations is obtainable through the same formula:

$$L = \frac{\mu_0}{2\pi}\, d\, \ln\left(\frac{r_{\text{ext}}}{r_{\text{int}}}\right) ,$$

where, in the case of coaxial cylinders

$$\begin{aligned} r_{\text{int}} &= \text{external radius of the inner cylinder} \\ r_{\text{ext}} &= \text{inner radius of the outer cylinder} \\ d &= \text{height of the cylinders} \end{aligned}$$

while for circular plates

$$\begin{aligned} r_{\text{int}} &= \text{inner radius} \\ r_{\text{ext}} &= \text{outer radius} \\ d &= \text{plates distance} \end{aligned}$$

The vacuum magnetic permeability $\mu_0 = 1.26 \cdot 10^{-6}$ F/m can be extended to whole the insulator materials separating the conductors with no appreciable error. Because of the skin effect [60] related to the high frequencies of the discharge phenomena, the current is supposed to flow on a conductor of zero-thickness and the exponential current density profile inside the conductor is neglected.

The total inductance is related to the magnetic flux through the closed surface S crossed by the current following the law

$$LI = \Phi = \int_S B \,\mathrm{d}S ,$$

or to the magnetic energy density integrated over the volume V encircled by the current as

$$\frac{1}{2} L I^2 = W_{\text{m}} = \frac{1}{2\mu_0} \int_V B^2 \,\mathrm{d}V .$$

Due to the integral form of these relations, the application of the superposition principle is justified. Moreover, volumes not interested by a current flow do not contribute to the total inductance of the device.

Simply making use of the resistance definition for a conductor of length l and section S, it's possible to deduce a general expression of the resistance for a general conductor in axial-symmetry through the general electrical relation of resistance parallel and series. In particular, for a coaxial cylinder one obtains

$$R_{\text{cyl}} = \left(\frac{1}{\rho h} \int_0^{2\pi} \int_{r_{\text{int}}}^{r_{\text{ext}}} r \,\mathrm{d}r \,\mathrm{d}\theta\right)^{-1} = \rho \frac{h}{\pi(r_{\text{ext}}^2 - r_{\text{int}}^2)} \simeq \rho \frac{h}{2\pi r_{\text{int}} s} ,$$

where ρ represents the material resistivity and

$$\begin{aligned} r_{\text{int}} &= \text{inner radius} \\ r_{\text{ext}} &= \text{outer radius} \\ h &= \text{cylinder height} \\ s &= \frac{r_{\text{ext}}^2 - r_{\text{int}}^2}{2r_{\text{int}}} = \text{cylinder effective thickness for } s \ll r_{\text{int}}) \end{aligned}$$

From analogous considerations, a circular plate resistance is given by

$$R_{\text{pla}} = \left(\frac{1}{\rho \ln\left(\frac{r_{\text{ext}}}{r_{\text{int}}}\right)} \int_0^s \int_0^{2\pi} \mathrm{d}\theta \, \mathrm{d}z \right)^{-1} = \rho \frac{\ln\left(\frac{r_{\text{ext}}}{r_{\text{int}}}\right)}{2\pi s}$$

with

$$\begin{aligned} r_{\text{int}} &= \text{inner radius} \\ r_{\text{ext}} &= \text{outer radius} \\ s &= \text{plate thickness} \end{aligned}$$

Both in the case of cylinders and plates, the skin depth [60] due to the high frequency discharge is the effective thickness s to be considered in the above formulae.

The capacitance of cylinders and plates are commonly known and are simply reported hereafter for an insulator material with a relative dielectric constant ϵ_{r}:

$$C_{\text{cyl}} = \epsilon_0 \epsilon_{\text{r}} \frac{2\pi h}{\ln\left(\frac{r_{\text{ext}}}{r_{\text{int}}}\right)},$$

and

$$C_{\text{pla}} = \epsilon_0 \epsilon_{\text{r}} \frac{\pi (r_{\text{ext}}^2 - r_{\text{int}}^2)}{d},$$

where the geometrical notations follow those used for the resistance. In the case of capacitance, also the parts not crossed by a current contribute to the total value.

From the above simple relations, few basic design rules can be deduced:

- the inductance is reduced by lowering the cylinders height or plates distance as well as the radiuses ratio; this means that for equal inter-cylinder gaps $r_{\text{ext}} - r_{\text{int}}$ it's convenient to increase the outer radius; in the case of circular plates this rule is not easy to follow, but it is easier to reduce the plates distance d (with detrimental consequences on the necessary electrical insulation);
- the resistance decreases with the cylinder height and the radiuses ratio of the circular plate; the consequent rules are in good agreement with those deduced for the inductance, but the resistance effect is not of great importance;
- the capacitance is directly proportional to the dielectric constant ϵ_{r}; from the geometrical point of view, it increases with the height and decreases with the radiuses ratio in the case of cylinders, while increases with the surface extension and decreases with the distance in the case of circular plates.

It immediately follows that a reduction of the inductance and resistance is coupled with an increase in the total capacitance.

5.2.2 The overall dimensions

From the previous rules, a first rough design of the collector can be devised taking into account of the available space and of the coupling needs on the capacitor side and on the focus tube one.

The two main constraints are imposed: the first is the available space inside the capacitor bank array, taking into account the possibility to access the internal region; the second is related to the maximum bending radius of the coaxial cables and to the height of the capacitor+SG assembly. The dimensions of interest are reported in Figure 5.1, where the capacitors disposal is depicted, and in Figure 5.2, which gives a sketch of a DM. Obviously, the collector cannot be set at the height reported in

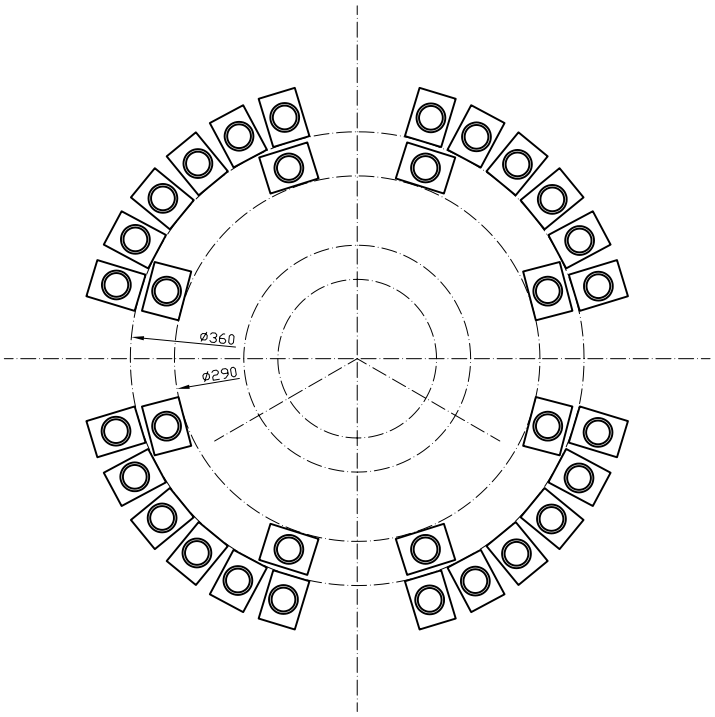

Figure 5.1: Layout of the capacitor array in plan (dimensions in cm).

Figure 5.2 without a proper support; in order to ensure a good stability it has to lay on, at least, three legs, sloping towards the axis of symmetry. This means that the available space is reduced by the support needs.

It is quite evident that two huge cylindrical coaxial rings are the best solution to connect both the grounded and HV conductors of the coaxial cables. A sufficient distance between them has to be kept in order to avoid surface tracking along the surface of the dielectric covering the inner conductor. In this specific case, 100 mm are enough for voltage greater than 30 kV, as arising from experiments.

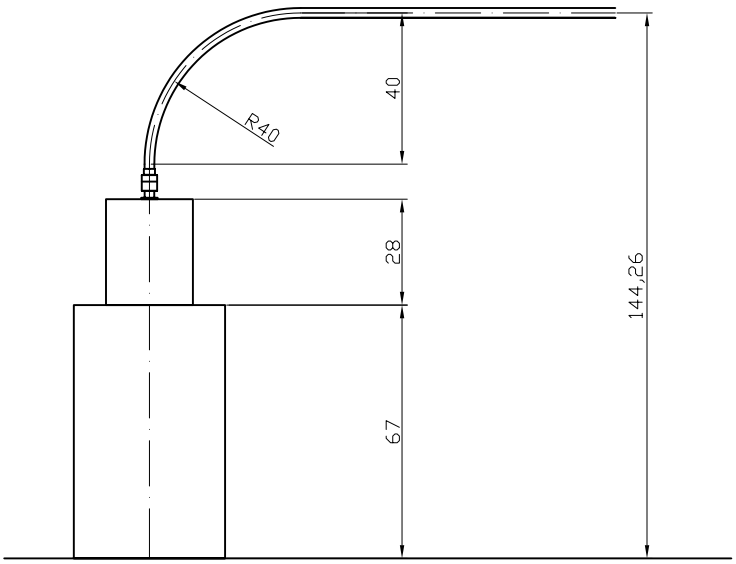

Figure 5.2: View of the capacitor, spark-gap and coaxial cable assembly with its relative bending radius (dimensions in cm).

The previous considerations on the available space inside the capacitor array and on the support stability have to match with the working space needed for the cables mounting. A special threaded nut has to be screwed onto the housing of the grounded conductor. The high number of cables ($N_{\text{cables}} = 128$) makes necessary to split in the connectors into $n_{\text{row}} = 2$ rows. From the connector diameter ϕ_{rmc} and the minimum working space d_{w}, a minimum external radius can be found as

$$r'_{\text{ext}} = \frac{N_{\text{cables}}(\phi_{rmc} + d_{\text{w}})}{2\pi n_{\text{row}}} \simeq 820 \text{ mm}\,.$$

The inner radius is then deduced from the distance d_{st} to avoid surface tracking and from the thickness of s the external ring. It follows that

$$r_{\text{ext}} = r'_{\text{ext}} - s \simeq 795 \text{ mm}$$
$$r_{\text{int}} = r_{\text{ext}} - d_{\text{st}} = 695 \text{ mm}\,.$$

The only constraint on the cylinder height is the working space, which lead to $h \simeq 100$ mm. In Figure 5.3, two complementary views of the connector seats on the outer ring are presented.

The two coaxial rings has then to be connected with the central core of the device where the focus tube is sited. Two circular plates separated by a thin insulating material are the best solution, in accordance with the practical rules above deduced for inductance minimization. A separation $d = 100$ mm is practically sufficient as volume insulation if a material with a high dielectric strength is used.

The central part of the collector increases in complexity, since a flexible way to replace the insulator sleeve and to experimentally tune the electrodes dimensions must be taken into account. The circular plates can then extend to an inner radius

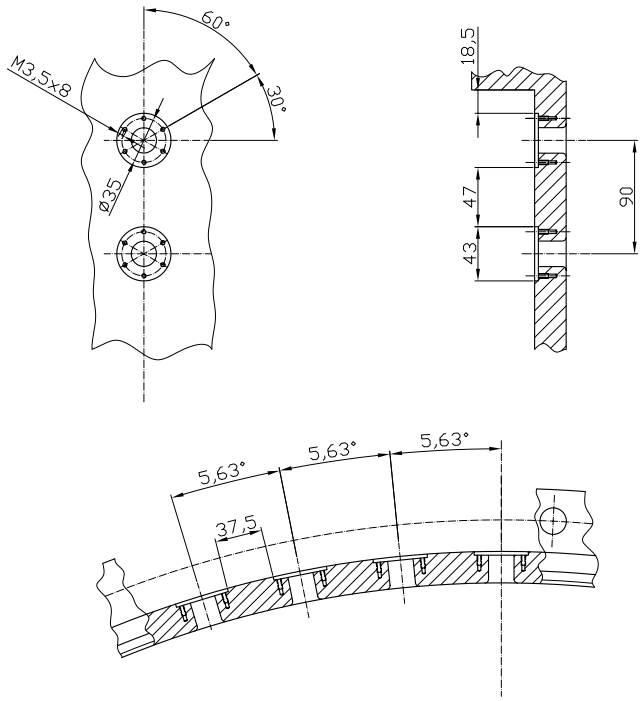

Figure 5.3: Housings for the HN88C connectors assembly on the outer ring of the collector (dimensions in mm).

of about $r_{\text{int}} = 150$ mm; here their separation has to increase to allow the connection of the electrodes through a bolted coupling flange. A distance of about 100 mm must be kept between HV and grounded conductors, but it can be decreased with a careful choice of the insulators geometry and coupling.

The electrodes dimensions of the focus tube are those obtained by the snowplow optimization presented in Section 4.2. The inner radius has been slightly increased to fit with standard ceramic cylinders used as insulator sleeve.

5.2.3 Electrical parameters

From the above evaluations, the general sketch of the collector device, as reported in Figure 5.4–5.5–5.6, can be depicted.

Making deep use of the relations presented in Section 5.2.1, a first rough estimation of the electrical parameters can be performed. The analytical calculation needs few simplifying hypothesis:

- negligible boundary effects (they influence mainly the capacitance);
- perfect axial symmetry (absence of holes and mechanical interconnection elements);
- perfect conductivity at the interfaces;
- currents flowing on a thin layer facing the autoinduced magnetic field (skin effect);

– current input and output at about 100 mm from the lower plate;

A self-inductance calculation requires a closed current path; the electrodes have been short-circuited at their top to take into account their whole contribution. From the values in Table 5.2 it's clear that the greatest contribution comes just from the electrodes (6). Moreover, it can be noticed that the circular plates and external ring contributions is rather small notwithstanding their encumbrance. The higher values are those of the central part, but nothing can be done if a sufficient flexibility is wanted.

Usually, the resistance of the electrodes and of the plasma sheat is negligible if compared with that of the external circuit. For this reason the electrodes are supposed to be short-circuited at their closed end. The conductivity here used are those of AISI304 for the whole collector ($\sigma_{304} = 4.032 \cdot 10^6$ S/m) and of the copper for the first part of the inner electrode ($\sigma_{\mathrm{Cu}} = 5.998 \cdot 10^7$ S/m). The obtained value is surely lower that the real one (evaluable only by shot circuit tests) due to the simplifying hypothesis of null contact resistance.

From the values of the capacitance value reported in Table 5.4 it arises evident that the greatest contribute is given by the circular plates, due to their high surface. The delrin is here considered as dielectric material, for its workability with machine tools and its thermal and electrical properties (high relaxing temperature, high dielectric rigidity, ...); a dielectric relative constant $\epsilon_{\mathrm{r}} = 4$ is assumed from data-sheets.

The previous analytical results were compared with those of numerical simulations obtained with a commercial finite element code (*FemLab 3.1* – electromagnetical module). The simulation domain is still considered perfectly axial-symmetric; the modeled bidimensional geometry, proposed in Figure 5.7, was created by importing directly the CAD drawings of a section of the collector. A current path of 6 mm was imposed on the conductive surfaces facing the magnetic field to take into account the skin effect. The simplifying hypothesis of the analytical calculation are still assumed, even if the numerical simulation allow to better estimate the contribution of boundary effects.

The PDE solver allows to obtain the electromagnetic quantities of interest, as represented in Figure 5.7. In particular, the domain integration tool automatically evaluates the total magnetic energy $W_{\mathrm{m}} = LI^2/2$ stored in the domain and the total magnetic flux through a closed surface $\Phi = LI$, as a consequence of a current flow. Combining the two expression, the total inductance can be evaluated as

$$L = \frac{\Phi^2}{2W_{\mathrm{m}}} = 39.09 \text{ nH}\,.$$

Excluding the electrodes contribution, the inductance is lowered to 20.83 nH.

Applying the well-known *Ohm's law*, the resistance of the whole collector is

$$R = \frac{V}{I} = 4.353 \cdot 10^{-2} \text{ m}\Omega\,.$$

Removing the short-circuit at the open end of the electrodes, the electric potential can be evaluated in the whole domain. Applying the generalized expression for the electrostatic energy W_{m} with a space dependent electric rigidity $\epsilon_{\mathrm{r}}(\vec{r})$, one obtains

$$W_e = \frac{1}{2}\epsilon_0 \int_{\mathcal{V}} \epsilon_{\mathrm{r}}(\vec{r}) E(\vec{r})^2 \,\mathrm{d}\vec{r} = \frac{1}{2} C V_0^2\,,$$

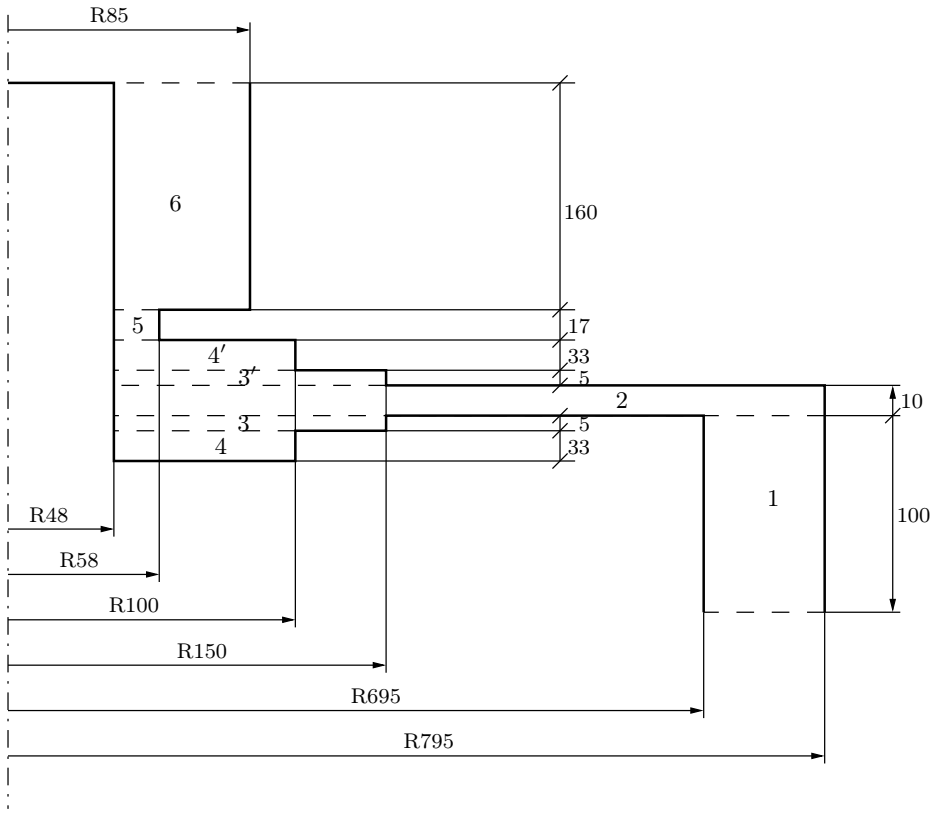

Figure 5.4: Schematic sketch of the assembly (dimensions in mm, not to scale); each zone is labeled and the corresponding number reported in Table 5.2 (1- ring for coaxial cables connection; 2- circular plates of connection with the core; 3-3′,4-4′,5 - central part to match the electrodes; 6- electrodes).

Zone	d (mm)	r_{ext} (mm)	r_{int} (mm)	L (nH)	Total (nH)
1	100	795	695	2.69	
2	10	795	48	5.61	
3-3′	5	150	48	1.14	
4-4′	33	100	48	4.85	
5	17	58	48	0.64	20.91
6	160	85	48	18.28	**39.20**

Table 5.2: Dimensions corresponding to each zone of interest (refer to Figure 5.4) and calculated inductance.

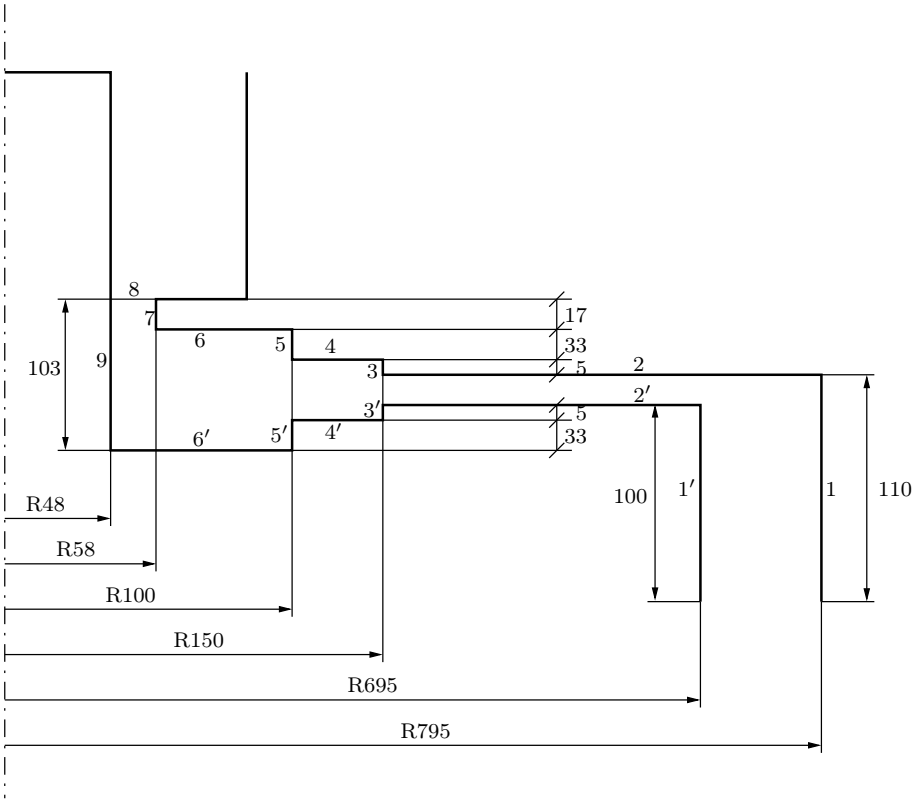

Figure 5.5: Schematic sketch of the collector assembly (dimensions in mm, not to scale) used for the resistance calculation (refer to Table 5.3).

Cylinders

Zone	h (mm)	r_{int} (mm)	R (mΩ)
1|1′	110|100	795|695	$9.11 \cdot 10^{-4}$|$9.47 \cdot 10^{-4}$
3-3′	5	150	$2.20 \cdot 10^{-4}$
5-5′	33	100	$2.17 \cdot 10^{-3}$
7	17	58	$1.93 \cdot 10^{-3}$
9	103	48	$9.49 \cdot 10^{-4}$

Circular plates

Zone	r_{ext} (mm)	r_{int} (mm)	R (mΩ)
2|2′	795|695	150	$1.10 \cdot 10^{-2}$|$1.01 \cdot 10^{-2}$
4-4′	150	100	$2.67 \cdot 10^{-3}$
6|6′	100	58|48	$3.59 \cdot 10^{-3}$|$4.83 \cdot 10^{-3}$
8	58	48	$1.25 \cdot 10^{-3}$

Total: $4.56 \cdot 10^{-2}$ mΩ

Table 5.3: Dimensions of each zone of Figure 5.5 separated by shape. The layer interested by an uniform current flow is assumed to have $s = 6$ mm as thickness.

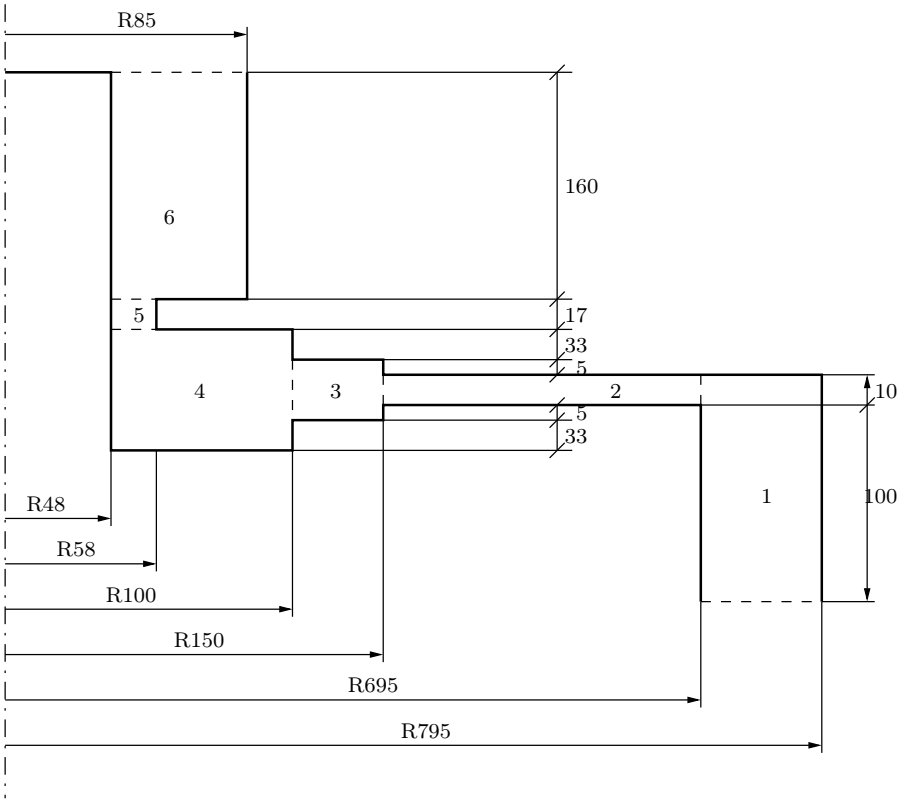

Figure 5.6: Schematic sketch of the collector assembly (dimensions in mm, not to scale), as used in the capacitance analytical evaluation reported in Table 5.4.

Cylinders

Zone	ϵ_r	h (mm)	r_{ext} (mm)	r_{int} (mm)	C (nF)
1	1	100	795	695	$4.14 \cdot 10^{-2}$
5	4	17	58	48	$2.00 \cdot 10^{-2}$
6	1	160	85	48	$1.56 \cdot 10^{-4}$

Circular plates

Zone	ϵ_r	d (mm)	r_{ext} (mm)	r_{int} (mm)	C (nF)
2	4	10	695	150	5.12
3	4	20	150	100	$6.95 \cdot 10^{-2}$
4	4	86	100	48	$9.95 \cdot 10^{-3}$

Total: 5.28 nF

Table 5.4: Dimensions of each zone of Figure 5.6 and corresponding contribute to the total capacitance. The table is split for the two cases of cylinders and circular plates.

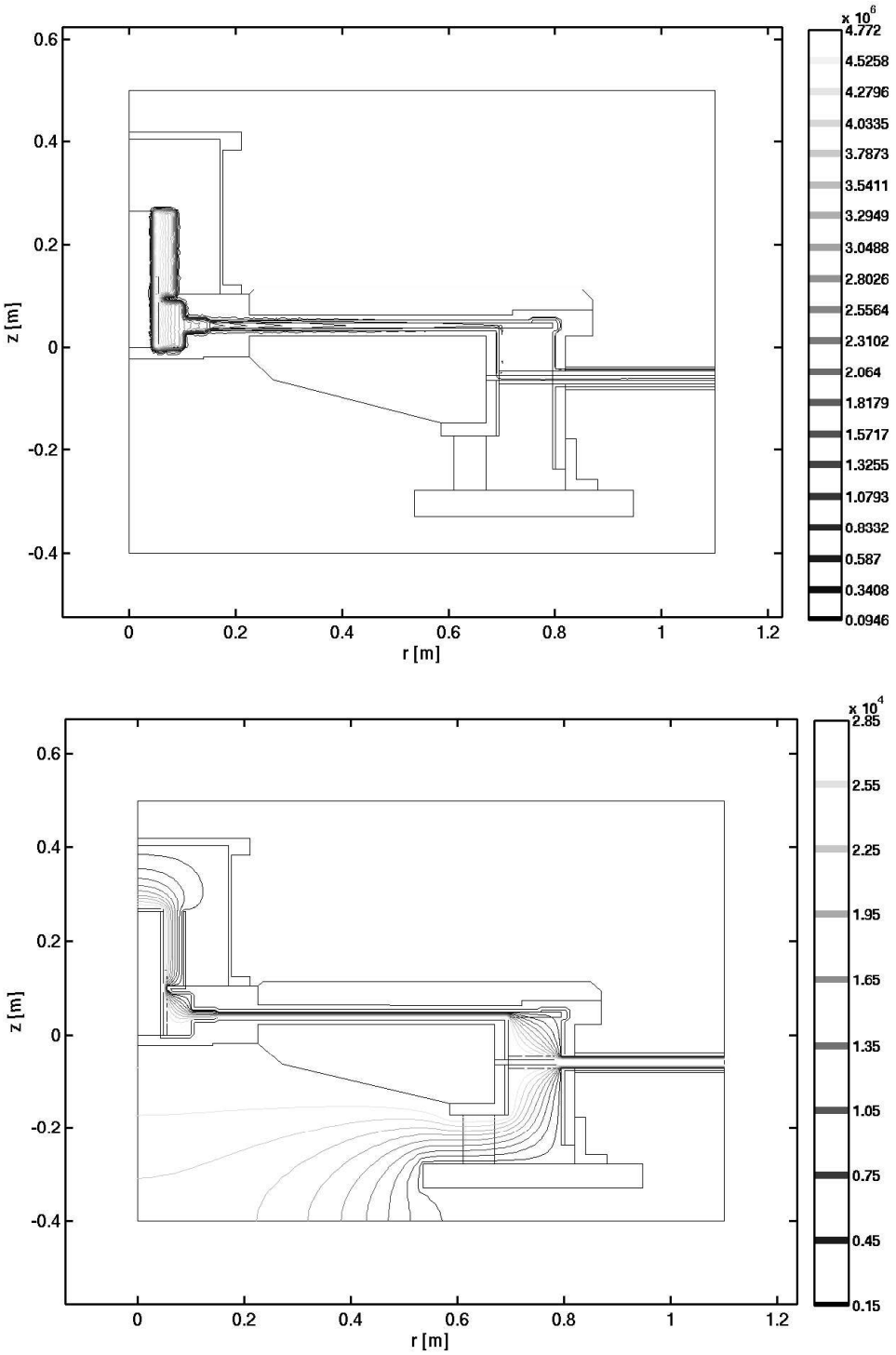

Figure 5.7: Magnetic field (top, short-circuited electrodes) and electric potential (bottom, open circuit) on the simulation domain.

and, consequently,

$$C = \frac{2W_e}{V_0^2} = 5.66 \text{ nF}\,.$$

The percentual relative error between the analytical and numerical calculation is about 1% for L, 5% for R and 7% for C. As previously stated, it can be assigned to the boundary effects, clearly higher in the case of capacitance calculations.

The obtained value of inductance is in perfect agreement with the expected one (see Section 2.3.2) of about 40 nH for the whole external circuit. Considering the inductance of the DMs ($L_{\text{DMs}} \simeq 5$ nH) and excluding that of the electrodes ($L_{\text{el}} = 18$ nH), the total inductance of the external circuit is about 25 nH. On the other hand, the obtained resistance is safely considerable an approximation by defect; reasonable values are of the order of few mΩ. Finally, the capacitance is an important electrical parameter since it is strictly related with the initial phase of the discharge, as it will be shown in Section 5.3.1.

5.2.4 Preliminary short-circuit tests

Short-circuit tests are typically conducted to evaluate experimentally electrical parameters of the external circuit. Assuming the nominal values of the DM parameters to be reliable, the following results can be used to confirm the analytical and numerical data [59].

Tests on PFMA1 machine were conducted firing a variable number N of parallel DMs, with $N = 1$, 4 and 8. In all cases, the remaining $32 - N$ DMs were not fired, but connected to the system. All tests were performed at a bank voltage in the range $12 \div 13$ kV, to maintain a sufficiently low spark-gap breakdown jitter. To monitor triggering, 32 B-dot probes were used, each positioned close to one of the four discharging cables of a module. Every transducer feeds into an optical converter, whose signal is sent through fiber optic cables to a multiple input DAQ analyzer. The latter is programmed to hold memory of the discharges and verify that time jitter is within given tolerance. Filtering is needed to discriminate the signal from the triggering pulse sent to the distortion ring, from that generated by the discharging capacitor current.

Devices used to collect current and voltage data were a Rogowski coil and a fast high voltage capacitive probe. The Rogowski coil encircles the high voltage collector plate (in both frames of Figure 5.7 the site of the probe can be found in the upper-left corner of the collector) on a diameter of about 161 cm and its conductor helix has 4400 turns around a bakelite core. The high voltage capacitive probe consists of an annular self-insulated copper slab 0.2 mm thick inserted between the upper grounded collector plate and the Delrin slab. The device acts like a typical capacitive AC voltage divider with an output voltage signal ideally following the law $V_{\text{probe}} = V\, C_{\text{coll}}/(C_{\text{coll}} + C_{\text{probe}})$, where V is the voltage on the capacitor bank, C_{coll} and C_{probe} the collector and probe capacitance respectively.

During the discharge, since the not firing DMs are connected, they still contributed capacitance towards the ground, and the overall circuit can be schematized as shown in Figure 5.8, where L_1 and C_1 are, respectively, the overall inductance of the N firing DM and the overall capacitance of their N capacitors, L_2 the inductance of

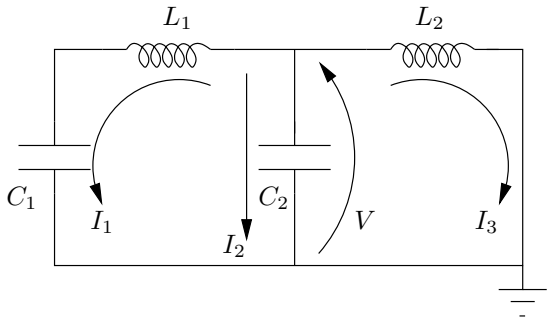

Figure 5.8: Two meshes LC circuit scheme used to model the short-circuit discharge.

the collector and head, and C_2 the capacitance of the $32 - N$ parasitic transmission lines. With C_0 being the capacitance of one single capacitor and L_0 the inductance of a single active DM, it results $C_1 = N\,C_0$ and $L_1 = L_0/N$. C_2 is given by the sum of the 32 parasitic capacitances C_p of each DM, essentially due to its 4 transmission lines.

Once the circuit equations are solved, values for the currents I_1, I_2 and I_3 are found and likewise the voltage V across the PF head, i.e. the inductance L_2 and the capacitance C_2. All the time dependent voltage and current functions can be considered as resulting from the sum of two components: one at the fundamental mode with essentially the frequency of the system without C_2, and a ripple at a much higher frequency and smaller amplitude. The fundamental mode matches the solution of the simple LC through a series expansion of the solution for $C_2 \ll C_1$. The great difference existing between the amplitudes of the two modes makes the ripple appreciable only on the voltage $V(t)$ and on the current $I_2(t)$.

Repeated firing with an increasing number of active DMs ($N = 1$, 4 and 8), gave a series of short-circuit waveforms that were automatically analyzed by a simple FFT algorithm to extract the two main frequencies modeled by the analytical solution. Deducing the total inductance, L_tot, from the fundamental frequency, $\omega = \sqrt{L_\mathrm{tot} C_1}$ of the approximately equivalent single-mesh LC circuit, a best-fitting procedure, based on a law of the type $L_\mathrm{tot} = a + b/N$, gave a perfect agreement ($R^2 = 0.9994$), with $a = 36.63$ nH and $b = 168.1$ nH as parameters. The first term is intended to represent the collector inductance, while the second one the inductance of each DM. Assuming $L_1 = 168.1/N$ nH and substituting the mean value of the fundamental and the ripple frequencies, as experimentally obtainable from the voltage waveform, in the solution of the two meshes circuit of Figure 5.8, it was possible to deduce the values of L_2 and C_2.

The data of the two analysis are comparatively presented in Table 5.5. While the collector inductance L_2 is perfectly independent on N, the total parasitic capacitance C_2 can be considered constant, consistently with the model, inside a relative error of the 7%, completely justifiable by the probes sensitivity and the data analysis propagation errors.

The capacitance data give only a rough check of the total capacitance of the device, making impossible a better estimation of the collector assembly contribution due to

N	1	4	8
L_{tot} (nH)	204.6	79.4	57.0
L_2 (nH)	36.61	36.60	36.66
C_2 (nF)	64	61	60

Table 5.5: Values of electrical parameters as determined from experiments.

experimental errors.

5.3 Additional notes

After the overall design of the collector, few additional problem will be highlighted focusing on the related solutions. In many cases, detrimental conditions cannot be completely avoided and a compromise must be found.

5.3.1 Surface tracking

As already stated, the dielectric materials are extremely important to insulate HV and grounded plates. Nevertheless, every time the edge of an insulator connects two conductors at different voltage, a favorable path for surface discharges is introduced. The most dangerous stage for this kind of phenomena is that preceding the breakdown: a voltage wave propagates through the collector towards the electrodes and a very fast voltage ramp is imposed between each faced element. Analytical calculations are usually not possible, but few considerations will be proposed hereafter together with the chosen solutions.

When the SGs are closed the capacitor bank is discharged on the capacitance of the collector, until the breakdown occurs and the electrodes result short-circuited by the plasma sheath. As shown in Section 5.A.2, event hough the charging voltage of the bank capacitor C_0 is V_0, the voltage on the secondary capacitance $C_{\text{load}} = C_{\text{coll}}$ (here the collector) can be rather higher than the first. Under the hypothesis $C_{\text{coll}} \ll C_0$ and $\zeta \ll \omega'$, typically verified for PF devices, the maximum voltage on C_{coll} can reach twice the value of V_0 (see equation (5.6)).

Since the breakdown inside the vacuum chamber develops in hundreds of ns, the voltage across the plates of the collector can reach values higher than the charging voltage. Even the propagation velocity of an electromagnetic wave is finite and given by $v = (\sqrt{L_{\text{coll}} C_{\text{coll}}})^{-1}$; this means that, looking at the collector as at a transmission line, the time needed to the propagation of the voltage wave is about 15 ns. The transient nature of the involved processes and the comparable time scale make extremely difficult the evaluation of a safety path length to avoid surface discharges on insulators above the focus tube. Experimental tests, performed by the cable supplier, suggest to take a separation distance at least of 100 mm along each dielectric surface. On the other hand, this distance must be kept as low as possible being usually related to an inductance growth.

Another fundamental aspect of the problem is the electric field intensity along the tangential direction of the insulating surface. The striking of a surface discharge

is dramatically higher if the nearby conductors present a sharp edge. As shown in Figure 5.9, obtained by a FEM simulation, the tangential electric field intensity can be halved by an edge rounding of 3 mm radius.

A delicate region for current discharges is the central part of the collector, near the electrodes. Here, the insulator must be split in more pieces to allow assembly and disassembly of the electrodes and of the insulator sleeve. Moreover, the possibility of electrodes tuning by experimental tests must be preserved. For these reasons, the core dielectric is made of 4 parts: two L-shaped rings (one threaded), a central part (to be screwed into the threaded ring) and the insulator sleeve, which is glued into the central block. The consequent geometry produces a high contribution to the total inductance (as shown in Table 5.2), but the radius of the inner electrode can be changed requiring only the substitution of the central dielectric block and of the electrodes flanges.

The design choices for the collector rings and for the central part are depicted and described in Figure 5.10.

5.3.2 The current path: the current gasketing

As previously stated, the *skin effect* produces a condensation of the current on the surfaces facing the magnetic field. In the case of interest, $\omega \simeq (\sqrt{L_0 C_0})^{-1} \simeq 0.26$ MHz and $\sigma_{304} \simeq 1.4\ \Omega^{-1}\mu m^{-1}$, the skin depth is

$$\delta = \sqrt{\frac{2}{\omega \sigma_{304} \mu}} \simeq 2\ \text{mm}\,.$$

The current profile decreases exponentially with depth; hence, an effective thickness of $3\delta \simeq 6$ mm can be considered for the current flow. In the design of the collector, the current path at the interface between two pieces must be defined with maximum care. To allow the disassembly, TIG welding cannot be used everywhere, even being the best way to ensure a good electric contact.

The problem can be solved making use of the so called *current gasketing*: a delimited region (with a thickness comparable with the calculated skin depth) is defined near the predicted current path and a high pressure must be applied between the two pieces to tighten the junction and reduce the contact resistance.

The best solution for the elements connection is through an high number of bolts uniformly distributed on the clamping circumference to increase the uniformity of pressure on the contact surface. Let n_b the number of bolts, S_b the resistant surface of each bolt, σ_b the tightening stress of the bolt, chosen a safety coefficient c_s on the yield stress σ_y for the material on the contact surface S_cg, the local induced stress is given, in first approximation, by

$$S_\text{cg} c_\text{s} \sigma_\text{y} = n_\text{b} S_\text{b} \sigma_\text{b} \quad \Longrightarrow \quad \sigma_\text{b} = \frac{S_\text{cg} c_\text{s} \sigma_\text{y}}{n_\text{b} S_\text{b}}$$

The presence of sharp edges is not only detrimental for the electric field on insulating surfaces, but also all along the current path, since a null radius would induce an infinite magnetic field with consequent vaporization of the material. Higher is the current density worse is the condition. The best choice is the rounding of all the sharp edges or cavities; everywhere possible, it's better to avoid notches on the surfaces interested by the current flow.

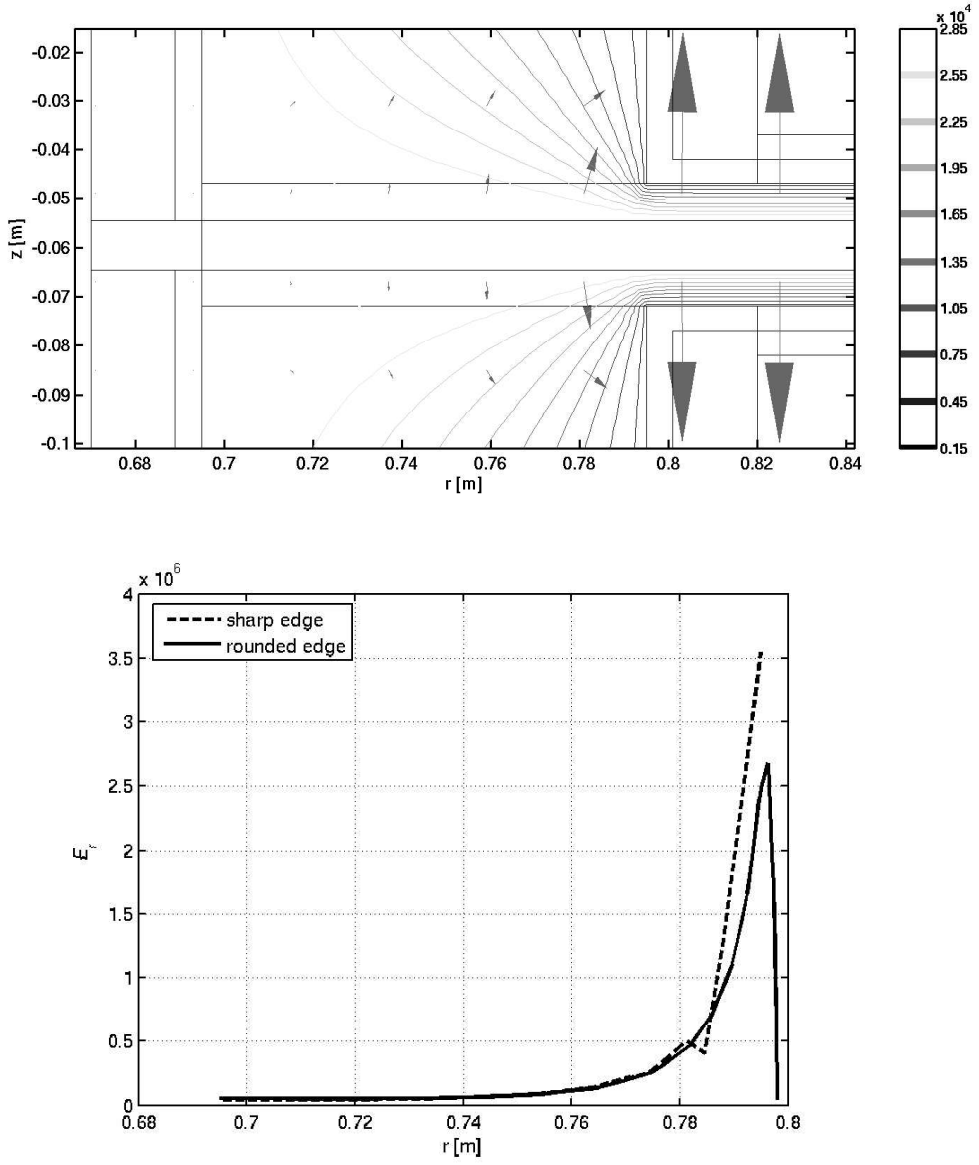

Figure 5.9: Isopotential lines and electric field vectors in the region of coaxial cables insertion (top) and comparison between the tangential electric field intensity in the case of a sharp edge (dashed line) and in that of a rounded edge (continuous line) for the insertion hole of the outer collector ring.

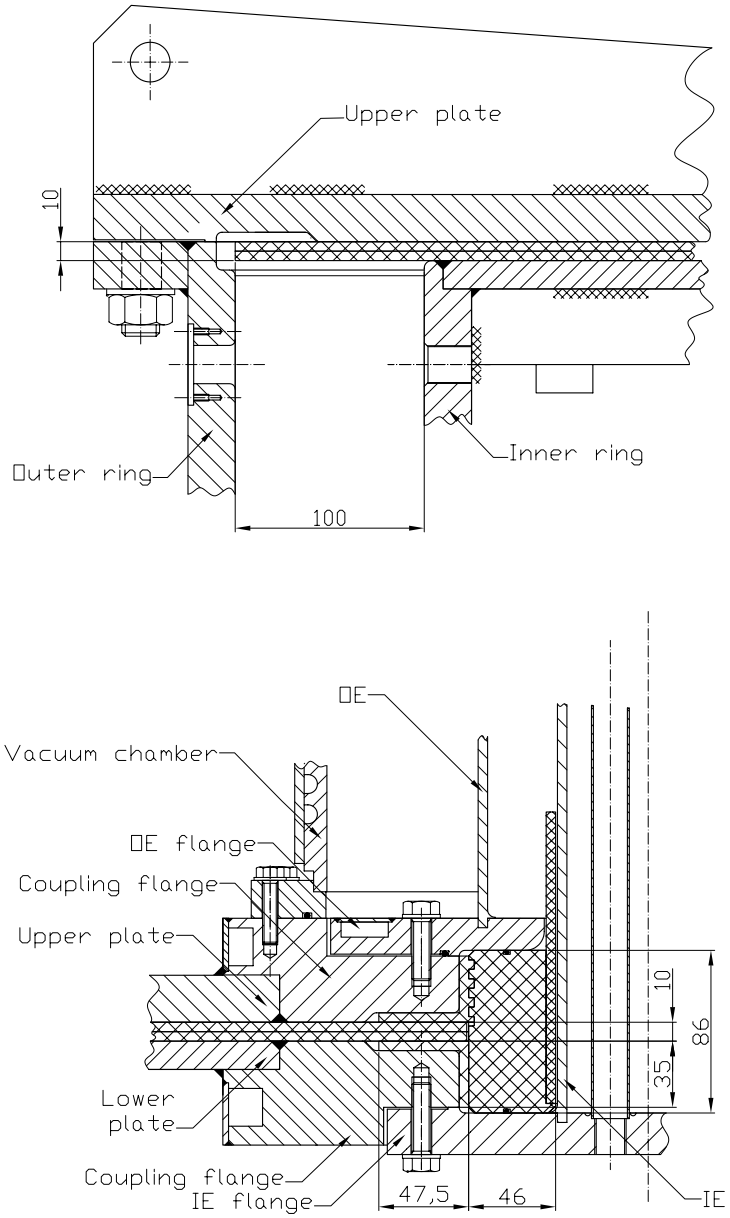

Figure 5.10: Design solutions for the 100 mm gap between the external collector rings in presence of the incoming coaxial cable and delrin slab (top) and for the central part of the device, where a high flexibility on electrodes dimensions is required (bottom).

For a better understanding of the practical solution, three sketches of the assembly drawings are represented in Figure 5.11. The first on the left is relative to the connection between the outer collector ring and the upper plate; the welding was avoided to allow the possibility of disassembly of these two huge parts. On the right, instead, the solution adopted for the electrodes connection is presented. For the external one (top), it can be noticed the positioning of the vacuum sealing o-ring in a region not interested by the current flow. In any case, the current path is defined through the gasket by making a 1 mm gap in order to reduce the contact surface S_b increasing the contact pressure; on the other side, a rounding with a radius of 3 mm is always ensured.

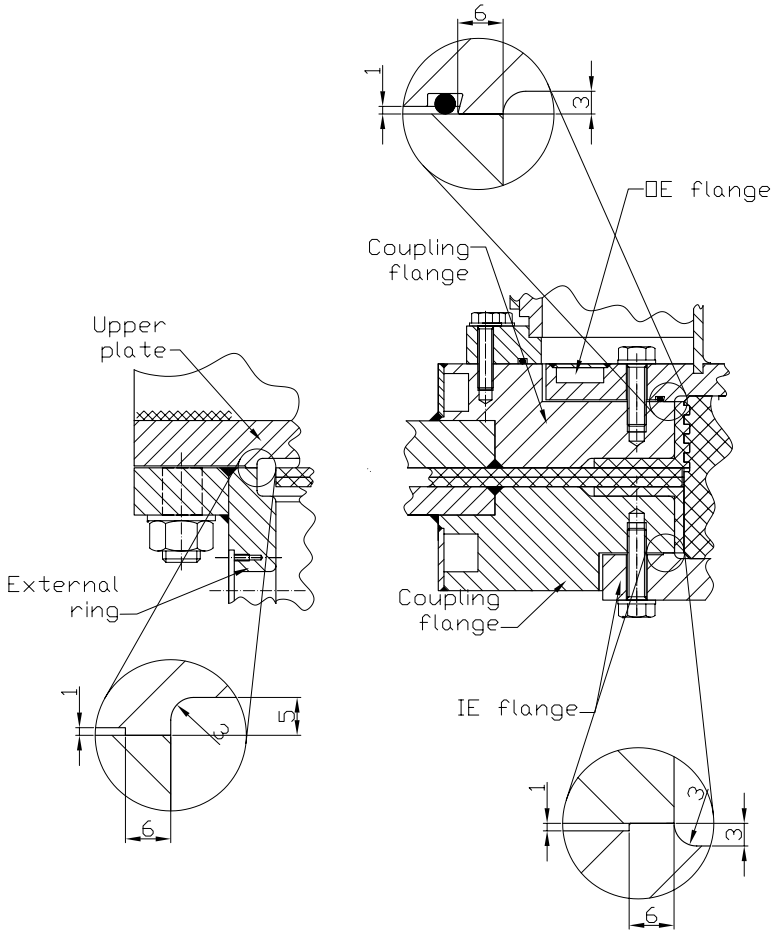

Figure 5.11: Assembly design details of the current-gaskets and edge roundings (dimensions in mm).

5.3.3 Ohmic and plasma heating

The evaluation of the device resistance made in Section 5.2.3 allow to estimate the ohmic heating of the conductors crossed by the current density. Since the collector plates are in direct contact with a delrin slab, few consideration on their heating are

of interest.

The resistance of the upper plate is $R_\mathrm{p} = 11\ \mu\Omega$, as reported in Table 5.3. As shown in Appendix 5.A, the current of the equivalent RLC circuit is

$$I(t) = V_0\sqrt{\frac{C_0}{L_0}}\exp\left(-\frac{R_0}{2L_0}t\right)\sin\left(\frac{1}{\sqrt{L_0C_0}}t\right).$$

Neglecting the resistance damping and considering a full period of the discharge, to take into account a part of the voltage reversal and to introduce a safety coefficient, the thermal power dissipated on the resistance is

$$P_\mathrm{th} = \int_0^T R_\mathrm{p}I^2\,\mathrm{d}t \simeq R_\mathrm{p}V_0^2\frac{C_0}{L_0}\int_0^T \sin^2\left(\frac{1}{\sqrt{L_0C_0}}t\right)\mathrm{d}t$$

For the electrical parameters of the device ($V_0 = 30\ \mathrm{kV}$, $L_0 = 43.4\ \mathrm{nH}$, $C_0 = 350\ \mu\mathrm{F}$), one obtains $P_\mathrm{th} = \pi R_\mathrm{p}V_0^2C_0/L_0\sqrt{L_0C_0} \simeq 978.7\ \mathrm{W}$. The heating source is concentrated in the skin depth of the plate of thickness $s \simeq 3\delta \simeq 6\ \mathrm{mm}$ (the current profile is supposed uniform for convenience). The volume of interest is hence $V_\mathrm{p} = \pi(r_\mathrm{ext}^2 - r_\mathrm{int}^2)s = 11.5\cdot10^{-3}\ \mathrm{m}^{-3}$ which corresponds to a total mass $m_\mathrm{p} = \rho V_\mathrm{p} = 90.2\ \mathrm{kg}$ for a stainless steel density $\rho = 7850\ \mathrm{kgm}^{-3}$. Referring to a specific heat $c_\mathrm{p} = 475\ \mathrm{Jkg^{-1}K^{-1}}$, the temperature increase due to a single shot (at equilibrium and with no cooling) is

$$\Delta T_\mathrm{p}^\mathrm{1shot} = \frac{P_\mathrm{th}}{m_\mathrm{p}c_\mathrm{p}} = 2.3\cdot10^{-2}\ \mathrm{K}.$$

When the device is operated at full regime (1 Hz) for two hours, the temperature increment would rise to 165 K, if no heat draining is considered. Such a high temperature would compromise the electrical insulation of delrin rated for 175 °C. However, it is enough to consider the total thickness of the plate s to coparticipate to the heat diffusion in order to have a ΔT of only 13.2 K.

The simple 0D average calculation here presented doesn't take into account the real current density profile which increases with decreasing radial coordinate. For precaution, a recirculating cooling system has been designed to remove any excessive heating; 16 cooling pipes are welded to each plate along radial directions and a spiral cave furrows the lateral wall of the vacuum chamber.

More interesting, but complex, is the heating due to the plasma-wall interaction on the electrodes and insulator in the vacuum chamber [13]. The heating of walls by direct plasma interaction has been studied in depth since the very beginning years of fusion reactors design [61]. A simple model based on the Fourier diffusion of heat into an infinitely thick wall subject to a uniform thermal power per unit surface W, constant in time, predicts a surface temperature increase ΔT given by

$$\Delta T = 2W\sqrt{\frac{t}{\pi k_\mathrm{th}\rho c_\mathrm{p}}}.$$

With this formula it is easy to evaluate the time t at which, for a given W, melting of a given material, represented by its conductivity k_th, specific heat c_p and density ρ, occurs.

This model doesn't represent correctly the interaction of the heat source with the wall in the case of a PF. In fact in a PF the heat source changes its position very quickly in time as the plasma sheath moves at supersonic velocity towards the open ends of the electrodes. However, since it is possible to estimate the thickness d of the plasma sheath and its macroscopic axial velocity, it is possible to evaluate the temperature increase for a surface extent of the order $2\pi rd$ where r is the inner electrode outer radius. A much better estimate of the temperature increase for an infinitely thick wall subject to a thermal power flux W is given by the exact solution of the Fourier equation

$$\begin{aligned}
&\frac{\partial T(x,t)}{\partial t} = \alpha \frac{\partial^2 T(x,t)}{\partial x^2} \qquad \text{with} \quad \alpha = \frac{K_{\text{th}}}{\rho c_{\text{p}}} \\
&T(x \to \infty, t) = T_0 \\
&\frac{\partial T}{\partial x}(0,t) = -\frac{1}{K_{\text{th}}} W \\
&T(x,0) = T_0
\end{aligned}$$

where x is the coordinate along the axis orthogonal and inward to the wall and T_0 is the temperature under no heat load. The solution of this equation is

$$T(x,t) = T_0 + \frac{W}{K_{\text{th}}} \left[-x \operatorname{erfc}\left(\frac{x}{2\sqrt{\alpha t}} \right) + 2\sqrt{\frac{\alpha t}{\pi}} \exp\left(-\frac{x^2}{4\alpha t} \right) \right] .$$

A simpler expression which can correlate time and position can be obtained by second order series expansion about $x = 0$:

$$T(x,t) \simeq \; T_0 + \frac{W}{K_{\text{th}}} \left[2\sqrt{\frac{\alpha t}{\pi}} - x + \mathrm{O}(x^2) \right] .$$

Conduction results to be the main cooling mechanism. In the analysis of the experimental data it will be made reference to the s.c. *Newton's Law for Cooling* [62]; this 0-D empirical law states that a given system ψ, immersed in its ambient A, cools down according to

$$T_\psi(t) = T_{\text{A}} + \Delta T \mathrm{e}^{-ct}$$

where T_ψ is the system temperature at time t, T_{A} is the constant environment (the laboratory) temperature, ΔT is the initial temperature difference between system (the electrode) and laboratory, and c is a real, positive defined, constant that determines the cooling rate. This constant is independent of T_ψ, T_{A} and ΔT. In the most general case of simultaneous presence of more than one cooling mechanisms it is possible to determine the value of c only experimentally by making temperature measurements. It is of course assumed that A behaves like a heat reservoir. This assumption is well verified in practice because the external apparati, which the inner electrode is connected to, have a heat capacity that is much larger than that of the electrode itself.

An experimental campaign was conducted on a 7 kJ non repetitive PF. The detailed description of the tests is out of the aim of this work, but can be found in [13].

The main results will be here summarized. The temperature increase on the inner electrode has been found to be independent from the filling gas pressure and from the formation of a good pinch. Viceversa, it depends almost linearly with the PF bank energy. The precise nature of the heating and cooling mechanisms for the inner electrode has been investigated theoretically and a good agreement between the above mentioned models and experiments has been found.

Even considering a single, isolated shot the knowledge of the energy dissipated into heat on the electrodes is important to assess the problem of the choice of the materials to be used in PF construction [63, 64]. The average heat flux on the inner electrode of a PF device results:

$$W = \frac{\Delta Q}{\tau_{\mathrm{p}} 2\pi r l}$$

where τ_{p} is the time-to-pinch of the order of few µs. Physically, this is the time that the plasma sheath takes to run over the whole active part of the inner electrode of length l. It is possible to estimate the surface temperature increase due to the heat flux W for a transit time τ_{T}. The transit time can be estimated using the macroscopic axial velocity of the sheath, which in turn is given by measurements or by theoretical and numerical calculations based on the snowplow model [1, 46]. For example, the insulator element surface temperature would rise at temperature of thousands degree, depending on the stored energy. This means that during the transit of the plasma sheath an extremely thin stratum of these materials is instantaneously vaporized, leading to a contamination of the PF plasma and to the embrittlement of the insulator itself.

In conclusion, proper cooling mechanisms must be foreseen for the inner electrode of a highly repetitive PF. In the case of PFMA1 the cooling system is connected with the hollow inner volume of the electrode and to the coupling flange of the external one. Only experimental tests on the cooling water temperature rise will allow to estimate correctly the electrode heating and the necessary mass flow to keep it at a proper working temperature.

5.3.4 Electrodynamical forces

During the discharge, currents of the order of the MA flow through the collector and produce intense magnetic fields; the interaction between them is the cause of high electrodynamical forces which, if applied statically, would destroy the device. In this case, the transient nature of the phenomena is of great advantage, reducing the total maximum deformation.

The electrodynamical forces can be calculated by the integral evaluation of the reciprocal interaction between each infinitesimal element of current. A simpler method is based on the Maxwell stress tensor, which is equivalent to the pressure exerted by the magnetic field on the conductors crossed by a current.

The magnetic field $\vec{H}$ in the volume between the two collector plates has only the poloidal component H_{theta}. The current density, instead, flows in a radial or axial direction on the plates or cylinders respectively. One can refer to the sketch of Figure 5.4 under the hypothesis of perfect symmetry and current flowing on a infinitesimal layer of the conductors. The *Ampere's law* on a closed line of radius r

encircling the axis of symmetry gives simply

$$H_\theta(r) = \frac{I}{2\pi r}\,,$$

as well as a current I flowing through a wire along the axis (*Biot-Savart's law*). Under the simplifying (but conservative) hypothesis of a sinusoidal (undamped) current $I(t) = I_0 \sin(\omega t)$, the resulting magnetic field is

$$H_\theta(r) = \frac{I_0}{2\pi}\frac{\sin(\omega t)}{r}\,.$$

The consequent magnetic pressure p_m is

$$p_\mathrm{m} = \frac{1}{2}\mu H^2(r,t) = \frac{I_0^2\mu}{8\pi^2}\frac{\sin^2(\omega t)}{r^2}$$

if the diffusion of the magnetic field along the conductor thickness is neglected [60]. For a peak current $I_0 = 1.5$ MA the proportionality coefficient is $a = I_0^2\mu/(8\pi^2) = 3.58 \cdot 10^4$ N. The integral of the maximum magnetic pressure between the IE and outer collector ring radiuses lead to a total force of ~ 0.7 MN, which would undoubtedly wreck the structure.

The static containment condition is strongly demanding. Nevertheless, in the present case, a dynamic containment condition can be used: the deformation work will be compared with the energy of the pulsed load leading to show that the static containment condition has to be weighted through the ratio between the structure vibration frequency and the characteristic time of the applied load.

If the lower plate of the collector is considered, it is possible to assume a perfect constraint on the outer radius $r_\mathrm{ext} = 695$ mm. The load is given by the magnetic pressure, hence following the law $p(r) = a/r^2$ up to the IE radius $r_\mathrm{int} = 48$ mm. The plate is considered perfectly coplanar and axial-symmetric with a constant thickness $s = 15$ mm. The Section 5.B.5 gives a static containment condition in a general case analogous to the present one. From the analysis of the maximum acceptable stress in static containment, the following condition on the coefficient a is derived:

$$a_\mathrm{stat} \leq c_\mathrm{s}\sigma_\mathrm{y}\frac{2s^2}{3(1+\nu)}\left(\ln\left(\frac{r_\mathrm{ext}}{r_\mathrm{int}}\right)\left(1-\ln\left(\frac{r_\mathrm{ext}}{r_\mathrm{int}}\right)\right)+\frac{1}{2}\left(\frac{r_\mathrm{int}^2}{r_\mathrm{ext}^2}-1\right)\right)^{-1}\,,$$

where a safety coefficient c_s has been introduced. For the present geometrical parameters, one obtains $a_\mathrm{stat} \leq c_\mathrm{s} 1.33 \cdot 10^4$ N, which is evidently unacceptable even for $c_\mathrm{s} = 1$.

An analysis based on an energetic method for a dynamic containment, in the case of a load of the type $p(r) = a/r^2 \sin^2(\omega t)$ applied for half a period T, allows to obtain the condition

$$\begin{aligned} a_\mathrm{dyn} \leq & 1.303\,\frac{T_1}{T}a_\mathrm{stat}\ln^{-1}\left(\frac{r_\mathrm{ext}}{r_\mathrm{int}}\right)\times \\ & \times\left(2\ln\left(\frac{r_\mathrm{ext}}{r_\mathrm{int}}\right)\left(\left(\frac{r_\mathrm{int}^2}{r_\mathrm{ext}^2}+1\right)\ln\left(\frac{r_\mathrm{ext}}{r_\mathrm{int}}\right)-\left(\frac{r_\mathrm{int}^2}{r_\mathrm{ext}^2}+2\right)\right)-\right. \\ & \left.-\frac{1}{2}\left(\frac{r_\mathrm{int}^4}{r_\mathrm{ext}^4}+4\frac{r_\mathrm{int}^2}{r_\mathrm{ext}^2}-5\right)\right)\,. \end{aligned}$$

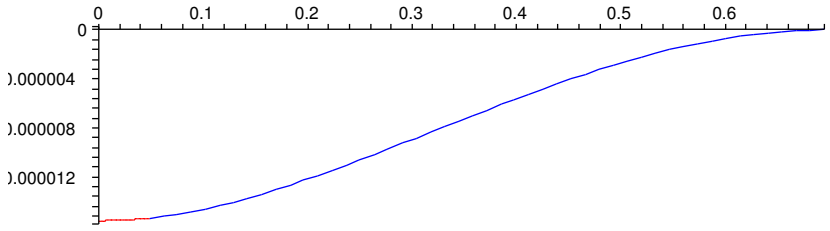

Figure 5.12: Maximum elastic deformed shape of the lower plate in dynamic load conditions (dimensions in m).

where the static parameter a_{stat} and the ratio between the plate and load periods is contained.

From the geometrical parameters of the present case (see Section 5.B.3 for more details), the vibration period $T_1 = 0.023\,\text{s}$ is obtained. The characteristic period of the LC discharge is, instead, $T = 2\pi\sqrt{L_0 C_0} \simeq 8.9\,\mu\text{s}$. Hence, the dynamic containment condition is much less demanding, leading to $a_{\text{din}} \leq c_{\text{s}} 2.70 \cdot 10^8$ N, which means no plastic strain for a load $p(r,t)$ with $a = 3.58 \cdot 10^4$ N.

The elastic buckling of the circular plate can be obtained but comparison of the momentum variation P_{e} (or the kinetic energy $P_{\text{e}}^2/2M$ transfered to the structure) with the deformation work L_{i}:

$$P_{\text{e}} = \int_0^{T/2} \int_A p(r,t)\,\mathrm{d}A\,\mathrm{d}t = \pi \int_0^{T/2} \tau(t)\,\mathrm{d}t \int_{r_{\text{int}}}^{r_{\text{ext}}} p(r) r\,\mathrm{d}r = \frac{T}{4}\pi a \ln\left(\frac{r_{\text{ext}}}{r_{\text{int}}}\right),$$

con $a = a_{\text{din}} = 3.58 \cdot 10^4$ N effective constant; moreover, from the equation (5.18), it follows

$$L_{\text{i}} = a_{\text{eq}}^2 \frac{\pi}{16B} r_{\text{ext}}^2 \left(2\ln\left(\frac{r_{\text{ext}}}{r_{\text{int}}}\right)\left(\left(\frac{r_{\text{int}}^2}{r_{\text{ext}}^2}+1\right)\ln\left(\frac{r_{\text{ext}}}{r_{\text{int}}}\right) - \left(\frac{r_{\text{int}}^2}{r_{\text{ext}}^2}+2\right)\right) - \right.$$
$$\left. - \frac{1}{2}\left(\frac{r_{\text{int}}^4}{r_{\text{ext}}^4} + 4\frac{r_{\text{int}}^2}{r_{\text{ext}}^2} - 5\right)\right).$$

The equilibrium condition $P_{\text{e}}^2/2M = L_{\text{i}}$ allows to determine a_{eq} as

$$a_{\text{eq}} = 0.651\, a_{\text{din}} \frac{T}{T_1} \ln\left(\frac{r_{\text{ext}}}{r_{\text{int}}}\right)\left(2\ln\left(\frac{r_{\text{ext}}}{r_{\text{int}}}\right)\left(\left(\frac{r_{\text{int}}^2}{r_{\text{ext}}^2}+1\right)\ln\left(\frac{r_{\text{ext}}}{r_{\text{int}}}\right) - \right.\right.$$
$$\left.\left. - \left(\frac{r_{\text{int}}^2}{r_{\text{ext}}^2}+2\right)\right) - \frac{1}{2}\left(\frac{r_{\text{int}}^4}{r_{\text{ext}}^4} + 4\frac{r_{\text{int}}^2}{r_{\text{ext}}^2} - 5\right)\right)^{-1/2},$$

where the equation (5.17) has been used.

From the previous data, the value $a_{\text{eq}} = 9.91$ N is obtained, and a corresponding maximum displacement of $f_{\text{max}} \simeq 15.6\,\mu\text{m}$ is deducted (see Section 5.B.2 for more details). In Figure 5.12, the maximum analytical buckling of the lower circular plate of the collector is depicted as obtained in the previously mentioned conditions.

The problem of the upper plate can be solved in an similar way, even if, strictly speaking, it should be considered as an annular plate (no condition of null derivative

on the axis of symmetry) with different geometrical parameters and load extension. Notwithstanding, the insertion of radial stiffening bars would increase the structure rigidity; the vacuum sealing can be considered safe even under the most demanding operative conditions.

More interesting, but even simpler, is the dynamic containment check over the copper OE. Under the hypothesis of free cylinder of thin thickness s, under an internal pressure $p(r,t)$ with r fixed to the inner radius r_{int} of the cylinder, the oscillating period is given by

$$T_1 = 2\pi\, r_0 \sqrt{\frac{\rho}{E}}\,.$$

The dynamic containment condition is here given by [60]

$$\frac{a}{r_{\text{int}}^2} \leq c_{\text{s}} \frac{2}{\pi} \frac{T_1}{T} \sigma_{\text{y}} \frac{s}{r_{\text{int}}} \qquad \text{or, equivalently,} \qquad a \leq c_{\text{s}} \frac{2}{\pi} \frac{T_1}{T} \sigma_{\text{y}}\, s\, r_{\text{int}}\,.$$

Assuming $r_{\text{int}} = 8.5$ cm and $s = 5$ mm ($E = 1.2 \cdot 10^5$ MPa, $\rho = 8900$ kgm^{-3}, $\sigma_{\text{y}} = 210$ MPa for copper), it follows $T_1 \simeq 145$ µs against a load period of $T \simeq 8.9$ µs. Hence, the dynamic containment condition $a_{\text{dyn}} \leq c_{\text{s}} 9.26 \cdot 10^5$ N, is fully verified for the case under exam ($a = 3.58 \cdot 10^4$ N).

The above evaluations demonstrate that electrodynamical forces, even if extremely high due to the high currents involved, don't represent a problem since their transient nature make their contribution to momentum transfer insufficient to cause strain and stresses such as to overcome the yield point.

5.A RLC circuits of interest

The *Laplace transform* is a widely diffused method to solve typical transient electrical circuit. Hereafter, the solution of the lumped circuits of interest will be presented.

5.A.1 The classical RLC circuit

Starting from the classical RLC circuit depicted in Figure 5.13, the circuit equation is

$$V_0 = L \frac{\mathrm{d}I(t)}{\mathrm{d}t} + RI(t) + \frac{1}{C} \int_0^t I(t')\, \mathrm{d}t'\,, \tag{5.2}$$

with $I(t=0) = 0$ and $V_C(t=0) = V_0$ as initial conditions.

Applying the Laplace transform, the algebraic equation

$$Ls\tilde{I} + R\tilde{I} + \frac{1}{C}\frac{1}{s}\tilde{I} + \frac{V_0}{s} = 0\,,$$

in the transformed space s is obtained. The denominator of the solution

$$\tilde{I} = \frac{V_0}{Ls^2 + Rs + C^{-1}}\,; \tag{5.3}$$

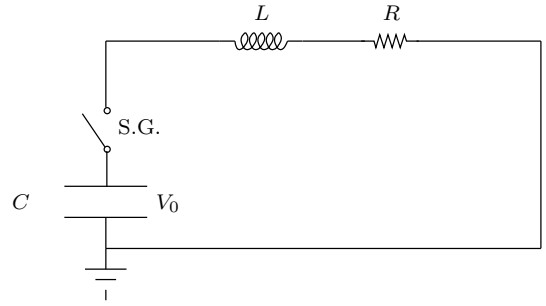

Figure 5.13: Scheme of a classical lumped RLC circuit.

presents two possible roots (complex or real):

$$s_{1,2} = -\frac{R}{2L} \pm \sqrt{\frac{R^2}{4L^2} - \frac{1}{LC}}\,.$$

PF devices are characterized by electrical parameters which satisfy the condition $R < L$ (*under-damping*) and make $s_{1,2}$ complex conjugate. Usually, the resonance frequency ω and the damping factor ζ are defined as

$$\omega = \sqrt{-\frac{R^2}{4L^2} + \frac{1}{LC}}$$
$$\zeta = \frac{R}{2L}\,,$$

leading to the solution

$$I(t) = \frac{V_0}{\omega L}\exp(-\zeta t)\sin(\omega t)\,. \tag{5.4}$$

obtained by splitting the denominator of $\tilde{I}$ and applying the Laplace inverse transform rules.

The current flowing in the circuit has a damped sinusoidal behavior, with a characterist period T defined as

$$T = \frac{2\pi}{\omega} = \frac{2\pi}{\sqrt{\frac{1}{LC} - \frac{R^2}{4L^2}}} = \frac{4\pi L}{\sqrt{\frac{4L}{C} - R^2}}\,.$$

Usual values of resistance, inductance and capacitance of PFs satisfy the relation $R^2 \ll 4L/C$ letting the following approximations:

$$\omega = \frac{1}{\sqrt{LC}} \qquad \text{e} \qquad T = 2\pi\sqrt{LC}\,.$$

The maximum current is then given by

$$I_{\max} = I(t = \tfrac{T}{4}) = \frac{2V_0}{\sqrt{\frac{4L}{C} - R^2}}\exp\left(-2\pi\frac{R}{\sqrt{\frac{4L}{C} - R^2}}\right) \simeq V_0\sqrt{\frac{C}{L}}\exp\left(-\frac{\pi}{4}R\sqrt{\frac{C}{L}}\right) \simeq V_0\sqrt{\frac{C}{L}}\,.$$

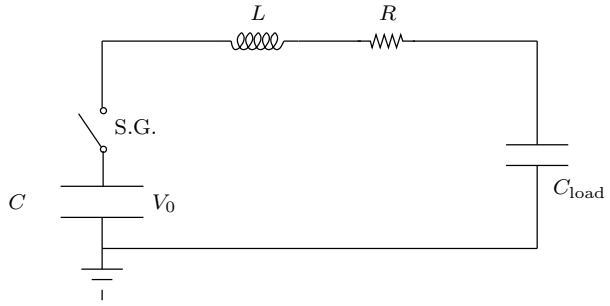

Figure 5.14: Sketch of a RLC circuit discharging on a secondary capacitance C_{load}.

Applying the capacitor laws, the voltage drop over it is:

$$V(t) = V_0 - \frac{1}{C}\int_0^t I(t')\,\mathrm{d}t' = V_0 \exp(-\zeta t)\left(\cos(\omega t) + \frac{\zeta}{\omega}\sin(\omega t)\right)$$
$$\simeq V_0 \exp\left(-\frac{R}{2L}t\right)\cos\left(\frac{t}{\sqrt{LC}}\right),$$

out of phase of $\pi/2$ with respect of the current profile $I(t)$.

5.A.2 Discharge on a secondary capacitance

Consider now the electrical circuit of Figure 5.14, where a secondary capacitance C_{load}, initially uncharged, is charged by the capacitor bank C charged at a voltage V_0 through a purely active (RL) branch.

If a balance equation of the voltage drops is written, it can be easily reduced to the following equation

$$V_0 = L\frac{\mathrm{d}I(t)}{\mathrm{d}t} + RI(t) + \frac{C + C_{\text{load}}}{CC_{\text{load}}}\int_0^t I(t')\,\mathrm{d}t',$$

with initial condition $I(t = 0) = 0$. Substituting $C' = CC_{\text{load}}/(C + C_{\text{load}})$, the equation assumes the same form of that for an RLC circuit with R, L and C' as parameters, whose solution is already known from the previous section.

Applying the capacitor law to C_{load}, the voltage on its plates is given by

$$V(t) = \frac{1}{C_{\text{load}}}\int_0^t I(t')\,\mathrm{d}t' = \frac{1}{C_{\text{load}}}\frac{V_0}{\omega' L}\int_0^t \exp(-\zeta t')\sin(\omega' t'),$$

which leads to

$$V(t) = \frac{C'}{C_{\text{load}}}V_0\left(1 - \exp(-\zeta t)\left(\cos(\omega' t) + \frac{\zeta}{\omega'}\sin(\omega' t)\right)\right). \tag{5.5}$$

The maximum voltage on C_{load} is given by

$$V_{\max} = \frac{C'}{C_{\text{load}}}V_0\left(1 + \exp\left(-\pi\frac{\zeta}{\omega'}\right)\right), \tag{5.6}$$

which is grater than V_0 if $C_{\text{load}} < C$.

Expanding in Taylor's series equation (5.5) near $t = 0$ one can deduce the approximate behavior

$$V(t) \simeq \frac{1}{2}(\zeta^2 + \omega'^2)\frac{C'}{C_{\text{load}}} V_0\, t^2 + \mathrm{o}(\mathrm{t}^2)\,.$$

Lower is C_{load} with respect to C, steeper will result the voltage growth. In the simplifying, but realistic, hypothesis of $C_{\text{load}} \ll C$ and $\zeta \ll \omega'$, one obtains

$$V(t) \simeq \frac{1}{2}\frac{1}{LC_{\text{load}}} V_0\, t^2\,. \tag{5.7}$$

5.B Circular plates: structural analysis

The present appendix will deal with the elastic theory of circular plates with axial symmetric loads and boundary conditions. Consideration on the elastic deformed shape in the most general case and evaluation of the deformation energy and eigenfrequencies will follow for a circular plate fully bounded on the external radius. Particular attention will be devoted to the particular case of a r^{-2} distributed load for its analogy with the magnetic pressure acting on the circular plates of the collector.

5.B.1 Hypothesis and basis

Let R be the external radius of a circular plate and s its thickness. The geometry, the loads and the boundary conditions are perfectly axial symmetric, that means no tangential stress ($\tau_{\theta r} = \tau_{\theta z} = 0$) on each radial section and normal stresses σ_θ equally distributed. On the cylindrical surfaces, the tangential and normal stresses τ_{rz}, σ_r are uniformly distributed. Refer to Figure 5.15, for a graphical representation of the equilibrium forces on an element of the circular plate.

Under the hypothesis of negligible vertical strain, the stresses σ_r and σ_θ are null on the mid plane of the plate ($z = 0$). For $s \ll R$, every rectilinear segment normal to the mid plane can be considered rectilinear and normal to the deformed shape even after the deformation (*Bernoulli-Navier's hypothesis*). Following the *Hooke's law*, the stresses vary linearly and proportionally to the distance z from the mid plane. For small vertical displacements ζ, the slope φ of the deformed line in the plane rz is given by elastic deformed shape, from the equation

$$\tan\varphi \simeq \varphi = -\frac{\mathrm{d}\zeta}{\mathrm{d}r}\,. \tag{5.8}$$

The stresses are related to the deformed shape given by $\zeta(r)$ through [65]

$$\sigma_r = \frac{E}{1-\nu^2}\left(\frac{\mathrm{d}\varphi}{\mathrm{d}r} + \nu\frac{\varphi}{r}\right) z\,, \tag{5.9a}$$

$$\sigma_\theta = \frac{E}{1-\nu^2}\left(\nu\frac{\mathrm{d}\varphi}{\mathrm{d}r} + \frac{\varphi}{r}\right) z\,. \tag{5.9b}$$

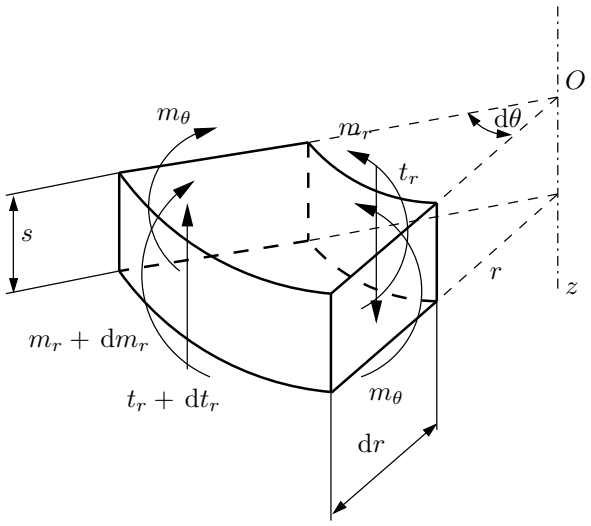

Figure 5.15: Sketch of a generic element of a circular plate, axial-symmetrically loaded.

The unitary moments on the faces normal to r and θ, are defined by

$$m_r = B\left(\frac{\mathrm{d}\varphi}{\mathrm{d}r} + \nu\frac{\varphi}{r}\right) \tag{5.10a}$$

$$m_\theta = B\left(\nu\frac{\mathrm{d}\varphi}{\mathrm{d}r} + \frac{\varphi}{r}\right), \tag{5.10b}$$

where

$$B = \frac{E}{1-\nu^2}\int_{-s/2}^{s/2} z^2\,\mathrm{d}z = \frac{Es^3}{12(1-\nu^2)}, \tag{5.11}$$

is termed *bending stiffness* of the plate.

5.B.2 Deformed shape of the circular plate

Referring to Figure 5.15, the equilibrium equation of the infinitesimal element in the rz plane gives

$$t_r = -B\frac{\mathrm{d}}{\mathrm{d}r}(\nabla_r^2\zeta(r)), \frac{\mathrm{d}t_r}{\mathrm{d}r} + \frac{t_r}{r} = \frac{1}{r}\frac{\mathrm{d}}{\mathrm{d}r}(rt_r(r)) = -p(r).$$

as equilibrium equation for rotation and translation respectively [65]. Combining the two equations, one obtains a fourth order differential equation

$$\frac{1}{r}\frac{\mathrm{d}}{\mathrm{d}r}\left(r\frac{\mathrm{d}}{\mathrm{d}r}(\nabla_r^2\zeta(r))\right) = \nabla_r^4\zeta = \frac{p(r)}{B}, \tag{5.13}$$

describing the deformed surface through $\zeta(r)$ (*Laplace's equation*).

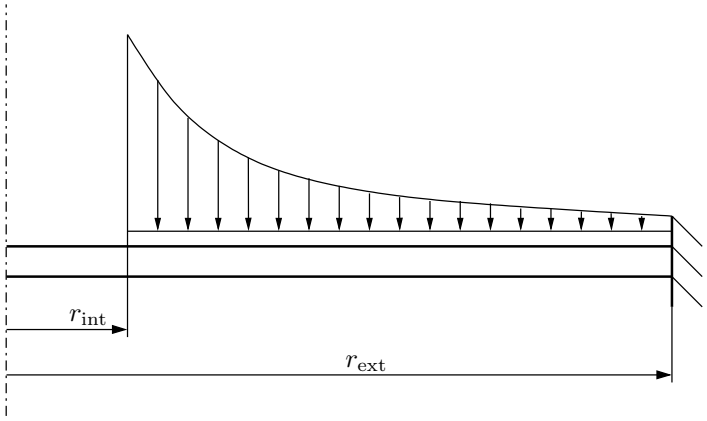

Figure 5.16: Circular plate on which a load proportional to r^{-2} is applied for r in the range $[r_{\text{int}}, r_{\text{ext}}]$.

The boundary conditions of the differential problems depend on the bounds of the circular plate. In the case of a fully bounded plate on the external radius R, it follows

$$\begin{aligned}\varphi(R) &= 0\\ \zeta(R) &= 0\,,\end{aligned}$$

while, for axial-symmetry, a null derivative must be imposed on $r = 0$ by

$$\varphi(0) = 0\,.$$

In the case of a distributed not uniform load $p(r) = ar^{-2}$ applied from r_{int} to r_{ext} (refer to Figure 5.16), the equation (5.13) must be split onto the two parts $[0, r_{\text{int}}]$ and $[r_{\text{int}}, r_{\text{ext}}]$ in a system of equations linked on r_{int} by equal φ and ζ. By substitution of $p(r)$ in the equation (5.13), a first integration on r leads to

$$t_r(r) = \frac{1}{r}\int_{r_{\text{int}}}^{r} p(r')r\,\mathrm{d}r' = \frac{a}{r}\ln\left(\frac{r}{r_{\text{int}}}\right)\,.$$

as right hand side of the equation. Splitting the problem into the two domains the system

$$\begin{aligned}&\frac{\mathrm{d}}{\mathrm{d}r}\left(\frac{1}{r}\frac{\mathrm{d}}{\mathrm{d}r}\left(r\frac{\mathrm{d}\zeta^-}{\mathrm{d}r}\right)\right) = 0 && \text{per} \quad r \in [0, r_{\text{int}}]\\ &\frac{\mathrm{d}}{\mathrm{d}r}\left(\frac{1}{r}\frac{\mathrm{d}}{\mathrm{d}r}\left(r\frac{\mathrm{d}\zeta^+}{\mathrm{d}r}\right)\right) = \frac{a}{B}\frac{1}{r}\ln\left(\frac{r}{r_{\text{int}}}\right) && \text{per} \quad r \in [r_{\text{int}}, r_{\text{ext}}]\end{aligned}$$

is obtained, with boundary conditions

$$\left.\frac{\mathrm{d}\zeta^-}{\mathrm{d}r}\right|_0 = 0 \tag{5.14a}$$

$$\zeta^-(r_{\mathrm{int}}) = \zeta^+(r_{\mathrm{int}}) \tag{5.14b}$$

$$\left.\frac{\mathrm{d}\zeta^-}{\mathrm{d}r}\right|_{r_{\mathrm{int}}} = \left.\frac{\mathrm{d}\zeta^+}{\mathrm{d}r}\right|_{r_{\mathrm{int}}} \tag{5.14c}$$

$$m_r^-(r_{\mathrm{int}}) = m_r^+(r_{\mathrm{int}}) \quad \text{equivalent to} \quad \left.\frac{\mathrm{d}\varphi^-}{\mathrm{d}r}\right|_{r_{\mathrm{int}}} = \left.\frac{\mathrm{d}\varphi^+}{\mathrm{d}r}\right|_{r_{\mathrm{int}}} \tag{5.14d}$$

$$\zeta^+(r_{\mathrm{ext}}) = 0 \tag{5.14e}$$

$$\left.\frac{\mathrm{d}\zeta^+}{\mathrm{d}r}\right|_{r_{\mathrm{ext}}} = 0 \tag{5.14f}$$

The solution of the two coupled differential equations leads to

$$\zeta^-(r) = \frac{a}{8B}(c_1^- r^2 + c_3^-) \tag{5.15a}$$

$$\zeta^+(r) = \frac{a}{8B}\left(r^2 \ln\left(\frac{r}{r_{\mathrm{int}}}\right)\left(\ln\left(\frac{r}{r_{\mathrm{int}}}\right) - 2\right) + \right.$$
$$\left. +(c_1^+ + 1)r^2 + 2c_2^+ \ln\left(\frac{r}{r_{\mathrm{int}}}\right) - c_3^+\right) \tag{5.15b}$$

where the coefficients c_1^-, c_3^-, c_1^+, c_2^+, c_3^+ are obtained through the boundary conditions of the equations (5.14a)

$$c_1^- = \ln\left(\frac{r_{\mathrm{ext}}}{r_{\mathrm{int}}}\right)\left(1 - \ln\left(\frac{r_{\mathrm{ext}}}{r_{\mathrm{int}}}\right)\right) + \frac{1}{2}\left(\frac{r_{\mathrm{int}}^2}{r_{\mathrm{ext}}^2} - 1\right)$$

$$c_3^- = \left(\ln\left(\frac{r_{\mathrm{ext}}}{r_{\mathrm{int}}}\right) - 1\right)(r_{\mathrm{ext}}^2 + r_{\mathrm{int}}^2) + 2r_{\mathrm{int}}^2$$

$$c_1^+ = \ln\left(\frac{r_{\mathrm{ext}}}{r_{\mathrm{int}}}\right)\left(1 - \ln\left(\frac{r_{\mathrm{ext}}}{r_{\mathrm{int}}}\right)\right) + \frac{1}{2}\frac{r_{\mathrm{int}}^2}{r_{\mathrm{ext}}^2}$$

$$c_2^+ = -\frac{1}{2}r_{\mathrm{int}}^2$$

$$c_3^+ = -\left(\ln\left(\frac{r_{\mathrm{ext}}}{r_{\mathrm{int}}} - 1\right)\right)(r_{\mathrm{ext}}^2 + r_{\mathrm{int}}^2) - \frac{1}{2}r_{\mathrm{int}}^2\,.$$

5.B.3 Circular plate oscillating frequencies

The oscillating behavior of a circular pate fully bounded on the boundary is obtained by the equation (5.13), replacing the load $p(r)$ with the inertia force

$$f_{\mathrm{i}} = -m\frac{\mathrm{d}^2\zeta}{\mathrm{d}t^2}\,,$$

where $m = \rho s$ represents the mass per surface unit ($m \cdot r\,\mathrm{d}r\,\mathrm{d}\theta$), s being the constant thickness of the whole plate. The Laplace's equation becomes

$$\nabla_r^4\zeta(r) = -\frac{m}{B}\frac{\partial^2\zeta}{\partial t^2}\,.$$

Looking for a stationary solution in the form of

$$\zeta(r,t) = \zeta(r)\sin(\omega t)\,,$$

the eigenvalue equation

$$\nabla_r^4 \zeta(r) = k^4 \zeta(r)\,,$$

is obtained, with

$$k^4 = \frac{m\omega^2}{B}\,.$$

By two order reduction of the previous equation, it can be substituted by

$$\frac{\mathrm{d}^2\zeta(r)}{\mathrm{d}(kr)^2} + \frac{1}{kr}\frac{\mathrm{d}\zeta(r)}{\mathrm{d}(kr)} \pm \zeta(r) = 0\,,$$

which represents a first order *Bessel's equation*, having

$$\zeta^+(r) = c_1^+ J_0(kr) + c_2^+ Y_0(kr) \qquad (+)$$
$$\zeta^-(r) = c_1^- K_0(kr) + c_2^- I_0(kr) \qquad (-)$$

as solutions.

In the case of a circular plate fully bounded on $r = r_{\mathrm{ext}}$ ($\zeta(r=0)$ finite, $\zeta(r_{\mathrm{ext}}) = 0$), the property of the Bessel functions lead to $c_2^+ = c_1^- = 0$ ($Y_n \to -\infty$ and $K_n \to \infty$ for $r \to 0$) and $c_2^- = 0$ (I_n are monotonically increasing with r). The functions J_n are, instead, oscillating and, neglecting the trivial solution for $c_1^+ = 0$, all the conditions are verified for kr_{ext} corresponding to the zeros of J_0. The first eigenvalue is

$$k_1 = \frac{2.405}{r_{\mathrm{ext}}}\,,$$

corresponding to the *fundamental eigenfrequency*

$$f_1 = \frac{\omega_1}{2\pi} = \frac{1}{2\pi}k_1^2\sqrt{\frac{B}{m}} = 0.921\frac{1}{r_{\mathrm{ext}}^2}\sqrt{\frac{B}{\rho s}}\,. \tag{5.17}$$

It can be noted that the eigenfrequencies don't depend on the applied load, but only on the geometrical parameters, material properties and boundary conditions of the structure. In particular, the oscillation frequency increases proportionally to the thickness s (being $B/m \propto s^2$) and to the inverse of the external radius r_{ext}^{-1} ($s \ll r_{\mathrm{ext}}^{-1}$ by hypothesis).

5.B.4 Deformation work

The internal deformation work for a volume element $\mathrm{d}V$ is defined as

$$\mathrm{d}L_{\mathrm{i}} = \frac{1}{2}\vec{\sigma}\cdot\vec{\varepsilon}\,\mathrm{d}V$$

which is reduced to

$$\mathrm{d}L_\mathrm{i} = \frac{1}{2}(\sigma_r\varepsilon_r + \sigma_\theta\varepsilon_\theta)\,\mathrm{d}V\,,$$

in the case of circular plates, being $\tau_{r\theta} = 0$.

By substitution of $\sigma_{r,\theta}$ and $\varepsilon_{r,\theta}$ with the unitary moments of equations (5.10) following the Hooke's law ($\sigma_i = 12m_iz/s^3$ and $\varepsilon_i = 12z/(Es^3)(m_i - \nu m_j)$ with $i,j = r,\theta$), the elementary work can be integrated over the thickness of the plate ($z \in [-s/2, s/2]$) and over the poloidal angle ($\theta \in [0, 2\pi]$), leading to

$$L_\mathrm{i} = \pi B \int_0^{r_\mathrm{ext}} \left(\left(\frac{\mathrm{d}\varphi}{\mathrm{d}r}\right)^2 + \left(\frac{\varphi}{r}\right)^2 + 2\nu\frac{\mathrm{d}\varphi}{\mathrm{d}r}\frac{\varphi}{r} \right) r\,\mathrm{d}r\,,$$

or, equivalently, from equation (5.8),

$$L_\mathrm{i} = \pi B \int_0^{r_\mathrm{ext}} \left(r\left(\frac{\mathrm{d}^2\zeta}{\mathrm{d}r^2}\right)^2 + \frac{1}{r}\left(\frac{\mathrm{d}\zeta}{\mathrm{d}r}\right)^2 + 2\nu\frac{\mathrm{d}^2\zeta}{\mathrm{d}r^2}\frac{\mathrm{d}\zeta}{\mathrm{d}r} \right) \mathrm{d}r\,.$$

For a circular plate fully bounded on its external radius, the third term in parenthesis is null [65], and the previous equation can be solved in

$$L_\mathrm{i} = \pi B \int_0^{r_\mathrm{ext}} \left(r\left(\frac{\mathrm{d}^2\zeta}{\mathrm{d}r^2}\right)^2 + \frac{1}{r}\left(\frac{\mathrm{d}\zeta}{\mathrm{d}r}\right)^2 \right) \mathrm{d}r\,.$$

By equating the internal deformation work to the external work of a generic load $p(r)$, given by

$$L_\mathrm{e} = \frac{1}{2}\int_A p(r)\zeta(r)\,\mathrm{d}A = \pi \int_{r_\mathrm{int}}^{r_\mathrm{ext}} p(r)\zeta(r) r\,\mathrm{d}r\,,$$

one could obtain an integro-differential equation to deduce the deformed shape $\zeta(r)$ of the plate. Since this result was already obtained in Section 5.B.2, the additional information can be used to evaluate the maximum allowable load in dynamic conditions.

In the particular case of interest of a load $p(r) = ar^{-2}$ applied between r_int and r_ext, substituting the solution given by equation (5.15) in the just derived expression of L_i, the following result is obtained

$$L_\mathrm{i} = a^2\frac{\pi}{16B}r_\mathrm{ext}^2 \left(2\ln\left(\frac{r_\mathrm{ext}}{r_\mathrm{int}}\right)\left(\left(\frac{r_\mathrm{int}^2}{r_\mathrm{ext}^2}+1\right)\ln\left(\frac{r_\mathrm{ext}}{r_\mathrm{int}}\right) - \left(\frac{r_\mathrm{int}^2}{r_\mathrm{ext}^2}+2\right)\right) - \right.$$
$$\left. -\frac{1}{2}\left(\frac{r_\mathrm{int}^4}{r_\mathrm{ext}^4} + 4\frac{r_\mathrm{int}^2}{r_\mathrm{ext}^2} - 5\right)\right)\,. \qquad (5.18)$$

5.B.5 Dynamic and static containment

When studying the structural analysis in the elastic field under static loads, the maximum stress σ_max has to be evaluated and compared with the maximum admissible material yield stress σ_y, taking into account a proper safety coefficient c_s. The maximum stress of a circular plate is obtained by equations (5.9) for $z = \pm s/2$ as

$$\sigma_\mathrm{max} = \max\{\sigma_{r,\theta}(z), z\} = \pm\frac{6}{s^2}m_{r,\theta}\,.$$

In the case of a distributed load proportional to r^{-2} previously studied, the analysis of the unitary moments allow to notice that they are constant where the load is not applied ($r \in [0, r_{\text{int}}]$) and decrease for increasing r in the range $[r_{\text{int}}, r_{\text{ext}}]$. The radial moment m_r is null where the deformed elastic line presents an inflexion point (second radial derivative of ζ equal to zero). The maximum is reached in unloaded region:

$$m_r = m_\theta = -\frac{a}{4} c_1^- (1+\nu)\,,$$

where $\mathrm{d}\varphi/\,\mathrm{d}r = \varphi/r$. The maximum stress is hence given by

$$\sigma_{\max} = \pm \frac{6}{s^2}\frac{a}{4}(1+\nu)\left(\ln\left(\frac{r_{\text{ext}}}{r_{\text{int}}}\right)\left(1-\ln\left(\frac{r_{\text{ext}}}{r_{\text{int}}}\right)\right)+\frac{1}{2}\left(\frac{r_{\text{int}}^2}{r_{\text{ext}}^2}-1\right)\right)\,.$$

The safety condition $\sigma_{\max} \leq c_{\text{s}}\sigma_{\text{y}}$ can be converted in a condition on the proportionality constant a of $p(r) = ar^{-2}$, leading to the *static containment condition*

$$a_{\text{stat}} \leq c_{\text{s}}\sigma_{\text{y}} \frac{2s^2}{3(1+\nu)}\left(\ln\left(\frac{r_{\text{ext}}}{r_{\text{int}}}\right)\left(1-\ln\left(\frac{r_{\text{ext}}}{r_{\text{int}}}\right)\right)+\frac{1}{2}\left(\frac{r_{\text{int}}^2}{r_{\text{ext}}^2}-1\right)\right)^{-1}\,. \tag{5.19}$$

When the load is dynamically applied, an energetic method has to be applied: the *impulse theorem* allow to evaluate the momentum transfer due to the load, as

$$P_{\text{e}} = \int_0^t \int_A p(r,t')\,\mathrm{d}A\,\mathrm{d}t,; \tag{5.20}$$

the kinetic energy $P_{\text{e}}^2/(2M)$, with M mass of the plate, is associated with the momentum variation P_{e}. The yield point will not be exceeded if the internal energy L_{y} (calculated as deformation work L_{i} to reach the deformation $\zeta(r)$ related to the yield stress σ_{y}) is less than the transferred kinetic energy.

Under the hypothesis of a time and spatially dependent load given by

$$p(r,t) = p(r)\tau(t) = \frac{a}{r^2}\sin^2(\omega t)\,,$$

applied for half a period $T/2 = \pi/\omega$, the momentum transfer is given by

$$P_{\text{e}} = \int_0^{T/2}\int_A p(r,t)\,\mathrm{d}A\,\mathrm{d}t = \pi\int_0^{T/2}\tau(t)\,\mathrm{d}t\int_{r_{\text{int}}}^{r_{\text{ext}}} p(r) r\,\mathrm{d}r = \frac{T}{4}\pi a \ln\left(\frac{r_{\text{ext}}}{r_{\text{int}}}\right)\,.$$

L_{y} is the internal deformation work that lead to the elastic deformed shape given by in the static containment conditions $\sigma_{\max} = c_{\text{s}}\sigma_{\text{y}}$. Substituting the value of a_{stat} of equation (5.19) into the expression of L_{i} given by equation (5.18), one obtains

$$L_{\text{y}} = a_{\text{stat}}^2 \frac{\pi}{16B} r_{\text{ext}}^2 \left(2\ln\left(\frac{r_{\text{ext}}}{r_{\text{int}}}\right)\left(\left(\frac{r_{\text{int}}^2}{r_{\text{ext}}^2}+1\right)\ln\left(\frac{r_{\text{ext}}}{r_{\text{int}}}\right)-\left(\frac{r_{\text{int}}^2}{r_{\text{ext}}^2}+2\right)\right)-\right.$$
$$\left.-\frac{1}{2}\left(\frac{r_{\text{int}}^4}{r_{\text{ext}}^4}+4\frac{r_{\text{int}}^2}{r_{\text{ext}}^2}-5\right)\right)\,.$$

The containment condition is, therefore, obtained through $P_e^2/(2M) \leq L_y$ as

$$a_{dyn} \leq \frac{\sqrt{2M}}{\pi}\frac{4}{T}\ln^{-1}\left(\frac{r_{ext}}{r_{int}}\right)\sqrt{L_y}\,.$$

In Section 5.B.3 the expression of the fundamental oscillating frequency for a circular plate was derived. Substituting the corresponding characteristic period coming from equation (5.17) into the above condition, a *dynamic containment condition* can be derived:

$$\begin{aligned} a_{dyn} \leq & 1.303\,\frac{T_1}{T}a_{stat.}\ln^{-1}\left(\frac{r_{ext}}{r_{int}}\right)\times \\ & \times\left(2\ln\left(\frac{r_{ext}}{r_{int}}\right)\left(\left(\frac{r_{int}^2}{r_{ext}^2}+1\right)\ln\left(\frac{r_{ext}}{r_{int}}\right)-\left(\frac{r_{int}^2}{r_{ext}^2}+2\right)\right)-\right. \\ & \left.-\frac{1}{2}\left(\frac{r_{int}^4}{r_{ext}^4}+4\frac{r_{int}^2}{r_{ext}^2}-5\right)\right)\,, \end{aligned} \tag{5.21}$$

where the total mass of the plate, $M = \rho(\pi r_{ext}^2 s)$ has been used.

When $r_{int} \ll r_{ext}$, the condition can be approximated by

$$a_{dyn} \leq 2.606\,\frac{T_1}{T}a_{stat.}\left(\ln\left(\frac{r_{ext}}{r_{int}}\right)-1-\frac{5}{4}\ln^{-1}\left(\frac{r_{ext}}{r_{int}}\right)\right)\,.$$

It is immediate to notice that the dynamic containment condition is much less demanding than the static containment one, when the fundamental oscillating period of the structural element is greater that that of the applied load: $T_1 \gg T$.

Part II

Microscopic Simulation: the gas breakdown

CHAPTER 6

Electrical breakdown in gases

Abstract. Each electrical discharge in gas is ignited by a transient process called *breakdown*. In this introductory Chapter, a brief description of the phenomenon is given, with a deep insight on the underlying kinetic physics processes. In particular, the breakdown in PF devices will be described to present an overview of the problem of interest.

6.1 Transient gas discharges

Among laboratory plasmas, many types of sources exist, such as gas discharges created by direct current, capacitively or inductively coupled RF and microwaves. The increasing interest on these sources is mainly due to the large variety of their technological applications (thin film deposition, semiconductor processing, materials treatment, ...). The electrical breakdown, intended as the transition between the dielectric and conducting state of a gas, is the common denominator for the plasma ignition.

An electrical discharge is usually built up by few seed electrons, which are accelerated by an external electric field. Their collisions with the neutral gas produce fresh ion-electron pairs in Townsend avalanches. The transient discharge proceeds until a steady-state condition is reached, in the sense that an equal number of charged particle is lost and produced: typically the maintenance mechanism consists in secondary electrons emission from the cathode. The efficiency of electrons in the production of new free charges depends on their energy distribution function (EDF) and on their microscopic interaction with the background neutral gas and with the boundaries.

What follows assumes DC conditions, being the operation regime of PF devices. RF breakdown is similar, except that, at high-frequency, the surface processes are not so important: electrons are confined by field oscillations and multiplication replenishes diffusive losses [66].

6.1.1 Breakdown

If an electric voltage V is applied between two plane parallel electrodes at a distance d, the gas contained at the pressure p, suddenly switches from insulating dielectric to conducting, if sufficiently high values of the electric field are reached.

From kinetic theory, the variation of the electron number N can be expressed as $\mathrm{d}N = N\,\mathrm{d}x/\lambda$, with $\mathrm{d}x$ the thickness of any gas slab and $\lambda = (n\sigma)^{-1}$ mean free path of the electron in a purely scattering medium, n being the neutral gas density, σ the total scattering cross section. Hence, the number N of electrons having free path of length greater than x is

$$N = N_0 \exp\left(-\frac{x}{\lambda}\right) , \tag{6.1}$$

with N_0 the starting electron number.

If a multiplicating medium is considered, one electron produces on average an electron-ion pair at each ionization collision, which has a threshold activation energy eV_i. However, a generic electron, accelerated by the electric field E, undergoes scattering collisions which modify its energy; hence, λE is the energy gained by the electron from the field. Exploiting the equation (6.1) with $x = \lambda_\mathrm{i}$, Townsend [67] related λ to λ_i through

$$\alpha = \frac{1}{\lambda_\mathrm{i}} \propto \frac{1}{\lambda} \exp\left(-\frac{V_\mathrm{i}}{E\lambda}\right)$$

which represents the number of ionizing collision per unit length of path, i.e. the number of free paths multiplied by the chance that one of them results greater

than ionizing length. The coefficient, named *Townsend's ionization coefficient*, can be then related to the gas pressure (inversely proportional to the mean free path) through

$$\alpha = Ap \exp\left(-\frac{Bp}{E}\right) . \tag{6.2}$$

The values of the constants A and B are reported in Table 6.1, for gases commonly used in electrical discharges [30].

A more exact theoretical calculation of α must include consideration of the probability that an electron with a certain energy, sampled from its EDF, will ionize a molecule by collision. However, by a judicious choice of the constant A and B, equation (6.2) gives reasonable agreement with the experimental data [52].

The electrons produced by the Townsend α-mechanism wouldn't be able to sustain the discharge, being destined to be absorbed by the anode. Moreover, the produced ion couldn't be able to acquire sufficient energy to induce ionizations. However, the electron collision with the background gas, besides giving ionization, also produce excited and metastable molecules, which decay with the emission of one or more photons [52, 68, 69]. Consequently, positive ions, photons and metastable atoms act as producers of secondary electrons by direct impact on the cathode.

Let firstly consider Secondary Electron Emission (SEE) by ion collisions. The number of electrons reaching the anode is $N = (N_0 + N_\mathrm{i}) \exp(\alpha d)$, where N_0 is the number of seed electrons and $N_\mathrm{i} = \gamma(N - (N_0 + N_\mathrm{i}))$ the number of those released by positive ion bombardment at the cathode, γ being the number of electrons released from the cathode per incident positive ion. Then, eliminating N_i, it results

$$N = N_0 \frac{\exp(\alpha d)}{1 - \gamma(\exp(\alpha d) - 1)} .$$

A similar expression can be obtained if even the secondary emission by photon impact is considered. Letting N_ν be the number of photons produced by an electron per unit length, η the fraction of photons able to produce an electron at the cathode, and Ω a geometrical factor giving the number of isotropically emitted photons which reach the cathode, one obtains

$$N = N_0 \frac{\alpha \exp(\alpha d)}{\alpha - \eta \Omega N_\nu \exp((\alpha - \mu) d)} ,$$

with μ the absorption coefficient of photons in the gas.

Due to the similarity between the two equations, it is usual to consider the various secondary ionization effects by the single ionization coefficient γ, knowing that it may represent one or more of several mechanisms [69]. The coefficient γ strictly depends on the gas and the cathode material; experimental behaviors as function of the reduced field[1] E/p can be found in literature [30, 52], as well as the dependence of the only ion contribution on the incident energy [70]. Typical values range between 0.01 and 0.1.

[1] The quantity E/p is usually referred to as *reduced electric field strength*, and measured in units of V/(cmTorr). In literature, E/n is also used as reduced electric field strength, with n the density of the gas in cm^{-3}; it is typically measured in Td, corresponding to 10^{-17} Vcm^2. At room temperature, for an ideal gas, 1 Td=0.32 V/(cmTorr).

Gas	A [1/(cm Torr)]	B [V/(cm Torr)]	E/p range [V/(cm Torr)]
Air	15	365	100÷800
Ar	12	180	50÷600
CO_2	20.0	465	100÷1000
H_2	5.0	130	20÷1000
He	2.8	34	6÷150

Table 6.1: Characteristic values of constant A and B in equation (6.2) for few commonly used gases.

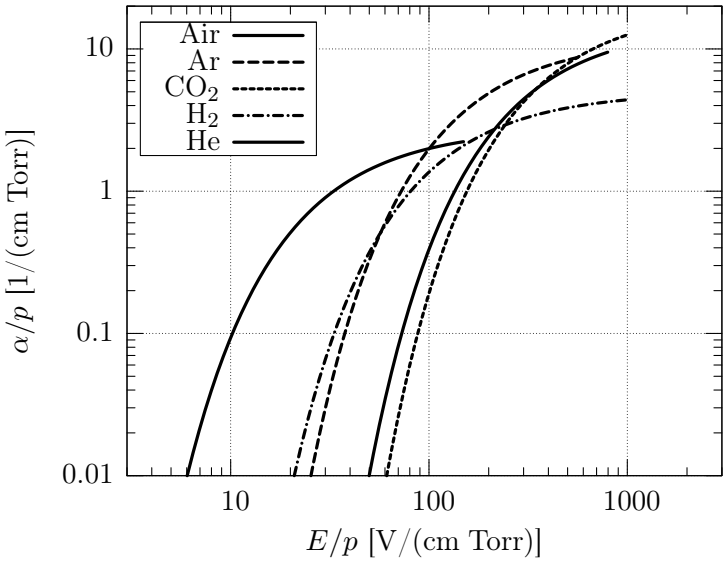

Figure 6.1: Dependence of α/p on the reduced electric field E/p for various gases.

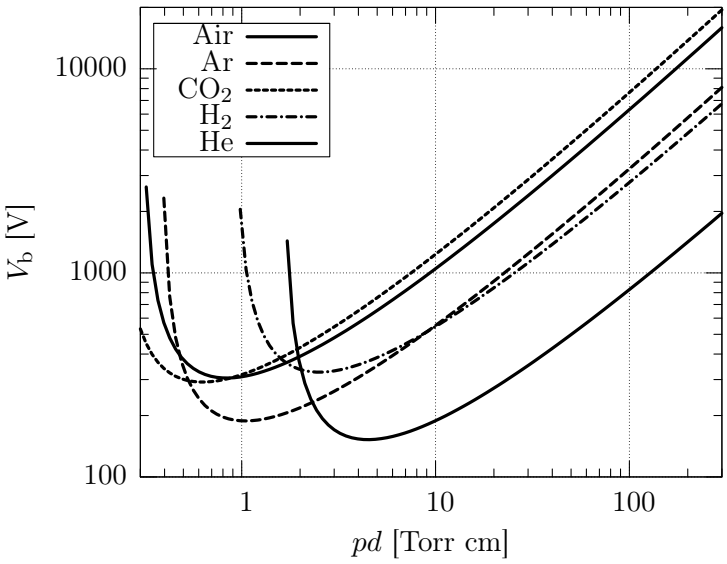

Figure 6.2: Paschen's curves for various gases.

The condition of self-sustainance of the discharge, obtained from the equilibrium between the initial electrons N_0 and those given by secondary emission, $\gamma N_0(\exp(\alpha d)-1)$, leads to

$$\alpha d = \ln\left(1+\frac{1}{\gamma}\right) .$$

As far as the planar geometry is considered ($V_\mathrm{b} = Ed$), by substitution of the equation (6.2), the *Paschen's law*

$$V_\mathrm{b} = \frac{Bpd}{\ln(Apd) - \ln(\ln(1+\gamma^{-1}))}$$

is obtained. It relates the voltage breakdown V_b with the filling gas pressure and the gap separation distance. As shown in Figure 6.2, the curve $V_\mathrm{b}(pd)$ presents a minimum, known as *Stoletov's point* [30], and increases both for decreasing (vacuum insulation) and increasing (high-pressure insulation) pd values.

The so called multiplication factor $M = \exp(\alpha d)$ is a typical parameter of breakdown. It is approximately $M = \gamma^{-1}$ at the Paschen curve, $V = V_\mathrm{b}(pd)$, and increases for voltages $V/V_\mathrm{b} > 1$, which are named *over-voltages*. The *Meek's criterion* [71] fix $M > 10^8$ (or, equivalently, $\alpha d \simeq 20$) as a threshold value for the development of *streamer* channels [72, 73], i.e. localized space charge regions created by the intense electron avalanches which concentrate the electric field driving the discharge.

At high values of the reduced electric field E/p, a decrease in the first Townsend coefficient α is observed. An ideal threshold can be defined for a Lorentz gas (like He), which shows that the effect is practically restricted to values between $60 \div 4000$ V/(cm Torr) [74]. It can, then, be expected that the behavior presented in Figure 6.1 for α/p, after reaching a maximum, starts to decrease rapidly for increasing values of E/p. A microscopic description of the effect, known as the *runaway effect* [75] will be presented in the following section.

6.1.2 Drift velocity and energy distribution function

The motion of charged particles is given by the superposition of a random thermal activity and of a steady drift due to the electric field. Langevin published a theory of the mobility of charged particles in gases based on the kinetic theory [76]: charged and neutral particles were considered as solid elastic spheres and only repulsive forces were considered at the instant of impact. Small values of E/p were assumed, so that the field energy would be negligible if compared with the thermal one. The rate of change of particle momentum $mv\nu$, depending on the collisional frequency ν, balances the electric field force eE. If the particle mean free path is much less than the dimension of any containing region, $\lambda \ll d$, the drift speed can be related to the electric field through

$$v_\mathrm{d} = \frac{e}{m\nu}E = \mu E\,, \tag{6.3}$$

where μ is the mobility. Kinetic theory links the diffusion coefficient D to the mobility through $D/\mu = kT/e$, known as *Einstein's relation*.

The above equation (6.3) can be used only for rough calculations of the electronic drift velocity, while for ions the linear dependence on the electric field is a good

approximation. In fact, due to their lower mass, electrons gain energy from the electric field faster than ions and lose little energy in elastic collisions, until they reach the thresholds for inelastic ones. Even with only weak field imposed on the gas, the average electronic energy may be far in excess of the thermal value associated with the gas. Moreover, the electrons energy distribution function (EEDF) can be approximated with a Maxwellian one, only for low values of E/p:

$$f(\mathcal{E}) = C\sqrt{\mathcal{E}} \exp\left(-\frac{\mathcal{E}}{kT}\right) ,$$

with T the temperature and k the Boltzmann's constant. On the other hand, the cross sections for elastic scattering of electrons are strong function of the particles energy; inelastic impacts assume an important role even for low energies, of the order of 10 eV for atomic gases and of 1 eV for molecular ones, due to the vibrational and rotational excitations.

The electron temperature definition T_e is usually related to an ideal collisional plasma with a Maxwellian EEDF. For moderate deviations from the Maxwellian distribution, the term "temperature" can still be used, in the sense of an effective collisional temperature, and related to the mean energy through the well-known relation $\langle\mathcal{E}\rangle = 3/2kT_c$. Generally, in gas discharges, the collisional temperature T_c is less than the dissociation and ionization threshold energies of the gas molecules. Nevertheless, these processes can occur for particles of the highly energetic tail of the EEDF.

Considering the loss of energy for electrons by elastic collisions, but ignoring the effects of inelastic ones, under the hypothesis of an electronic mean free path λ independent of the energy $\mathcal{E}$, Druyvesteyn [77, 78] deduced the following EEDF:

$$f(\mathcal{E}) = C\sqrt{\mathcal{E}} \exp\left(-\frac{3m_e}{M}\frac{\mathcal{E}^2}{(\lambda eE)^2}\right) , \tag{6.4}$$

with m_e the electron mass and M mass of the molecules of the background gas.

Studying the conductivity of an ionized gas, Margenau [79] derived the EEDF and the electronic drift velocity as a function of the gas pressure and the frequency of the electromagnetic wave; the expression for the DC case can be obtained by setting the frequency equal to zero:

$$f(\mathcal{E}) = C\sqrt{E}\left(1 + \frac{\mathcal{E}}{\alpha kT}\right)^{\alpha} \exp\left(-\frac{\mathcal{E}}{kT}\right) ,$$

with $\alpha = M/(12m_e)(\lambda eE/(kT))^2$.

In Figure 6.3, the above mentioned distribution functions are plotted against energy, both as EEDF, $f(\mathcal{E})$, and electron energy probability functions (EEPFs), $f(\mathcal{E})/\sqrt{\mathcal{E}}$, at the same mean energy. It can be observed that the Druyvensteyn distribution function presents a depressed bulk and tail, with a more populated middle energy range with respect of the Maxwellian one. The Margenau EDF has a less evident similar behavior.

The above approximate EEDF are derived without any consideration on the anisotropy of the scattering related to the momentum transfer cross section. This, combined with the strong decrease of cross section with energy, is one of the reason of the

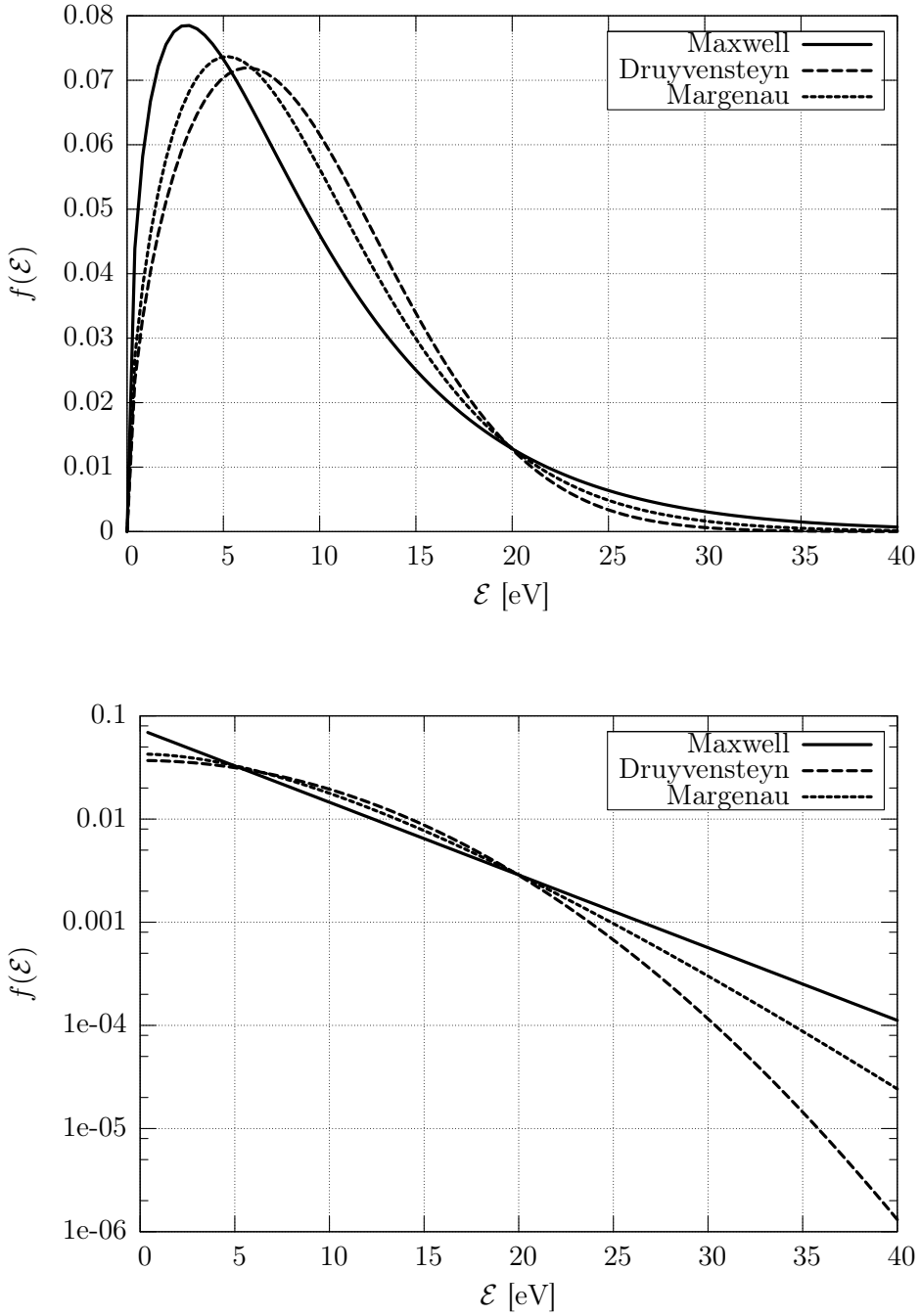

Figure 6.3: Typical shape of EEDF and of the EEPF at the same mean energy for Ar at 1 Torr ($\lambda \simeq 0.33$ mm) and 1000 Td, corresponding to an electric field of 320 V/cm. It can be pointed out that the Maxwellian EEPF in log-y scale corresponds to a straight line.

observed runaway effect, above mentioned in Section 6.1.1. At high values of the reduced electric field, the field acceleration on electrons is too strong and cannot be balanced by collisional friction. The phenomenon was explained [80] comparing the field acceleration of an electron, eE/m_e, with its mean deceleration by collisions, $v\nu_m$, where v is its velocity in the direction of the electric field and ν_m the momentum-transfer collision frequency. Due to the intrinsic Coulomb nature of all electron interaction, the related cross section decrease at a rate faster than $1/v^2$ and the effect is increased at high applied electric field. The electron velocity distribution function (EDVF) directed along the field lines can be thought as composed of three contributions: an energy loss region, for very low velocities, dominated by ohmic heating and collisional cooling; an angular scattering region, characterized by the balance between field acceleration and momentum loss in collisions; a runaway region where electrons are continuously accelerated with an arising strong anisotropy [74].

6.1.3 The distinction between a plasma and an ionized gas

It is convenient to introduce the concept of *Debye length* in order to distinguish a true plasma from an ordinary ionized gas. Assuming negligible ion temperature, the Debye length is defined as [81]

$$\lambda_{D,e} = \sqrt{\frac{\varepsilon_0 k T_e}{n_e e^2}} \simeq 7.43 \cdot 10^6 \sqrt{\frac{T_e}{n_e}},$$

where T_e (in eV) and n_e (in cm^{-3}) are the electron temperature and density respectively ($\varepsilon_0 = 8.854 \cdot 10^{-12}$ F/m being the vacuum permittivity and $e^2 = 1.602 \cdot 10^{-19}$ C the electron elementary charge). The Debye length represents a "screening" distance, i.e. the distance over which the Coulomb $1/r$ electric field is exponentially killed of by the polarization of the plasma: $V(r) \propto \exp(-r/\lambda_D)/r$. It means that, when an electric field is applied to a plasma, this polarizes and the new charge distribution reduces the magnitude of the electric field inside it: λ_D is that distance at which the electrostatic forces, which tend to impose charge neutrality, are balanced by the kinetic forces, which tend to produce non-neutrality. Evidently, in order to have the requisite electrostatic interaction between particles, the Debye length must be considerable less than the minimum dimension of the ionized medium: $\lambda_D \ll L$.

The Debye length, thus, defines a minimum length for the independent motion of electrons and ions: within a sphere of radius λ_D particle-to-particle processes take place, while, outside the Debye sphere, the particles behavior is collective and determined by the ambipolar electric field, i.e. by the long-range term of the electrostatic potential. In this case, the electric field induced by the effects of the spatial charge densities becomes of the order of the external source.

While the Debye length governs plasma behavior in equilibrium, the dynamics depends on another fundamental parameter called the *plasma frequency*, ω_p. It can be simply deduced in the case of an ideal infinite collisionless plasma by the application of the dispersion law in planar geometry for a longitudinal electric wave, as

$$\omega_{p,e} = \sqrt{\frac{n_e e^2}{\varepsilon_0 m_e}} \simeq 0.564 \cdot 10^{-3} \sqrt{n_e}$$

and corresponds to the typical electrostatic oscillation frequency of a given species (in this particular case, the electrons) in response to a small charge separation.

The simple dispersion relation $\omega^2 = \omega_p^2$ is modified if the plasma is finite in size or if it has finite temperature, as well as for other non-ideal or non-linear effects. The finite size effects depend on the complicated details of the geometry, but finite temperature simply modifies the dispersion relation to the famous *Bohm-Gross's relation*:

$$\omega^2 = \omega_p^2(1 + 3k^2\lambda_D^2)\,,$$

which links the Debye length to the plasma dynamics. For wavelengths much longer than the Debye length ($k\lambda_D \ll 1$) the oscillations are basically still at frequency ω_p. A more detailed theory shows that short wavelength waves are strongly damped, so any plasma waves is still basically near $\omega = \omega_p$.

The presence of an electrical varying driving source, the binary collisions with the background neutral gas, the interaction of charged particles with boundaries and the sustaining neutral ionization make the weakly ionized plasma discharges not ideal. The increasing density due to the Townsend avalanches multiplication and the increasing energy gained from the electric field, redistributed in the system through collisions, produce a transition from an ordinary ionized gas towards a collisional plasma. Hence, the Debye length and the plasma frequency are strictly related to the mean free path λ and to the collisional frequency ν with the background gas. If a Druyvensteyn distribution function is assumed, once calculated the normalization constant C, equation (6.4) can be used to derive the corresponding mean energy

$$\langle \mathcal{E} \rangle_{\text{Druyv.}} = \frac{\pi}{12}\Gamma^2\left(\frac{3}{4}\right)\sqrt{\frac{6M}{m_e}}\lambda eE\,,$$

which is evidently related to the mean free path λ. Hence, the extended temperature definition in the calculation of the Debye length implicitly links the two properties of interest.

6.1.4 Electron equilibration scales

When electrons experience a sufficient number of collisions, they can be considered in equilibrium with the local electric field: an electron loses a certain amount of energy at each collisional process and only if the energy gained by the electric field is dissipated in small length and time scales, then the species can be considered in equilibrium with the electric field. In this case, the EEDF can be assumed Maxwellian with a good approximation.

The characteristic length scale of the discharge is typically the smallest gradient length λ_E and has the smallest size of the vessel as upper limit. On the other hand, the time scale that characterizes the discharge is affected by the rate ν_E at which the field changes.

Collisions modify the electrons distribution through the typical length and time scales over which they lose a substantial part of their energy in collisions, i.e. energy relaxation length $\lambda_\mathcal{E}$ and frequency $\nu_\mathcal{E}$ [82]:

$$\lambda_\mathcal{E} = \lambda\sqrt{\frac{\nu}{\nu_\mathcal{E}}} \qquad \text{and} \qquad \nu_\mathcal{E} = \frac{2m_e}{M}\nu + \nu_i\,,$$

where $\lambda = (n_g\sigma)^{-1}$ is the electron mean free path, $\nu = n_g\sigma\sqrt{(2E/m_e)}$ the collision frequency for momentum transfer and ν_i that for inelastic impacts. Due to the large mass ratio of electrons and ions, energy transfer in elastic collisions is strongly inefficient producing long equilibration length and time scales for energy below the first excitation level. This means that the corresponding characteristic length scale is $\lambda_{exc} = \mathcal{E}_{exc}/(eE)$, with $\mathcal{E}_{exc}$ in eV. For the specific case of Argon, one can refer to Figure 6.4. For molecular gases, the problem is less evident due to the low vibrational and rotational excitation energy threshold.

Hence, it is required that both the conditions $\lambda_\mathcal{E} \ll \min\{\lambda_E, \lambda_{exc}\}$ and $\nu_\mathcal{E} \gg \nu_E$ in order to have the EEDF in equilibrium with the electric field and avoid locality effects. However, the dependence of cross sections on energy makes $\lambda_\mathcal{E}$ and $\nu_\mathcal{E}$ strongly varying on the whole EEDF energetic range.

6.1.5 Flow of current through a ionized gas

Another macroscopic quantity of interest for electrical discharges in gases is the current flowing through the circuit when the potential difference is applied. It can be determined in two ways [30]: either by counting the number of charges arriving and leaving the electrodes in unit time, or by determining the rate of charge change induced by the moving charges on one of the electrodes, which corresponds to the so called *displacement current*.

According to the first view, no current is recorded while the charge moves through the gap and the whole charge is delivered exactly at the instant when the charge hits the electrode. However, this model is not fully coherent, since the generic charge e moving in the gas modifies the field lines (or lines of displacement) ending on the anode and cathode. Thus, according to the second view, when a charge moves through a gas, the induced charge on the electrodes varies as long as the motion persists: the rate of change of the charge at the anode is opposite to that at the cathode. In the meantime, the charge flow through the external circuit is equal to the corresponding change of charge felt on the electrodes[2].

Though the first approach is in principle inaccurate, it leads to the same numerical result as those of the displacement current, if applied to a sufficiently large number of charged particles flowing uniformly and continuously between the electrodes. However, under unsteady conditions, i.e. when the discharge current grows or decreases, only the second approach gives the exact answer.

It is possible to evaluate the instantaneous value of current flowing through a circuit as a charge e moves between two electrodes of general shape. The work done on e by the electric field $\vec{E}$ when e moves of $\mathrm{d}\vec{s}$ along its path in $\mathrm{d}t$ corresponds to the energy it receives from the source V of the applied potential. A general sketch of the involved quantities is presented in Figure 6.5. Hence,

$$V I(t)\,\mathrm{d}t = \vec{E}\cdot\mathrm{d}\vec{s} = eE\;\mathrm{d}s\;\cos\vartheta \quad \text{or, equivalently,} \quad I(t) = e\frac{E}{V}v\cos\vartheta\,.$$

It can be noted that the current at any instant t depends on the velocity v of the charge e and on its position through the field configuration E/V, which is

[2]This approach is correct only if the acceleration of the charge is sufficiently small to make negligible the radiation induced by the field change.

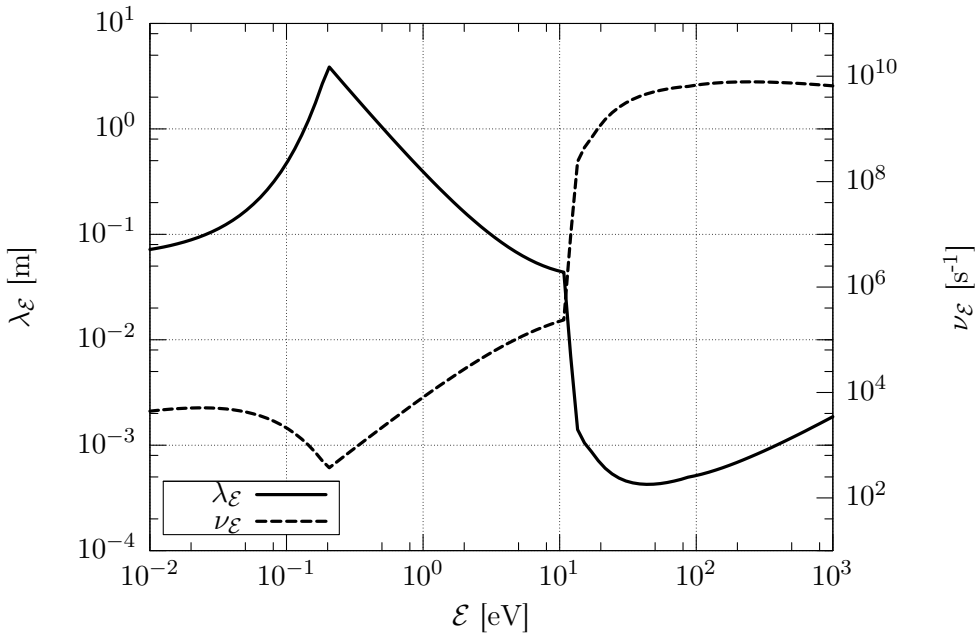

Figure 6.4: Energy relaxation length and time scales at 1 Torr: $\nu_\mathcal{E}$ scales with pressure p, while $\lambda_\mathcal{E}$ with its reciprocal. The Ar cross sections are shown in Figure 7.10.

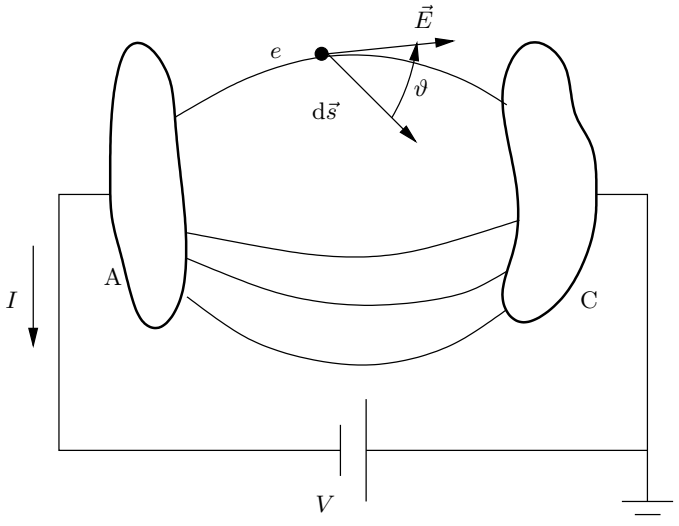

Figure 6.5: Motion of a free charge e in an electric field $\vec{E}$ between two electrodes of generic shape inducing a current I in the external circuit.

independent of V. Obviously, integrating over time the current flowing in the circuit one obtains the total charge deposited on the electrodes.

Returning to the first approach and looking at the current pulse produced by each single charge hitting the electrodes, the total current can be seen as the superimposition of two contributions: a steady component and a randomly fluctuating one, which is the consequence of the discrete nature of the charges. If a large time interval containing a high number of fluctuations is considered, then the time integral of the random component of the current is approximately zero.

6.2 Kinetic description

The kinetic description of a stationary gas is based on a large population of gas atoms, whose energy distribution is linked to the temperature kT through the mean energy $\langle \mathcal{E} \rangle$. For an ideal gas, $p = n_g kT$ at the thermal equilibrium. Similar concepts apply to charged particles population, even if their charge is a source of electric field through which every charge exerts forces on any other charge proportionally to the inverse of the squared distance. Similarly, an external applied electric field influences the motion of any charge immersed in it. The work done $eV = \int_{x_1}^{x_2} eE \, \mathrm{d}x$ by the electric field on a particle modifies its energy $eV = (mv_d)^2/2$, imposing to it the drift velocity v_d.

Collisions and boundaries interactions strongly influences the particle motion and distribution functions redistributing their velocity, even representing sources and sinks for particles.

6.2.1 Scattering

The most common encounter in weakly ionized gases is between pairs of particles. In particular, binary collisions between neutral particles are not considered since the background gas is thought to be at the thermal equilibrium following a Maxwellian energy distribution function at the temperature kT.

The collisional events in a complex multi-body system can be treated as statistical processes based on the quantum mechanics principles [70, 83]: the collision probability, as well as the energetic and angular distribution of the emerging particle, are governed by the *differential cross sections* $Q(\mathcal{E}, \Omega)$, defined such that $Q(\mathcal{E}, \Omega)\, \mathrm{d}\Omega$ gives the number of particles per unit time falling into the solid angle $\mathrm{d}\Omega(\chi, \psi)$ per unit flux density of an hypothetical incoming beam directed as the incident particle (see Figure 6.6). The integral of the differential cross section over all solid angles is the *total cross section* $\sigma(\mathcal{E})$, related to the mean free path λ of the particle and extensively used in Section 6.1. Usually, any target of interest can be considered spherically symmetric allowing to integrate over the azimuthal angle ψ to obtain

$$\frac{1}{\sigma(\mathcal{E})} \int_{S_\Omega = 4\pi} Q(\mathcal{E}, \Omega)\, \mathrm{d}\Omega = 2\pi \int_0^\pi I(\mathcal{E}, \chi) \sin\chi \, \mathrm{d}\chi = 1 \,.$$

$I(\mathcal{E}, \chi)\, \mathrm{d}\chi$ is then the probability the particle has to be scattered in the range $\mathrm{d}\chi$ centered around χ. The precise form of $I(\mathcal{E}, \chi)$ depends on the nature of the collision and needs to be considered for each species pair and collision type.

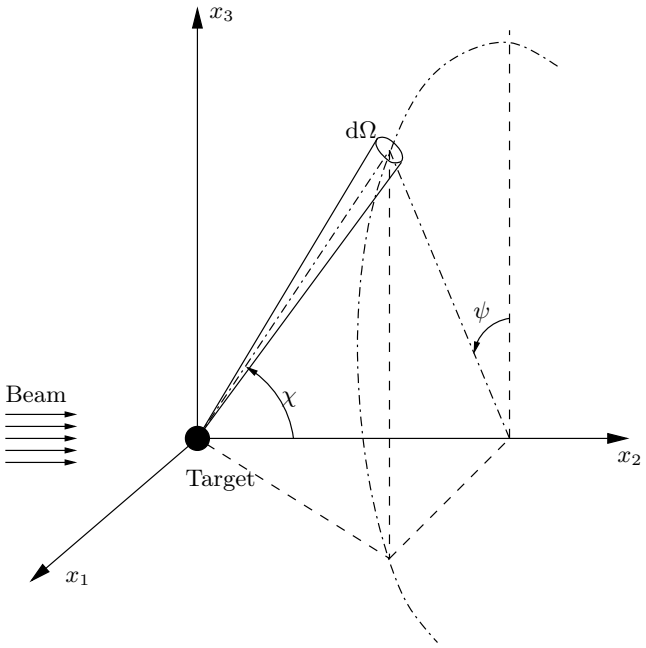

Figure 6.6: Scattering angles for a monoenergetic beam colliding with a fixed target.

The differential cross section is typically known in the center of mass frame. The collision itself is best described in the center of mass reference of the two colliding particles making use of their relative velocity $\vec{v}_r$ (see Appendix 6.A).

Once evaluated the new velocities in the center of mass frame, they have to be rotated back to the laboratory frame. The velocity unit vector after collision, $\widehat{v}^{\rm scat}$, depends on the direction of the incident one, $\widehat{v}^{\rm inc}$, and on the scattering angles χ, ψ through

$$\widehat{v}_{\rm r}^{\rm scat} = \widehat{v}_{\rm r}^{\rm inc}\cos\chi + \widehat{v}_{\rm r}^{\rm inc}\times\widehat{i}\frac{\sin\chi\sin\psi}{\sin\theta} + \widehat{v}_{\rm r}^{\rm inc}\times(\widehat{i}\times\widehat{v}_{\rm r}^{\rm inc})\frac{\sin\chi\cos\psi}{\sin\theta}\,, \tag{6.5}$$

where the term $\sin\theta$ just give a normalized expression for $\widehat{v}_{\rm r}^{\rm scat}$, as deducible from Figure 6.7. The scattered velocity has then to be projected on the laboratory reference, depending only on the angles θ and ϕ defining $\widehat{v}^{\rm inc}$. A detailed matrix description is given in Section 6.A.2.

Each colliding particles undergo a change of momentum and energy depending on the scattering angle. In the limit cases $m_1 \ll m_2$ and $m_1 = m_2$, a more rapid way to evaluate the energy loss factor is to consider the frame where target particle is at rest, as described in Section 6.A.3. In the case $m_1 \ll m_2$, the differential scattering cross section is equally defined in the two frames, while in the case $m_1 = m_2$ an isotropic scattering is usually considered in the center of mass frame.

6.2.2 Volume collisional processes

The collision between charged particles (assumed to be the projectile) and atoms or molecules of the background gas (the target) can be *elastic* (the total kinetic energy

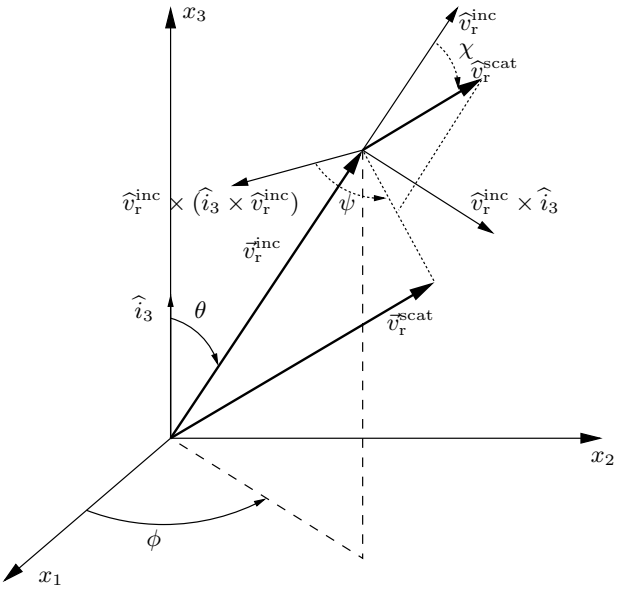

Figure 6.7: Velocity versors in the laboratory frame and center of mass frame attached to the plane of collision.

of the system remains unchanged and momentum is redistributed between the two particles) or *inelastic* (momentum is redistributed but a fraction of the initial kinetic energy is transferred to internal energy of one or both particles).

The energy and momentum conservation laws have to be satisfied and all binary collisions can be treated according to the theory presented in Section 6.2.1 and Appendix 6.A. In particular, electrons are characterized by very low mass if compared with those of the gas particles ($m_{\mathrm{e}} \ll m_{\mathrm{g}}$); due to the favorable mass ratio, even without accounting for their ready gain of energy from the electric field, the target can be considered perturbed by the event, simplifying the model of the kinetic collision (see Section 6.A.3). On the other end, the ions and gas particles are characterized by roughly equal masses ($m_{\mathrm{i}} = m_{\mathrm{g}}$), which makes necessary that evaluation of the relative velocity between the two approaching particles.

Inelastic collisions can be induced only when the relative energy between particles is sufficiently high to overcome the characteristic threshold energy of the process: the corresponding cross section is therefore zero for lower energies. When a molecular background gas is considered, the number of possible excited states rises, while the characteristic energies of the excited molecular states (vibrational and rotational) decrease sensibly. Moreover, other processes involving the molecule dissociation (dissociative excitation, dissociative recombination, dissociative attachment) may arise.

A fundamental inelastic collision in gas discharges is represented by the ionization process, induced by electron-neutral collisions. It cannot be considered a binary collision: even if the neutral particle, becoming an ion, continues on its trajectory virtually undisturbed (no change in momentum), the electron strips another electron off the neutral and momentum and energy need to be conserved among the three

bodies. An experimental expression [84] of the distribution function $I(\mathcal{E}_{\mathrm{ej}}, \mathcal{E})$ for the partitioning of the excess energy $\mathcal{E} - \mathcal{E}_{\mathrm{exc}}$ between the scattered electron and the ejected one is often used, as will be better discussed in Section 7.2.3. In conjunction with the conservation laws, it allows to evaluate the flight directions of the scattered and ejected electrons.

The ionization induced by ion-neutral, or even neutral-neutral, collisions becomes not negligible at very high temperatures, which is the regime of high-pressure arcs and thermal equilibrium [52, 66]. At lower energies, a typical collisional process induced by ions is the charge exchange: an ion strips an electron from a neutral and the roles of the two particles are reversed. This is an efficient mechanism for energy redistribution on a time scale comparable with the ions one.

Other volume collisional phenomena like de-excitation or two-step ionization can be considered negligible until sufficiently high values of excited densities and de-excitation rates are reached [85]. The same can be stated for the Penning effect (a long-lived metastable excited combines with a neutral producing de-excitation and an ion-electron pair) and photo-ionization, since radiation energies from de-excitation photons are typically lower than the ionization energies (except when already excited neutrals are involved as targets).

Finally, recombination and dielectronic recombination could be considered. This processes show a strong dependence of their microscopic cross section on some power of the electron mean energy[30]; hence, even if charge density and and collision rates increase in time, the growing kinetic energy induced by the electric field makes these processes negligible, until thermal equilibrium and densities comparable with the neutral gas are reached. Direct recombination with no radiation emission is far less probable since it requires three incoming body to satisfy the energy and momentum conservation laws.

The above mentioned gas phase reactions are summarized in Table 6.2 for electrons and in Table 6.3 for ions.

6.2.3 Secondary electron emission

As observed in Section 6.1, boundary phenomena play an important role in the sustaining of DC discharges, by SEE.

It is known from quantum mechanics [86] that the lowest energy required to remove an electron from a solid is the so called *work function*, $e\psi$. A less impinging energy (thermal, radiative, potential or kinetic) results not sufficient to make the electron overcome its potential barrier, that bounds it to the metal lattice; consequently the particle, or radiation, will be simply adsorbed or reflected by the surface.

Traditionally [67, 68, 70], the first mechanism of SEE is by impact of ions and metastable excited states on a surface (generally the cathode). Two main mechanisms can be observed. The first is the direct emission of an electron from the most outer metal atom shell, due to the particle impact and consequent kinetic energy exchange. The second mechanism is the recombination of a particle (with a characteristic potential energy: eV_{i} for an ion, eV^* for an excited atom) on the surface: when the projectile has a total energy $mv^2/2 + eV \geq e\psi$, then it can interact with the potential well of the material undergoing recombination or de-excitation, while a secondary electron could be emitted thanks to the release of internal energy. This

Reactions	Description
$e^- + A \rightarrow A + e^-$	elastic scattering
$e^- + A \rightarrow A^* + e^-$	inelastic scattering
$e^- + A \rightarrow A + 2e^-$	ionization
$e^- + A^* \rightarrow A + e^- + h\nu$	de-excitation
$e^- + A^* \rightarrow A + 2e^-$	two-step ionization
$e^- + AB \rightarrow A + B + e^-$	dissociation
$e^- + AB \rightarrow A^+ + B + 2e^-$	dissociative ionization
$e^- + AB \rightarrow A^- + B$	dissociative attachment
$e^- + A^+ + B \rightarrow A + B$	volume recombination
$e^- + A^+ \rightarrow A + h\nu$	recombination with photo-emission
$e^- + A^+ + B \rightarrow A + B$	volume recombination

Table 6.2: Gas phase volume collisional processes involving electrons.

Reactions	Description
$A^+ + B \rightarrow A^+ + B$	elastic scattering
$A^+ + B \rightarrow A + B^*$	inelastic scattering
$A^+ + B \rightarrow A + B^+$	charge exchange
$A^+ + B \rightarrow A^+ + B^+ + e^-$	ionization
$A^+ + B^* \rightarrow A^+ + B + e^-$	Penning ionization
$A^+ + BC \rightarrow A^+ + B + C$	dissociation

Table 6.3: Gas phase volume collisional processes involving ions.

second mechanism takes place mainly on metals, their work function being generally of the order of $4 \div 5$ eV. The escape of the electron from the material is subject to a statistical factor; the secondary emission coefficient γ takes into account the effectiveness of electron release as the average number of electrons per incident ion. Typical values range between 0.05 and 0.3; while depending on the interacting ion and material, γ is not strongly affected by the incident kinetic energy.

Often the secondary emission coefficient is considered as the sum of four terms related to ions, photons, metastables and neutrals [30, 52]. However, in the early stage of the discharge, since heavy particles have not sufficient energy to travel long distances, the photoelectric effect can be considered the main source of fresh electrons [87, 88]. Photons are effective removers of electrons from surface, provided that $h\nu \geq e\psi$, the excessive energy being transformed in kinetic energy of the emitted electron as follows from the Einstein's equation [89, 90]. The source of photons can be external or internal, since characteristic decay times of short-lived excited states and low values of work function in metals make the process possible. The energy distribution function of photo-electrons has an ideal triangular shape at 0 K with

$h\nu - e\psi$ as maximum energy, depending on the Fermi-Dirac electron distribution function in the metal, which presents a sharp edge at the Fermi level $\mathcal{E}_{\mathrm{F}}(T=0)$ [86]. When the temperature is raised, the Fermi energy drops slightly, following

$$\mathcal{E}_{\mathrm{F}}(T) \simeq \mathcal{E}_{\mathrm{F}}(T=0)\left(1-\frac{\pi^2}{12}\left(\frac{kT}{\mathcal{E}_{\mathrm{F}}(T=0)}\right)^2\right), \tag{6.6}$$

and the Fermi level no longer represents a sharp energy cutoff. Hence, even the photoelectrons spectral distribution deviates slightly from the 0 K triangular shape [87, 91, 92]. The photo-electric secondary emission coefficient lies in the range $10^{-3} \div 10^{-1}$, strongly depending on the surface polishing and on the material [93].

Even in the case of electron impact on a surface, a secondary electron can be emitted if the energy of the primary one is greater than the work function of the material. The physics of surface reflection and secondary emission is quite complex [93, 94, 95, 96]: some of the electrons impinging on a target are reflected at the surface barrier, while most of them cross the potential barrier and interacts many times with the target material nuclei and electrons. In low-Z targets the energy degradation of primary electrons is rapid, while the opposite situation prevails in high-Z materials. This means that even a primary electron could be scattered back to the surface and escape if it has sufficient residual energy. However, highly energetic electrons produce excitation and ionization within the solid and the emission of true secondary is possible. The analysis of the spectrum of the outcoming electrons can be split in three regions: a first peak at energies near that of primaries, $\mathcal{E}_{\mathrm{pr}}$, corresponds to the reflected electrons, while a second diffuse peak at low energies (few eV) contains the true secondaries; the region of intermediate energies is less populated by multiple scattered primaries [97]. The secondary emission coefficient δ can be split in two contributions: the average number of the true secondaries per incident electron and that of rediffused primaries. The coefficient δ depends on the energy of the primary electron and on the angle of incidence: in particular, at low and high energies $\delta < 1$ ($\mathcal{E}_{\mathrm{pr}} < e\psi$ and no secondary is produced or $\mathcal{E}_{\mathrm{pr}} \gg e\psi$ and secondaries are produced too deep within the target), while, for energies in the range $200 \div 2000$ eV (strongly dependent on the material and its surface status), $\delta > 1$ and secondaries start to arise. Recently analytical formulas have been proposed [97, 98, 99] for δ and electrons spectrum.

Because of their low conductivity, insulators usually tend to adsorb charged particles hitting their surfaces: i.e. at low and high energies (when $\delta < 1$), a primary electron will be adsorbed and the surface will charge negatively until it reaches the primary electrons accelerating potential; then, other electrons will be accelerate with difficulty to energies such that $\delta > 1$; however, in this case, electrons will desorb from the surface leaving on it a surplus of positive charge (maximum values of δ can be greater than 2) [97, 100]. Consequently, charged dielectric surfaces are an optimum situ for electron-ion recombinations.

The above described surface interactions are symbolically summarized in Table 6.4, where the surface symbol is omitted on both sides.

Thermionic emission fluxes of electrons and ions from surface are strongly dependent on the body temperature ($j_{\mathrm{e,i}} \propto T^2 \exp(-e\psi/kT)$), this being connected with the vibrational energies of the particles in their shells and lattice respectively [101, 102]. Therefore, it results not negligible only at high temperatures

Reactions	Description
$h\nu \rightarrow e^-$	secondary emission by photons
$A^* \rightarrow A + e^-$	secondary emission by excited
$A^+ \rightarrow A + e^-$	secondary emission by ions
$e^- + A^+ \rightarrow A$	recombination
$A^* \rightarrow A$	de-excitation

Table 6.4: Surface enhanced reactions.

($T = 1000 \div 2000$ K).

Lastly, another possible source of electrons from surfaces is the field emission: an applied electric potential can interfere with the external potential barrier of a solid increasing the probability of electrons emission by tunnel effect. Combining the flux of electrons directed outwards the metal surface with the tunnel effect probability, and using the Wentzel-Kramers-Brillouin approximation, which ignores the temperature influence and the lowering of the barrier by the Schottky effect, the Fowler-Nordheim current density can be written as [103, 104]

$$j_e = \frac{C_1(\beta E)^2}{e\psi} \exp\left(-C_2 \frac{e\psi^{3/2}}{\beta E}\right) \tag{6.7}$$

depending on the applied electric field E (in V/m) and on the work function $e\psi$ (in eV), $C_1 = 1.54 \cdot 10^{-6}$ and $C_2 = 9.83 \cdot 10^9$ being constants depending on the mobility of electrons in the metal μ and on the Fermi level of equation (6.6). Only for electric field values of the order of E=10^8 V/m, the electron current flowing from the metal, and measured in A/cm^2, becomes not negligible. Notwithstanding, the dimensionless constant β is intended as a field enhancer to take into account the microscopic harshness of the metal surfaces; typical values are of the order of $200 \div 300$, but particularly sharp edges (like the s.c. knife-edge [20]) could increase the value even of one order of magnitude.

6.3 The breakdown phase in PF devices

After the above general introduction to the breakdown in gases, the main features of the phenomenon of interest will be hereafter examined. The characteristic operative conditions of the device make critical most of the experimental analysis. Hence, the numerical approach seems to be the best suited for breakdown investigations in PF devices.

6.3.1 Operative conditions

As already seen in Chapter 1 and Chapter 2, the PF device is typically operated with pressures ranging between 1 and 10 Torr and charging voltages of the order of few tens of kV. The spatial distribution and time evolution of the ionization in the first stage of the breakdown is essentially determined by the reduced electric field $\vec{E}(\vec{r},t)/p$; $\vec{E}(\vec{r},t)$ within the gun can be split in the product of time-dependent

component $\tau(t)$ and in a spatial dependent one $\rho(\vec{r})$ which are independent from the pressure.

The discharge breakdown is known to develop at the closed end of the electrodes over the insulator sleeve. In this region, the electrical potential does not present a uniform gradient over the interelectrode gap, as supposed in Section 6.1.1 deriving the Paschen's law; the presence of the dielectric and of the cathode backwall determine a strong electric field (high values of $\rho(\vec{r})$) near the cathode edge facing the insulator. Other regions of enhanced spatial component of the electric field are the radial gap between the electrode at the end of the insulator and the open end of the electrodes (edge intensification).

The discharge of the capacitor bank over the open load makes the PF behave like a capacitor until a continuous current, flowing between the electrodes, closes the circuit. Therefore, the applied voltage is not stationary and equal to the charging one, but grows following the rules of a discharge over a secondary small capacitance as presented in Section 5.A.2. A first order approximation of equation (5.5) can be assumed; typical operating parameters of PF devices lead to a voltage increasing rate (proportional to $\tau(t)$) of about $200 \div 500$ V/ns, in good agreement with experimental data registered through voltage probes [15].

The spatial and temporal dependence of the electric field highly complicates any attempt to find an analytical solution of the problem. Even if in a small region of the domain, the strong local electric field, the relatively low pressure and the rapid growth of the applied potential, very soon lead to an over-voltage condition $V/V_\mathrm{b} > 1$, which is known to induce very fast and inhomogeneous breakdowns. Even if the Meek criterion is not reached, the high values of the reduced electric field make the role of runaway electrons not negligible. Any solving model must then take into account the anisotropy of the momentum transfer cross section which reflects in decreasing values of α for increasing E/p.

Even if the development of pulsed, high-voltage gas discharges has been thoroughly studied [105], the microscopic picture of the breakdown in a PF device is not yet completely understood. The process starts with the acceleration of few seed electrons (present in the gas with densities of $0.5\,\mathrm{cm}^{-3}\mathrm{Torr}^{-1}$[71]) to energies sufficiently high to induce ionizing electron avalanches. Field emission from the cathode and thermionic effect does not seem to play a relevant role in the initial stages of the breakdown. The space charge effects start to be relevant on the electric field, when the number of electrons produced in the head of an avalanche reaches a value of 10^8 cm^{-3} [52]. At this stage, also surface charge build-up on the insulator starts to play an important role and cannot be neglected. The corresponding EEDF is far from Maxwellian and the key parameter of the ionization growth is the local value of $\vec{E}(\vec{r},t)/p$ [106]. When the density of charged particles n reaches values of the order of 10^{13} cm^{-3}, the energy equipartition time between electrons shortens to about 1 ns which is equal or lower than the characteristic time of electric power input (see Section 6.1.4). The ionization evolution is no longer ruled by E/p but by T_e and n_e. The input power is transferred through ionization and excitation processes plus the heating of the new electrons up to T_e. The mean energy and collisional rates reach then a plateau.

The SEE by ion or excited impact seems to play a negligible role due to the short characteristic time of the phenomenon. Until sufficiently high values of electric

field are reached to enhance the electron field emission, the only reasonable way for the production of secondaries is the photoelectric effect induced by the de-excitation photons. Due to the low pressure, no photoionization and recombination is expected.

6.3.2 Experimental results

Experimental studies of the initial phase in PF devices concern mainly the macroscopic sheath formation (observed through image converter pictures and magnetic probes) and electrical macroscopic quantities (measured with fast voltage dividers and Rogowski coils) [15, 107, 108]. Usually, optical measurements allow to observe the formation of rather uniform sheaths on the insulator surface. Sometimes they are coupled with radial filamentary discharges at the end of the insulator length [19]. Others [15, 18] found the formation of a uniform sheath over the insulator only for pressures ranging between 1 and few Torr; at lower pressures ($p \in [0.1, 1]$ Torr) a diffuse volume discharge filling the interelectrode gap above the insulator was observed, extending to the electrodes open end for decreasing pressures; at high pressures ($p \in [5, 20]$ mbar) a second radial CS with filamentary structure develops at the end of the insulator. In the middle of this pressure range, in devices with small electrode diameters ($r_{\text{int}} < 1$ cm), a third filamentary CS bridges the electrodes at their open end and further increasing values of p make the insulator sheath disappear. It was observed that the minimum pressure, at which the static voltage breakdown is minimum and the CS forms on the insulator, approximately coincides with the values predicted from the standard Paschen's curves, using the interelectrode gap as d [15]; hence, at decreasing pressures, it is reasonable to find that the discharge occupies large volumes since the electron mean free path increases over d and the chance of producing ionization is uniformly increased.

The time delay t_{d} between the switching of the spark gap and the electrical breakdown in the gun was measured and observed to fit the empirical relation [18]

$$t_{\text{d}} = 220\, p^{-1/3 \div -1}\,,$$

with $[t_{\text{p}}] = \text{ns}$ for $[p] = \text{mbar}$. In the pressure range in which CS forms on the insulator, the values of t_{d} usually become comparable with, or even smaller than, the voltage rise time, i.e. the breakdown occurs before the charging voltage is reached.

The plasma resistance R_{p}, instead, decreases exponentially as $R_{\text{p}} \propto \exp(-t/\tau)$ with $\tau \simeq 5/p$ in ns/mbar. When the EEDF starts to approach a Maxwellian distribution and the ionization is no more ruled by E/p, assuming that a single CS forms on the insulator of length l with a small thickness s compared with r_{int}, its resistance is approximately given by $R_{\text{p}} = l/(2\pi r_{\text{int}} s\sigma)$. The conductivity σ at low ionization degrees was derived including electron and neutral collisions to be

$$\sigma \simeq 2760 \left(T_{\text{e}}^{-3/2} + 0.015 T_{\text{e}}^{1/2} \frac{n_{\text{g}}}{n_{\text{e}}} \right)^{-1}\,,$$

with T_{e} in eV and σ in $\Omega^{-1}\text{m}^{-1}$. The electron-neutral collisions (second term in parenthesis) depends on the ionization degree $n_{\text{g}}/n_{\text{e}}$ and is relevant only for values less than 1% and, under the hypothesis of slightly variable T_{e}, σ changes only with

n_g/n_e. Typical PF parameters ($l/r_{int} \simeq 1.5$, $R \simeq \sqrt{L_0/C} \simeq 0.05\ \Omega$) and experimental observations ($s \simeq 0.5 \div 1$ cm), allow to estimate $\sigma \simeq 500 \div 1000\ \Omega^{-1}m^{-1}$, corresponding to an ionization degree of less than 1%.

Peak currents of few tens of kA were reached in tens of ns corresponding to current densities of about 10 kA/cm^2 [109].

The long delay times and relatively slow fall of the resistance cannot be explained by well-known breakdown and spark models.

Analogous studies performed with different insulator materials showed that the choice of the dielectric does affect the breakdown and the formation of the plasma layer. Therefore, for various insulator materials there have been found different ranges of the operational pressures [107]. Moreover, the insulator surface alteration due to successive discharges (*conditioning*) was found to be responsible for an improved stabilization in performances: the development of microscopic conductive sites (size of the order of 1 µm) on the insulator surface, due to deposition of metal ablated particles, increases the efficiency of the breakdown [16].

Even the geometry of the cathode and insulator sleeve strongly influences the breakdown initiation, being connected to the change in the spatial component $\rho(\vec{r})$ of the electric field. The presence of proper field-intensifier (called *knife-edge*) seems to enhance the initial breakdown process along the insulator surface [20] allowing to extend the pressure ranges for a proper CS formation on the insulator sleeve [107]. Moreover, while the choice of a cylindrical OE or of a squirrel cage one does not seem to influence the initial phase considerably, the choice of the insulator length is more decisive [110].

All the above cited experimental activities have been conducted in order to better understand the breakdown role in PF discharges. Numerous experiments have shown that final PF characteristics depend considerably on the initial phase of the discharge. Since, in the past, large PF facilities failed to reach the expected efficiency [110], investigations of the current sheath formation are of primary importance for the optimization of high-current discharges. Similarly, the reproducibility of the phenomenon is of primary importance in repetitive devices.

Experimental evidences are not enough to fully understand the PF breakdown, since many physical processes concur to complicate data acquisition and analysis. A deeper insight is needed.

6.3.3 Numerical models

Due to the not perfectly cylindrical geometry and to the nonlinear feature of the equations, analytical solutions of discharge breakdown models cannot be faced even at the initial stage, when space-charge effects are negligible and low current densities are involved. Moreover, at high voltages and currents, the ionization coefficient make non linear the set of equations. Many numerical fluid models have been developed for discharge simulations, based on the method of characteristics [111], flux-corrected transport algorithm [112, 113, 114] or finite elements methods [115]. The reader is referred to [116] for an interesting review on discharge simulation through fluid codes. Both one- and two-dimensional hydrodynamic models were developed in the past years to simulate PF dynamics [34, 37, 40]; recently, particular interest has been devoted to the breakdown phase [41, 117].

The main drawback of fluid codes is the assumption of a Maxwellian EEDF, that means the assumption of macroscopic parameters like temperature, mobility and diffusion coefficient in the balance equations. Nevertheless, as shown in Section 6.1.2, the presence of a strong electric field induces strong deviations from the thermodynamic equilibrium. Moreover, at high values of the reduced electric field, the first Townsend ionization coefficient shows a decreasing behavior, due to the above described runaway effect. A kinetic approach, able to describe a generic local non-stationary EEDF, appears more suited for the breakdown modeling of the very early stage of gas discharge development, dominated firstly by elastic collisions and then by electron impact ionizations.

The coupling of the Newton law to follow particles trajectories and of sampling methods to describe microscopic interactions is an effective kinetic method, able to treat species behavior with a minimal amount of assumptions. When space-charge effects are not negligible a self-consistent treatment of electric field must be added. The drawback of similar detailed and complete description is the significant calculation time required. Similar approaches have been widely used in the simulation of RF and DC glow discharges [118, 119, 120, 121] at relatively low values of filling gas pressures ($1 \div 100$ mTorr); even if coupled in few cases with chemical and diffusive modules [122], the models are usually limited to mono-dimensional geometries and seldom simulate all the breakdown evolution starting, at least, from a weakly ionized condition. Other authors investigated the avalanche development and its transition into streamers even at higher pressures with particular interest to localized effects [123, 124, 125, 126]. Recently, interest was devoted even to fast ionization waves and to nanosecond discharges [127, 128], characterized by very fast ramp of applied potential (up to about 10^{13} V/s). Although more similar to the breakdown development of interest for the important role played by runaway electrons, even the results of these works were based on a simplified mono-dimensional geometry and cannot be applied to the more complex case of PF devices.

In the present work, a PIC-MCC code has been implemented in order to simulate the gas breakdown in a bidimensional cylindrical geometry representative of the closed end of a PF device electrodes. The model will be described in details in the next chapter, while the following one will be devoted to the development of numerical techniques able to keep under control the exponentially increasing number of simulation particles. The code reveals an effective tool to study the microscopic time evolution of the phenomenon, allowing to deduce the role played by each physical mechanism and to obtain macroscopic quantities of interest.

6.A Classical collisions of smooth elastic spheres

Few considerations will follow on the subject of scattering processes between smooth hard spheres. In particular, the relative velocity after the collision will be obtained through a matrix analysis of angle rotations and the loss of energy will be derived as a function of the mass ratio and scattering angle.

6.A.1 Laboratory and center of mass frames

Consider two smooth spheres of masses m_1 and m_2 which are about to collide. Let $\vec{v}_1$ and $\vec{v}_2$ be their (intersecting) velocities in the laboratory frame. The total mass $M = m_1+m_2$, momentum $\vec{p} = m_1\vec{v}_1+m_2\vec{v}_2$ and kinetic energy $\mathcal{E} = (m_1v_1^2+m_2v_2^2)/2$ are conserved after the impact, which is considered instantaneous. The system can be described through the center of mass velocity $\vec{v}_{\mathrm{CM}} = \vec{p}/M$ and the relative velocity $\vec{v}_{\mathrm{r}} = \vec{v}_1 - \vec{v}_2$; the original velocities expressed as a function of these are

$$\vec{v}_1 = \vec{v}_{\mathrm{CM}} + \frac{m_{\mathrm{r}}}{m_1}\vec{v}_{\mathrm{r}} \tag{6.8a}$$

$$\vec{v}_2 = \vec{v}_{\mathrm{CM}} - \frac{m_{\mathrm{r}}}{m_2}\vec{v}_{\mathrm{r}}\,, \tag{6.8b}$$

while the total kinetic energy results

$$\mathcal{E} = \frac{1}{2}(Mv_{\mathrm{CM}}^2 + m_{\mathrm{r}}v_{\mathrm{r}}^2)\,,$$

with $m_{\mathrm{r}} = m_1m_2/M$ the so called reduced mass.

The velocities can be rewritten in the center of mass frame, moving in the laboratory one with velocity $\vec{v}_{\mathrm{CM}}$. Denoting with $\vec{u}$ all the velocities in this reference frame, then $\vec{u}_{\mathrm{CM}} = 0$, while the velocities of the two particles are

$$\vec{u}_1 = +\frac{m_{\mathrm{r}}}{m_1}\vec{v}_{\mathrm{r}}$$
$$\vec{u}_2 = -\frac{m_{\mathrm{r}}}{m_2}\vec{v}_{\mathrm{r}}\,,$$

which means they are moving in opposite direction with a consequent zero momentum (all given by $\vec{p} = M\vec{v}_{\mathrm{CM}}$). Obviously, the relative velocity $\vec{v}_{\mathrm{r}}$ is independent of the considered frame.

6.A.2 Scattering matrix

If the force between the two particles is a central force, they move in a fixed plane within the laboratory frame on which both the velocities before and after the collision lie. Hence, the relative velocity after the collision will belong to the same plane, being rotated of the scattering angle χ from $\vec{v}_{\mathrm{r}}$.

Let then consider the laboratory frame, defined by $(\widehat{\imath}_1, \widehat{\imath}_2, \widehat{\imath}_3)$, in which the relative velocity is identified by the two angles ϕ, lying on the plane $\widehat{\imath}_1, \widehat{\imath}_2$ and measured from $\widehat{\imath}_1$ direction, and θ, measured from $\widehat{\imath}_3$. A second frame, the center of mass one, can be chosen in order to have $\vec{v}_{\mathrm{r}}$ directed as $\widehat{\iota}_3$; in this second reference, the plane containing the relative velocity after the collision $\vec{v}'_{\mathrm{r}}$ is identified by the angle ψ measured from $\widehat{\iota}_1$, and $\vec{v}'_{\mathrm{r}}$ fully identified by χ measured on it starting from $\vec{v}_{\mathrm{r}}$ as the scattering angle. Since no particular limit is placed on the choice of $\widehat{\iota}_1$ and $\widehat{\iota}_2$, one can select $\widehat{v}_{\mathrm{r}} \times \widehat{\imath}_1$ and $\widehat{v}_{\mathrm{r}} \times (\widehat{\imath}_1 \times \widehat{v}_{\mathrm{r}})$ in order to form an orthonormal basis with $\widehat{v}_{\mathrm{r}}$, as shown in Figure 6.7.

Since the collision is studied in the center of mass frame, the combination of two 3D rotations gives the expression of $\vec{v}'_{\mathrm{r}}$ in the laboratory reference, each given by a double 2D rotation. The first is connected to the change of reference from i to ι,

determined by the two rotations of ϕ around $\widehat{i}_3$ and of θ around the new $\widehat{i}'_2$ axis. Hence the velocity $\vec{v}'_{\rm r}$ in the center of mass frame is obtained multiplying the one in the laboratory frame, $\vec{v}^{\,i}_{\rm r}$, by the double rotation matrix

$$\vec{\vec{R}}^{\,i}_{\phi\theta} = \vec{\vec{R}}^{\,i}_{\theta}\vec{\vec{R}}^{\,i}_{\phi} = \begin{pmatrix} \cos\theta & 0 & -\sin\theta \\ 0 & 1 & 0 \\ \sin\theta & 0 & \cos\theta \end{pmatrix} \begin{pmatrix} \cos\phi & \sin\phi & 0 \\ -\sin\phi & \cos\phi & 0 \\ 0 & 0 & 1 \end{pmatrix} = \\ = \begin{pmatrix} \cos\theta\cos\phi & \cos\theta\sin\phi & -\sin\phi \\ -\sin\phi & \cos\phi & 0 \\ \sin\theta\sin\phi & \sin\theta\sin\phi & \cos\theta \end{pmatrix} .$$

through which: $\vec{v}'_{\rm r} = \vec{\vec{R}}^{\,i}_{\phi\theta}\vec{v}^{\,i}_{\rm r}$. The inverse rotation is obtained by

$$(\vec{\vec{R}}^{\,i}_{\phi\theta})^{-1} = \begin{pmatrix} \cos\theta\cos\phi & -\sin\phi & \sin\theta\cos\phi \\ \cos\theta\sin\phi & \cos\phi & \sin\theta\sin\phi \\ -\sin\theta & 0 & \cos\theta \end{pmatrix} .$$

Then, the new velocity $\vec{v}'^{\,\prime}_{\rm r}$ can be obtain through the rotation by the scattering angles χ and ψ around $\widehat{\imath}_3 = \widehat{v}_{\rm r}$, which simply gives

$$\vec{\vec{R}}^{\,\prime}_{\chi\psi} = \begin{pmatrix} 0 & 0 & \sin\chi\cos\psi \\ 0 & 0 & \sin\chi\sin\psi \\ 0 & 0 & \cos\chi \end{pmatrix} .$$

The new relative velocity in the laboratory frame $\vec{v}'^{\,i}_{\rm r}$ is, therefore, obtained from a first rotation of $\vec{v}^{\,i}_{\rm r}$ to $\vec{v}'_{\rm r}$ through $\vec{\vec{R}}^{\,i}_{\phi\theta}$, composed with the scattering rotation $\vec{\vec{R}}^{\,\prime}_{\chi\psi}$ to obtain $\vec{\vec{R}}^{\,\prime}_{\phi\theta}$ in the center of mass reference, and then again with $(\vec{\vec{R}}^{\,i}_{\phi\theta})^{-1}$ to go back to the laboratory frame:

$$\vec{v}'^{\,\prime}_{\rm r} = (\vec{\vec{R}}^{\,i}_{\phi\theta})^{-1}\vec{\vec{R}}^{\,\prime}_{\chi\psi}\vec{\vec{R}}^{\,i}_{\phi\theta}\vec{v}_{\rm r} = \\ = |\vec{v}_{\rm r}| \begin{pmatrix} \cos\theta\cos\phi\sin\chi\cos\psi - \sin\phi\sin\chi\sin\psi + \sin\theta\cos\phi\cos\chi \\ \cos\theta\sin\phi\cos\chi\cos\psi + \cos\phi\sin\chi\sin\psi + \sin\theta\sin\phi\cos\chi \\ \cos\theta\cos\chi - \sin\theta\sin\chi\cos\psi \end{pmatrix} .$$

6.A.3 Emerging velocities and energy loss

If the collision is not elastic, then an amount of the energy $\Delta\mathcal{E}$ may become available (positive, in the superelastic scattering) or may be lost (negative, in the inelastic scattering). This modifies the magnitude of $\vec{v}'_{\rm r}$, independently of the change of direction, through the relation

$$|\vec{v}''_{\rm r}| = \sqrt{\frac{\mathcal{E}_{\rm r} + \Delta\mathcal{E}}{\mathcal{E}_{\rm r}}}\,\vec{v}'_{\rm r} .$$

Once the new relative velocity direction is determined and is scaled in magnitude, the new velocities in the laboratory frame, $\vec{v}'_1$ and $\vec{v}'_2$, can be computed through equations (6.8a), using $\vec{v}''_{\rm r}$ instead of $\vec{v}_{\rm r}$.

When the interest is centered only on one of the two particles undergoing the collision, it can be useful to change a little the approach as follows: a new reference frame is defined to follow the target particle, which is, therefore, considered at rest in it, while the projectile will move with the relative velocity $\vec{v}_\mathrm{r} = \vec{v}_1 - \vec{v}_2$. In this reference, the scattering angle χ_0 is related to that in the center of mass frame through [83]

$$\tan\chi_0 = \frac{\sin\chi}{m_1/m_2 + \cos\chi}\,.$$

The projectile undergoes an energy loss factor

$$\epsilon = \frac{\Delta\mathcal{E}}{\mathcal{E}} = 2\frac{m_1 m_2}{(m_1+m_2)^2}(1-\cos\chi) = 2\frac{m_\mathrm{r}}{M}(1-\cos\chi)\,, \tag{6.9}$$

which depends on the scattering angle in the center of mass reference, as easily deducible by the momentum and energy conservation laws remembering that the initial and final velocities lie on the same plane.

In the particular frame of interest, the particle will be scattered with the angle χ_0 and the transformation rules of Section 6.A.2 can be directly applied to $\vec{v}_\mathrm{r}$ using χ_0 instead of χ. Finally, the projectile is put back in the laboratory frame adding the velocity $\vec{v}_2$ of the target.

Two limit cases can be of interest. The first is that of a small mass hitting a heavy target ($m_1 \ll m_2$). In this case $\chi_0 = \chi$. Once determined the scattering angle, the energy loss of the lighter particle in the elastic recoil is computed as

$$\epsilon = 2\frac{m_1}{m_2}(1-\cos\chi)\,, \tag{6.10}$$

even if almost negligible due to the low mass ratio. If the target can be considered at rest, then the projectile velocity has not to be modified before and after the collision (there is no need to calculate the relative and center-of-mass velocities).

The second case is that of equally weighted particles ($m_1 = m_2$). In this case, $\chi = 2\chi_0$, while the energy loss factor is given by

$$\epsilon = \frac{1-\cos\chi}{2} = \sin^2\chi_0\,. \tag{6.11}$$

CHAPTER 7

The 2D electrostatic PIC-MCC code

Abstract. The microscopic description of the breakdown phase in a PF device is performed coupling a bidimensional electrostatic PIC code with a MCC module: the first allows to study the motion of the particles consistently with the space-charge effects which modify the applied external field; the stochastic module is used to sample the collisions between charged particles and a background uniform neutral gas. After a brief introduction of the PIC methods, limited to the electrostatic case of interest, the attention will be drawn to its coupling with the collisional module. A brief description of the implemented code will follow, while few numerical optimization will be collected in appendix.

7.1 Particle In Cell method

The major strength of PIC methods is the absence of any particular assumption on the distribution function of the simulation particles allowing to fully describe the system from a microscopic point of view, including all the related nonlinear and collective effects. The associated drawback is the low computational efficiency, related to the high number of simulation particles which implies both a high demand of CPU-time and memory resources.

The general flowchart of an electrostatic PIC code is presented in Figure 7.1: while particles are described in a continuum phase space domain (both in position and in velocity, but not in time), the fields are solved on the nodes of a discrete mesh. Hence, the particles charge has to be assigned to the mesh as source term for the electric field solution; on the other hand, this has to be interpolated on the particles position to obtain the pushing force needed for their advance. The procedure is then iterated for each timestep in a loop over time.

Since it is usually not possible to follow all the particles in a system, only a limited number of them is treated assuming their behavior to be representative of all the real particles. Hence, the difference between the term "simulation particles" and "real particles" (see Chapter 8 for a more detailed explanation).

7.1.1 Interpolation schemes

The interaction between "continuum particles" and "discrete fields" is achieved by means of interpolation schemes. All the physical quantities related to the particles are weighted on the grid points through the so called *shape factor* [129, 130], this being related to the effective finite shape of the particles as seen from the grid. The charge density felt in the node of coordinate $\vec{x}_g$ due to a charge in $\vec{x}_p$ is changed from $q\delta(\vec{x}_g - \vec{x}_p)$ to $qS(\vec{x}_g - \vec{x}_p)$, where $q = \int S(\vec{x}_g - \vec{x}_p)\,\mathrm{d}\vec{x}_g$ is the total charge of the particle and $\delta(\vec{x})$ the N_D dimensional Dirac delta function.

The grid charge density in the generic node $\{\vec{x}_g\}$ due to a set of N_p particles

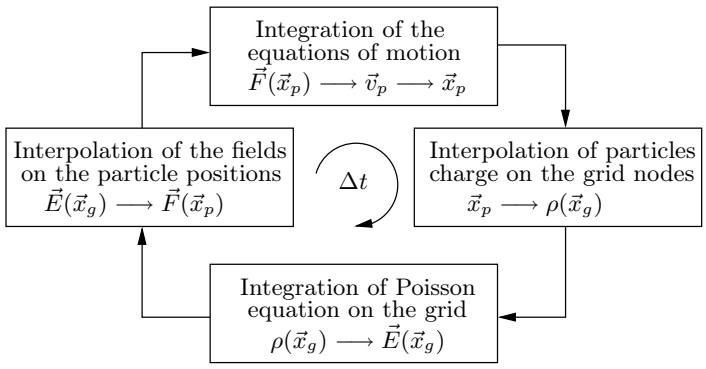

Figure 7.1: Schematic flowchart of an electrostatic PIC code.

positioned in $\vec{x_p}$ is obtained as

$$\rho_g = \rho(\vec{x}_g) = \sum_p q_p S(\vec{x}_g - \vec{x}_p)\,. \tag{7.1}$$

Once solved the electric field of the space charge $\rho(\vec{x}_g)$ as described in more details in the next section, the force $\vec{F} = q\vec{E}$ acting on particles is exactly known only on the grid nodes; hence, it has to be interpolated from the grid to the particle positions as

$$\vec{F}_p = q_p \sum \vec{E}_g S(\vec{x}_g - \vec{x}_p)\,,$$

where $\Delta x_{g,j}$ is the cell width along the j-th of the N_D directions. The use of the same weight function eliminates the possibility of induced self-forces (gravitation-like instability) and ensures conservation of momentum [43, 130].

For example, a widely diffuse choice in PIC code is the first order weighting (PIC-CIC); in this case the shape factor assumes the form

$$S(\vec{x}_g - \vec{x}_p) = \begin{cases} \dfrac{\prod_{j=1}^{N_\mathrm{D}} (\Delta x_{g,j} - |x_{p,j} - x_{g,j}|)}{\prod_{j=1}^{N_\mathrm{D}} \Delta x_{g,j}} & \text{if } |x_{p,j} - x_{g,j}| \le \Delta x_{g,j}\ \forall j \\ 0 \quad \text{otherwise} \end{cases} \tag{7.2}$$

The first-order weighting is usually called *area weighting* in 2D codes, as easily deducible from Figure 7.2. Even if more sophisticated and generalized weighting schemes have been developed, with corrections intended to avoid systematic errors in density calculation when curvilinear coordinates are involved [131], the induced error for the area weighting in an uniform grid scales with $\Delta x_{g,j}^2$, which is considered acceptable in the present case.

The particles can be viewed as having a finite size, with a box-shaped dimension roughly of the order of the cell dimensions, resulting as a tenuous cloud-like charge spot (hence the name Cloud In Cell or CIC) [43, 132, 133]. When two finite particles belong to the same cell, the inter-particle force drops to zero and they can cross each other. The zero, rather than infinite, force as $r \to 0$ results in a loss of resolution for the short-range Coulomb collisions at impact parameters less than a cell size. This can be interpreted as a smoothing effect of the grid, and it is desirable when primarily seeking long-range effects. As far as collisions with a background gas are considered, in a breakdown process simulation, the effect of short-range Coulomb collisions is usually negligible.

7.1.2 Electric field solution

When the dynamic coupling between electric and magnetic fields can be ignored, the Maxwell's equations system is reduced to the electrostatic case. Generally, both its source term (charge density, ρ) and solution (electric potential, ϕ) are known at the grid nodes. Combining the Gauss' law ($\nabla \cdot \vec{D} = \rho$) with the definition of the scalar potential ($\vec{E} = -\nabla\phi$), the Poisson's equation

$$\nabla \cdot (\epsilon \nabla \phi(\vec{x}, t)) = \rho(\vec{x}, t) \tag{7.3}$$

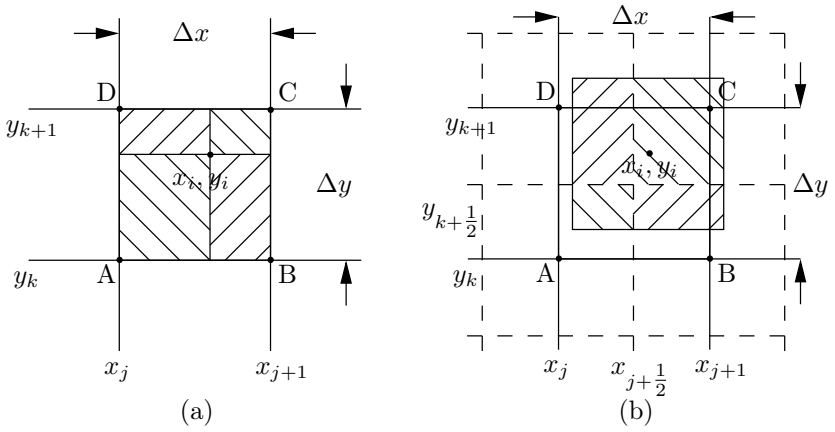

Figure 7.2: Charge assignment for linear weighting in two dimensions; areas are assigned in the PIC bilinear interpolation interpretation (a) and in the CIC cloud one (b). The two methods lead to the same result in cartesian geometry.

is obtained. Instead of solving the above elliptic partial differential equation (PDE) through finite differencing, a finite volume approach is used. The Poisson's equation is differenced through a Gaussian pillbox, which allows to include directly the boundary conditions on both internal and bounding, conductive and dielectric surfaces [134]. The Gauss' law can be written in integral form for each finite volume surrounding a node of the mesh as

$$\int_S \epsilon \vec{E} \cdot \mathrm{d}\vec{S} = \int_V \rho \, \mathrm{d}V + \int_S \sigma \, \mathrm{d}S = Q$$

or

$$\begin{aligned} &2\pi\Delta z(\epsilon_{i+1/2,j}\, r_{i+1/2}\, E_{r_{i+1/2,j}} - \epsilon_{i-1/2,j}\, r_{i-1/2}\, E_{r_{i-1/2,j}}) + \\ &\quad + \pi(r^2_{i+1/2} - r^2_{i-1/2})(\epsilon_{i,j+1/2}\, E_{z_{i,j+1/2}} - \epsilon_{i,j-1/2}\, E_{z_{i,j-1/2}}) = Q_{i,j} \end{aligned} \tag{7.4}$$

where an axial-symmetric problem in cylindrical coordinate (r, z), corresponding to the couple of indexes (i, j) of the mesh, has been considered.

The dielectric constant ϵ is assigned to each center of the grid cells, assuming it uniformly constant over the cell. The dielectric constant on the cell interface, take $\epsilon_{i-1/2,j}$ as reference, is then obtained as average between the $\epsilon_{i-1/2,j-1/2}$ and $\epsilon_{i-1/2,j+1/2}$. This assumption allows to have dielectric and conducting surfaces falling exactly on the cell interfaces.

The total charge inside the volume $Q_{i,j}$ corresponds to the sum of all charged particles weighted on the grid point (i, j). At an external boundary or internal interface, $Q_{i,j}$ can be written as

$$Q_{i,j} = \rho_{i,j} \Delta V_{i,j} + \sigma_{i,j} \Delta S_{i,j}$$

where $\Delta V_{i,j}$ is the volume containing all the free charges associated with the grid point, while $\Delta S_{i,j}$ is the area of the physical interface on which charge density can accumulate. In principle, the method is perfectly coherent with the cloud interpretation of charged particles (see Figure 7.2-(b)), where the charge occupies a volume equivalent to the Gaussian pillbox of interest, but is centered on the $i-$th particle position, only partially contributing to the charge contained in the finite volume. A particle crossing a dielectric free-space boundary is split on the adjacent nodes through a linear weighting procedure [130].

In the electrostatic approximation, the electric potential can be derived from the electric field in finite difference form through

$$E_{r_{i-1/2,j}} = \frac{\phi_{i-1,j} - \phi_{i,j}}{\Delta r} \qquad E_{r_{i+1/2,j}} = \frac{\phi_{i,j} - \phi_{i+1,j}}{\Delta r} \tag{7.5a}$$

$$E_{z_{i,j-1/2}} = \frac{\phi_{i,j-1} - \phi_{i,j}}{\Delta z} \qquad E_{z_{i,j+1/2}} = \frac{\phi_{i,j} - \phi_{i,j+1}}{\Delta z}\,. \tag{7.5b}$$

When substituting the above formulation in equation (7.4), a finite difference Poisson's equation is obtained, having the electric potential as unknown, defined on the grid nodes (while the electric field is defined at the interface between two finite volumes).

The electric field in free-space, needed for advancing particles, is obtained by finite central differencing over two cells[1]. On the dielectric free-space boundaries, the field is obtained using half-Gaussian pill-boxes [134]: as the grid spacing approaches zero, the equations reduce to the electrostatic jump condition $\epsilon_1 E_1 - \epsilon_2 E_2 = \sigma_s$, with σ_s the surface charge density.

When an external potential is applied, the field can be solved by superposition of two contributes: a Poisson's equation $\nabla \cdot \epsilon \nabla \phi_{\text{Poisson}} = -\rho/\epsilon$ with zero boundary conditions is solved at each time-step to account for the space charge effect, while a Laplace's equation $\nabla \cdot \epsilon \nabla \overline{\phi}_{\text{Laplace}} = 0$, with a mix of Dirichlet (applied potentials normalized to 1) and Neumann[2] (applied surface charge densities) boundary conditions needs to be solved only once to account for the field effects. Indicating with $\phi_0^{(t)}$ the external applied time varying potential, the electric potential in the system at time t is then obtained as $\phi_{ij}^{(t)} = \phi_{ij,\text{Poisson}}^{(t)} + \phi_0^{(t)} \overline{\phi}_{ij,\text{Laplace}}$.

The unknown $\phi_{ij}^{(t)}$ matrix can be obtained through many different solvers, both iterative or direct [129]. In the present work, a classic Successive Over Relaxation (SOR) method has been implemented exploiting the solution at the previous time-iteration as first trial for the next one, as the iterative nature of the solver suggests [135]. The over-relaxation coefficient, for the elliptic problem in a uniform rectangular grid $N_i \times N_j$, is chosen as $\omega = 2(1 - \pi\sqrt{N_i/N_j})$ [129]. More efficient methods for elliptic problems, Multigrid as first, are under investigation for future implementation and parallelization.

[1] The same strategy is followed on internal dielectric corners where a normal direction cannot be defined.

[2] Mathematically, a Dirichlet boundary condition is required for a unique solution; often, one chooses a reference potential of zero at the grounded electrodes.

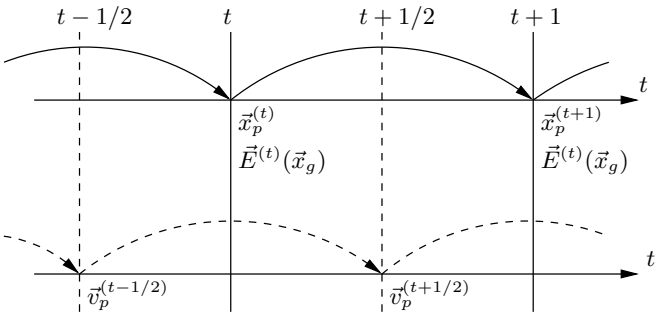

Figure 7.3: Schematic representation of the staggered leapfrog scheme.

7.1.3 Particle advance scheme

Once obtained the total electric field as superposition of both the space-charge effect and the external driving potential, the particles can be advanced through the solution of the Newton's equation of motion $\mathrm{d}(\gamma m\vec{v})/\,\mathrm{d}t = \vec{F}$, having the Lorentz's force $\vec{F} = q(\vec{E} + \vec{v} \times \vec{B})$ as pushing force. The Newton-Lorentz system in the discretized form is often solved through a staggered second-order accurate center difference scheme, often referred to as the *leapfrog scheme* [130], having the advantage of requiring few operations and minimal storage, since the update can be done in place. Neglecting the relativistic factor $\gamma = (1 - (v/c)^2)^{-1/2}$ and the contribution of the magnetic field[3] $\vec{B}$, the finite difference form of the leapfrog method gives

$$\frac{\vec{v}^{(t+1/2)} - \vec{v}^{(t-1/2)}}{\Delta t} = \frac{q}{m}\vec{E}^{(t)} \tag{7.6a}$$

$$\frac{\vec{x}^{(t+1)} - \vec{x}^{(t)}}{\Delta t} = \vec{v}^{(t+1/2)} \tag{7.6b}$$

where $t \pm 1/2$ is used to label the time-instant $t \pm \Delta/2$. The value of $\vec{E}^{(t)}$ is obtained through the solution of the electric field and interpolated over the particle position through the weight function, as described in Section 7.1.1.

As shown in Figure 7.3, integration starts from known $\vec{x}^{(t)}$ and $\vec{v}^{(t-1/2)}$ producing later on $\vec{x}^{(t+1)}$ and $\vec{v}^{(t+1/2)}$. The charge density on the nodes, the electric potential and the electric field are also known at integer multiple of Δt. The simultaneous solution of the two time-centered difference equations is second order accurate (Δt^2 error term).

The initial conditions for $t = 0$, $\vec{v}^{(-1/2)}$ being undefined, necessitate of a first half-time integration of the first equation in the system. When a starting Maxwellian distribution function is considered as stationary initial condition, before the application of an external voltage $V(t)$, the electrostatic problem under investigation can be solved consistently.

Once the cycle over the simulation particles has been completed, the new charge

[3] In the case of an electromagnetic PIC, an efficient integration of the scheme, which avoids the full cross product calculation is due to Boris [136].

distribution on the grid nodes can be obtained through equation (7.1), and the time-iteration is restarted.

7.1.4 Accuracy and stability limits

Many efforts have been devoted to the analysis of the numerical stability and accuracy of the above proposed numerical methods based on the interaction between particles and a discretized time-space [130, 131, 137]. The main conclusions of interest will be reported hereafter.

The presence of a numerical grid is "felt" by the particles moving in it. The interaction force $F(x_1, x_2)$ acting on a particle at x_2 due to a particle at x_1 in a mono-dimensional physical system depends only on the separation $x = x_2 - x_1$ and is invariant under displacement. When a spatial grid is introduced, the displacement invariance is lost since the particles can be displaced while the grid is fixed. Thus, F also depends on the location relative to the grid of the midpoint $x_\mathrm{m} = (x_1 + x_2)/2$; in a grid of uniform spacing Δx, the force $F(x_\mathrm{m} - x/2, x_\mathrm{m} + x/2)$ is periodic with period Δx. The Fourier integral transform in x and the Fourier series in x_m can be used to study the effect of nonuniformity on an infinite periodic plasma [130]:

$$F\left(x_\mathrm{m} - \frac{x}{2}, x_\mathrm{m} + \frac{x}{2}\right) = \int_{-\infty}^{\infty} \frac{\mathrm{d}k}{2\pi} \exp(\,\mathrm{i}kx) \sum_{p=-\infty}^{\infty} \exp(\,\mathrm{i}pk_\mathrm{g}x_\mathrm{m})\tilde{F}_p(k)\,,$$

with $k_\mathrm{g} = 2\pi/\Delta x$ the associated *grid wave number*, and

$$\tilde{F}_p(k) = \int_{-\infty}^{\infty} \mathrm{d}x\, F_p(x) \exp(-\,\mathrm{i}kx)$$
$$F_p(x) = \frac{1}{\Delta x} \int_{\Delta x} \mathrm{d}x_\mathrm{m} \exp(\,\mathrm{i}k_\mathrm{g}x_\mathrm{m}) F\left(x_\mathrm{m} - \frac{x}{2}, x_\mathrm{m} + \frac{x}{2}\right)\,.$$

The difference $\delta F = F - F_0$, between the real force F and the average force $F_0(x)$ corresponding to the first mode $p = 0$ of the Fourier series, represents a nonphysical grid force. Considering a system of particles with density $n(x)$, the force $F(x)$ on a particle is the superimposition of all the contributions:

$$F(x) = \int \mathrm{d}x' F(x', x) n(x')\,,$$

which is transformed into

$$\tilde{F}(k) = \sum_{-\infty}^{\infty} \tilde{F}_p\left(k - \frac{1}{2}pk_\mathrm{g}\right) \tilde{n}(k_p)\,,$$

where $k_p = k - pk_\mathrm{g}$. Comparing it with the expression of the force in a continuum free space

$$\tilde{F}(k) = \tilde{n}(k)\tilde{F}_{p=0}(k)\,,$$

it arises that the grid introduces a coupling of the force and density perturbations which differs by integer multiples of the grid wave number k_g. All the terms corresponding to $p \neq 0$ are named *aliases*: the grid cannot solve properly the harmonics having a wavenumber greater than the grid one [130].

The analysis of the dielectric function for an unmagnetized electrostatic Vlasov plasma leads to two dispersion relation for the gridless and gridded cases. The alias coupling appears unimportant for $\lambda_D/\Delta x = 1$ and the averaged force appears to properly work. Approximately, for linear weighting, $\lambda_D/\Delta x \geq 1/\pi \simeq 0.3$ gives an ignorable growth of this nonphysical instability [138]. In many applications, a cold plasma component provides accurate, noise-free collective behavior even for $\lambda_D/\Delta x \simeq 0.1$ [139, 43].

The stability of the leapfrog scheme can be derived for particles in simple mono-dimensional harmonic motion:

$$\frac{\mathrm{d}^2 x}{\mathrm{d}t^2} = -\omega_0^2 x\,.$$

Center differencing and combining the velocity and position equations as obtained from the leapfrog scheme leads to

$$\frac{x^{(t+1)} - 2x^{(t)} + x^{(t-1)}}{\Delta t^2} = -\omega_0^2 x^{(t)}\,,$$

whose solutions are in the form of

$$x^{(t)} = C\exp(-\mathrm{i}\omega t) \qquad \text{and} \qquad x^{(t+1)} = C\exp(-\mathrm{i}\omega(t+\Delta t))\,.$$

By means of the Euler's identity $\sin(\xi) = (\exp(\mathrm{i}\xi) - \mathrm{i}\exp(-\mathrm{i}\xi))/2$, by substitution of the above solutions in the finite difference form of the differential problem, one obtains

$$\sin\left(\frac{\omega\Delta t}{2}\right) = \pm\frac{\omega_0\Delta t}{2}\,;$$

it follows that the numerical stability of the method is limited by the condition $\omega_0\Delta t \leq 2$, since in the opposite case an imaginary component would be obtained [130]. Since the phase error is quadratic for small $\omega\Delta t \ll 1$

$$\frac{\omega\Delta t}{2}\left(1 - \frac{1}{6}\left(\frac{\omega\Delta t}{2}\right)^2 + \mathrm{O}\left(\frac{\omega\Delta t}{2}\right)^4\right) = \frac{\omega_0\Delta t}{2}\,,$$

$\omega_0\Delta t \leq 0.2$ is usually assumed as good accuracy condition, with ω_0 the maximum plasma frequency [43].

The stability of the center difference methods employed both for the discretized space and time can be analyzed through the wave equation

$$\frac{\partial^2\psi}{\partial t^2} = c^2\frac{\partial^2\psi}{\partial x^2}$$

in the mono-dimensional space. Center differencing both in time and space with Δt as time-step and Δx as grid-space, one obtains

$$\psi_j^{(t+1)} = \left(c\frac{\Delta t}{\Delta x}\right)^2(\psi_{j+1}^{(t)} - 2\psi_j^{(t)} + \psi_{j-1}^{(t)}) + 2\psi_j^{(t)} - \psi_j^{(t-1)}\,. \tag{7.7}$$

The sinusoidal wave, $\psi(x,t) = \exp(\,\mathrm{i}(\omega t - kx))$, is numerically translated into $\psi_j^{(t)} = \exp(\,\mathrm{i}(\omega t - \kappa(j\Delta x))$, with κ the numerical wavenumber. Substituting this in

equation (7.7) for varying j and t and properly combining the arising exponential terms, a dispersion equation is obtained:

$$\cos(\omega\Delta t) = \left(c\frac{\Delta t}{\Delta x}\right)^2 (\cos(\kappa\Delta x) - 1) + 1\,.$$

For $c\Delta t/\Delta x = 1$ the numerical and theoretical wavenumbers coincide: $\kappa = k = \pm\omega/c$, as well as for $\Delta x \to 0$ and $\Delta t \to 0$. For $c\Delta t/\Delta x > 1$, as predicted by the *Courant-Levy stability condition*, an imaginary root starts growing representing a numerical instability [131]. In multiple N_D dimensions, the time step given by the Courant-Levy stability criterion is

$$\Delta t \leq \frac{1}{c}\left(\sum_{j=1}^{N_\mathrm{D}} (\Delta x_j)^{-2}\right)^{-1/2} . \tag{7.8}$$

Looking at the solver of the electric field, substituting the equations (7.5) into equation (7.4) for a uniform electric constant ϵ, a Taylor expansion of $\nabla^2\phi_{ij} - \nabla^2\phi(r,z)$ gives a general expression of the truncation error. On a uniform mesh, only the second order error term remains; even on a slowly varying mesh, the first-order term may result smaller than the second-order one [131].

The above considerations fix few first limits both for the grid spacing and for the time step through $\lambda_\mathrm{D}/\Delta x$ and $\omega_\mathrm{p}/\Delta t$ respectively as consequences of how the particles "feel" the discretized space-time. Moreover, the two constraints are related together by the Courant-Levy stability condition. Few rough rules of thumb have been derived to avoid nonphysical behaviors. On the accuracy side, both the field solver and the advance scheme are second order accurate.

7.2 Monte Carlo Collisional module

The match between the statistical nature of the microscopic collisions in the transport equation and the basic spirit of the Monte Carlo (MC) methods is intuitive [140, 141, 142, 143]. Recently, the MCC has been showed to be a technique to solve the linear Boltzmann equation (LBE) [144], including space- and time-dependent volume forces (like the Lorentz's force). Thus, the MC method can be effectively coupled with a PIC module to take into account the collisions between charged particles and a background uniform neutral gas.

7.2.1 Monte Carlo basic rules

Charged particles are assumed to experience only instantaneous binary collisions with neutral particles of a background mixture of species and to move of free flight between collisions. As stated above, even the MC method follows a statistically representative sample of particles, since it would be unpractical to follow all the real particles as soon as their number rises over $10^6 \div 10^7$ on a commodity workstation. Because of the disparity between the number of simulation particles and real particles, one has to deal with an output affected by statistical noise: the relative error on the macroscopic quantities decreases slowly with the number N of contributing samples, typically as $1/\sqrt{N}$ (assuming a Poisson distribution) [145].

Each MC method is based on a pseudo-random sequence of numbers, i.e. a sequence of numbers showing an apparent randomness appearing not related to any other extracted number. From a uniform sequence of random numbers R_i in the interval $[0, 1[$, a collection of random numbers r_i distributed according to the function $f(r)$ in $[r_1, r_2]$ can be obtained through the following probability theorem

$$\int_{r_1}^{r_i} f(r)\,\mathrm{d}r = R_i \int_{r_1}^{r_2} f(r)\,\mathrm{d}r\,, \tag{7.9}$$

which results in an equation for r_i. Depending on the case, the integrals have to be evaluated analytically or numerically.

Thus, the MC method can be used to evaluate the free flight time of a particle from the total sum of the collisional frequencies for all processes that it could experience. During the free flight the equations of motion for the particle need to be solved in order to calculate its trajectory. Once reached the collision time, a process need to be selected among all the possible on the basis of its contribution to the total collisional frequency. Finally the effect of the collision on the velocity vectors of the particles and the loss and generation of new particles have to be evaluated.

Similarly, the stochastic nature of the charged particles interaction with a boundary surface can be modeled through random numbers sampled from a proper distribution function, while the position of the impact and of the eventually emerging particles is determined by the intersection between the trajectories and the boundaries.

An outline of the algorithm here presented to follow the path of a single particle is depicted in Figure 7.4. In the following sections a more detailed description of each step will be given.

7.2.2 PIC coupling and free-flight

Since the cross sections $\sigma_i(\mathcal{E})$ are function of the charged particle energy $\mathcal{E}$ in the center of mass frame (see Section 6.2.2), they have to be evaluated after the particle advance and acceleration performed in the PIC module, presented in Section 7.1.3. The cross section is assumed to be constant along the path of the particle, until the particle undergoes a collision or the next time-step is reached. The leap-frog scheme perfectly matches this requirement if the linearly increasing velocity (being the acceleration term fairly constant during the time-step) is approximated with a constant velocity during $[t, t + \Delta t]$ increasing like a step-wise function at t. Hence, the flow-chart of the MCC module presented in Figure 7.4 can be integrated in that of Figure 7.1 for the PIC code producing sequence depicted in Figure 7.5.

The collision probability of the i-th particle can be written as

$$P_{\mathrm{coll},i} = 1 - \exp(-n_{\mathrm{g}}\sigma_{\mathrm{tot}}(\mathcal{E}_i)v_i t_{\mathrm{coll}})\,, \tag{7.10}$$

where $\sigma_{\mathrm{tot}}(\mathcal{E}_i) = \sum_j \sigma_j(\mathcal{E}_i)$ is the total cross section obtained as the sum over all the possible processes and $v_i = \sqrt{2\mathcal{E}_i/m}$ is the particle velocity; the mean free flight time is the inverse of the total collisional frequency given by

$$\nu_{\mathrm{tot}}(\mathcal{E}_i) = \sqrt{\frac{2\mathcal{E}_i}{m}} n_{\mathrm{g}} \sum_j \sigma_j(\mathcal{E}_i)\,,$$

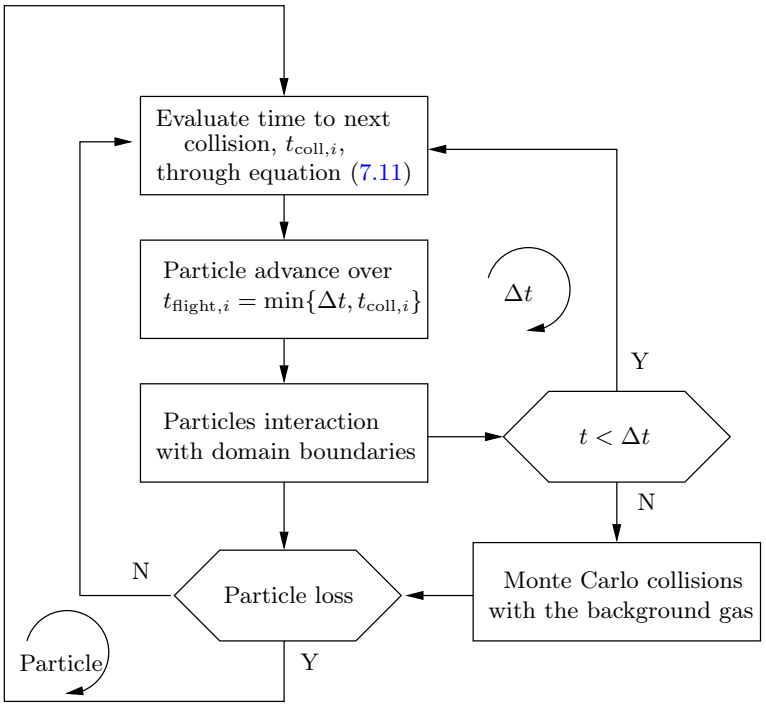

Figure 7.4: Schematic flow-chart of the MC method in a plasma simulation.

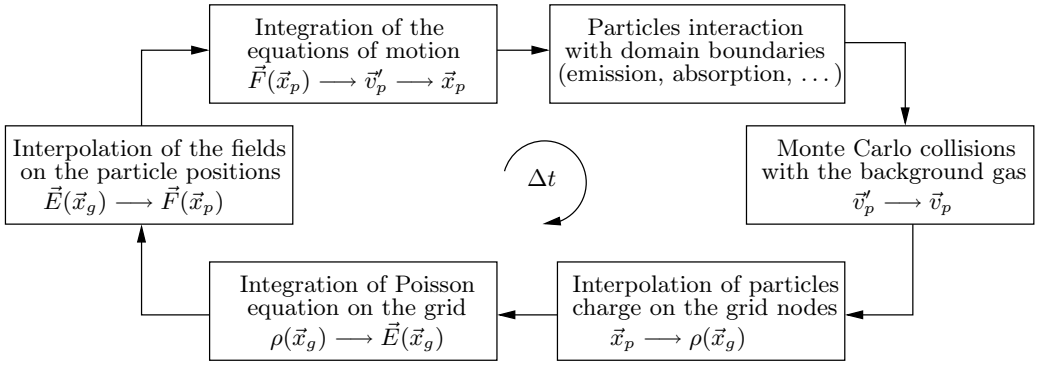

Figure 7.5: Schematic flow-chart of the PIC-MCC method in a plasma simulation.

having assumed n_g uniform over all the volume of interest. Making use of $P_{\text{coll},i}$ as distribution function in equation (7.9), the time to next collision can be evaluated as

$$t_{\text{coll},i} = -\frac{1}{\nu_{\text{tot}}(\mathcal{E}_i)} \ln(1 - R_1)\,, \tag{7.11}$$

with R_1 a random number sampled from a uniform distribution function in $[0, 1[$.

Once determined $t_{\text{coll},i}$, the i-th particle is advanced of $t_{\text{flight},i} = \min\{\Delta t, t_{\text{coll},i}\}$ and if $t_{\text{flight},i} < \Delta t$ the particle trajectory will be evaluated for surface interaction (Section 7.2.4); in the case the final position is inside the computational domain, the collision event with the neutral gas will be evaluated (Section 7.2.3).

The next time-to-collision evaluation can be performed equivalently by sampling a new random number or by employing the just used one by taking into account the probability of no collision in the performed flight[4] of duration t_{flight}:

$$P_{\text{coll},i} = (1 - \exp(-n_g \sigma \text{tot}(\mathcal{E}_i) v_i t_{\text{coll}})) \prod_j \exp(-n_g \sigma \text{tot}(\mathcal{E}_i^{(j)}) v_i^{(j)} t_{\text{flight},i}^{(j)})\,,$$

where the prime is used for the energy and velocity corresponding to the previous time-of-flight, t_{flight} being equal to Δt for each j except $j = 0$.

A more performing algorithm strongly limiting the time-step length is presented in details in Section 7.4.2, together with a slightly different selection technique known as *null collision*.

7.2.3 Collision with the background gas

A number of electron/ion-neutral collisions are possible, as shown in Table 6.2 and Table 6.3 of Section 6.2.2. Sampling a random number R_2 from a uniform distribution, the collision type k can be selected by scaling the partial cumulate of the collision frequency with the total one:

$$\frac{1}{\nu_{\text{tot}}} \sum_{i=0}^{k-1} \nu_j \leq R_2 < \frac{1}{\nu_{\text{tot}}} \sum_{i=1}^{k} \nu_j\,.$$

Once determined the collision type depending on the incident particle species, its effect has to be evaluated.

As first, the electron-neutral elastic collisions are considered. As stated in Section 6.2.1, the probability distribution of the poloidal angle ψ can be taken to be uniform in $[0, 2\pi[$ and can be simply sampled through a uniformly distributed random number

$$\psi = 2\pi R_3\,.$$

A normalized differential (azimuthally integrated) cross section $I(\mathcal{E}, \chi)$ can be used to generate a scattering angle χ, by inverting the corresponding equation (7.9), given

[4] The method is equivalent to that used in Monte Carlo transport simulation for multi-layer screen; here the interfaces are only virtual being represented by the time-step, while the particle energy can grow due to the external applied volume force.

by

$$R_4 = 2\pi \int_0^{\chi} I(\mathcal{E}, \chi') \sin\chi' \, \mathrm{d}\chi' \, .$$

Few commonly used approximations of $I(\mathcal{E}, \chi)$ are listed together with the resulting $\chi(R_4)$ expression in Table 7.6 and plotted for comparison in Figure 7.7 for two reference energies. As can be seen, the scattering process results in a larger probability in the forward direction for higher energies.

As widely explained in Appendix 6.A, the energy loss of the incident electron can be evaluated through equation (6.10), while the scattered velocity components are deducible from equation (6.5).

An inelastic process can be selected only if a particular threshold energy is overcome by the incident electron. For excitation processes, the energy balance between reactants and products is $\mathcal{E}_{\mathrm{ej}} + \mathcal{E}_{\mathrm{g}} = \mathcal{E}_{\mathrm{inc}} + \mathcal{E}_{\mathrm{g}^*} - \mathcal{E}_{\mathrm{exc}}$, where "ej" and "inc" labels the ejected and incident electron respectively. Since the mass of the electron is small compared to the mass of the neutral, its energy is not perturbed by the collision leading to the simplifying condition $\mathcal{E}_{\mathrm{g}} = \mathcal{E}_{\mathrm{g}^*}$ (see Appendix 6.A for a complete treatment). The velocity components of the ejected electron are calculated as in the case of elastic scattering.

For ionization, the process is ternary on the products side. Hence, the energy balance gives $\mathcal{E}_{\mathrm{inc}} + \mathcal{E}_{\mathrm{g}} = \mathcal{E}_{\mathrm{ej}} + \mathcal{E}_{\mathrm{sec}} + \mathcal{E}_{\mathrm{g}^+} - \mathcal{E}_{\mathrm{ion}}$, where "sec" stands for the secondary electron produced by ionization, while $\mathcal{E}_{\mathrm{g}}$ and $\mathcal{E}_{\mathrm{ion}}$ are the energies of the neutral target and of the outcoming ion. Even in this case the energy conservation between the neutral and the ion ($\mathcal{E}_{\mathrm{g}} = \mathcal{E}_{\mathrm{g}^+}$) is assumed. The excess energy $\mathcal{E}_{\mathrm{inc}} - \mathcal{E}_{\mathrm{ion}}$ is partitioned between the ejected and the secondary electron according to the distribution function

$$I(\mathcal{E}_{\mathrm{sec}}, \mathcal{E}_{\mathrm{inc}}) = \frac{B(\mathcal{E}_{\mathrm{inc}})}{\mathcal{E}_{\mathrm{ej}}^2 + B^2(\mathcal{E}_{\mathrm{inc}})} \arctan\left(\frac{\mathcal{E}_{\mathrm{inc}} - \mathcal{E}_{\mathrm{ion}}}{2B(\mathcal{E}_{\mathrm{inc}})}\right) ,$$

where $B(\mathcal{E}_{\mathrm{inc}})$ is a known function for many gases [84]. The inversion of the equation (7.9), using $I(\mathcal{E}_{\mathrm{sec}}, \mathcal{E}_{\mathrm{inc}})$ as distribution function, allows to obtain an expression for the energy of the emitted electron

$$\mathcal{E}_{\mathrm{sec}} = B(\mathcal{E}_{\mathrm{inc}}) \tan\left(R_5 \arctan\left(\frac{\mathcal{E}_{\mathrm{inc}} - \mathcal{E}_{\mathrm{ion}}}{2B(\mathcal{E}_{\mathrm{inc}})}\right)\right) .$$

The energy of the primary scattered electron $\mathcal{E}_{\mathrm{ej}}$ is then given by the above discussed energy balance. For high incident energies the incident electrons is likely to keep most of their energy. The directions of the two electrons after the collision could be obtained through the Surendra approximation [150], but the scheme would not conserve the system momentum. Neglecting the ion in the interaction and treating it as the collision between two electrons (one of which initially at rest), the momentum and energy conservation laws state that the velocities of the scattered and ejected electrons are perpendicular [151]:

$$\chi_{\mathrm{ej}} = \arccos\sqrt{\frac{\mathcal{E}_{\mathrm{ej}}}{\mathcal{E}_{\mathrm{inc}} - \mathcal{E}_{\mathrm{ion}}}} \qquad \chi_{\mathrm{sec}} = \chi_{\mathrm{ej}} - \frac{\pi}{2} \, .$$

Approximation	$I(\mathcal{E},\chi)$	$\chi(R_4)$	Ref.
Isotropic	$1/4\pi$	$\arccos(1-2R_4)$	–
Born	$\frac{\eta(\eta+1)}{\pi(2\eta+1-\cos\chi)^2}$, $\eta=\frac{10.9Z^{2/3}}{\mathcal{E}}$	$\arccos\left(\frac{\eta+1-(2\eta+1)R_4}{\eta+1-R_4}\right)$	[146]
Surendra	$\frac{\mathcal{E}}{4\pi(1+\mathcal{E}\sin^2(\chi/2))\ln(1+\mathcal{E})}$	$\arccos\left(\frac{2+\mathcal{E}-2(1+\mathcal{E})^{R_4}}{\mathcal{E}}\right)$	[147]
Okhrimovskyy	$\frac{1+8\eta}{4\pi(1+4\eta-4\eta\cos\chi)^2}$, $\eta=\frac{\mathcal{E}}{27.21\text{ eV}}$	$\arccos\left(1-\frac{2R_4}{1+8\eta(1-R_4)}\right)$	[148]
Kushner	$\frac{n+2}{8\pi}\cos^\eta\frac{\chi}{2}$, $\eta=\eta(\mathcal{E})$	$2\arccos\left((1-R_4)^{\frac{1}{\eta+2}}\right)$	[149]

Figure 7.6: Commonly used differential cross section approximations.

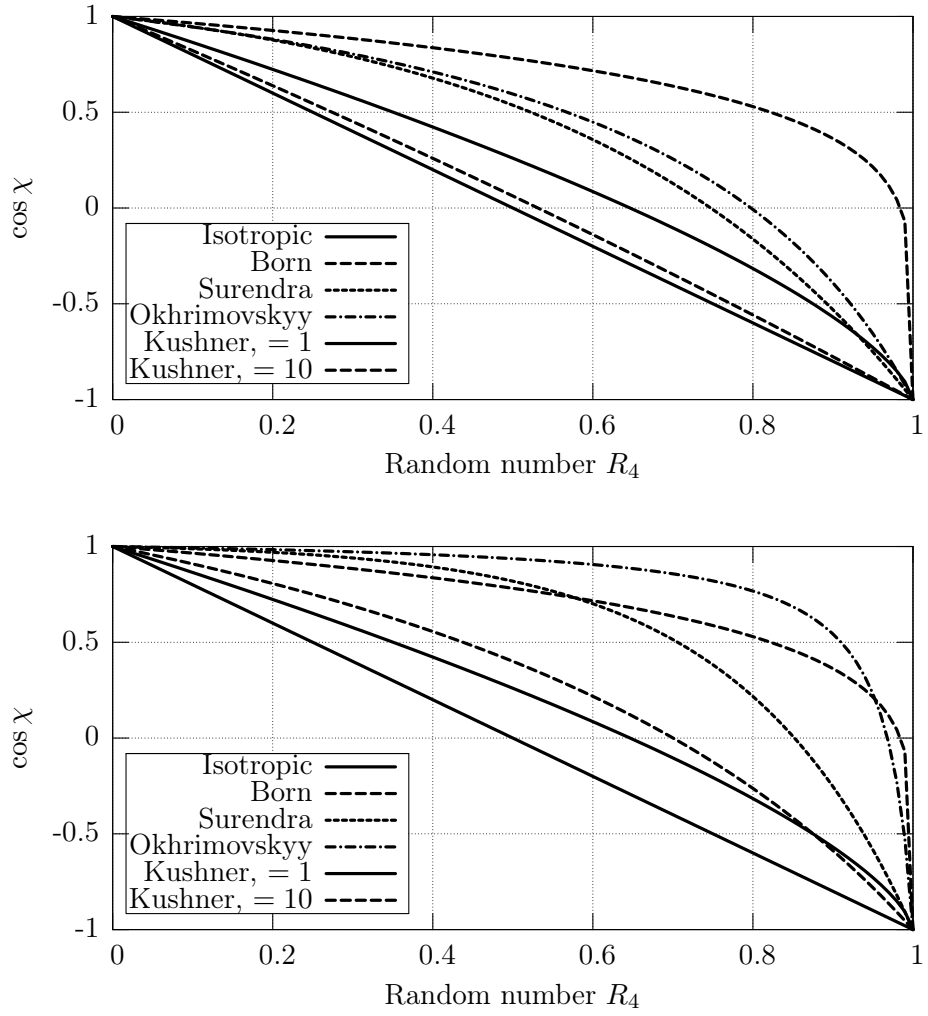

Figure 7.7: Plot of the scattering angle χ arising from the commonly used differential of Table 7.6 for $\mathcal{E} = 10$ eV (top) and 100 eV (bottom).

Ion-neutral collisions are similar to the electron-neutral ones, except the momenta of the involved particles are similar and, consequently, the collision mechanics has to be performed in the rest frame of the neutral (see Section 6.A.3).

The ion velocity $\vec{v}_\mathrm{i}$ is converted into $\vec{v}'_\mathrm{i} = \vec{v}_\mathrm{i} - \vec{v}_\mathrm{g}$ sampling $\vec{v}_\mathrm{g}$ from a Maxwellian distribution, and its energy $\mathcal{E}'_\mathrm{i}$ is recomputed. For elastic scattering the scattered ion energy can be deduced by equation (6.9), or by equation (6.11) for an atomic single species gas ($m_\mathrm{i} = m_\mathrm{g}$), with $\cos\chi = 1 - 2R_6$. The poloidal angle ψ is chosen uniformly and the scattered velocity in the rest frame of the neutral is calculated by means of the angles χ and ψ. Lastly the resulting energy has to be converted back in the laboratory frame.

Charge exchange is even simpler, since based on the identity exchange between a sampled neutral and an ion.

All the emerging particles from a collision are then followed for the residual time $t_\mathrm{res} = \Delta t - t_\mathrm{coll}$ and checked for other collisions before the end of the time-step.

7.2.4 Surface interaction

If the charged particles reach a boundary or an internal surface during their free flight, then they will undergo an interaction with a material instead of the neutral gas. As stated in Section 6.2.3 and summarized in Table 6.4, many surface collisions and interactions can produce particle losses and secondary electron emissions.

The secondary emission by ion impact is roughly treated sampling a random number R_7 and comparing it with the emission probability γ depending on the colliding ion and on the surface material. The energetic distribution function of the true secondaries is assumed as a Maxwell-Boltzmann, while the angular distribution is chosen randomly through

$$f(\theta) = \frac{\cos\theta}{2}\,.$$

A more sophisticated method is used for the secondary emission due to electron impact [97]; assuming

$$\delta(\theta, \mathcal{E}) = 2.6\delta_\mathrm{max}\epsilon^{2/3}\frac{1 + 2\epsilon(\cos\theta)^{1/(n-1/3)}}{(1 + \epsilon(\cos\theta)^{1/(n-1/3)})^3}$$

as secondary emission coefficient, with $\epsilon = 0.72\mathcal{E}/\mathcal{E}_\mathrm{max}$ depending on the incident electron energy $\mathcal{E}$ and on the energy $\mathcal{E}_\mathrm{max}$ corresponding to the maximum value of the secondary emission coefficient, δ_max; θ is the incident direction with respect to the surface normal, while n is the angular exponent, typically in the range $4/3 \div 5/3$. A typical energy distribution of the emitted secondaries has been described in Section 6.2.3: the 90% emission probability lies between 0 and 20 eV(low energy – true secondaries), 7% for energies ranging between 20 and 90 eV(medium energy – scattered primaries or secondaries produced in first layers) and the last 3% for higher energies (high energy – reflected primaries). This characteristic shape is essentially independent of the energy of the incident primary [152] and given by:

$$f_\mathrm{se}(\mathcal{E}_\mathrm{se}) = \frac{6\mathcal{E}_\mathrm{se}(e\psi)^2}{(E_\mathrm{se} + e\psi)^4}\,. \tag{7.12}$$

For each primary electron striking a conducting surface, it is considered lost and the number secondary emitted electrons, $\delta(\theta, \mathcal{E})$, is computed. For each created secondary, its energy is sampled through a random number R_7 from the energy distribution function given by equation (7.12). The angular distribution is assumed to be uniform in the azimuthal plane and cosine in the polar angle relative to the surface normal.

7.2.5 Photoemission by de-excitation

As previously described in Section 7.2.4, the SEE by ion impact is negligible at the first stages of a discharge development. However, any inelastic collision produces an excited state of a neutral molecule or atom. This will return to its ground state isotropically emitting a photon ν with a characteristic vacuum radiative decay time τ depending on the species and on the excitation type. The photons will travel roughly unperturbed in the background gas, due to the low pressure of the medium and to the low attenuation parameters μ (their characteristic energies being of about 10 eV); once colliding with a boundary or an external surface, a photon can induce electron emission by photoelectric effect. The complete MC simulation of the photon transport would be excessively demanding; a simplified model is required.

Since the characteristic time of the electrical discharge of interest are very short (few tens to one hundred ns), the time evolution of the excited state densities can be neglected (see Section 7.4.3 for a description of a possible implementation for longer time scales).

The source of excited states is known from he MCC module which gives the time- and space-dependent inelastic collision rate $\nu_{k,\mathrm{exc}}(\vec{r}, t)$ for each species k:

$$\Delta N_k^+ = (N_k(\vec{r}, t + \Delta t) - N_k(\vec{r}, t))^+ = \nu_{k,\mathrm{exc}}(\vec{r}, t)\Delta t\,.$$

The number of photons emitted at each time step Δt depends on the number of excited molecule $N_k(\vec{r}, t)$ and on their characteristic life-time τ_k:

$$\begin{aligned}\Delta N_k^- = (N_k(\vec{r}, t) - N_k(\vec{r}, t + \Delta t))^- &= -\int_0^{\Delta t} \frac{N_k}{\tau_k} \exp\left(-\frac{t'}{\tau_k}\right) \mathrm{d}t' \\ &\simeq N_k(\vec{r}, t)\left(1 - \exp\left(-\frac{\Delta t}{\tau_k}\right)\right) \simeq N_k(\vec{r}, t)\frac{\Delta t}{\tau_k}\,,\end{aligned}$$

where the main approximation is the assumption of a sufficiently small Δt to consider a constant number of excited molecules during Δt and to allow the substitution of the exponential form with its first order series expansion. The net effect in Δt is then

$$\Delta N_k = \Delta N_k^+ - \Delta N_k^-\,,$$

which is summed to $N_k(\vec{r}, t)$ to obtain the number of excited states $N_k(\vec{r}, t + \Delta t)$ at the next time step.

Not all the photons by de-excitation will produce an electron through photo-electric effect. At first, they must have an energy greater than the work function ϕ of the material on which they collide; the energy depends only on the kind of de-excitation

process and is fully deterministic. Secondly, assuming an isotropic source, a "sight-factor" $\Omega(\vec{r},\vec{r}_0)$ will give the portion of photons emitted from $\vec{r}$ and impinging the boundary in $\vec{r}_0$. Lastly, the secondary emission coefficient γ_ν gives the probability of emission of an electron per each photon impacting on the surface. Thus, the number of electrons emitted per de-excitation photon is

$$N_{\mathrm{e}}(\vec{r}_0) = \Omega(\vec{r},\vec{r}_0)\gamma_\nu(\vec{r}_0)\sum_k \Delta N_k^-(\vec{r})\,,$$

where a nearest integer has to be calculated in order to obtain an integer number of electrons.

The generic outcoming electron is isotropically sampled in direction as done for secondary emission by electron or ion impact. Under the hypothesis of a cool emitting surface, the electron energy distribution function is approximately triangular-shaped with $\mathcal{E}_{\mathrm{F}}(T=0)$ as sharp maximum cutoff energy (see Section 6.2.3 for details). Once sampled a random number R_8, the energy is simply given by equation (7.9) as $\mathcal{E} = \sqrt{R_8}\mathcal{E}_{\mathrm{F}}$.

In many cases, the calculation of a precise sight factor is a hard task and a MC ray-tracing procedure is often the only practicable solution. Alternatively, an approximate 0D model can be used, assuming a generic averaged sight factor for all the excited molecules depending on the expected region of maximum concentration.

7.3 Microscopic simulation of PF breakdown

The PIC-MCC code description given in Section 7.1 and Section 7.2 is completely general and, thus, applicable to any particle simulation. On the basis of the theoretical models and experimental data presented in the Chapter 6, the main simulation parameters, assumptions and approximations are hereafter discussed: domain definition, boundary and initial conditions, gas data and interaction models are described and followed by a general flow chart scheme. The reader is referred to Appendix 7.B for more details on the modules dependencies, input and output management and post-processor tool.

7.3.1 Approximations and assumptions

While a one-dimensional radial simulation of the phenomenon would be excessively coarser due to the presence of a finite length insulator and of a cathode back-wall, a two-dimensional (r,z) model appears a worthwhile choice which allows to exploit the axial-symmetry of the electrodes. Although computationally less expensive than a fully three-dimensional simulation, the choice limits a bit the obtainable results (no filamentary structures can be observed since the sheath is supposed azimuthally symmetric).

The simulation domain is depicted in Figure 7.8. All the geometrical dimensions are input parameters and can be modified to account for an insulator sleeve fully or partially inserted in the inner electrode ($s_{\mathrm{ins}} \geq s_{\mathrm{ind}}$), as well as completely lying on it ($s_{\mathrm{ind}} = 0$). The dielectric constant of the insulator material is tunable as input parameter, while both the anode, partially enclosed in the simulation domain, and the cathode are supposed to be perfect conductors. The driving potential is applied

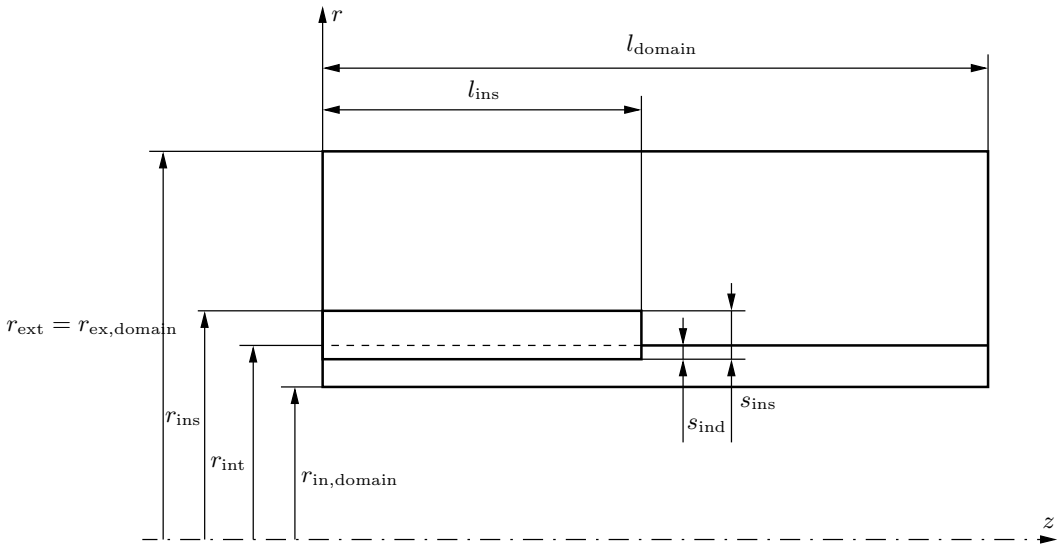

Figure 7.8: Sketch of the 2D simulation domain.

to the anode boundary, while the cathode is supposed at a null reference potential (ground). On the "electrodes open end" contained in the simulation domain, a symmetry boundary condition (both for potential and particles) is applied: if a sufficient part of the electrodes active length is studied, the high-z region can be considered unperturbed, at least, as far as sliding discharge on the insulator sleeve are considered. The boundary condition on the insulator sleeve thickness is more delicate: to derive a correct potential behavior along the radial direction an expanded geometry including a portion of the cathode back-wall has been solved, leading to a good agreement with the $1/r$ function of a cylindrical capacitor [135]. The solution on the corresponding radial section is imposed as boundary condition in the problem of interest, under the hypothesis that the region will be fairly influenced by the space-charge evolution, being bounded between two surfaces with imposed potentials.

A first order approximation of the RLC circuit discharge on a secondary capacitance is supposed (see Section 5.A.2), leading to a linearly increasing driving potential at a rate of $200 \div 500$ V/ns (input parameter), in good agreement both with experimental data and with rough evaluation based on typical electric parameter for PF devices. The anode potential is approximated to the potential of the external circuit, $V(t) = \phi_0^{(t)}$; this assumption is valid until a macroscopic ohmic current short-circuits the secondary capacitance determining a relevant voltage drop on the external circuit main capacitor; the coupling with an external circuit solver is the only way to observe the phenomenon (refer to Section 7.4.1 for a possible implementation).

The filling pressure of the background gas is given in input in Torr and automatically converted in a uniform particle density; moreover, a Maxwellian distribution function at $T = 300$ K (input parameter) is sampled to define the initial conditions for the simulation particles. A uniform spatial density of 0.5 $\text{cm}^{-3}\text{Torr}^{-1}$ is con-

sidered for each charged species [71], corresponding to a number of real particles linearly increasing with the radial coordinate.

The background gas is supposed to maintain an uniform and steady-state distribution, even if, locally, ionization collisions depauperate neutral atoms; since the ionization ratio is less than 10^{-4}, the effect on the collisional frequency computed in the MC module is neglected. Due to the low time-scales of interest, the evolution of the excited states density is neglected (in Section 7.4.3 few details of a possible implementation for transport of excited states is given).

From a strictly numerical viewpoint, few evaluations can be done on the limits for grid spacing and time step.

As shown in Section 7.1.4, PIC models can be considered accurate as far as the grid spacing is maintained lower than the shortest Debye length of the plasma species. A value of $2.5 \cdot 10^{-4}$ m represents a good compromise between accuracy and computational time associated with the Poisson solver of the electric field. Moreover, the relative error of the potential on the computational domain compared with the solution obtained through a finite element solver is everywhere lower than 0.01.

The time-step must respect three main conditions. However, the maximum value $\Delta t = 1/(4\omega_p)$, associated with the plasma frequency of each plasma species, is always larger than the maximum time-step given by collisional considerations: at 1 Torr, the condition $\nu_{max}\Delta t \sim 0.2$ is satisfied by a value of 10^{-5} µs. The Courant-Levy condition is permanently checked at each time iteration and the time-step is adaptively tuned to avoid particles to travel more than one cell per Δt.

7.3.2 Zero-dimensional model for photoelectric effect

Preliminary estimations show that the mean time needed for an ion, created in the region of highest electric field, to impinge on the cathode is greater than tens of nanoseconds: if collisions are neglected and a rise rate of 10^{11} V/s is assumed for an uniform planar gap of $d = 1$ cm, the time-to-impact of an initially stationary ion can be evaluated as $t = \sqrt[3]{6md/(qE_{0,t})} \sim 10^{-7}$ s.

First simulations confirmed the result showing only spurious secondary emissions due to ion impacts, which lead to a non-continuity between the sheath and the cathode preventing the electrode short-circuiting. Since experimental data predict characteristic closure times of the order of tens of nanoseconds, an alternative mean of electrons emission from the cathode had to be investigated. As previously stated in Section 6.2.3, UV photons from de-excitation or external sources can produce electrons through the photoelectric effect when impinging on materials with low work functions (like conductors).

The hypothesis of internal excited states decay as source of photons and secondary electron has been recently confirmed [153]. A zero-dimensional model has been developed to take into account an average global effect and to sample, via MC techniques, a source of electrons from the back-wall of the cathode: since excitation energy threshold is firstly reached in the region of highest electric field (the cathode edge on the insulator sleeve), the excited gas atoms or molecules can be thought localized on the insulator sleeve and following the maximum deposited charge on it (mainly given by the more mobile electrons impacting on its surface). This allows to easily calculate a global approximate sight-factor of the cathode wall from the

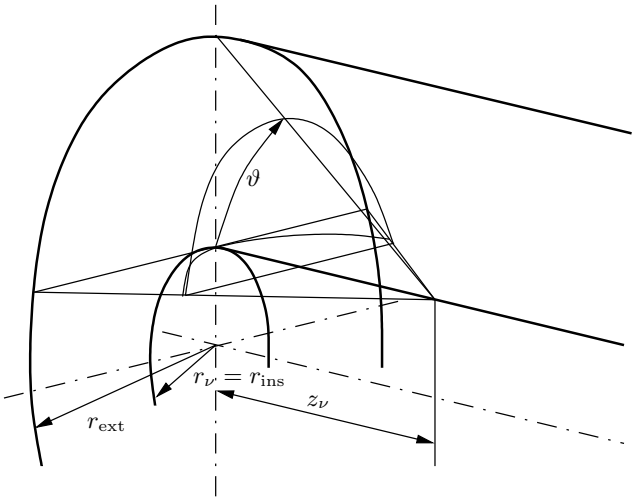

Figure 7.9: Sketch of the closed end of the electrodes and of the pointwise isotropic photon source used to estimate a global sight factor.

pointwise isotropic source: as shown in Figure 7.9, less than one quarter of the photons emitted in 4π are directed towards the wall, depending on the radial and axial position $(r_\nu = r_{\text{int}}, z_\nu)$ of the emitting source. Referring to the notations of Figure 7.9, one can estimate

$$\Omega = \int_0^{\pi} \mathrm{d}\varphi \int_0^{\vartheta_{\max}} \sin\vartheta \,\mathrm{d}\vartheta = \pi \cos\left(\arctan\left(\frac{r_{\text{ext}} - r_{\text{int}}}{z_\nu}\right)\right) = \pi \frac{z_\nu}{\sqrt{z_\nu^2 + (r_{\text{ext}} - r_{\text{int}})^2}},$$

assuming $r_{\text{ext}} \simeq r_{\text{ext}} - r_{\text{int}}$. In seek of a refinement step, one should consider the distance of the source point from the generic element of the cathode wall in order to define a source of secondary electrons to sample as a function of the radial coordinate on the cathode back-wall.

The contribution on the insulator sleeve are neglected due to the high work function of dielectric materials; the effect of photons directed towards the cathode cylindrical electrode is assumed negligible due to the unfavorable sight factor, even lowered if the cathode is made of rods.

An extension to a 2D case should start from a local count of the excited states and decay fractions. The evaluation of a cell by cell sight factor would allow to calculate the cumulate of impinging photons on each radial position of the cathode back-wall and to define a more precise source distribution function. The same could be done for all the boundary surfaces of the simulation domain.

7.3.3 Gas and material data

Argon (Ar) and hydrogen (H_2) have been so far considered as filling gas for gas breakdown simulations. While the first is commonly used in PF devices for x-ray production and material processing [154, 155], the difficulties met to find deuterium

Reaction	Description	Ref.
$e + Ar \rightarrow e + Ar$	Electron elastic scattering	[161, 162, 163, 164, 165]
$e + Ar \rightarrow e + Ar^*$	Electron impact excitation	[159, 166]
$e + Ar \rightarrow e + Ar^+ + e$	Electron impact ionization	[158, 161]
$Ar^+ + Ar \rightarrow Ar + Ar^+$	Ion-neutral charge exchange	[167]
$Ar^+ + Ar \rightarrow Ar^+ + Ar$	Ion elastic scattering	[167]

Table 7.1: Electron and ion collision types in Argon simulations.

cross-sections databases have been overcome with the choice of hydrogen as diatomic low-weight; moreover, hydrogen has been used in the few simulations of the PF device breakdown found in literature [41, 42, 117, 156], which have been used as comparison cases [135]. For the same reason, copper has been considered as conductive material.

The filling gas and conductive/dielectric material are input parameters, at user choice.

Argon (Ar)

Argon is commonly used as filling gas in many PIC-MCC simulations [147, 150, 157]. Hence, it is quite easy to find reliable cross sections data both as tabulated values [157, 158, 159] and as interpolating functions [157, 160].

The ion and electron collisions considered in the MCC module are summarized in Table 7.1.

Since access to tabulated values is a strongly inefficient method from a numerical point of view, analytical interpolating formulae are always preferable. The cross sections in use are represented in Figure 7.10 and in Figure 7.11 for electrons and ions respectively. The electron elastic scattering cross section presents a minimum at low energies, related *Ramsauer* or *Townsend effect*, common to all the noble gases: no good explanation for the phenomenon existed until the introduction of quantum mechanics, which explains that the effect results from the wave-like properties of the electron. A simple model of the collision that makes use of wave theory can predict the existence of the Ramsauer-Townsend minimum. Predicting from theory the kinetic energy that will produce a Ramsauer-Townsend minimum is quite complicated since the problem involves relativistic, electron exchange, and spin polarization effects. However, the problem has been extensively investigated both experimentally and theoretically, and today is well understood []. Here, the inelastic electron collision has to be considered as the cumulate of all the possible excitation processes, having as threshold value the lowest one of $\mathcal{E}_{\text{th}} = 11.62$ eV ($Ar[1s^2.2s^2.2p^6.3s^2.3p^6] + e \rightarrow Ar[1s^2.2s^2.2p^6.3p^5.4s^1] + e$). The data of interest related to Ar excitation threshold energy and characteristic life-time are collected in Table 7.2. Other collisions are possible, but characterized by a multiple de-excitation path, which means an energy of the emitted photons lower than the metal work-function, or by a too high life-time if compared with the time scales of the studied

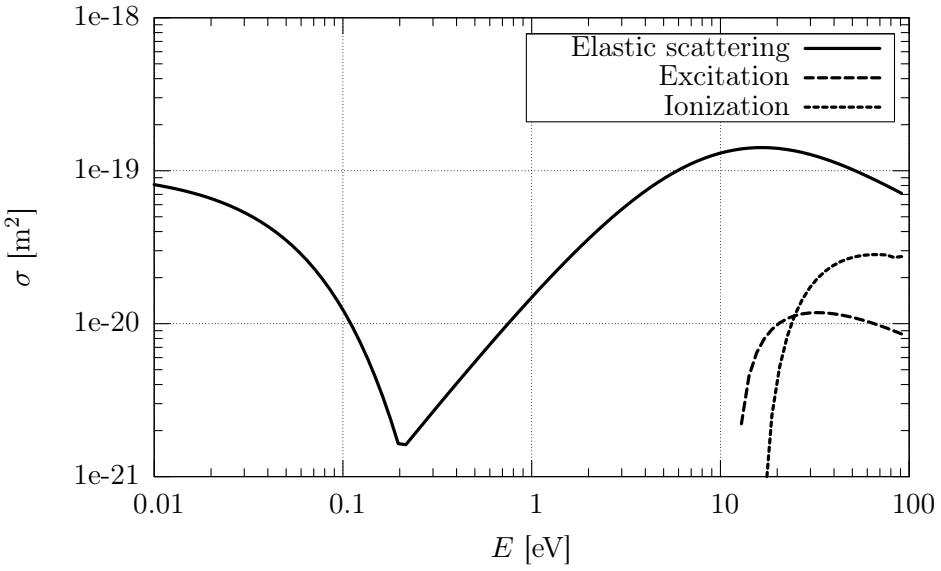

Figure 7.10: Electron-neutral cross section in Argon as obtained by interpolating formulae.

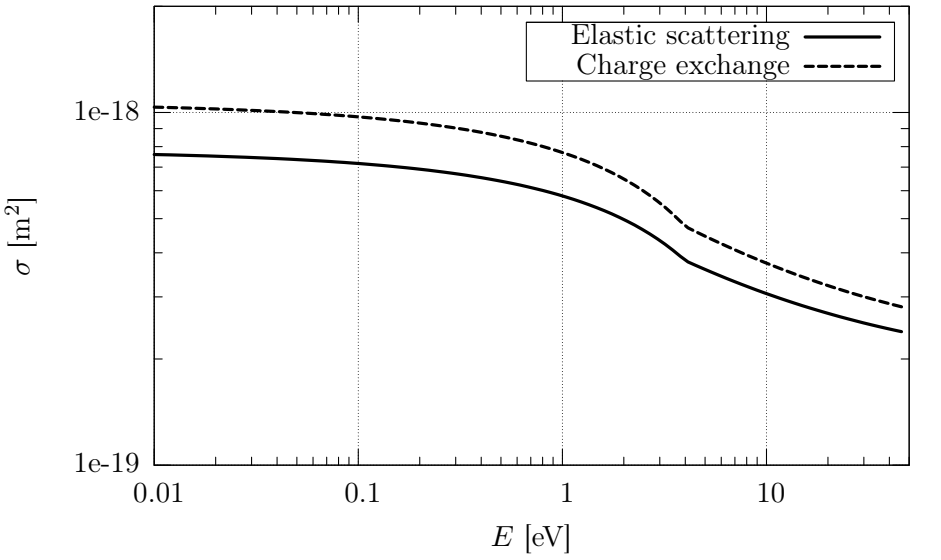

Figure 7.11: Ion-neutral cross section in Argon as obtained by interpolating formulae.

Excitation	$\mathcal{E}_{\text{th}}$ [eV]	τ [µs]
$3s^2.3p^6 \rightarrow 3s^2.3p^5.(2P * \langle 1/2 \rangle).3d^1$	14.30	3.19
$3s^2.3p^6 \rightarrow 3s^2.3p^5.(2P * \langle 1/2 \rangle).5s^1$	14.26	28.6
$3s^2.3p^6 \rightarrow 3s^2.3p^5.(2P * \langle 3/2 \rangle).3d^1$	14.15	3.70
$3s^2.3p^6 \rightarrow 3s^2.3p^5.(2P * \langle 3/2 \rangle).5s^1$	14.09	13.0
$3s^2.3p^6 \rightarrow 3s^2.3p^5.(2P * \langle 1/2 \rangle).4s^1$	11.83	1.96
$3s^2.3p^6 \rightarrow 3s^2.3p^5.(2P * \langle 3/2 \rangle).4s^1$	11.62	8.40

Table 7.2: Argon excitation inelastic scattering collisions of interest and related threshold energy $\mathcal{E}_{\text{th}}$, corresponding to the energy of the emitted photon, and characteristic life-time τ.

phenomenon.

Since only one inelastic scattering cross section is in use, a weighted average of the life-time τ_k has been done on the basis of the excitation cross sections [168] for the reactions listed in Table 7.2: a mean characteristic life-time of $\tau = 5.1$ µs and a mean energy of emitted photons of $\mathcal{E}_\nu = 13.03$ eV is considered in the simulations.

Hydrogen (H_2)

The multiplicity of allowed excited states for the hydrogen molecule makes quite complex the scenario of possible collisions. Many tabulated data has been collected [84, 169, 170, 171, 172, 173], while few interpolating functions have been found, mostly for inelastic processes [174, 175, 176].

The events considered for electron and ion impact are summarized in Table 7.3. Only impacts with ground state diatomic molecules have been considered, neglecting the densities of excited states. Everywhere possible, analytical expressions [174, 175, 176] have been preferred to tabulated data [178].

The cross sections in use are reported in Figure 7.12 for electrons.

In the case of Hydrogen, many excitation processes can be distinguished, even if only few of them are characterized by sufficiently high energies or sufficiently low decay-time: the de-excitation of the $c^3\Pi_u$ and $d^3\Pi_u$ states are considered to be not compatible with the photo-electron secondary emission process.

Conductor and dielectric materials

The insulator sleeve material can be chosen in input. Only SEE by electron impact is considered, with characteristic energies such that $\delta(\mathcal{E}) = 1$ and to the maximum number of secondaries $\delta_{\max}$ and its corresponding energy $\mathcal{E}_{\max}$ (see Section 6.2.3 are input parameters, depending on the chosen material. The surface parameters $k_{s\delta}$ and k_{sw} complete the model presented in Section 7.2.4. No photo-electric effect is considered on the insulator surface, while ion impacts contribute only to modify the deposited charge. The parameters of interest are collected in Table 7.5 for pyrex.

The electrodes and the cathode back-wall inside the vacuum chamber are supposed

Reaction	Description	Ref.
$e + H_2 \rightarrow e + H_2$	Electron elastic scattering	[173, 177, 178]
$e + H_2(X^1\Sigma_g^+) \rightarrow e + H_2^*(B^1\Sigma_u^+)$	Electron impact excitation	[175, 179, 178]
$e + H_2(X^1\Sigma_g^+) \rightarrow e + H_2^*(C^1\Pi_u)$	Electron impact excitation	[175, 180, 178]
$e + H_2(X^1\Sigma_g^+) \rightarrow e + H_2^*(a^3\Sigma_u^+)$	Electron impact excitation	[172, 176, 178]
$e + H_2(X^1\Sigma_g^+) \rightarrow e + H_2^*(b^3\Sigma_u^+)$	Electron impact excitation	[172, 176, 178]
$e + H_2(X^1\Sigma_g^+) \rightarrow e + H_2^*(c^3\Pi_u)$	Electron impact excitation	[172, 176, 178]
$e + H_2(X^1\Sigma_g^+) \rightarrow e + H_2^*(d^3\Pi_u)$	Electron impact excitation	[172, 176, 178]
$e + H_2(v = 0) \rightarrow e + H_2(v = 1)$	Vibrational excitation	[172, 176, 178]
$e + H_2(j = 0) \rightarrow e + H_2(j = 2)$	Rotational excitation	[172, 176, 178]
$e + H_2 \rightarrow e + H_2^+ + e$	Electron impact ionization	[174, 171, 178]
$e + H_2 \rightarrow e + H + H^+ + e$	Dissociative ionization	[175, 181, 178]
$H_2^+ + H_2 \rightarrow H_2 + H_2^+$	Ion-neutral charge exchange	[169]
$H_2^+ + H_2 \rightarrow H_2^+ + H_2$	Ion elastic scattering	[169]

Table 7.3: Electron and ion collision types in Hydrogen simulations.

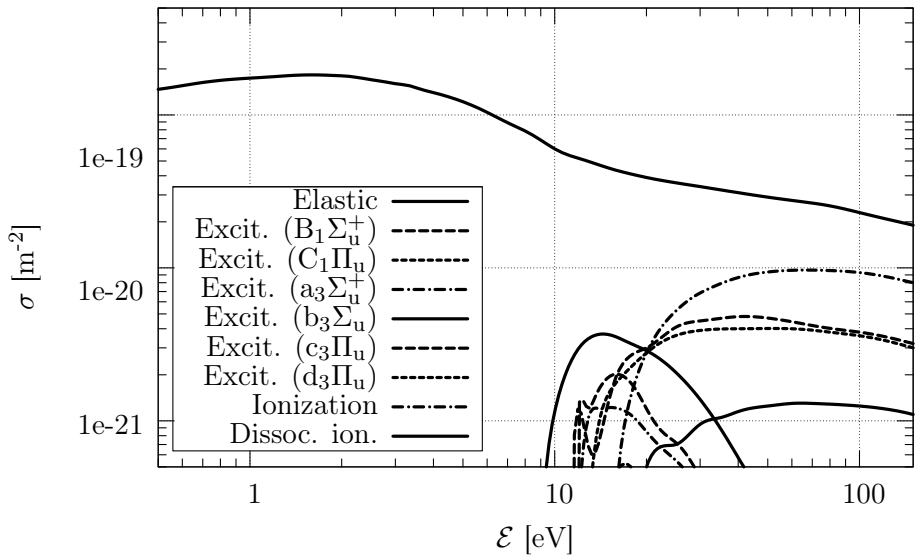

Figure 7.12: Electron-neutral cross section in H_2 as obtained by interpolating formulae and tabulated data.

Excitation	$\mathcal{E}_{\text{th}}$ [eV]	τ [ns]
$X^1\Sigma_g^+ \rightarrow B^1\Sigma_u^+$	11.37	0.8
$X^1\Sigma_g^+ \rightarrow C^1\Pi_u$	12.41	0.6
$X^1\Sigma_g^+ \rightarrow a^3\Sigma_g^+$	11.90	11.1
$X^1\Sigma_g^+ \rightarrow c^3\Pi_u$	11.89	10^6
$X^1\Sigma_g^+ \rightarrow d^3\Pi_u$	13.98	68.0

Table 7.4: Hydrogen excitation inelastic scattering collisions of interest and related threshold energy $\mathcal{E}_{\text{th}}$, corresponding to the energy of the emitted photon, and characteristic life-time τ.

Parameter	Value
Work Functions (ϕ)	11.34 eV
Dielectric relative constant (ϵ_{r})	5.0 eV
SEE lower energy ($\mathcal{E}_{\text{inf}}$)	40.0 eV
SEE higher energy ($\mathcal{E}_{\text{sup}}$)	2400.0 eV
SEE energy of maximum ($\mathcal{E}_{\text{max}}$)	350.0 eV
SEE maximum number of secondaries (δ_{max})	2.3

Table 7.5: Dielectric material properties for pyrex.

Parameter	Value
Work Functions (ϕ)	4.65 eV
Secondary emission coefficient for ions (γ_{i})	0.15
Secondary emission coefficient for photons (γ_ν)	0.075
SEE lower energy ($\mathcal{E}_{\text{inf}}$)	200.0 eV
SEE higher energy ($\mathcal{E}_{\text{sup}}$)	1500.0 eV
SSE energy of maximum ($\mathcal{E}_{\text{max}}$)	600.0 eV
SEE maximum number of secondaries (δ_{max})	1.3
Fermi energy ($\mathcal{E}_{\text{F}}$)	7.0 eV

Table 7.6: Electrodes material properties for copper.

made of copper, even if, in many cases stainless steel or copper-beryllium alloys are used. The secondary emission coefficients strongly depend on the surface status: they are listed in Table 7.6 for ion impact, photo-electric effect, and electron impact. Other secondary emission processes, as listed in Section 6.2.3, are evaluated to be negligible in the initial phase of the electrical breakdown in typical PF devices.

7.3.4 Flow chart

The global flow-chart of the developed code is represented in Figure 7.13. After the initialization module, the classic scheme of a PIC-MCC is followed with collisional instants evaluated for each particle during the main loop. An hybrid counting sort technique, fully described in Section 7.A.1, is used to accelerate the code and to obtain a particles array sorted by cell at each time-iteration. This is useful to call the merging and splitting technique which will be presented in the next chapter. A detailed description of the modules and file contents can be found in Appendix 7.B.

7.4 Future improvements

The here presented PIC-MCC code contains many well tested techniques and methods employed in particle plasma simulations. Particular care has been devoted to the correct description of the binary collisions and to the complete treatment of the surface interactions considered of interest for the problem under examination. Innovative techniques for the particle control, surface events statistical enhancing and variance induced noise reduction will be presented in the next chapter. Hereafter, few consolidate advanced numerical add-ons are described being under study as possible future improvements.

7.4.1 Coupling with an external circuit

An external circuit model can be coupled with the Poisson's equation solver [134, 182]. The model presented in Section 7.1.2 remains unchanged as well as the specified Dirichlet and Neumann boundary conditions.

Supposing the driven electrode a perfect conductor, the potential $\phi_0^{(t)}$ on it is equal to the voltage drop on the external circuit side. The electric field, normal to any conductor, is proportional to the surface charge density through $E_{\widehat{n},ij} = \sigma_{ij}/\epsilon$, which, in a discretized form, results in

$$E_{i,1/2}^{(t)} = \frac{\phi_0^{(t)} - \phi_{i1}^{(t)}}{\Delta x_j} = \frac{\sigma_{i0}^{(t)} + \rho_{i0}^{(t)} \Delta x_j/2}{\epsilon} \,.$$

Since the surface charge σ_{i0} can be considered immediately redistributed on the conductor surface, the total surface charge density $\sigma_{\text{tot}} = \sum_{\text{el.}} \sigma_{i0}$ time variation depends on the deposited charge on the electrode as current $I(t)$ flowing in the external circuit and convective current density $J(t)$ deposited at the boundary by charged particles:

$$S \frac{\mathrm{d}\sigma_{\text{tot}}}{\mathrm{d}t} = I(t) + SJ(t) \,,$$

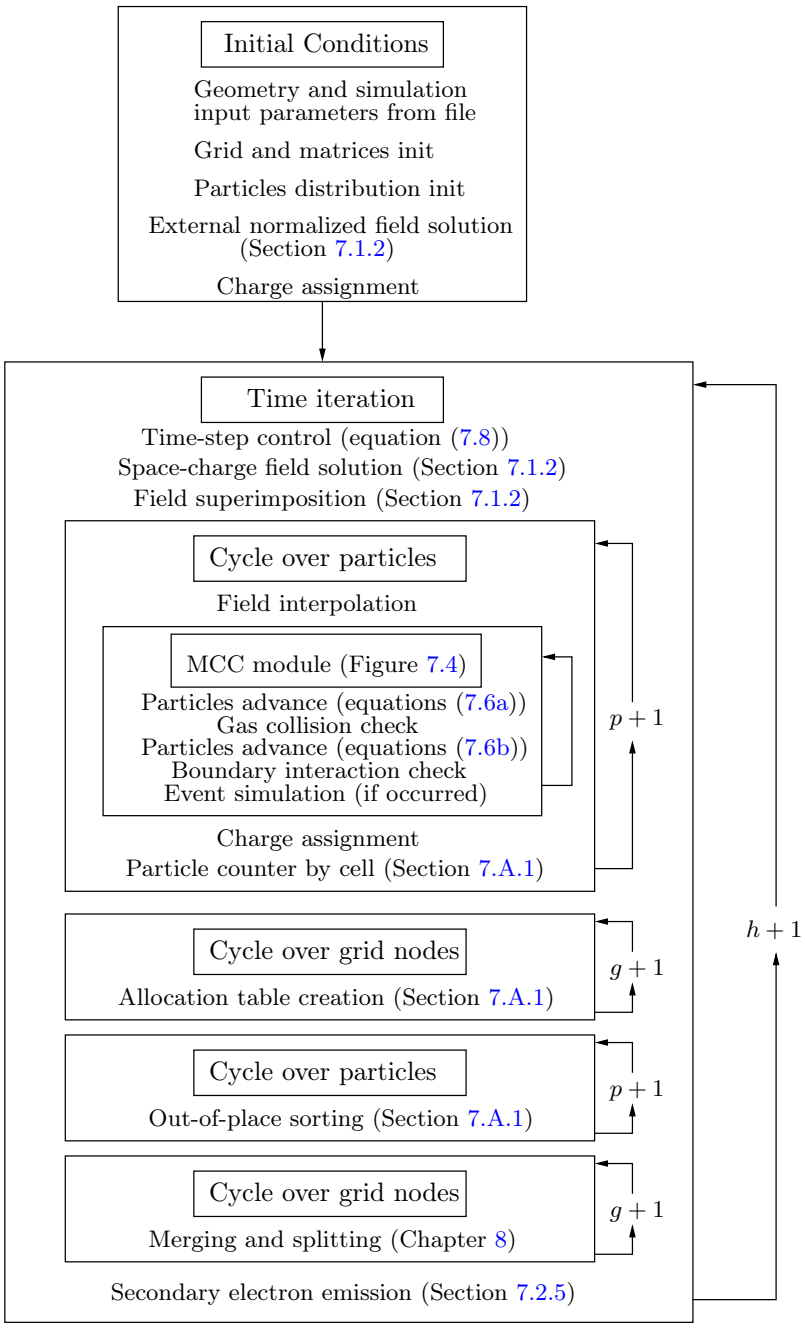

Figure 7.13: Flow chart of the developed code.

finite differenced in

$$S\sigma_{\text{tot}}^{(t)} = S\sigma_{\text{tot}}^{(t-1)} + I^{(t)} - S\sum_{t-\Delta t}^{t} J^t \,,$$

A general RLC circuit evolution can be studied solving the coupled equation for the charge Q

$$L\frac{\mathrm{d}^2Q(t)}{\mathrm{d}t^2} + R\frac{\mathrm{d}Q(t)}{\mathrm{d}t} + \frac{Q(t)}{C} = V(t) + \phi_J(t) - \phi_0(t)$$

(for a discharging capacitor the voltage source $V(t)$ is zero for $t > 0$). The potential drop $\phi_J - \phi_0$ between the electrodes can be then computed starting from the total charge $\sigma_{\text{tot}}^{(t-1)}$, the charge on the capacitor $Q^{(t-1)}$ and the deposited charge $Q_{\text{conv}}^{(t)}$ by plasma interaction.

A single second-order backward difference equation is obtained, having the property of being stable over all values of numerical and real physical parameters.

7.4.2 Null collision

A more efficient [150, 183] method to study the collisional events needs a sufficiently low simulation time step, such that a negligible probability exists for a particle multiple scattering in the same Δt. If collisions characterized by a nearly null energy loss (e.g. elastic scattering with a high mass target), the probability of N_{coll} collisions in a time interval Δt is given by $P_{\text{coll}}^{N_{\text{coll}}}$, being

$$P_{\text{coll}} = 1 - \exp(-n_{\text{g}}(\vec{r})\sigma_{rmtot}(\mathcal{E})v\Delta t)$$

the probability of collision in a time step for a particle having energy $\mathcal{E}$. Thus, the total number of possible missed collisions is

$$N_{\text{miss}} \sim \sum_{j=2}^{\infty} P_{\text{coll}}^{j} = \frac{P_{\text{coll}}^2}{1 - P_{\text{coll}}} \,.$$

Being usually $P_{\text{coll}} \ll 1$, then $N_{\text{miss}} \sim P_{\text{coll}}^2$ provides a measure of the under-representation of the approximated collision operator. Once fixed

$$\nu_{\text{tot,max}} = \max_{\forall E, \forall \vec{r}} \{n_{\text{g}}(\vec{r})\sigma_{\text{tot}}(\mathcal{E})v\}$$

as the maximum collision frequency over all the possible energies and positions (assuming n_{g} varying with position, see Section 7.4.3), the discussed PIC-MCC method is constrained by the supplementary condition $\nu_{\text{tot,max}}\Delta t \ll 1$, which must be added to those discussed in Section 7.1.4.

The alternative approach to the collisional time sampling strongly reduces the computational time needed to study the particle histories making the method convenient even if requiring a smaller time step of that strictly needed by the PIC module. The computational effort can be further reduced, if the so called *null collision* is used. A fictitious collision frequency can be added to $\nu_{\text{tot}}(\vec{r}, \mathcal{E})$ in order to have a constant ν'_{tot} over the space and energy. The total number of particles undergoing collision is

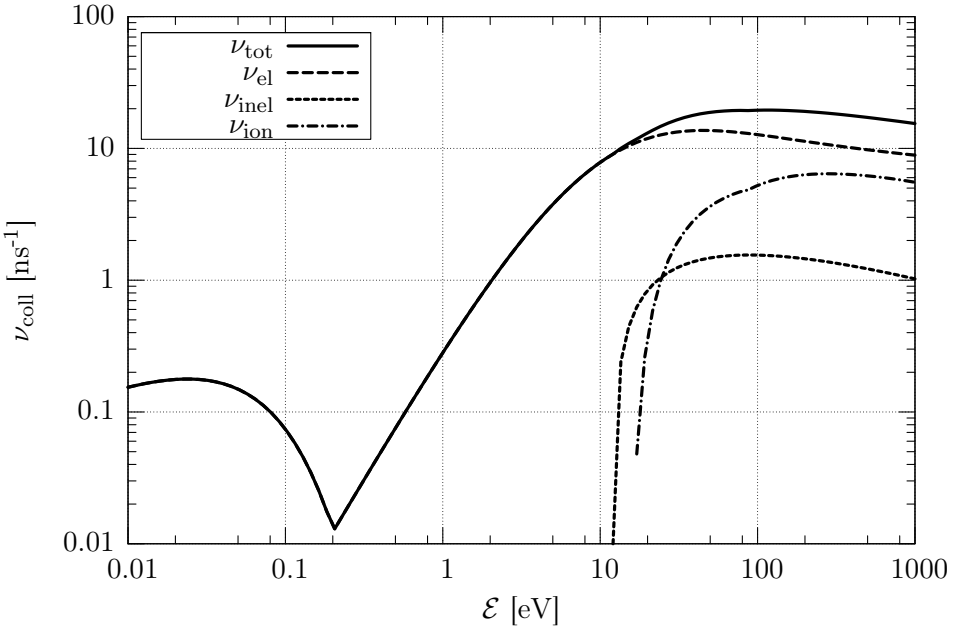

Figure 7.14: Electron-neutral collisional frequencies for Argon at 1 Torr.

then given by $NP_{\max} = N(1 - \exp(-\nu'_{\mathrm{tot}}\Delta t))$, which can be randomly chosen from the particle list. For each of them the cross sections at the corresponding energy are calculated and the collision is chosen as described in Section 7.2.3 taking into account also the null-collision probability, related to the added fictitious collision frequency. In Figure 7.14, the collisional frequencies for Ar (single types and total) is given at a pressure of 1 Torr as an explanatory example (refer to Figure 7.10 for cross sections behavior).

This method avoids the need of computing the particle energy and all its cross sections for all the studied particles, limiting these time consuming operations only to the subset of randomly picked particles. Even in this case the method is efficient only if the number of colliding particles is small with respect to the total number of particles in the system, which means a small value of $\nu'_{\mathrm{tot}}\Delta t$.

If the cross sections are strongly variable with energy[5] (or space) the null-collision efficiency can be further improved by introducing ranges on which a local and rather constant null-collision frequency is defined.

7.4.3 Radiation transport

When larger time-scales are involved, the evolution densities of the excited and background species must be followed [184]. The transport of the fluid species is solved through a propagator method [185] with characteristic time interval such

[5]It's the case of Ar, characterized by the Ramsauer minimum in the elastic scattering cross section

that $\Delta t < \Delta t_* < \Delta t_g$, where the time steps are related to the characteristic time scales of the charged particles in the classical PIC, of the excited species and of the neutral one.

The excited state density is given by the solution of

$$\frac{\partial}{\partial t} n_*(\vec{r}, t) + \nabla \cdot \vec{\Gamma} = S(\vec{r}, t) - \frac{n_*(\vec{r}, t)}{\tau} + \frac{1}{\tau} \int n_*(\vec{r}', t) G(\vec{r}, \vec{r}') \, \mathrm{d}\vec{r}' \,,$$

where n_* is the excited state density, $\vec{\Gamma}$ the flux of the excited molecules and τ the radiative decay frequency. The function G is the kernel of the radiation transport, while S represents the source of excited species, already discussed in Section 7.2.5, coupled to the MCC module and PIC grid.

The spatio-temporal discretized form of the equation can be numerically solved for each excited species, usually considered to decay into the ground state. It results in a time dependent and domain distributed isotropic and multi-energetic source of photons. The definition of a rough model for the photons transport and for the geometrical efficiency related to their impinging on the surfaces is advisable for a more detailed study of the SEE.

7.4.4 Parallelization and AMR

The recent development of parallel computing techniques has improved the performances in many field of numerics. A PIC-MCC code is amenable of performance enhancement since it involves a large number of brief calculations which require primarily localized data. Great care must be devoted to the decomposition choices in order to achieve a good *load balancing*.

Three main approaches can be devised:

- *particle decomposition*: the whole spatial domain is assigned to each node which completely solves a subset of particles; the load balancing is intrinsic and no communication is needed for interface-crossing particles. Notwithstanding, all the field properties must be common to each node with an useless waste of memory; the charge assignment and the electric field solution are computed locally, but each contribution must be communicated to all the nodes for superimposition before the particle advance at the next time step.

- *domain decomposition*: different portions of the domain, together with the particles properties and fields on them, are assigned to different nodes; the memory consumption is limited since the data are localized, but the field solution needs the communication of the data of the *ghost regions* between the different nodes, as well as the communication of the particles crossing the virtual interfaces of the decomposed domain is needed before their advance. The number of sub-domain scales with the number of nodes: the spatial extension decreases while the particle communications increase.

- *domain cloning*: it gathers the main advantages of the domain and particle decomposition, but it is suited only for clustered SMP computers. The first approach is used inside the same node in order to exploit the shared memory to accelerate the particle and ghost regions communication; the second, instead, is used on the different nodes.

The particle decomposition method (commonly used in MC codes) is the simplest way to transform a serial code into a parallel one. However, it is evident how much a similar choice would be ineffective for a PIC-MCC code. The domain decomposition requires a heavy programming effort, since the processes of interest are usually non-stationary and the decomposition should be often redefined following the regions with high particle densities and determining an unbalanced field solution. The merging and splitting techniques proposed in the next Chapter could be of interest to keep artificially uniform the number of particles in each region.

Nevertheless, in many cases, an increase in the particle densities and energies requires a refinement of the mesh due to the limiting conditions presented in Section 7.1.4. The *Adaptive Mesh Refinement* (AMR) would hence be a good solution: the domain is decomposed and the mesh adaptively refined in the regions of highest density through the definition of mesh patches on different levels of refinement. Moving from the finest to the roughest level, each cell is analyzed and labeled on the basis of a refinement criterion, usually based on the particle density or on the gradient of a particular property. Usually the cells of interest are regularly distributed but the new patches must be initialized and organized in order to make sufficiently easy both the vertical passage between levels and the horizontal one between communicating patches.

The package of Fortran 90 subroutines PARAMESH [186] is under study to extend the developed serial code into a parallel code with AMR.

7.A Accelerating techniques

A number of schemes have been implemented to improve performances of particle simulations. The most common strategy is to exploit a basilar feature of particle simulations, involving a large number of simple calculations (rather than one for each particle). On the other hand, this requires primarily localized data. The parallel computing is only one side of the solution, since this peculiar feature can be exploited even on modern commodity workstations in order to enhance the cache-hits from L2 cache memory. A consolidate and employed technique will be described as well as common high performance computing hints in scientific applications. A quick sight will be finally drawn on the possible parallelization techniques and domain decomposition and refinement.

7.A.1 Hybrid counting sort

The memory subsystem of modern commodity workstation (main memory - L2 cache - L1 cache - ALU registers) and cache-trashing during the advance and accumulate procedure are known to severely limit the speed of PIC simulations.

Caches store recently used data through a paging techniques, responding to memory transactions faster than main memory. Data requested by the CPU and found in cache are called “cache-hits”; most processors automatically decide which data are to be stored for future transactions (*prefetching*) transferring to the cache entire blocks of data occupying continuous addresses on the main memory. Hence, randomly accessing large amounts of data (as in the case of particles stored in an array and accessed according to the position occupied on the mesh) increases cache-trashing

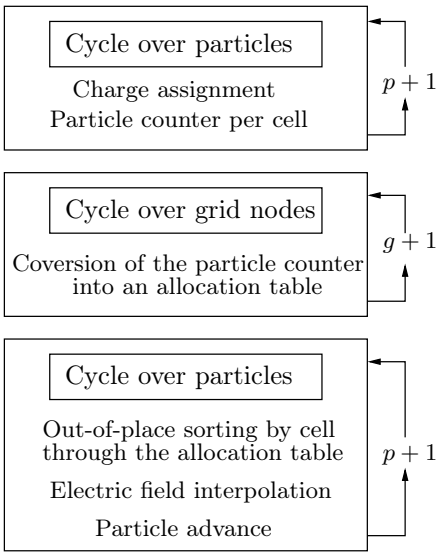

Figure 7.15: Schematic flowchart of a hybrid counting sort procedure.

lowering performances.

However, an out-of-place[6] counting sort algorithm can be implemented in order to keep the particle array following the same order of the mesh elements. A counting sort is an algorithm for sorting N elements into M different baskets (order-N in time and order-M in auxiliary storage) [187]. Recent developments have enhanced the power of the method by hybridizing its two main steps (counting and sorting) in the particle advance and particle accumulation procedures, resulting in a performance increase of $\sim 80\%$ for benchmark cases [188].

The main idea, shown in Figure 7.15, is to count the number of particles per cell during the particle accumulate cycle (where the mesh cell must be deduced from the particle position to accumulate its charge on the grid), to convert the counting array into an allocation table in a dedicated loop on the mesh nodes, and to sort the particle array (out-of-place) during the particle advance (the interpolation of the electric field needs the cell nodes corresponding to the particle position).

In the present case, as it will be discussed in more detail in the next chapter, the sort is done, not only for speed enhancement, but also to apply other algorithms needing an exactly sorted particles array. The coupling with an MCC module and the bounded system under analysis produce particle losses and sources, which force to keep the count updated. This limitations make the method a bit slower due to the increase of memory traffic, but it still results faster than sorting particles in an independent routine.

[6] The out-of-place sorting increases the necessary memory of, at least, one more particle array on the total of species.

7.A.2 High performance computing hints

As it will described in the next chapter, the code is entirely written in *Fortran90*. Few features of the object oriented programming have been exploited and particular care has been devoted to the optimization of memory management and access.

The data related to the simulation particles (statistical weight, position, velocity and other support parameters) are collected in user-defined data-type and stored in dynamically allocated array of fixed size. All the data needed in many particle loops (charge assignment, advance, collisions) are stored in contiguous block of memory avoiding multiple access memory and cache trashing. The particle losses and creations are treated respectively by transferring an element from the end of the array to the position left void or by adding a new element to the array tail, without any swap operation. This method is preferable to the commonly used *linked-lists* [189], since more effective from the point of view of memory management. The choice perfectly matches the basis of the hybrid counting sort described in the previous section.

To avoid useless numerical operations, all the data analysis has been deferred to a post-processing tool (see Section 7.B.3 for a detailed description). Raw data are written in binary format to output files to avoid expensive format conversion operations; this allows to highly reduce the disc access times and the occupied space, also enabling any desired estimation of microscopic or macroscopic properties.

All the data necessary to restart the simulation are periodically written onto a *dump-file* creating a complete check-point; feeding in the file as input, the simulation can be easily recovered if a forced or wanted break stopped it.

7.B Description of the code

The code development is not to be considered at its end, but a sufficiently mature version has been reached. A detailed description of the file contents and modules dependencies will follow, in order to make the code usability and future improvements as easy as possible.

7.B.1 Directories and files

The main root of the directories structure contains the following sub-directories:

- `src` collects all the source files (`.f90`, `.mod`, `.o` and a local `Makefile`);
- `input` contains an example for the input file;
- `output` is the default directory for the output files (can be changed in input);
- `data` collects the cross sections libraries and the chemical properties tables for the gas and both the insulator and electrodes materials used for the simulation (at present, only molecular Hydrogen and monoatomic Argon).

An install script and a dedicated Makefile are also at disposal in the main directory. The last one refers to the Intel Fortran Compiler for Linux platforms to resolve dependencies between modules (`install` option) and to generate the executable file

(`all` option) in the root directory, exploiting the inter-procedural, floating-point operation, processor specific and fine tuning optimizations [190, 191]; in addition to the classic `cleanobj`, `cleanmod` and `cleanall` modes, a `debug` option allows to compile the program enabling all the format, array-bounds and floating-exception checks and adding a route to traceback any segmentation-fault error (no optimization option is available).

The modules, and related files, dependencies are shown in Figure 7.16, while the files contents will be readily described.

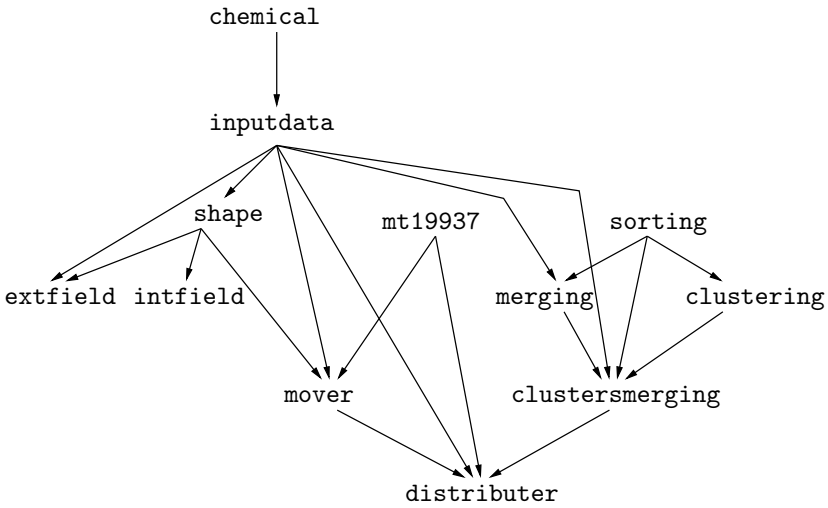

Figure 7.16: Source files and modules dependencies.

7.B.2 Source files and code structure

A Main file contains the program declaration, while all the others (with the exception of a single-subroutine file for the matrix problem solver) define the various modules in use. Each module is related to a particular numerical or physical aspect (as described below); it contains all the variable declarations together with a proper set of subroutines and functions.

All the subroutines and the main variables names have a five characters prefix to denote the module in which they have been declared. The prefix has the form `MNnn_`, the first character standing for "Module", the following three being an unique identifier for the module name with an upper case first letter "`Nnn`"; the last character, "`_`", separates the prefix from the variable name. Usually, a single, lower case character precede the main variable name to identify its kind, following the notation presented in Table 7.7

`Main.f90`

The main file contains the program structure definition. Within this file, several simulation parameters are defined, all the matrices and arrays for particles and

Character	Meaning
i	integer
f	real (float)
d	double precision
c	character
l	logical

Table 7.7: Variable name prefix character used as kind identifier.

fields properties are allocated and the main functions for initial condition and time iteration control are implemented.

`chemical.f90`

This file contains a single module directed to retrieve from proper tables in the `data` directory all the chemical properties of the filling gas and of the insulator and conductor materials.

`inputdata.f90`

The module contained in the file is called at the beginning of the code for the main simulation parameters input read (both from file or by user input). In this module all particles, materials and device properties are defined, in order to make them easily available to all the other modules.

The module also contains a subroutine for the creation of both the spatial and the temporal grid, and another one for the initial mapping of the dielectric relative constant on the grid.

`randomgen.f90`

The file contains excluding modules based on different (Pseudo)Random Number Generator ((P)RGN). The most tested one is the Marsenne-Twister 19937 RNG recently developed by M. Matsumoto and T. Nishimura [192, 193, 194]. The module, freely distributed under the GPL license, implements a fast and efficient generator (most of all for systems with pipeline and cache memory) with far longer period and higher order of equidistribution than other available generators (the period is proved to be $2^{19937} - 1$ and 623-dimensional equidistribution property is assured). Since the choice of the RNG is crucial in MC codes, other known generators have been tested and left available as alternative modules: the `ran1()` generator from Numerical Recipes for Fortran90 based on the Lagged-Fibonacci and coupled with two Marsiglia shift sequences (period of $8.5 \cdot 10^{37}$) is known to be a fast and reliable choice for scalar code versions [195, 196]; for future parallel versions of the code the SPRNG (Scalable Parallel Random Number Generators) library designed for scalable and distributed architecture has been implemented [197, 198].

`shape.f90`

`Shape` is the module dedicated to the computation related to the "numerical shape" used for the interpolation scheme (see Section 7.1.1). The module contains the subroutines, needed for charge assignment to grid nodes and field interpolation from nodes to particle positions; the zeroth (Nearest Grid Point - NPG) and first order (bilinear area weighting and Cloud In Cell - CIC) schemes are available to the user.

`intfield.f90`, `extfield.f90`

Within these modules are defined all the subroutines for the coefficient matrix definition used in the self-consistent and the external field solvers respectively (see Section 7.1.2). The `extfield` also contains a subroutine to calculate the potential applied to the electrodes through the external circuit.

`mover.f90`

The file is one of the most complex in structure. It implements both the particles advance (Section 7.1.3) and the collisional functions (described in Section 7.2.3 and Section 7.2.4). The collision probability is computed from the cross sections tables in a proper subroutine, then a random number is extracted to determine the collision type. After moving the particle in the main subroutine of the module, proper calls to subroutines for boundary check and collision event estimators are defined to treat correctly the motion of the particle.

`sorting.f90`, `clustering.f90`, `merging.f90`, `clustersmerging.f90`

This set of files contains multiple modules used for particle clustering and merging procedures. The reader is referred to Chapter 8 for a more detailed description of the modules and for a dedicated flow-chart. The merging and splitting procedures are here considered a sort of black-box.

`distributer.f90`

The `Distributer` module defines the initial distribution function for charged particles (both in position and velocity space) and is called for dynamic control of simulation particles number. The main subroutine (`LocalReshape`) sorts the particles by cells through the hybrid counting sort, as described in Section 7.A.1. If a cell is found to have a number of particles greater than an optimum number, the merging technique is called. Similarly, if a cell undergoes an excessive depletion, the splitting procedure is called instead. The thresholds for these checks are not general but they have to be specifically tuned for the application of interest (as input parameters).

`photo.f90`

The `Photo` module collects all the subroutines necessary to evaluate the variation of excited molecules and their impinging fraction on the back-wall cathode surface in order to evaluate the number, the statistical weight and the energy distribution function of emitted electrons through the photoelectric effect.

`plotter.f90`

The last module contains all the output operations: it includes several subroutines for formatted and unformatted data output. By default, raw binary data of the simulation particles (positions, velocities and statistical weight) are printed every n_t time-steps, with n_t at user choice. While the external field is printed only once in a normalized form for a 1 V applied potential external, the potential induced by the space-charge (as computed by the code on the grid) is written in unformatted form every n_t time-steps. The collisions with boundaries and neutral gas are monitored at each time-step in two proper formatted output files, as well as the time-evolution of the excited states and photo-electrons. All the simulation parameters (iteration, time-step, time instant, number of simulation and real particles for each species, ...) are available in a specific formatted file. Finally, at each n_{dump} time-step a dump file containing the last checkpoint is created (or overwritten) in binary format.

7.B.3 Post-processor

A particle code gives information about the microscopic properties of the simulation particles, which would be impossible to examine in details. Hence, macroscopic informations have to be generated in order to facilitate an analysis of the results. A suite of post-analysis subroutines in Fortran90 has been combined with a bash-shell script to readily manipulate the unformatted output files and produce scientific plot of the physical quantities of interest.

Few advanced features of shell-scripting [199] have been exploited to check the directory paths and the files conformity under a set of input parameters chosen by the user. Proper temporary files are created and fed into the compiled version of the optimized analysis procedures. Mainly, the following quantities are derived from the particle raw data:

- time-evolution quantities: growth of simulation and real particles numbers, collisional frequencies for each collision type, frequency of boundary interactions, excited states, contributes to secondary emission particles; mean energy, mean velocity components; current and voltage;
- distribution functions: energy distribution function of all the species and their comparison with Maxwell-Boltzmann, Druyvesteyn and Margenau distribution functions (see Section 6.1.2); velocity distribution functions (velocity components, planar velocity, direction of flight);
- meshed maps: number of particles/density per cell, mean energy/energy density per cell, number of simulation particles per cell, Debye length and plasma frequency; charge density distribution, external electric potential, space-charge potential, total potential, electric field components;

for each of them a plot is generated through the command-line driven data and function plotting *Gnuplot* freeware utility [200].

The plot can be produced for a single time instant investigation or for a sequence of multiple equally spaced iterations. In this case, the user can choose to automatically create an animation of the color or contour maps combining a sequence of gif frames.

The developed tool is quite simple to use and provided with a short-help on input parameters and default values, automatically displayed in case of inconsistencies. More graphical formats are available for plots. The modularity of the analysis procedures makes the tool easy to be extended.

CHAPTER 8

Merging and splitting techniques

Abstract. PIC simulations require large machine-time to process particles charge assignment and motion. Moreover coupling such methods with MCC modules causes another expensive computational cost to simulate particle collisions with background gas and domain boundaries. Merging many particles in few particles with increased weights is a widely used accelerating technique. A merging procedure based on charge conservation on a spatial 2D domain is here proposed to avoid an exponentially increasing number of particles per cell during the simulation. Particular attention will be devoted to the particles selection, through a clustering procedure extended to the phase space. If coupled with a splitting technique, the method reveals itself efficient to increase performances of both PIC and MCC module reducing noise in electric field solution, making more uniform the variance on the distribution functions and increasing samples representativeness in stochastic calculations.

8.1 Introduction

Many simulation particles control procedure have been developed for kinetic simulations. The concept of importance, or statistical weight, of Monte Carlo techniques has been successfully extended to PIC codes in order to limit the number of simulation particles used to represent the whole system. On the contrary, regions where the number of particles diminishes could be characterized by a bad representativeness of the statistical sample and be affected by numerical noise. In these cases, a splitting technique could help allowing to increase the number of particles decreasing their importance. The intuitive concepts here proposed can be better formalized from a physical and mathematical point of view.

8.1.1 Particles number control techniques

The PIC method is based upon super-particles (or simulation) particles, which represent an ensemble of many real particles. A weight w, equal to the number of real particles represented by the super-particle, can be assigned to each simulation particle in order to account for the total charge of the collapsed ensemble and to preserve the charge-mass ratio q/m.

PIC codes require considerably large computation time, since it scales with the number of particles N, which must be kept sufficiently high to reduce the simulation noise (proportional to $1/\sqrt{N}$) [43]. In the case of plasma discharge evolution, the number of charged particles increases exponentially, varying typically of several orders of magnitude. This consequently leads to an increasing computation time demand. When the number N of super-particles grows rapidly, a way to improve considerably the simulation speed is the reduction of N with a consequent increase of their weight w. Such a procedure has to be performed without the violation of charge and energy conservation laws.

A first rough approach could be based on a typical variance reduction technique of the Monte Carlo methods, called *russian roulette* [141]. When a threshold for N is reached, a survival probability P_s is defined as the ratio between the reduced number N' of super-particle and the actual number N. Cycling on the N simulation particles, a survival probability P_s will be common to each one and a random number R will be extracted from a pseudo-random sequence to check if the particle will die or survive (by comparison with P_s). Moreover, each survived particle ($\sim N'$ in total) will have an increased weight $w' = wN/N'$. The total charge will be globally conserved if the sample of particles is sufficiently large. Nonetheless, little fluctuations in the mean energy of the charged particles can be observed, since the technique is careless of their energy; locally, any conservation law is not satisfied: lower is the number of particles per cell, greater is the induced error. Finally, the technique isn't optimal from the point of view of the MCC module: if a region of space undergoes a depletion of particles during the simulation, the application of the russian-roulette will further decrease their density and, consequently, the statistics associated to the possible events will result poorer and poorer. Similar techniques, applied with different survival probabilities P_s on three portions of the energetic axis, were successfully employed to study the avalanches and streamers formation and evolution in the electrical breakdown in gases [123, 124, 126], where

the simulation domain was relatively small and entirely occupied by the discharge.

In the past, particle splitting and shifting methods were developed in one-dimensional systems [118, 201] to overcome the usual problem of particles rise and contemporaneous depletion in the cathode fall region. This method was based on the separation of the particle into two species for the bulk and cathode regions of the system: large-weighted particles are used in the bulk and small-weighted ones in the depleted region. The net effect is a speed-up of the simulation and a reduction of spurious fluctuations.

Shon *et al.* [202] presented an alternative approach aimed, not only to satisfy the conservation laws, but also to reduce the time of simulation. If the particle number reaches the limit suggested by a certain criteria, new large-weighted particle species are created by meshing the phase space. The particle number is reduced without discriminating the bulk and cathode fall region. The method was extended to two-dimensional systems: at least two new super-particles are necessary to merge the particles of a cell in order to conserve the charge densities on the nodes of the grid. Lapenta [203], instead, proposed binary and ternary procedures for particle rezoning in collisionless PIC with generic spline weighting functions.

In the next section, an analysis of a merging technique for the bidimensional spatial coordinates of the phase space is presented together with an interesting analogy with well-known mechanical properties. Only the PIC bilinear interpolation weighting is studied in this first stage, since it can be successfully applied both in cartesian and cylindrical coordinate systems.

8.1.2 Conservation rules

As shown in Section 7.1.1, all the physical quantities related to the particles are weighted on the grid points through the so called shape factor. All the moments of the particle distribution on the grid points are easily defined by [203]

$$M_g = \sum_p q_p S(\vec{x}_g - \vec{x}_p)\vec{f}(\vec{v}_p)\,,$$

where q_p is the particle charge and $\vec{f}(\vec{v}_p)$ is a generic function of the particle velocity. In particular, when $\vec{f}(\vec{v}_p) = 1$, $\vec{v}_p$ and $\vec{v}_p\vec{v}_p$ one obtains the charge density, current density and pressure tensor respectively.

In kinetic PIC codes, the equivalence between two sets of particles is based on two conditions:

1. the two ensembles equally contributes to the grid moments appearing indistinguishable;

2. the two sets sample the same velocity distribution function.

In electrostatic codes, the only moment involved in electric field calculation is the first order one: in other words, if a set of N particles has to be merged in a set of $N' < N$, the contribution to charge density on grid points must be the same for the two sets. It will be shown that, for linear interpolation weighting in two dimensions, at least two particles are required to merge an ensemble of N particles lying in the same cell.

The first criterion will be treated in the next section, postponing the distribution function conservation rules and sampling to Section 8.3 and Section 8.4 respectively. The same criteria must be respected when splitting simulation particles. When the plasma is collisional, the MCC module reveals of great help as a tool to randomize position and velocities through collisions. The main problem, treated in details in Section 8.5, is then the choice of the particles to be split in the cell and the number of new particles depending on their starting energy distribution in order to reduce its variance on the whole energetic axis.

8.2 Spatial merging

It's widely known [43] that linear-weighting (first-order) charge assignment with PIC and CIC logic are equivalent in cartesian coordinates, while they differ in cylindrical and spherical coordinate systems. The PIC bilinear interpolation is widely used as weighting function both in cartesian and cylindrical coordinate systems.

8.2.1 Conservation laws

Referring to Figure 7.2-a for variables meaning, the generic i-th particle of local coordinates inside the cell (x_i, y_i), weight w_i and charge q ($q_i = w_i q$ is the effective charge of the simulation particle) contributes to node charges on the basis of the following fractions:

$$q_{\mathrm{A},i} = w_i q \frac{(\Delta x - x_i)(\Delta y - y_i)}{\Delta x \Delta y} = q w_i \rho_{\mathrm{A},i} \tag{8.1a}$$

$$q_{\mathrm{B},i} = w_i q \frac{x_i(\Delta y - y_i)}{\Delta x \Delta y} = q w_i \rho_{\mathrm{B},i} \tag{8.1b}$$

$$q_{\mathrm{C},i} = w_i q \frac{x_i y_i}{\Delta x \Delta y} = q w_i \rho_{\mathrm{C},i} \tag{8.1c}$$

$$q_{\mathrm{D},i} = w_i q \frac{(\Delta x - x_i) y_i}{\Delta x \Delta y} = q w_i \rho_{\mathrm{D},i}\,. \tag{8.1d}$$

Assuming a generic subset of N particles in the cell, their total charge contribution to the generic node P (with P=A,B,C or D) results

$$q_P = q \sum_{i=1}^{N} w_i \rho_{P,i}\,; \tag{8.2}$$

then, the total charge in the cell is given by

$$\sum_{P=\mathrm{A}}^{\mathrm{D}} q_P = q \sum_{P=\mathrm{A}}^{\mathrm{D}} \sum_{i=1}^{N} w_i \rho_{P,i} = q \sum_{i=1}^{N} w_i \sum_{P=\mathrm{A}}^{\mathrm{D}} \rho_{P,i} = q \sum_{i=1}^{N} w_i\,. \tag{8.3}$$

The fraction of the total charge to each node can be defined by the ratio between the total charge in P (equation (8.2)) and the total charge in the cell (equation (8.3)):

$$\rho_P = \frac{q_P}{\sum_{P=\mathrm{A}}^{\mathrm{D}} q_P} = \frac{\sum_{i=1}^{N} w_i \rho_{P,i}}{\sum_{i=1}^{N} w_i}\,,$$

which obviously represents a weighted average value.

By definition of $\rho_{P,i}$, it's evident that $\sum_{P=\mathrm{A}}^{\mathrm{D}} \rho_{P,i} = 1$ for each i; then, it follows that

$$\sum_{P=\mathrm{A}}^{\mathrm{D}} \rho_P = \sum_{P=\mathrm{A}}^{\mathrm{D}} \frac{\sum_{i=1}^{N} w_i \rho_{P,i}}{\sum_{i=1}^{N} w_i} = \frac{\sum_{i=1}^{N} w_i \sum_{P=\mathrm{A}}^{\mathrm{D}} \rho_{P,i}}{\sum_{i=1}^{N} w_i} = 1\,, \tag{8.4}$$

as foreseeable by reasoning on superposition effects.

Finally, from equations (8.1) it arises also the identity

$$\rho_{\mathrm{A},i}\rho_{\mathrm{C},i} = \rho_{\mathrm{B},i}\rho_{\mathrm{D},i}\,,$$

which cannot be extended by summation to $\rho_{\mathrm{A}}\rho_{\mathrm{C}} = \rho_{\mathrm{B}}\rho_{\mathrm{D}}$, because of crossed products between different particles.

8.2.2 Non dimensional quantities and change of reference

Generally speaking, the substitution of a set of N particles with a set of N' particles, one should conserve the total charge on each grid node; shifting the problem to the cell and summing the contributions of each cell on the corresponding nodes, the condition can be expressed in terms of conservation of the charge fractions on the cell nodes. For greater convenience, the local coordinates on the cell will be normalized to Δx and Δy as

$$\begin{aligned} \xi_i &= \frac{x_i}{\Delta x} \\ \eta_i &= \frac{y_i}{\Delta y}\,, \end{aligned}$$

with $\xi_i, \eta_i \in [0,1]$. Moreover, the weights w_i will be referred to the total weight $\sum_{i=1}^{N} w_i$ introducing

$$\omega_i = \frac{w_i}{\sum_{i=1}^{N} w_i}\,.$$

Making use of the prime to identify the merged particles properties, equations (8.1) lead to the following conditions:

$$\sum_{i=1}^{N} \omega_i(1-\xi_i)(1-\eta_i) = \sum_{i'=1'}^{N'} \omega_{i'}(1-\xi_{i'})(1-\eta_{i'}) = \rho_{\mathrm{A}} \tag{8.6a}$$

$$\sum_{i=1}^{N} \omega_i\xi_i(1-\eta_i) = \sum_{i'=1'}^{N'} \omega_{i'}\xi_{i'}(1-\eta_{i'}) = \rho_{\mathrm{B}} \tag{8.6b}$$

$$\sum_{i=1}^{N} \omega_i\xi_i\eta_i = \sum_{i'=1'}^{N'} \omega_{i'}\xi_{i'}\eta_{i'} = \rho_{\mathrm{C}} \tag{8.6c}$$

$$\sum_{i=1}^{N} \omega_i(1-\xi_i)\eta_i = \sum_{i'=1'}^{N'} \omega_{i'}(1-\xi_{i'})\eta_{i'} = \rho_{\mathrm{D}}\,. \tag{8.6d}$$

where the leftmost and rightmost sides are known. The normalization condition of equation (8.4) makes the four equations linearly dependent. A further condition must be added in order to conserve the total weight of the ensemble:

$$\sum_{i=1}^{N} \omega_i = \sum_{i'=1'}^{N'} \omega_{i'} = 1\,.$$

A total of 4 equations, is obtained for the unknowns $(\omega_{i'}, \xi_{i'}, \eta_{i'})$. One particle is not enough to satisfy all of them: it would indeed introduce a second closure equation given by $\rho'_{\mathrm{A}}\rho'_{\mathrm{D}} = \rho'_{\mathrm{B}}\rho'_{\mathrm{C}}$ which, in general, is not satisfied by an ensemble of more than one particle: $\rho_{\mathrm{A}}\rho_{\mathrm{D}} \neq \rho_{\mathrm{B}}\rho_{\mathrm{C}}$.

Hence, at least two particles are necessary to solve the system. Having only 4 equations in 6 unknowns, one can chose arbitrarily 2 of these. While it would be wise to merge N particles into two equally weighted particles, no particular condition can be imposed on the particles coordinates a priori. Only bounding conditions could be used: the two new particles must belong to the same cell of the old set.

Summing equation (8.6c) with equation (8.6b) and equation (8.6d) respectively, the system is simplified in

$$\sum_{i=1}^{N} \omega_i = \sum_{i'=1'}^{N'} \omega_{i'} = 1 \tag{8.7a}$$

$$\sum_{i=1}^{N} \omega_i\xi_i = \sum_{i'=1'}^{N'} \omega_{i'}\xi_{i'} = \rho_{\mathrm{B}} + \rho_{\mathrm{C}} \tag{8.7b}$$

$$\sum_{i=1}^{N} \omega_i\eta_i = \sum_{i'=1'}^{N'} \omega_{i'}\eta_{i'} = \rho_{\mathrm{C}} + \rho_{\mathrm{D}} \tag{8.7c}$$

$$\sum_{i=1}^{N} \omega_i\xi_i\eta_i = \sum_{i'=1'}^{N'} \omega_{i'}\xi_{i'}\eta_{i'} = \rho_{\mathrm{C}}\,. \tag{8.7d}$$

The first two equations represent the equivalence between the barycenter (or centroid) coordinates of the two sets of particles, being

$$\xi_{\mathrm{G}} = \frac{1}{\Delta x}\frac{\sum_{i=1}^{N} w_i x_i}{\sum_{i=1}^{N} w_i} = \sum_{i=1}^{N} \omega_i\xi_i \tag{8.8a}$$

$$\eta_{\mathrm{G}} = \frac{1}{\Delta y}\frac{\sum_{i=1}^{N} w_i y_i}{\sum_{i=1}^{N} w_i} = \sum_{i=1}^{N} \omega_i\eta_i\,. \tag{8.8b}$$

This shouldn't astonish the reader since the two terms $\rho_{\mathrm{B}}+\rho_{\mathrm{C}}$ and $\rho_{\mathrm{C}}+\rho_{\mathrm{D}}$ represent respectively the fraction of the total charge in the second horizontal and vertical halves of the cell.

Since $\sum_{i=1}^{N} \omega_i = 1$, it's useful to change the reference shifting it to the barycenter

of the ensembles:

$$\sum_{i'=1'}^{N'} \omega_{i'}(\xi'_i - \xi_G) = \sum_{i'=1'}^{N'} \omega_{i'}\zeta_{i'} = 0 \tag{8.9a}$$

$$\sum_{i'=1'}^{N'} \omega_{i'}(\eta'_i - \eta_G) = \sum_{i'=1'}^{N'} \omega_{i'}\gamma_{i'} = 0\,, \tag{8.9b}$$

with $\zeta_{i'} \in [-\xi_G, 1-\xi_G]$ and $\gamma_{i'} \in [-\eta_G, 1-\eta_G]$. Working on equation (8.7d) in order to obtain ζ_i and γ_i, it follows that

$$\rho_C = \sum_{i=1}^{N} \omega_i\xi_i\eta_i = \sum_{i=1}^{N} \omega_i(\zeta_i\gamma_i + \gamma_i\xi_G + \eta_G\zeta_i + \xi_G\eta_G) = \sum_{i=1}^{N} \omega_i\zeta_i\gamma_i + \xi_G\eta_G\,, \tag{8.10}$$

where equations (8.9) have been used. Equation (8.7d) can thus be substituted by

$$\sum_{i=1}^{N} \omega_i\zeta_i\gamma_i = \sum_{i'=1'}^{N'} \omega_{i'}\zeta_{i'}\gamma_{i'} = \rho_C - (\rho_B + \rho_C)(\rho_C + \rho_D)\,. \tag{8.11}$$

8.2.3 The inertia tensor analogy

In addition to the centroid conservation, equation (8.11) represents a sort of non-diagonal component of a pseudo-inertia tensor. In classical mechanics, the inertia tensor is defined as a symmetric matrix in the form of

$$\vec{\vec{I}} = \begin{pmatrix} I_{xx} & I_{xy} & I_{xz} \\ I_{yx} & I_{yy} & I_{yz} \\ I_{zx} & I_{zy} & I_{zz} \end{pmatrix},$$

with components I_{jk} given by

$$I_{jk} = \delta_{jk} \sum_{i=1}^{N} w_i(x_{l,i}^2 + x_{m,i}^2) + (\delta_{jk} - 1) \sum_{i=1}^{N} w_i x_{j,i} x_{k,i}\,,$$

where $x_{j,i}$ is the coordinate along the j-th direction (x, y or z) of the generic i-th particle with weight w_i in the system (k, l, m having the same meaning of j); δ_{lm} is the Kroneker delta function. If the moment of inertia tensor has been calculated for rotations about the centroid of the system, it is relatively easy to compute the tensor for rotations offset from the centroid, by the shifting formula (known as *Huygens law*)

$$I_{jk}^{\text{displaced}} = I_{jk}^{\text{centroid}} + w(r^2\delta_{jk} - r_j r_k)\,, \tag{8.12}$$

$\vec{r} = (r_x, r_y, r_z)$ being the 3D vector by which the rotation axis is displaced from the centroid. Equation (8.12) explains the meaning of equation (8.10) which modifies the $\xi\eta$ component of the inertia tensor changing reference to the barycenter G centered (ζ, γ) one. The mechanical analogy suggests to consider the fourth conservation equation (8.13d) as describing the particles distribution disuniformity in the cell: its

sign depends on the particles distribution in the four quarters defined by the (ζ, γ) axis.

The conservation of the charge fractions on the nodes doesn't require any other condition if a first order interpolation is used. The system obtained by imposition of charge conservation on the nodes has multiple acceptable solutions. However, it would be wise to choose the lower number of equally weighted merging particles in order to optimize the particles number reduction and to homogenize weights distribution. The choice $N' = 2$ allows to reduce the number of unknowns to the 6 particles coordinates; it will be shown that equal weights $\omega_{1'} = \omega_{2'} = 1/2$ is a not always acceptable choice.

8.2.4 The merged particles coordinates

The system of conservation equations (8.13) can be easily rewritten for $N' = 2$ particles, leading to

$$\omega_{1'} + \omega_{2'} = 1 \tag{8.13a}$$

$$\zeta_{1'} = -\frac{\omega_{2'}}{\omega_{1'}}\zeta_{2'} \tag{8.13b}$$

$$\gamma_{1'} = -\frac{\omega_{2'}}{\omega_{1'}}\gamma_{2'} \tag{8.13c}$$

$$\omega_{1'}\zeta_{1'}\gamma_{1'} + \omega_{2'}\zeta_{2'}\gamma_{2'} = I_{\zeta\gamma}\,. \tag{8.13d}$$

Having four equations in six unknowns, the system is not closed. One of the particles coordinates and one of their weights can be arbitrarily chosen as parameters; then the other three coordinates will be expressed as functions of them. Moreover, it can be noticed by the first two equations (conservation of the system barycenter) that the particles must lie on a line containing the charge centroid, on opposite sides of it, at distances from it depending on their weights. The symmetry of the system allows to reduce the field of variability for the coordinate chosen as parameter to positive values only. Once fixed $\zeta_{1'} > 0$, the other three coordinates are

$$\omega_{2'} = 1 - \omega_{1'} \tag{8.14a}$$

$$\zeta_{2'} = -\frac{1}{\omega_{\mathrm{r}}}\zeta_{1'} \tag{8.14b}$$

$$\gamma_{1'} = \omega_{\mathrm{r}}\frac{I_{\zeta\gamma}}{\zeta_{1'}} \tag{8.14c}$$

$$\gamma_{2'} = -\frac{I_{\zeta\gamma}}{\zeta_{1'}}\,, \tag{8.14d}$$

with $\omega_{\mathrm{r}} = \omega_{2'}/\omega_{1'} = (1 - \omega_{1'})/\omega_{1'}$. To assure that particles belong to the same cell, a bounded interval of variability must be defined for $\zeta_{1'}$ and $\omega_{1'}$.

8.2.5 Cell coordinates limits

The new particles coordinates are not free in the whole 2D space, but must be bounded by the cell limits. For the coordinate systems considered up to now, one

has

$$x \in [0, \Delta x]\,, \qquad \xi \in [0,1]\,, \qquad \zeta \in [-\xi_\mathrm{G}, 1-\xi_\mathrm{G}]\,,$$
$$y \in [0, \Delta y]\,, \qquad \eta \in [0,1]\,, \qquad \gamma \in [-\eta_\mathrm{G}, 1-\eta_\mathrm{G}]\,.$$

Working in the (ζ, γ) reference for convenience, the coordinates limits on $\zeta_{1'}$, $\zeta_{2'}$, $\gamma_{1'}$ and $\gamma_{2'}$ and the assumptions on $\zeta_{1'}$ affect the restriction limits over $\zeta_{1'}$ as follows

$$\begin{aligned}
&\zeta_{1'} \in [-\xi_\mathrm{G}, 1-\xi_\mathrm{G}] \quad \Rightarrow \quad \zeta_{1'} \in \,]0, 1-\xi_\mathrm{G}] \\
&\zeta_{2'} \in [-\xi_\mathrm{G}, 1-\xi_\mathrm{G}] \quad \Rightarrow \quad \zeta_{1'} \in \,]0, \omega_\mathrm{r}\xi_\mathrm{G}] \\
&\gamma_{1'} \in [-\eta_\mathrm{G}, 1-\eta_\mathrm{G}] \quad \Rightarrow \quad \begin{cases} \zeta_{1'} \in \,]-\omega_\mathrm{r}\frac{I_{\zeta\gamma}}{\eta_\mathrm{G}}, \infty[& \text{if } I_{\zeta\gamma} < 0 \\ \zeta_{1'} \in \,]\omega_\mathrm{r}\frac{I_{\zeta\gamma}}{(1-\eta_\mathrm{G})}, \infty[& \text{if } I_{\zeta\gamma} > 0 \end{cases} \\
&\gamma_{2'} \in [-\eta_\mathrm{G}, 1-\eta_\mathrm{G}] \quad \Rightarrow \quad \begin{cases} \zeta_{1'} \in \,]-\frac{I_{\zeta\gamma}}{1-\eta_\mathrm{G}}, \infty[& \text{if } I_{\zeta\gamma} < 0 \\ \zeta_{1'} \in \,]\frac{I_{\zeta\gamma}}{\eta_\mathrm{G}}, \infty[& \text{if } I_{\zeta\gamma} > 0\,. \end{cases}
\end{aligned}$$

The multiple conditions obtained for $\zeta_{1'}$ can be gathered in

$$\max\left\{-\omega_\mathrm{r}\frac{I_{\zeta\gamma}}{\eta_\mathrm{G}}, -\frac{I_{\zeta\gamma}}{1-\eta_\mathrm{G}}\right\} < \zeta_{1'} < \min\{\omega_\mathrm{r}\xi_\mathrm{G}, (1-\xi_\mathrm{G})\} \quad \text{if } I_{\zeta\gamma} < 0 \tag{8.15a}$$

$$\max\left\{\frac{I_{\zeta\gamma}}{\eta_\mathrm{G}}, \omega_\mathrm{r}\frac{I_{\zeta\gamma}}{1-\eta_\mathrm{G}}\right\} < \zeta_{1'} < \min\{\omega_\mathrm{r}\xi_\mathrm{G}, (1-\xi_\mathrm{G})\} \quad \text{if } I_{\zeta\gamma} > 0 \tag{8.15b}$$

where the min and max functions allow to obtain the smallest variability interval.

A solution can exist if and only if the obtained variability interval for $\zeta_{1'}$ is not void. Each of the two cases $I_{\zeta\gamma} < 0$ and $I_{\zeta\gamma} > 0$ can be exploded in four conditions, two not depending on ω_r and two depending on it, then giving a variability interval for it. In the case $I_{\zeta\gamma} > 0$, the following four disequations are obtained:

$$\begin{aligned}
\xi_\mathrm{G} > \frac{I_{\zeta\gamma}}{1-\eta_\mathrm{G}} \;\Leftrightarrow \quad \xi_\mathrm{G} = \sum_{i=1}^{N}\omega_i\xi_i > I_{\xi\eta} = \sum_{i=1}^{N}\omega_i\xi_i\eta_i \\
1-\xi_\mathrm{G} > \frac{I_{\zeta\gamma}}{\eta_\mathrm{G}} \;\Leftrightarrow \quad \eta_\mathrm{G} = \sum_{i=1}^{N}\omega_i\eta_i > I_{\xi\eta} = \sum_{i=1}^{N}\omega_i\xi_i\eta_i \\
\omega_\mathrm{r}\xi_\mathrm{G} > \frac{I_{\zeta\gamma}}{\eta_\mathrm{G}} \quad \Leftrightarrow \quad \omega_\mathrm{r} > \frac{I_{\zeta\gamma}}{\xi_\mathrm{G}\eta_\mathrm{G}} \\
1-\xi_\mathrm{G} > \omega_\mathrm{r}\frac{I_{\zeta\gamma}}{1-\eta_\mathrm{G}} \quad \Leftrightarrow \quad \omega_\mathrm{r} < \frac{(1-\xi_\mathrm{G})(1-\eta_\mathrm{G})}{I_{\zeta\gamma}}\,.
\end{aligned}$$

In the first two cases, the definition of the centroid coordinates (equations (8.8)), the Huygens law for the centrifugal moment, $I_{\zeta\gamma} = I_{\xi\eta} - \xi_\mathrm{G}\eta_\mathrm{G}$, and its definition (equation (8.10)) have been used; the obtained condition are immediately verified being both ξ_i and η_i less than 1 for each i. The last two conditions give a variability interval for ω_r

$$\frac{I_{\zeta\gamma}}{\xi_\mathrm{G}\eta_\mathrm{G}} < \omega_\mathrm{r} < \frac{(1-\xi_\mathrm{G})(1-\eta_\mathrm{G})}{I_{\zeta\gamma}}\,, \tag{8.16}$$

non-void thanks to the combination of the first two just verified disequations.

Paying attention to the disequations inversion due to negative signs, something analogous can be obtained in the case $I_{\zeta\gamma} < 0$:

$$\begin{aligned}
\xi_G > -\frac{I_{\zeta\gamma}}{\eta_G} &\Leftrightarrow \quad I_{\xi\eta} = \sum_{i=1}^{N} \omega_i \xi_i \eta_i > 0 \\
1 - \xi_G > -\frac{I_{\zeta\gamma}}{1-\eta_G} &\Leftrightarrow \quad 1 - \xi_G = \sum_{i=1}^{N} \omega_i (1-\xi_i) > \eta_G - I_{\xi\eta} = \sum_{i=1}^{N} \omega_i \eta_i (1-\xi_i) \\
\omega_r \xi_G > -\frac{I_{\zeta\gamma}}{1-\eta_G} &\Leftrightarrow \quad \omega_r > -\frac{I_{\zeta\gamma}}{\xi_G(1-\eta_G)} \\
1 - \xi_G > -\omega_r \frac{I_{\zeta\gamma}}{\eta_G} &\Leftrightarrow \quad \omega_r < -\frac{(1-\xi_G)\eta_G}{I_{\zeta\gamma}} \,.
\end{aligned}$$

The first condition is verified being $\omega_i, \xi_i, \eta_i \geq 0$ in general and $\omega_i, \xi_i, \eta_i > 0$ for at least one $i \in [1, N]$; the second one is true since $\eta_i \leq 1 \, \forall i$ (at least for one i, η_i must be strictly less than 1, otherwise $I_{\xi\eta}$ would be null). The last two disequations give a variability interval for ω_r

$$-\frac{I_{\zeta\gamma}}{\xi_G(1-\eta_G)} < \omega_r < -\frac{(1-\xi_G)\eta_G}{I_{\zeta\gamma}} \,, \tag{8.17}$$

which can be easily verified to be not void combining the first two conditions.

The last case $I_{\zeta\gamma} = 0$ is trivial, since one can choose one of the following solutions:

$$\begin{aligned}
&\zeta_{1'} = \zeta_{2'} = 0, \; \omega_r = 1, \; 0 \leq \gamma_{1'} = -\gamma_{2'} \leq \max\{\eta_G, 1-\eta_G\} \,; \\
&\gamma_{1'} = \gamma_{2'} = 0, \; \omega_r = 1, \; 0 \leq \zeta_{1'} = -\zeta_{2'} \leq \max\{\xi_G, 1-\xi_G\} \,.
\end{aligned}$$

8.2.6 A graphical interpretation

The previous evaluations of the variability interval for $\zeta_{1'}$ and ω_r can be graphically represented in seek of a greater clearness. From equations (8.14), one can immediately note that the coordinates of the two new particles lie on one branch of the two hyperbola in the centroid reference (see Figure 8.1), given by:

$$\begin{aligned}
\zeta_{1'}\gamma_{1'} &= \omega_r I_{\zeta\gamma} \\
\zeta_{2'}\gamma_{2'} &= \frac{1}{\omega_r} I_{\zeta\gamma} \,.
\end{aligned}$$

The distance of each branch from the reference center depends on the two weights through ω_r. If, for a fixed value of ω_r, one of the two branches falls completely outside the cell, then no solution is acceptable. The value of ω_r has to be contained in the interval given by equation (8.16) if $I_{\zeta\gamma} > 0$ or in those of equation (8.17) in the opposite case of $I_{\zeta\gamma} < 0$. Within this choice of ω_r, the two hyperbola weighted branches have at least one point inside the cell allowing an acceptable solution. As shown in Figure 8.1, the first new particle will fall always on the right branch (being $\zeta_{1'} > 0$). For each choice of ω_r, many possible solutions are acceptable since no other hypothesis is done. When ω_r is chosen as the maximum or minimum value of the allowed interval, only one solution is possible since one of the two weighted branches

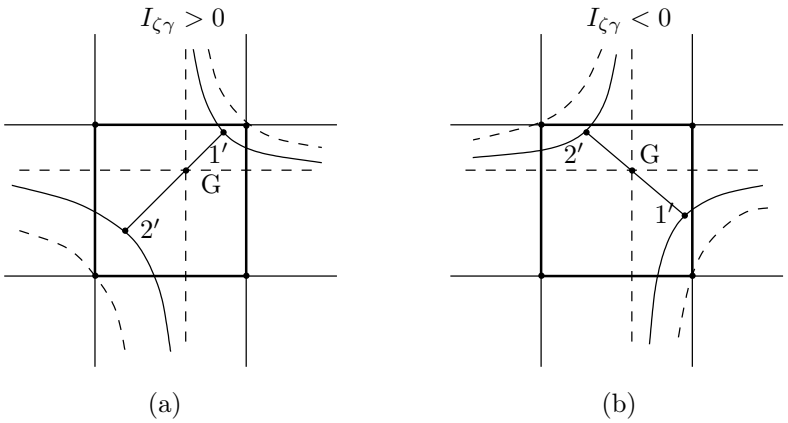

Figure 8.1: Graphical interpretation of the weight and coordinate choices in the two cases of $I_{\zeta\gamma} > 0$ (a) and $I_{\zeta\gamma} < 0$ (b). The dotted lines represent the limiting hyperbola branches.

of the hyperbola crosses one cell vertex. The two cases $I_{\zeta\gamma} > 0$ and $I_{\zeta\gamma} < 0$ are completely analogous.

The graphical interpretation of the variability interval and new particles positioning, can be effectively used to show that the choice of equally weighted particles $\omega_{\mathrm{r}} = 1$ is not always acceptable.

In the case $I_{\zeta\gamma} > 0$, one should show that it exists at least one configuration $\{\omega_i, \xi_i, \eta_i\}_{i=1,N}$ such as 1 is not contained in $[\frac{I_{\zeta\gamma}}{\xi_{\mathrm{G}}\eta_{\mathrm{G}}}, \frac{(1-\xi_{\mathrm{G}})(1-\eta_{\mathrm{G}})}{I_{\zeta\gamma}}]$. Giving a look at the case (a) of Figure 8.1, in order to make the lower limit greater than one, one should try to place the centroid near to the lower-left corner of the cell and place particles near the opposite corner increasing the centrifugal moment. Therefore, choosing

$$\omega_i = \frac{\varepsilon}{N-1},\ \xi_i = \eta_i = 1-\varepsilon \qquad \forall i = 1, N-1$$
$$\omega_N = 1-\varepsilon,\ \xi_N = \eta_N = \varepsilon$$

with $\varepsilon \ll 1$, it's easy to show

$$1 < \frac{I_{\zeta\gamma}}{\xi_{\mathrm{G}}\eta_{\mathrm{G}}} \quad \Leftrightarrow \quad 2\xi_{\mathrm{G}}\eta_{\mathrm{G}} < I_{\xi\eta} \quad \Leftrightarrow \quad 8(\varepsilon(1-\varepsilon))^2 < \varepsilon(1-\varepsilon) \quad \Leftrightarrow \quad \varepsilon(1-\varepsilon) < \frac{1}{8},$$

which can be true due to the arbitrariness on ε.

Analogous is the case for $I_{\xi\gamma} < 0$.

When the variability interval for ω_{r} contains the unit value, it's convenient to choose equally weighted particles: once fixed $\omega_{\mathrm{r}} = 1$, the $\zeta_{1'}$ positive coordinate can be extracted in the interval given by the proper one of equations (8.15). In the opposite case, ω_{r} has to be randomly extracted in its variability interval and then $\zeta_{1'}$ between the bounds depending on the chosen ω_{r}.

8.2.7 Correction to the first coordinate random choice

By definition, the centrifugal inertia moment $I_{\zeta\gamma} = \sum \omega_i \zeta_i \gamma_i$ is independent from the choice of the reference axis: an exchange between ζ and γ would preserve $I_{\zeta\gamma}$ thanks to the commutative property of the product. Moreover, the variability interval for $\zeta_{1'}$, given by equations (8.15), fixes a non-zero lower limit for the coordinate randomly extracted and assumed positive.

The combination of the two factors lead to a polarization of the solution: when $|I_{\zeta\gamma}|$ assumes high values, $\zeta_{1'}$ is sampled uniformly on a tight interval containing only high values, which would give low values for $\gamma_{1'}$, obtained through equation (8.14c); on the other hand, if $|I_{\zeta\gamma}|$ is low, the variability interval for $\zeta_{1'}$ is wider, but all the high values sampled for $\zeta_{1'}$ would lead to low values for $\gamma_{1'}$. In most cases, the new merged particles occupy a narrow strip along the ζ axis resulting in a not-uniformly distributed spatial configuration inside the cell.

To solve the problem, the $I_{\zeta\zeta}$ and $I_{\gamma\gamma}$ inertia moments, defined through (see Appendix 8.A for more details)

$$\sum_{i=1}^{N} \omega_i \zeta_i^2 = \sum_{i'=1'}^{N'} \omega_{i'} \zeta_{i'}^2 = I_{\gamma\gamma}$$
$$\sum_{i=1}^{N} \omega_i \gamma_i^2 = \sum_{i'=1'}^{N'} \omega_{i'} \gamma_{i'}^2 = I_{\zeta\zeta}\,,$$

can be of help. The two additional moments give a sort of quadratic deviation for each main coordinate ζ and γ of the set of particles. Comparing the two inertia moments, one has information about the spatial distribution of the particles in the cell: higher is the value of $I_{\gamma\gamma}$ higher are the particles ζ coordinates, and analogously for $I_{\zeta\zeta}$ and the γ coordinates. Hence, when $I_{\gamma\gamma} \geq I_{\zeta\zeta}$ the ζ coordinate can be chosen randomly leading to higher values of $\zeta_{1',2'}$, while, if $I_{\gamma\gamma} < I_{\zeta\zeta}$, the γ coordinate will be sampled to better reproduce the spatial distribution.

The variability interval for $\zeta_{1'}$ and ω_{r} of equations (8.15) and (8.16)-(8.17) can be similarly obtained for the randomly sampled $\gamma_{1'}$. Due to the above mentioned symmetry between ζ and γ in the $I_{\zeta\gamma}$ definition, the two coordinates of the main reference can be exchanged ($\xi \leftrightarrow \eta$ and $\zeta \leftrightarrow \gamma$) to obtain the $\gamma_{1'}$ variability interval:

$$\max\left\{-\omega_{\mathrm{r}}\frac{I_{\zeta\gamma}}{\xi_{\mathrm{G}}}, -\frac{I_{\zeta\gamma}}{1-\xi_{\mathrm{G}}}\right\} < \gamma_{1'} < \min\{\omega_{\mathrm{r}}\eta_{\mathrm{G}}, (1-\eta_{\mathrm{G}})\} \qquad \text{if } I_{\zeta\gamma} < 0\,,$$
$$\max\left\{\frac{I_{\zeta\gamma}}{\xi_{\mathrm{G}}}, \omega_{\mathrm{r}}\frac{I_{\zeta\gamma}}{1-\xi_{\mathrm{G}}}\right\} < \gamma_{1'} < \min\{\omega_{\mathrm{r}}\eta_{\mathrm{G}}, (1-\eta_{\mathrm{G}})\} \qquad \text{if } I_{\zeta\gamma} > 0\,.$$

Consequently, the lower and upper bounds for ω_{r} are given by

$$\frac{I_{\zeta\gamma}}{\xi_{\mathrm{G}}\eta_{\mathrm{G}}} < \omega_{\mathrm{r}} < \frac{(1-\xi_{\mathrm{G}})(1-\eta_{\mathrm{G}})}{I_{\zeta\gamma}} \qquad \text{if } I_{\zeta\gamma} < 0\,,$$
$$-\frac{I_{\zeta\gamma}}{(1-\xi_{\mathrm{G}})\eta_{\mathrm{G}}} < \omega_{\mathrm{r}} < -\frac{\xi_{\mathrm{G}}(1-\eta_{\mathrm{G}})}{I_{\zeta\gamma}} \qquad \text{if } I_{\zeta\gamma} > 0\,.$$

8.3 Velocities merging

When a particle substitution is performed, as proposed in the previous section, charge and mass are not the only physical properties to be conserved. To avoid numerical heating of the system, even the energy and momentum of the starting set has to be preserved. Two possible solution will be here proposed to close the system of four equation in six unknowns.

8.3.1 Momentum and energy conservation

The presented two-dimensional PIC-MCC code follows particles with two position coordinates and three components of velocities (equivalent to two components plus total energy). When merging N particles, the momentum must be conserved in all its components and total energy as a scalar. Following the same notation used in the previous section and labeling the new N' particles with the prime, the conservation laws can be written as

$$\sum_{i=1}^{N} m_i v_{j,i} = \sum_{i'=1}^{N'} m_{i'} v_{j,i'} = M_j \quad \forall\, j = 1,2,3$$
$$\sum_{i=1}^{N} \frac{1}{2} m_i \sum_{j=1}^{3} v_{j,i}^2 = \sum_{i'=1}^{N'} \frac{1}{2} m_{i'} \sum_{j=1}^{3} v_{j,i'}^2 = \mathcal{E}\,,$$

where v_j with $j = 1,2,3$ are the three components of velocity, M_j the total momentum in the j-th direction and $\mathcal{E}$ the total energy of the set. The conservation of the momentum in the third direction could be neglected, but it must be remembered that the poloidal velocity contributes to the total energy of the particles.

In the previous section, it was derived that to replace a generic set of N particles the number of new particles cannot be lower than $N' = 2$ to guarantee the charge conservation on the grid nodes. The resultant system can be rewritten as

$$m_{1'} v_{j,1'} + m_{2'} v_{j,2'} = \sum_{i=1}^{N} m_i v_{j,i} = M_j \quad \forall\, j = 1,2,3 \tag{8.19a}$$
$$\sum_{j=1}^{3} (m_{1'} v_{j,1'}^2 + m_{2'} v_{j,2'}^2) = \sum_{j=1}^{3} \sum_{i=1}^{N} m_i v_{j,i}^2 = \sum_{j=1}^{3} (2\mathcal{E}_j) \tag{8.19b}$$

M_j and $\mathcal{E}_j$ being respectively the momentum and energy in the j-th direction.

Moreover, the spatial merging already conserves the total mass of the system, since the ratio q/m must be preserved for each species apart of the particle weight. The mass m_i of the i-th generic particle is given by $m_i = w_i m$, where m is the mass of the particle species. Denoting the total weight of the considered set of particles with w, and their total mass with $mw = m \sum_{i=1}^{N} w_i$, equations (8.19) can be made dimensionless, by dividing each mass m_i by the total mass mw and each velocity component $v_{j,i}$ by the ratio of the total momentum and total mass

$M_j/(mw)$, obtaining

$$\omega_{1'}\nu_{j,1'} + \omega_{2'}\nu_{j,2'} = 1 \quad \forall\, j = 1,2,3 \tag{8.20a}$$

$$\sum_{j=1}^{3}(\omega_{1'}\nu_{j,1'}^2 + \omega_{2'}\nu_{j,2'}^2) = \sum_{j=1}^{3}\varepsilon_j\,, \tag{8.20b}$$

where

$$\omega_i = \frac{m_i}{mw} = \frac{w_i}{w} \qquad \nu_{j,i} = mw\frac{v_{j,i}}{M_j} \qquad \varepsilon_j = 2mw\frac{\mathcal{E}_j}{M_j^2}\,. \tag{8.21}$$

The system of equations (8.20) contains 6 unknowns but only 4 equations. Two additional conditions must be imposed to avoid the arbitrariness on the solution, or two random numbers can be extracted to fix two unknowns. Since the particles are firstly collected in clusters on the basis of similar velocity components (as widely described in Section 8.4), the random extraction of velocity components should be limited to the same interval of variability of the starting set. To avoid the sampling of particles velocities, two fictitious conservation rules can be added to have a system of equations in a closed form. Two different methods will be proposed.

8.3.2 Equal velocities

A first simple way to deceive the arbitrariness problem of the system of equations (8.20) consists in reducing the number of unknowns. Since the third velocity component is strictly necessary only to correctly estimate the particles energy, the momentum conservation in the poloidal direction can be neglected. In this way, the number of equations is reduced to three giving a closed system if the three velocity components of only one particle are considered. Under the hypothesis that the merged particles have equal velocities in the three directions ($v_{j,1'} = v_{j,2'}$ for each $j = 1,2,3$) and, consequently equal energies ($\mathcal{E}_{1'} = \mathcal{E}_{2'}$), the system of equations (8.20) can be easily solved obtaining

$$\nu_{j,1'} = \nu_{j,2'} = 1 \quad \forall\, j = 1,2$$

$$\nu_{3,1'} = \pm\nu_{3,2'} = \pm\sqrt{\sum_{j=1}^{3}\varepsilon_j - 2}\,.$$

Going back to the dimensional quantities of interest, by inversion of the equations (8.21), the new particles velocities are

$$v_{j,1'} = v_{j,2'} = \frac{M_j}{w} \quad \forall\, j = 1,2$$

$$v_{3,1'} = \pm v_{3,2'} = \pm\frac{1}{w}\sqrt{w\mathcal{E} - (M_1^2 + M_2^2)}\,.$$

The argument of the square root in the expression of $v_{3,i'}$ is clearly positive, even if, numerically speaking, care must be devoted to protect from negative values caused by truncation or rounding errors. Two random numbers can be extracted to define the sign of $v_{3,1'}$ and $\pm v_{3,2'}$.

The main drawback of this first rough but effective method is the loss of any separation of the two particles in the velocity space. However, this is not a problem since the two merged particles occupy different positions inside the cell and will, therefore, feel different pushing forces. Moreover, in PIC-MCC simulations, the collisions between charged particles and the background gas will accelerate the particles spreading them in the 3D velocity space.

8.3.3 Conservation of energy in three directions

A second strategy to close the system of equations (8.20) is to split the equation (8.20b) in a set of three equations, one for each direction of the velocity space. The resulting system of 6 equations is

$$\omega_{1'}\nu_{j,1'} + \omega_{2'}\nu_{j,2'} = 1 \quad \forall\, j = 1,2,3 \tag{8.24a}$$

$$\omega_{1'}\nu_{j,1'}^2 + \omega_{2'}\nu_{j,2'}^2 = \varepsilon_j \quad \forall\, j = 1,2,3\,, \tag{8.24b}$$

where a pair of two equations is obtained for each j with different known ε_j.

Extracting $\nu_{j,2'}$ from equation (8.24a) and substituting it into equation (8.24b), a quadratic equation in $\nu_{j,1'}$ is obtained, having

$$\nu_{j,1'} = 1 \pm \sqrt{\frac{\omega_{2'}}{\omega_{1'}}(\varepsilon_j - 1)}\,, \tag{8.25}$$

as possible solutions ($\omega_{1'} + \omega_{2'} = 1$ have been extensively used). The velocity components of the particle $2'$ are derived by equation (8.24a):

$$\nu_{j,2'} = \frac{1}{\omega_{2'}}(1 - \omega_{1'}\nu_{j,1'}) = 1 \mp \sqrt{\frac{\omega_{1'}}{\omega_{2'}}(\varepsilon_j - 1)}\,. \tag{8.26}$$

Note that the weight fractions $\omega_{1'}$ are defined by the spatial merging procedure of Section 8.2; in particular, for equally weighted merging particles, the ratio $\omega_{1'}/\omega_{2'}$ is equal to 1, leading to simplified expressions.

Looking at, equation (8.25) and equation (8.26) it arises necessary to show that $\varepsilon_j - 1 \geq 0$ in order to obtain real valued $\nu_{j,1'}$ and $\nu_{j,2'}$. The mentioned condition is equivalent to

$$2mw\frac{\mathcal{E}_j}{M_j^2} \geq 1\,;$$

multiplying both hands by $M_j^2 \geq 0$ and applying the definition of $\mathcal{E}_j$ and M_j for the initial set of N particles, the relation becomes

$$\sum_{k=1}^{N} w_k \sum_{i=1}^{N} w_i v_{j,i}^2 \geq \left(\sum_{i=1}^{N} w_i v_{j,i}\right)^2 .$$

The square terms of the rhs equal the terms of the lhs for $k = i$, then the two summations can be simplified in

$$\sum_{k=1}^{N}\sum_{i=1,i\neq k}^{N} w_k w_i v_{j,i}^2 \geq 2\sum_{k=1}^{N}\sum_{i=k}^{N} w_k w_i v_{j,k} v_{j,i} = \sum_{k=1}^{N}\sum_{i=1,i\neq k}^{N} w_k w_i v_{j,k} v_{j,i}\,;$$

moving all the terms to the lhs and adding the generic terms given by the couple of indexes $k = l$, $i = n \neq l$ and $k = n$, $i = l \neq n$, the generic addendum $w_l w_m (v_{j,l} - v_{j,m})^2$ is obtained. Therefore, the disequation containing the double summation assumes the form

$$\sum_{k=1}^{N} \sum_{i=k}^{N} w_k w_i (v_{j,k} - v_{j,i})^2 \geq 0 \,,$$

which is evidently verified being the summation of positive terms.

It's, finally, trivial to go back from equations (8.25)-(8.26) to the real velocity components:

$$v_{j,1'} = \frac{M_j \pm \sqrt{\frac{m_{2'}}{m_{1'}} \left(2(m_{1'} + m_{2'}) \mathcal{E}_j - M_j^2 \right)}}{m_{1'} + m_{2'}}$$

$$v_{j,2'} = \frac{M_j \mp \sqrt{\frac{m_{1'}}{m_{2'}} \left(2(m_{1'} + m_{2'}) \mathcal{E}_j - M_j^2 \right)}}{m_{1'} + m_{2'}} \,.$$

Three random numbers can be extracted to fix the plus or minus sign of the three square roots in $v_{j,1'}$ for $j = 1, 2, 3$, those of $v_{j,2'}$ being the opposite. For example, the second term could be multiplied by $(-1)^{\mathrm{nint}(R)}$, with $\mathrm{nint}(R)$ the nearest integer of the random number R chosen in $[0, 1]$ with a uniform distribution.

8.4 Particles clustering

The conservation of grid moments, momentum and energy is not enough to assure the equivalence between the starting and final set of particles, since the two sets must sample the same distribution function in the phase space (rule 2. stated in Section 8.1.2). In the present section, a hybrid method will be proposed to select "near" particles.

8.4.1 Mesh-free particles selection

Three are the main general strategies to select similar particles, which could undergo a merging procedure avoiding too strong perturbation in the initial distribution function:

- mesh-based methods: the phase space is meshed into small multi-dimensional bins which create a sort of containment box for the simulation particles;

- mesh-free methods: the particles are selected on the basis of a proximity principle looking for "near" particles in the phase space;

- hybrid methods: the mesh and mesh-free methods can be combined together to exploit the advantages of each one in connection with the PIC-MCC algorithm structure.

The first approach appears simpler: a grid of the 2D space domain is already available for the solution of the fields on the nodes; the addition of a 3D mesh in the velocity space can be easily added to create bins able to contain particles with similar velocity components. The mesh could be uniform or not, and for a 2D-3V simulation, the first two components could be substituted by the direction of flight and the planar velocity of the particles, while the third by their energy.

The mesh-free methods are more complex but even more flexible. The particles can be selected grouping a fixed (or free) number of them into clusters having similar properties in the phase space and then merged together in a new pair. The main advantage of this method is the absence of a mesh bounding the particles, independently from the real distance. However, the absence of a mesh makes necessary the definition of searching rules to select "near" particles.

Finally, hybrid techniques could be used to exploit the advantages of both the methods, like the presence of a spatial grid proper of the PIC codes and the flexibility of the mesh-free selection for the continuous velocity components.

As proposed by Shon *et al.* [202], the particles could be grouped in the two-dimensional velocity sub-domain phase space corresponding to the plane of simulation. The method is based on a meshing of the $v_x - v_y$ phase space into several domains through the direction of flight of the particles. After grouping particles, they are sorted out separately by velocity magnitude ($\sqrt{v_x^2 + v_y^2}$) and ordinately grouped in ensemble containing an a priori fixed number of particles. If a MCC module is coupled with the PIC one, energy of the particles is of fundamental importance being related to the cross sections of the interactions with the background gas. No consideration was found about this issue; furthermore, apparently, after the angular binning, the particles are grouped together in a sorted order without any check on their real proximity in planar velocity magnitude.

Lapenta [203] proposes two algorithms for generic spline weighting function. The first coalesces $N = 2$ particles into $N' = 1$ ones for 1D, 2D or 3D systems allowing to preserve the overall charge and momentum and charge densities but perturbing the velocity distribution function; a diatomic search is performed to sort the particles into two bins and select the largest one; then the binning is repeated in sequence for each spatial direction and component of velocity until the number of particles in the largest bin is small enough to use a pair search. The second scheme is valid only in 1D systems.

The main drawbacks of the existing methods are the rigidity in the choice of a fixed number of starting, equally-weighted particles, and the complete absence of any consideration about the MCC module.

The schemes hereafter proposed are quite different since based on clustering procedures typical of the statistical analysis. Using the particle velocity components (or related quantities like direction of flight, planar velocity and total energy) as attributes, a multi-property data clustering procedure is presented to group closer particles in the velocity phase space. The method is hybrid: the PIC grid is used as spatial mesh, while the velocity dependent attributes are considered as continuous; moreover, the number of particles in each group is not fixed a priori: this allows to reduce the number of residual particles and maximize the effectiveness of the merging method. After a brief introduction on the data clustering topic, two general

algorithms are described.

8.4.2 Data mining basis

Data clustering is a common technique for statistical data analysis [204]. It is commonly used in many fields, including machine learning, data mining, pattern recognition, image analysis and bioinformatics. Clustering is the classification of similar objects into different groups, or more precisely, the partitioning of a data set into subsets (clusters), so that the data in each subset (ideally) share some common trait – often proximity according to some defined distance measure.

If each object in a set of N objects is represented by a set of D measurements (or attributes), each object is represented by a pattern, or D-place vector. The set itself is viewed as a $N \times D$ pattern matrix, whose rows define a pattern and each column a feature (or measurement). One can figure the D features as a set of orthogonal axes defining a D-dimensional pattern space. A cluster can be thought as a collection of patterns which are close to one another or which satisfy some spatial relationships. The task of a clustering algorithm is to identify such natural groupings in spaces of many dimensions. Clustering methods require the establishment of an index of proximity (alikeness, affinity or association) between pairs of patterns. This index can be computed from a pattern matrix or from raw data.

A proximity index between the i-th and k-th patterns is denoted $d_{i,k}$ and must satisfy the following three properties:

1. $d_{i,i} = 0 \qquad \forall i$
2. $d_{i,k} = d_{k,i} \qquad \forall i, k$
3. $d_{i,k} \geq 0 \qquad \forall i, k$

Let $[x_{ij}]$ be a pattern matrix, where x_{ij} is the j-th feature of the i-th pattern. Usually the proximity index is based on a metric distance, which measure dissimilarity. Denoted the i-th pattern, i.e. the i-th row of the pattern matrix, by the column vector $\vec{x}_i$

$$\vec{x}_i = (x_{i1}\ x_{i2}\ \ldots\ x_{iD})^{\mathrm{T}} \quad \text{for } i = 1, 2, \ldots, N$$

where T is used as symbol of transpose, the *Minkowski metric* is defined as

$$d(i,k) = \left(\sum_{j=1}^{D} |x_{ij} - x_{kj}|^r \right)^{1/r} \qquad \text{for } r \geq 1\,.$$

All the Minkowski metrics satisfy two additional properties for $d_{i,k}$:

4. $d_{i,k} = 0 \qquad \text{only if} \quad \vec{x}_i = \vec{x}_k$
5. $d_{i,k} \leq d_{i,m} + d_{m,k} \qquad \forall i, k, m \quad (\textit{triangle inequality})$

The three most common Minkowski metrics are obtained for $r = 1$, $r = 2$ and $r \to \infty$, respectively known as *Manhattan distance*, *Euclidean distance* and *"Sup" distance* [204]. The Euclidean distance is the most common metrics, even because

the familiar geometric notions of invariance to translations and rotations of the pattern space are valid only for it.

Making use of a metric distance as index of patterns dissimilarity, different methods can be developed to collect the objects into clusters [204].

Data clustering algorithms can be *exclusive* or *non-exclusive* (overlapping): an exclusive classification is a partition of the set of objects and each object belongs to exactly one subset; on the contrary, non-exclusive classification can assign the same object to several classes. The first category is then splittable into *intrinsic* (or unsupervised) and *extrinsic* (or supervised) classification, the first using only the proximity matrix to perform the classification (also called unsupervised since no category labels denoting an a priori partition of the objects are used). Exclusive, intrinsic classifications are subdivided into *hierarchical* and *partitional*. Hierarchical algorithms find successive clusters using previously established clusters, whereas partitional algorithms determine all clusters at once. Hierarchical algorithms can be *agglomerative* (bottom-up) or *divisive* (top-down). Agglomerative algorithms begin with each element as a separate cluster and merge them in successively larger clusters. Divisive algorithms begin with the whole set and proceed to divide it into successively smaller clusters.

8.4.3 Hierarchical agglomerative clustering

The above general considerations about data mining allow to deduce that hierarchical clustering methods represent a procedure for transforming a proximity matrix into a sequence of nested partitions. A mathematical formulation of the present concept can be devised.

The N objects to be clustered are denoted by $\mathcal{S} = \{x_1, x_2, \ldots, x_N\}$, where x_i is the i-th object. A partition $\mathcal{C}$ of $\mathcal{S}$ breaks $\mathcal{S}$ into subsets $\{C_1, C_2, \ldots, C_M\}$ which satisfy the following properties:

$$C_i \cap C_j = \oslash \qquad \text{for} \quad i, j = 1, \ldots, M \quad i \neq j$$
$$C_1 \cup C_2 \cup \ldots \cup C_M = \mathcal{S}\,.$$

The generic component C_i of the partition $\mathcal{C}$ is called cluster. Partition $\mathcal{C}^{(l-1)}$ is nested into partition $\mathcal{C}^{(l)}$ if every component of $\mathcal{C}^{(l-1)}$ is a subset of a component of $\mathcal{C}^{(l)}$. In other words, $\mathcal{C}^{(l)}$ is formed by merging components of $\mathcal{C}^{(l-1)}$. Hence, a hierarchical clustering is a sequence of partitions in which each partition is nested into the next partition in the sequence; an agglomerative algorithm for hierarchical clustering starts from the set of disjoint objects $\mathcal{S} \equiv \mathcal{C}^{(0)}$ (which can be seen as a set of clusters containing a single object each) and, on the basis of the proximity matrix, merges two or more of these trivial clusters into higher order partitions. The process lead to a sequence of nested clusters containing all N objects. At last, the partition $\mathcal{C}^{(N)}$ contains a single cluster of all the N starting objects.

A picture of a hierarchical clustering is more readable and intuitive: a *dendrogram* is a special type of tree structure which provides a convenient representation of all the steps of a hierarchical clustering. Starting from the leaves (elements of $\mathcal{S}$), several branches are created to connect them on the basis of dissimilarity rules. The branches are then nested into one another creating a multi-level clustering.

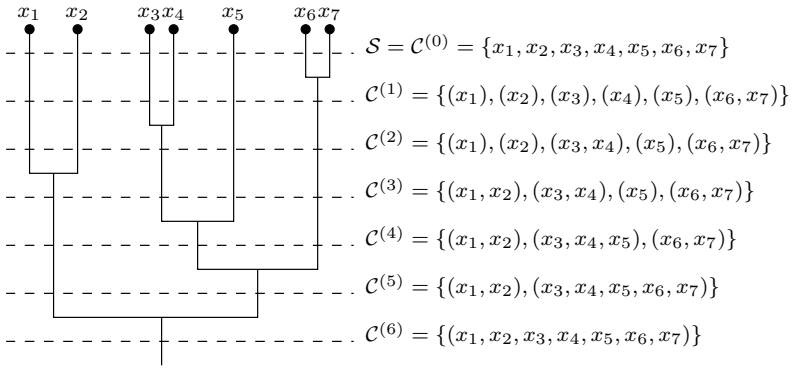

Figure 8.2: Example of a dendrogram. The subsequent clustering of an agglomerative method can be seen reading it top-bottom, while a divisive algorithm (not discussed here) is obtained scrolling bottom-up.

Cutting the dendrogram horizontally, a generic partition $\mathcal{C}^{(l)}$ of $\mathcal{S}$ is created. Refer to Figure 8.2 for a simplified example starting with 7 objects.

The creation order for the nested partitions is usually based on few simple rules which allow to fix criteria to merge clusters starting from the data collected in the proximity (or dissimilarity) matrix. The main problem is how to modify the proximity matrix when a cluster is created, or, in other terms, how to define the distance $d(i^{(l)}, j^{(l)})$ between two clusters $C_i^{(l)}, C_j^{(l)} \in \mathcal{C}^{(l)}$. Many strategies can be followed when a Minkowski metric is used:

$$d(i^{(l)}, j^{(l)}) = \min\{d(i,j) : x_i \in C_i^{(l)}, x_j \in C_j^{(l)}\} \qquad \textit{Single-linkage}$$

$$d(i^{(l)}, j^{(l)}) = \max\{d(i,j) : x_i \in C_i^{(l)}, x_j \in C_j^{(l)}\} \qquad \textit{Complete-linkage}$$

$$d(i^{(l)}, j^{(l)}) = \frac{1}{\mathrm{card}(C_i^{(l)})\mathrm{card}(C_j^{(l)})} \sum_{x_i \in C_i^{(l)}} \sum_{x_j \in C_j^{(l)}} d(i,j) \qquad \textit{Average-linkage}$$

which correspond respectively to the minimum distance, maximum distance and average distance between elements of two different clusters. More complex rules can be defined (sum of all intra-cluster variance, increase in variance for the cluster being merged, probability that candidate clusters spawn from the same distribution function, ...) but their detailed description is out of the aim of the present work.

In particular, when trying to merge objects in a physical space, the interest is to obtain sets of "near" objects, where "near" is intended in term of Euclidean distance for the considered property (space coordinate, velocity, energy, mass, ...). Moreover, an upper limit d_{th} can be fixed on the distance, in order to obtain clusters which contain as many elements as possible but all inside a maximum distance. Under this viewpoint, the complete-linkage agglomerative clustering method is considered the most suitable.

Hence, a simple algorithm can be implemented to iteratively modify the proximity

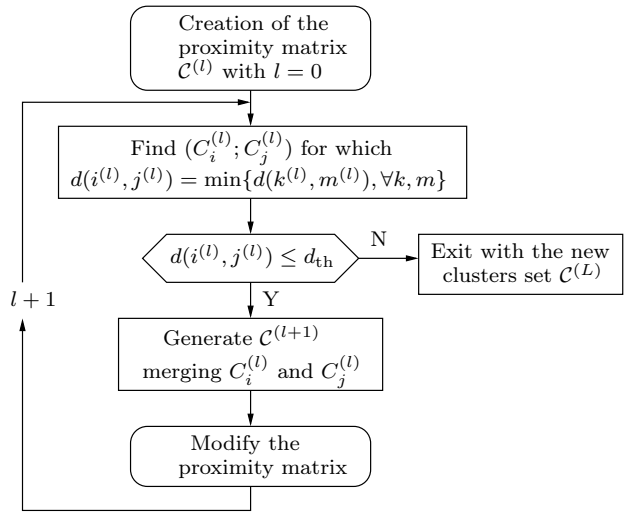

Figure 8.3: Flow chart of the hierarchical agglomerative complete-linkage clustering iterative procedure.

matrix when a new cluster is created. Starting from the disjoint clustering of zero-th level, the proximity matrix is generated for $\mathcal{C}^{(l)}$ with $l = 0$. The most similar pair $(C_i^{(l)}; C_j^{(l)})$ is found in the current clustering configuration $\mathcal{C}^{(l)}$ looking for the minimum of the proximity matrix

$$d(i^{(l)}, j^{(l)}) = \min\{d(k^{(l)}, m^{(l)})\, \forall k, m\}\,,$$

and asking for $d(i^{(l)}, j^{(l)}) \leq d_{\text{th}}$. The clustering level l is incremented to $l+1$ and the clusters $C_i^{(l)}$ and $C_j^{(l)}$ merged together to obtain the new configuration $\mathcal{C}^{(l+1)}$, which corresponds to $\mathcal{C}^{(l)}$ where $C_i^{(l)}$ and $C_j^{(l)}$ has generated $C_r^{(l+1)}$. The proximity matrix is then updated for the new configuration following a complete-linkage clustering strategy: the rows and columns corresponding to $C_i^{(l)}$ and $C_j^{(l)}$ are deleted and a new row-column corresponding to $C_r^{(l+1)}$ is added; moreover, the distance between the new cluster $C_r^{(l+1)}$ and the generic $C_s^{(l+1)} = C_k^{(l)}$ (which has not been modified from the previous level l) is updated to

$$d(r^{(l+1)}, s^{(l+1)}) = \max\{d(i^{(l)}, k^{(l)}), d(j^{(l)}, k^{(l)})\}\,.$$

If all the distances $d(r^{(l+1)}, s^{(l+1)})$ are greater than d_{th} for each $r^{(l+1)}, s^{(l+1)}$ or if all the objects are in one single cluster, then the algorithm ends with $\mathcal{C}^{(L)}$ as last cluster configuration, else the level index l is again incremented and the iterative procedure continues.

8.4.4 Multi-properties clustering

Basically, the above described clustering method can be used to create group of "near" elements in a generic D-dimensional space where a Minkowski metric can be

defined. For instance, if the six dimensional phase space of particles positions and velocities is considered ($D = 6$), the method could be employed to obtain clusters of particles in it: they would be contained in hyper-spheres with a maximum threshold radius which combine both properties of positions and velocities spaces. To maintain a physical meaning for the threshold distances, the starting attributes have usually to be renormalized through a scaling constant: returning to the original phase space, the hyper-sphere defined for the scaled properties is transformed in a hyper-ellipsoid with not equal axis along the main directions. In similar cases, a more intuitive and physical way to select particles is to subdivide the 6D phase space into a 3D spatial space and a 3D velocity space, defining two threshold distances, one for the spatial coordinates and one for the particles velocities. Hence, the proposed technique can be generalized to nest more than one clustering procedure applied to the clusters obtained for the previous property.

Let ${}^{(k)}\mathcal{P}$ be the set of clusters ${}^{(k-1)}\mathcal{C} \equiv \mathcal{C}^{({}^{(k-1)}L)}$ obtained as last configuration of the hierarchical agglomerative complete-linkage clustering method applied to the elements for the generic $k-1$ property (or set of properties), ${}^{(k-1)}L$ being the last level index of the clustering, corresponding to condition $d(r^{({}^{(k-1)}L+1)}, s^{({}^{(k-1)}L+1)}) > {}^{(k-1)}d_{\mathrm{th}}\ \forall r, s$. The above denoted $\mathcal{S}$ set corresponds to the only element of the starting set for $k = 0$: ${}^{(0)}\mathcal{P} \equiv \{{}^{(0)}\mathcal{S}\}$. The clustering procedure is firstly applied to the set ${}^{(0)}\mathcal{S}$ of single elements, with a threshold distance ${}^{(0)}d_{\mathrm{th}}$, leading to a new set of clusters ${}^{(0)}\mathcal{C} \equiv \mathcal{C}^{({}^{(0)}L)}$, whose elements represents the starting sets ${}^{(k)}\mathcal{S}$ for the next property, all collected in ${}^{(k)}\mathcal{P}$ for $k = 1$; then, for each element ${}^{(k)}\mathcal{S}_i \in {}^{(k)}\mathcal{P}$, equivalent to one of the clusters ${}^{(k-1)}C_k \equiv C_i^{({}^{(k-1)}L)}$ collected in ${}^{(k-1)}\mathcal{C}_i$, the clustering procedure is repeated with the next threshold distance ${}^{(k)}d_{\mathrm{th}}$. Once terminated the sequence of new starting sets ${}^{(k)}\mathcal{S}_i$, the clustering is completed for the properties k and the new sub-clusters are recollected in ${}^{(k+1)}\mathcal{P}$. The index k is then incremented to $k+1$ and the procedure repeated for the new sub-cluster sets. A sketch of the flow chart of the procedure is reported in Figure 8.4.

The described sub-clustering technique will produce new clusters for a new property starting from the old ones obtained for the previous attribute. Hence, the elements of each cluster cannot be exchanged between clusters pertaining to different property levels.

The main advantage of this second approach to multi-dimensional clustering is the possibility to define separate threshold distances for the physical properties of interest. The main drawback lies in the need of defining a fixed order in clusters creation: two particles very closed in velocity cannot be merged together if belonging to different clusters obtained for spatial separation, even if their velocity distance is lower than the threshold distance for the velocity clustering.

8.5 Splitting

In PIC codes, when the charge spatial distribution fluctuates rapidly on the grid, usually because of a too low number of particles per cell, the solution of the electric field is affected by numerical noise. Moreover, it's widely known that Monte Carlo techniques effectiveness depends on a sufficiently high number of sample. Great care must be devoted to avoid local depletion of simulation particles, due to adsorbing

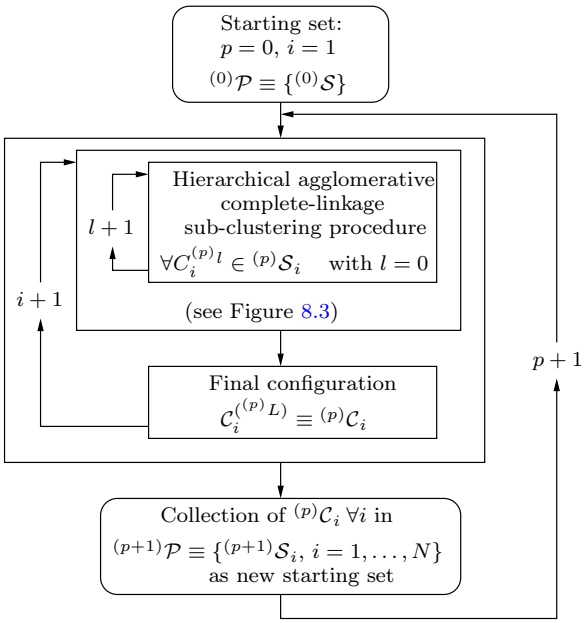

Figure 8.4: Flow chart of the multi-properties sub-clustering iterative procedure. The reader is referred to Figure 8.3 for a detailed flow chart of the main block (d_{th} has to be intended for the k-th property, ${}^{(k)}d_{\text{th}}$).

events or charge neutralization. A splitting technique, successfully employed in Monte Carlo simulations, can be adapted to hybrid PIC-MCC codes in order to reduce noise and to improve representativeness in the phase-space domain.

8.5.1 Introduction

In many simulation of industrial plasma application a depletion of particles in certain domain regions is observed [118]. This phenomenon is essentially related to an excessive weight of the simulation particles: typically $10^7 \div 10^8$ real charges are represented by one simulation particle, seeking a reduction of total computation time. Nevertheless, plasma dynamics simulations could lead to a not uniform distribution of simulation particles in the domain of interest; moreover, if weight-based technique are implemented to randomly reduce the number of simulation particles (for instance, *russian roulette*), some specific region (like the cathode-fall one [118]) could undergo a heavy depletion of particles.

Since the MC technique [140, 141, 142, 143, 145] requires a sufficiently high sampling to reduce the variance of the stochastic processes, the problem of low number of particles per cell does not influence only the solution of the electric field. For a classical MC model, the variance is proportional to inverse of the square root of the number of samples (if no variance reduction technique is used and a Poisson distribution is assumed), which means that the representativeness of the results is heavily influenced by the particles number N_{p}; on the other hand, as mentioned before, the

CPU-time is directly proportional to N_p (in unbiased simulations). Moreover, the study of phenomena characterized by a threshold energy (i.e. ionization, inelastic scattering, ...) usually makes the statistics of high energy particles less representative with respect to those of bulk energy ones.

A logical approach of the problem is the development of weight-based variance and noise reduction techniques acting on the whole phase-space and combined with proper conservation rules.

In the past, few authors developed similar techniques [118] based on ion splitting at the interface between cathode-fall and bulk regions in glow discharges. The method presented can be extended and generalized to the whole phase space defining few basic rules not specific for a particular simulation.

8.5.2 Spatial splitting

Splitting technique are widely used in MC simulations. Here they will be briefly presented underlining the weight meaning and its importance for conservation rules.

The weight w_i of the i-th simulation particle is exactly the number (or fraction) of real charges it represents. During its motion the particle can be splitted into N_c^{split}; consequently its weight has to be updated to the value

$$w_i^{\text{new}} = \frac{w_i^{\text{old}}}{N_c^{\text{split}}}\,, \tag{8.27}$$

since the number of simulation particles increases artificially while that of real charges is unchanged. Particles weight acts on both charge q and mass m of the species: it means that $q_i = qw_i$ and $m_i = mw_i$, while the ratio $q/m = q_i/m_i$ remains unchanged. As far as energy and momentum are considered, the new weighted particle represents a particle of the same species of the original one with its energy and momentum properties but a reduced importance w_i. A rigorous weighting management assures the satisfaction of all conservation laws and the right values of tallied quantities.

After the splitting procedure, all the splitted particles will have the same velocity and position of the unsplit original one: conservation laws of momentum, energy, mass and charge are all satisfied and no noise effect is artificially introduced. This implies that, at a first stage, all the reduced weight particles will move along the same trajectory; the randomness of the collisions with the neutral gas, governed by the P_{coll} of equation (7.10), will then separate the particles histories. In a collisionless system, the splitting technique wouldn't lead to any different result. The degree of homogenization, and thus the efficiency of the scheme, increases with L/λ, where L is the characteristic length of the low-density region and λ the mean free path of the charged particle in the background gas.

Inside the MCC module, the simulation particles will undergo collisions as real charged particles and not as simulation weighted particles. Consistently, a simulation particle with weight w_i generates w_i-weighted electrons and ions in an ionization event.

In MC simulations the splitting technique is applied when a particle undergoes an event or when it crosses an interface (real or virtual). The second criterion was followed in [118] by separation of the domain in a bulk and cathode-fall re-

gion. Nevertheless, in addition to MC models, PIC algorithms introduce the time discretization and, consequently, the virtual time-interfaces to call the splitting procedure. Every N_t time steps a check is made over the number of particles N_c per each cell; if it is less than a threshold value $N_c^{\min}$, the particles will be splitted in order to obtain an optimum number $N_\mathrm{c}^{\mathrm{opt}} > N_c^{\min}$ of simulation particles per cell; chosen a number of splitted particle N_c^{split} per each original one, they will gain new weights given by equation (8.27).

A slightly different approach let to calculate how many particles in the cell ($\underline{N}_c$ of N_c) have to be splitted into $\underline{N}_c^{\mathrm{split}} = \mathrm{floor}(N_\mathrm{c}^{\mathrm{res}}/N_c^{w_i>w_{\min}})$ and how many ($\overline{N}_c$) in $\overline{N}_c^{\mathrm{split}} = \underline{N}_c^{\mathrm{split}} + 1 = \mathrm{ceiling}(N_\mathrm{c}^{\mathrm{res}}/N_c^{w_i>w_{\min}})$ in order to obtain exactly $N_\mathrm{c}^{\mathrm{opt}}$. The answer is given by the solution of the following system

$$\begin{aligned}
&\underline{N}_c\underline{N}_c^{\mathrm{split}} + \overline{N}_c\overline{N}_c^{\mathrm{split}} = N_\mathrm{c}^{\mathrm{res}} \\
&\underline{N}_c + \overline{N}_c = N_c^{w_i>w_{\min}} .
\end{aligned}$$

Combining the two equations, one obtains

$$\underline{N}_c = N_c^{w_i>w_{\min}}\overline{N}_c^{\mathrm{split}} - N_\mathrm{c}^{\mathrm{res}} \tag{8.28a}$$

$$\overline{N}_c = N_c^{w_i>w_{\min}} - \underline{N}_c . \tag{8.28b}$$

A sorting of the particle on the basis of their weight would be useful seeking maximum uniformity. Since the weights of the splitted particles are obtained by dividing the old weights by the number of particles in which the original has been splitted, they will vary of $1/\underline{N}_c^{\mathrm{split}} - 1/\overline{N}_c^{\mathrm{split}}$ ($1/2 - 1/3 \simeq 0,1667$ as maximum) between the two ensemble of $\underline{N}_c^{\mathrm{split}}$ and $\overline{N}_c^{\mathrm{split}}$ particles. It is easy to show that the number $\overline{N}_c$ is simply given by the remainder of the ratio between the number of particles wanted after the splitting, N_c^{res}, and the number of splittable ones, $N_c^{w_i>w_{\min}}$: by substitution of equation (8.28a) in equation (8.28b) one obtains

$$\begin{aligned}
\overline{N}_c = N_c^{w_i>w_{\min}} - \underline{N}_c = N_c^{w_i>w_{\min}}(1 - \overline{N}_c^{\mathrm{split}}) + N_\mathrm{c}^{\mathrm{res}} = \\
= N_\mathrm{c}^{\mathrm{res}} - N_c^{w_i>w_{\min}}\underline{N}_c^{\mathrm{split}}
\end{aligned}$$

as well as through the definition of the remainder function

$$\begin{aligned}
\mathrm{mod}(N_\mathrm{c}^{\mathrm{res}}, N_c^{w_i>w_{\min}}) = N_\mathrm{c}^{\mathrm{res}} - \mathrm{floor}\left(\frac{N_\mathrm{c}^{\mathrm{res}}}{N_c^{w_i>w_{\min}}}\right) N_c^{w_i>w_{\min}} = \\
= N_\mathrm{c}^{\mathrm{res}} - N_c^{w_i>w_{\min}}\underline{N}_c^{\mathrm{split}} .
\end{aligned}$$

8.5.3 Energetic splitting

As seen in Section 6.1.2, plasma electron species in rapidly varying and highly intense electric fields is usually characterized by Maxwellian-shaped EEDF, with a more populated energetic tail. Notwithstanding this, the number of particles with high energies is sensitively lower than that of the bulk ones. In plasma simulations with particle-codes, this affects the variance of the obtained EEDF. A way to reduce the arising fluctuations is the artificial increase of energetic particles, achievable by particle splitting based on an energetic-check.

While, in real space, the grid helps the splitting technique by definition of cells, PIC codes treat energy in continuum. Then, the first step is the discretization of energy in proper bins $\Delta\mathcal{E}_b(\mathcal{E})$ and the definition of the optimum number of particles per bin $N_b^{\rm opt}$. The total number of particles should be substituted by their density $\rho_b^{\rm opt} = N_b^{\rm opt}/\Delta\mathcal{E}_b$ in the energetic bin b of width $\Delta\mathcal{E}_b$: asking for a constant $\rho_b^{\rm opt}$, it follows that $N_b^{\rm opt}$ varies over b. Following a strategy similar to that of spatial splitting, a minimum acceptable density $\rho_b^{\rm min}$ is defined as a threshold and $N_b^{w_i>w_{\rm min}}$ is the number of particles to be splitted into $N_b^{\rm split}$ new particles, for each energetic bin. Since $N_b^{\rm opt}$ must be an integer, it has to be defined as

$$N_b^{\rm opt} = {\rm int}(\rho_b^{\rm opt}\Delta\mathcal{E}_b)\,,$$

where the choice of the ${\rm int}(x)$ seems here the best one. Note that $N_b^{w_i<w_{\rm min}}$ particles cannot be splitted having a too low weight; then the number of particles to be obtained from the splitting is given by

$$N_b^{\rm res} = N_b^{\rm opt} - N_b^{w_i<w_{\rm min}} = {\rm int}(\rho_b^{\rm opt}\Delta\mathcal{E}_b) + N_b^{w_i>w_{\rm min}} - N_b\,.$$

If an energy bin results completely emptied of particles, then the constant density $\rho_b^{\rm opt}$ cannot be achieved over it in any way. To avoid this, the void bins should be merged together adjacent ones until they contain at least one particle: broadening the width of the energy bin, the optimum number of particles $N_b^{\rm opt}$ increases. Note that the splitted particles will have the same energy of the original one and only after few collisions they will be redistributed in space and velocity components.

A higher sampling rate for energetic particles improves the representativeness of high energy events, like ionization and inelastic scattering, reducing the variance of the high energetic distribution tail. In any case, this does not modify the time-evolution of the species: collisions will redistribute energies with no influence on the exponential growth due to ionization phenomenon. From the collisional point of view, there is no reason to discretize the whole velocity field, since cross sections depend only on the incident particle energy (see equation (7.10)).

8.5.4 Spatial and energetic splitting

The procedures presented in Section 8.5.2 and Section 8.5.3 are not mutually excluding. On the contrary, it's reasonable to apply both of them. If the spatial splitting is applied as first, the energetic splitting could modify the number of particles per cell increasing it over $N_c^{\rm opt}$, or, also, over $N_c^{\rm max}$; the reverse order would modify the optimum choice for $\rho_b^{\rm opt}$. This means that a coupled technique has to be developed.

The three dimensional space of coordinates $(x_1, x_2, \mathcal{E})$ can be easily meshed by composition of the spatial grid and of an energetic binning. The possible strategy is based on the definition of an optimal density $\rho_{c,b}^{\rm opt}$ of simulation particles per each 3D $\Delta x_1\Delta x_2\Delta\mathcal{E}_b$ element of the virtual phase space, which corresponds to an optimal varying total number $N_{c,b}^{\rm opt}$. The same strategy followed in the energetic splitting should be followed locally for each grid cell.

The new number of particles per spatial cell is obtained as the projection of the particles of each bin under the same cell in the spatial plane or, in other terms, as the summation of $N_{c,b}^{\rm opt}$.

Since the preservation of an optimum number of particles per cell $N_c^{\rm opt}$ is the main task, the density of particle per 3D element has to be defined in order to obtain

$$N_c^{\rm opt} = \sum_b \rho_{c,b}^{\rm opt} \Delta x_1 \Delta x_2 \Delta \mathcal{E}_b = \rho_b^{\rm opt} \sum_b \Delta \mathcal{E}_b = \rho_b^{\rm opt} (\mathcal{E}_{\rm max} - \mathcal{E}_{\rm min}) \,,$$

since $\Delta x_1 \Delta x_2$ is independent of b: $\rho_b^{\rm opt} = \rho_{c,b}^{\rm opt} \Delta x_1 \Delta x_2$; this means

$$\rho_b^{\rm opt} = \frac{N_c^{\rm opt}}{\mathcal{E}_{\rm max} - \mathcal{E}_{\rm min}} \,,$$

known for a fixed $N_c^{\rm opt}$.

The splitting procedure has to be applied to each 3D element, producing the total number of particle $N_{c,b}^{\rm opt}$, given by

$$N_{c,b}^{\rm opt} = {\rm int}(\rho_{c,b}^{\rm opt} \Delta x_1 \Delta x_2 \Delta \mathcal{E}_b) = {\rm int}(\rho_b^{\rm opt} \Delta \mathcal{E}_b) \,.$$

The choice of the function int(x), instead of floor(x) or ceiling(x), modifies the number of $N_{c,b}^{\rm opt}$ of ± 1 and, then, could drastically modify the total value of $N_c^{\rm opt}$ or produce a compensation of the effects. If the energetic bins are equally spaced, the local effect is always the same, being $\rho_b^{\rm opt}$ constant, and so the total effect (in excess or defect) is equal to the total number of energetic bins. To artificially avoid this, one could use alternatively the floor(x) and ceiling(x) function varying the index b. This can be mathematically translated in

$$N_{c,b}^{\rm opt} = {\rm floor}(\rho_b^{\rm opt} \Delta \mathcal{E}_b) + \frac{1 + (-1)^b}{2} \,,$$

where the second addendum gives an exceeding particle when b is even and no exceeding particle when it is odd.

Once $N_{c,b}^{\rm opt}$ is known, the number of particles $N_{c,b}^{\rm res}$ to be obtained by splitting, per each bin b over the cell c, is given by

$$N_{c,b}^{\rm res} = N_{\rm c,b}^{\rm opt} - N_{c,b}^{w_i < w_{\rm min}} = {\rm floor}(\rho_b^{\rm opt} \Delta \mathcal{E}_b) + \frac{1 + (-1)^b}{2} - N_{c,b}^{w_i < w_{\rm min}} \,, \qquad (8.29)$$

where subscripts and superscripts have the usual meaning. Following a strategy similar to the one presented in the spatial case, the number of particle $N_{c,b}^{\rm split}$ in which each particle of the 3D element with indexes b, c have to be splitted can be defined as:

$$N_{c,b}^{\rm split} = {\rm int} \left(\frac{N_{c,b}^{\rm res}}{N_{c,b}^{w_i > w_{\rm min}}} \right) \,, \qquad (8.30)$$

or, even better, the couple of values $\underline{N}_{c,b}$ and $\overline{N}_{c,b}$ can be obtained starting from $N_{c,b}^{w_i > w_{\rm min}}$ and $N_{c,b}^{\rm res}$ and defining $\underline{N}_{c,b}^{\rm split} = {\rm floor}(N_{\rm c}^{\rm res} / N_c^{w_i > w_{\rm min}})$ and $\overline{N}_{c,b}^{\rm split} = \underline{N}_c^{\rm split} + 1 = {\rm ceiling}(N_{\rm c}^{\rm res} / N_c^{w_i > w_{\rm min}})$, as presented in equations (8.28).

8.5.5 Implicit splitting and forced generation

Another MC technique which could be superimposed to the just described splitting procedure, is the implicit splitting. Usually the depletion of particles arises in the cathode-fall region; right here secondary electrons are produced by interaction of ions with the cathode boundary. Then, whenever an ion hits the cathode, it can be supposed as composed of N^{split} ions of weight $1/N^{\text{split}}$ increasing artificially the number of samples on which the secondary electron emission test will be made by comparison of its probability γ with a random number R.

Alternatively, the forced generation can be implemented: every time an ion hits the cathode boundary it will produce a secondary electron with weight given by the product of the ion weight and the secondary emission probability, only if the ion weight is greater than the inverse of the related emission probability. In this way a secondary electron able to sustain the discharge will be certainly produced but with a reduced weight proportional to the real probability associated to its production. Even without increasing the samples number, the statistics is improved acting on particle weight.

The same strategy can be successfully adopted in the case of secondary electron emission by photons hitting the cathode (photoelectric effect). Since excited atoms emitting UV photons increases exponentially in time, the contribution of emitted secondary electrons could lead to overcome the maximum allowable number of simulation particles. This can be easily avoided defining a threshold value N_{th} for the number of emitted electrons: when the number of secondary electrons $N_{\nu\text{e}}$ is greater than N_{th}, then it is artificially imposed equal to N_{th}, while the weight of emitted electrons is increased by a factor $N_{\nu\text{e}}/N_{\text{th}}$.

8.6 Algorithms details

In Section 7.3, the global description of the developed code was given together with the assumptions and approximations of the model. In particular, the flowchart of Figure 7.13 included a last block related to merging and splitting technique as a black-box. Now that the basic theory of the two methods have been worked out, a more detailed description of their implementation and code integration will be given.

8.6.1 Clustering and merging

The data clustering techniques proposed in Section 8.4 can be successfully used to select particles with similar properties in the phase space.

A hybrid method was chosen to exploit the presence of the uniform spatial grid. The hybrid counting sort, implemented to accelerate the simulation, increasing the number of cache-hits (see Section 7.A.1), allows to obtain particles already divided into cells.

A hierarchical agglomerative complete-linkage sub-clustering technique is, instead, used to select near particles in the velocity space. Many tests were done combining velocity components in multiple sets of attributes. In particular, the direction of flight ($\theta_v = \pm \arctan(v_1/v_2)$), the planar velocity ($v_{1,2} = \sqrt{v_1^2 + v_2^2}$) and the total energy ($\mathcal{E} = 1/2m(v_{1,2}^2 + v_3^2)$) were chosen as final properties: the direction of flight

and planar velocity are of great importance to maintain a good representativeness of the macroscopic motions in the 2D spatial domain of the simulation; on the other hand, the cross sections of the collisional module are strictly connected with the energy of the particles. In many cases, the cross sections energy dependence is smoother if the logarithm of the energy is considered; therefore the total energy attribute has been substituted with a sort of particle lethargy property, $\log \mathcal{E}$.

Once the hybrid counting sort and the hierarchical sub-clustering have grouped particles by cells and $(\theta_v, v_{1,2}, \log \mathcal{E})$ properties, the merging techniques described in Section 8.2 and Section 8.3 can be applied to each set containing more than two particles. The spatial merging guarantees the grid moments conservation for starting particles belonging to the same cell, while the velocities merging preserves the momentum components and the total energy of the set. In particular, the formulation of Section 8.3.2 appears as accurate as that of Section 8.3.3, at a lower computational cost: the MCC module is effective in redistributing the new equal velocities of the particles.

One of the main disadvantage of the method is a variance increase in the distribution functions of the particles, since the merging procedure imply a decrease in the number of samples. However, the net effect is a homogenization of the variance over the whole distribution spectrum: the merging is more effective in overpopulated regions being easier to find particles with similar properties, while is rather useless in low density regions of the velocity space where the number of samples would remain unchanged. Hence, the method can be defined as a variance "homogeneization" technique. The reader is referred to Chapter 9 for a detailed analysis of the results, both from a physical and numerical point of view.

8.6.2 Splitting algorithm

The effectiveness of the splitting algorithm cannot be fully tested in the application of interest: the high values of the external electric fields reduces the numerical noise induced by depleted regions, where the particle number per cell decreases; moreover, the electron secondary emission by ion impact is negligible in the first stage of the discharge, thus reducing the importance of a good statistics in the regions near the cathode. Moreover, the implementation of a local merging technique against a global particle number reduction of the "russian roulette" type, prevents from an excessive particle depletion. In any case, the splitting technique has been implemented in order to test if any bias on the solution is introduced or not. The results show no appreciable perturbation; since the splitting increases the global number of particles (and then the CPU-time and memory consumption) without any essential improvement, the technique has not been intensively employed.

On the other hand, the forced emission technique described in Section 8.5.5 has revealed itself an effective method to make the most of the low number of ions colliding on the cathode surface. The opposite approach is exploited from secondary electrons emission for photo-electric effect (see Section 7.2.5): when the number of impinging photons is so high to induce the emission of too many electrons, these are merged together before being emitted increasing their statistical weight in order to keep under control their contribution to the total number of simulation particles in the system.

8.6.3 Code integration and flowcharts

The above described technique have to be integrated in the developed code. The already mentioned hybrid counting sort has been implemented, not only to accelerate the code improving the number of cache hits, but even to obtain an sorted array of particles grouped by spatial cell of the simulation domain. The allocation table built in the intermediate cycle over cells (see Figure 7.15) contains the total number N_c of particles for each cell. Once fixed a maximum acceptable number $N_{\max}$ and a minimum number $N_{\min}$ of particles contained in the generic cell, the comparison of N_c with these threshold values is performed in order to decide if a merging or splitting procedure has to be applied or if any action is required.

In the case $N_c > N_{\max}$, the grouping of particles in the phase-space is performed. The counting sort is slightly modified to maintain the particles with a weight $w_i > w_{\max}$ separated from the others, to avoid an excessive increase of their weight through the merging with other super-particles. Hence the subset of particles in the cell with $w_i < w_{\max}$ are analyzed: the properties of interest are evaluated from the velocity components for each particle and the hierarchical agglomerative sub-clustering technique is performed on the multi-properties array. To avoid time and memory losses a sorting is performed on the initial array and on any sub-array corresponding to the generic sub-cluster ${}^{(k)}\mathcal{C}_i$ of ${}^{(k+1)}\mathcal{P}$ for the k-th property (see Section 8.4), in order to allow the evaluation of the distance between adjacent elements without the need of a distance matrix allocation. The employed sorting routine is a classic quick-sort through index-array key-table [195], which avoids the swap of elements, simply sorting their array indexes in a pointer-like viewpoint. Once the loop on properties k is ended, the final cub-clusters are cycled: if the generic l-th cluster contains more than 2 particles, the spatial and velocities merging is performed and the new particles data are written on the original particle array closing the out-of-place counting sort; if the cluster contains only 1 or 2 particle, the merging routine resulting ineffective, they are simply swapped back to the original particle array together with the particles having $w_i > w_{\max}$. All the operations of the clustering and merging procedures are performed making deep use of the masked packing (`PACK(Array,Mask)` function) of the Fortran90.

On the other hand, if $N_c < N_{\min}$, the splitting routine is called. A first loop on the particles is performed to count the number $N_{c,b}^{w>w_{\min}}$ of them contained in each energy bin, having a weight greater than $w_{\min}$, and their array indexes are stored. If the energetic binning and the spatial grid are not modified during the simulation, the optimum number of particle $N_{c,b}^{\text{opt}}$ is fixed, and the number of particles $N_{c,b}^{\text{split}}$ can be evaluated combining equation (8.29) and equation (8.30). The weight of the original particles are modified and the properties rewritten to the original particle array together with the new splitted particles.

Obviously, if $N_{\min} < N_c < N_{\max}$ then nothing is done, but the particles properties are swapped back to the original array.

A sketch which schematize the above description is given in Figure 8.5; the flowchart is intended to be added to that of Figure 7.13, expanding the black-box corresponding to the last cycle over grid nodes.

The characteristic numbers employed in the clustering, merging and splitting procedures are summarized in Table 8.1. They have been tuned on the particular case

of interest and cannot be considered of general validity.

8.A Spatial merging: looking for an alternative solution

The solution presented in Section 8.2 is self-consistent but allows a degree of freedom in the choice of the weight and one coordinate for one of the particles. Exploiting the inertia tensor analogy, one could expect that the conservation of higher order moments allow to determine exactly the position of the two particles in the cell without any arbitrarily chosen parameter. Unfortunately, it will be shown that this is not possible and, moreover, the additional conditions could lead to unacceptable solutions when mixed with the cell bounds.

8.A.1 Second order moments for two particles

In Section 8.2.3, it was shown that the system of conservation equations (8.13) is equivalent to total charge, charge centroid and centrifugal pseudo-inertia moment conservation.

The analogy with the inertia tensor and the not closed form of the system suggest to add more inertia moments conservation laws in order to determine univocally all the 6 unknowns. Therefore, three further conditions can be written:

$$\sum_{i=1}^{N} \omega_i \zeta_i^2 = \sum_{i'=1'}^{N'} \omega_{i'} \zeta_{i'}^2 = I_{\gamma\gamma} \tag{8.31a}$$

$$\sum_{i=1}^{N} \omega_i \gamma_i^2 = \sum_{i'=1'}^{N'} \omega_{i'} \gamma_{i'}^2 = I_{\zeta\zeta} \tag{8.31b}$$

$$\sum_{i=1}^{N} \omega_i (\zeta_i^2 + \gamma_i^2) = \sum_{i'=1'}^{N'} \omega_{i'} (\zeta_{i'}^2 + \gamma_{i'}^2) = I_{\varsigma\varsigma}\,, \tag{8.31c}$$

where ς betoken the third direction, perpendicular to the plane (ζ, γ); the other components are all zero since $\varsigma_i = 0 \; \forall \, i$. It's clear that equations (8.31) are linearly dependent: for a system of particles lying on a plane, $I_{\varsigma\varsigma}$ is known as polar moment and it represents the invariant of the reduced 2×2 tensor for the ζ and γ components. Then, for $N' = 2$ particles, a system of 6 equations in 6 unknowns is obtained. It can be shown that it is not closed. As far as a system of 2 particles is considered, they lie on a line passing through the centroid of the system and have distances inversely proportional to their weights . This condition implies

$$I_{\gamma\gamma} I_{\zeta\zeta} = I_{\zeta\gamma}^2\,, \tag{8.32}$$

not valid, in general, for a system of $N' > 2$ particles. Then, one must conclude that a system of $N > 2$ particles cannot be replaced by only two particles on the basis of total weight, centroid position and inertia moments conservation.

8.A.2 Polar inertia moment conservation

Since the axial inertia moments cannot be both conserved, one could ask for the conservation of the polar one, at least.

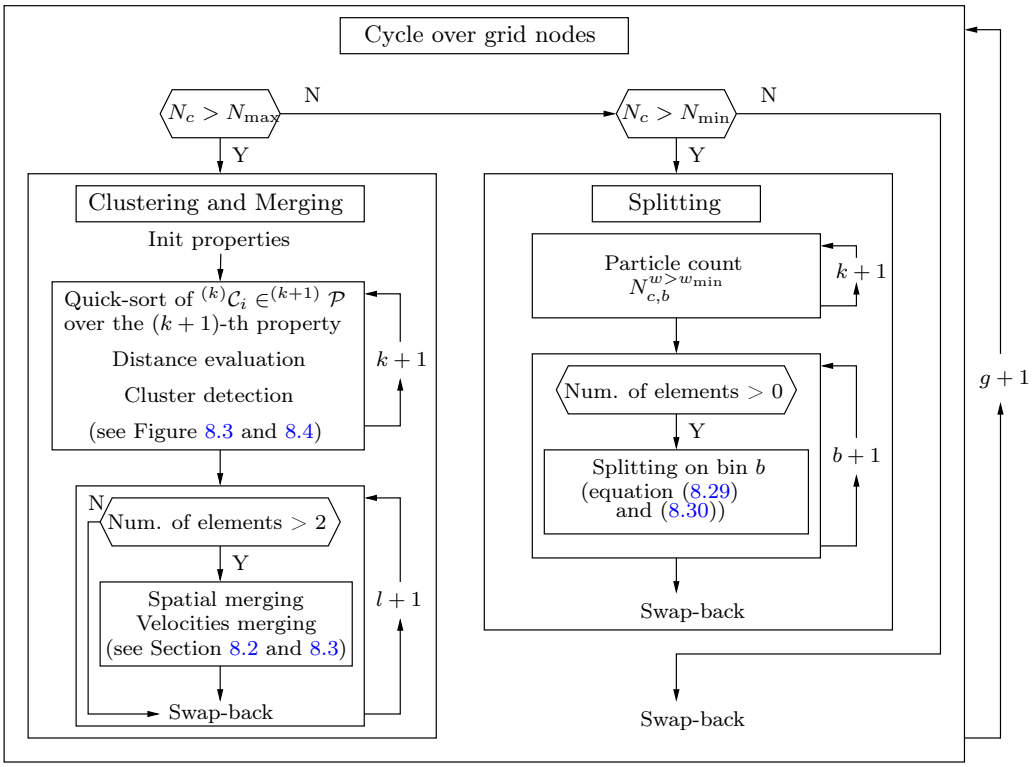

Figure 8.5: Flowchart of the merging and splitting techniques as integrated in the developed code of Figure 7.13.

Description	Expression	Value
Threshold distance on direction of flight	$d_{\text{th}}^{\theta_v}$	0.15π
Threshold distance on planar velocity	$d_{\text{th}}^{v_{1,2}}$	10^6 for electrons 500 for ions
Threshold distance on lethargy	$d_{\text{th}}^{\log \mathcal{E}}$	0.3
Maximum weight for particles undergoing merging	$w_{\max}$	10^9
Minimum weight for particles undergoing splitting	$w_{\min}$	10^{-3}
Optimum number of particles per cell	N_c^{opt}	60
Maximum number of particles per cell	$N_c^{\max}$	100
Minimum number of particles per cell	$N_c^{\min}$	5

Table 8.1: Values of threshold distances, maximum and minimum weight, maximum, minimum and optimum number of particles per cell used in clustering, merging and splitting procedures.

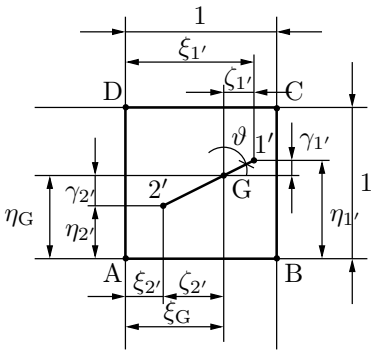

Figure 8.6: Position of the two merged particles in the normalized reference $(\xi, \eta) - (\zeta, \gamma)$.

If one considers $N' = 2$ and works with $\omega_{1'}$ and $\omega_{1'}$ as parameters, the two particles coordinates would then be given by the system of equations (8.14) with the additional condition

$$\zeta_{1'}^2 + \gamma_{1'}^2 = \omega_r I_{\varsigma\varsigma} \tag{8.33}$$

where the first two equations define the positions of the two particles as aligned with the centroid on opposite sides of it; the third equation gives the direction in the plane (ζ, γ) of the line connecting the two particles and containing the centroid, while the last equation represents a weighted distance of the particles with respect to their barycenter. Introducing $\varrho_{1'} = \sqrt{\zeta_{1'}^2 + \gamma_{1'}^2} = \sqrt{\omega_r I_{\varsigma\varsigma}}$ and the angle ϑ between the line containing the two particles and the direction of ζ, as represented in Figure 8.6, by trigonometric relations, equations (8.14b) and (8.14c) are rewritten in the form

$$\zeta_{1'} = -\omega_r \zeta_{2'} = \varrho_{1'} \cos\vartheta \tag{8.34a}$$

$$\gamma_{1'} = -\omega_r \gamma_{2'} = \varrho_{1'} \sin\vartheta \tag{8.34b}$$

and, then, equation (8.14d) gives

$$I_{\zeta\gamma} = \frac{1}{\omega_r}\zeta_{1'}\gamma_{1'} = \frac{1}{\omega_r}\varrho_{1'}^2 \cos\vartheta \sin\vartheta = \frac{1}{2} I_{\varsigma\varsigma} \sin(2\vartheta)\,, \tag{8.35}$$

with $\vartheta \in [-\pi/2, \pi/2[$, due to symmetry reasons. The last equation can be inverted in order to obtain the angle ϑ defined as

$$\vartheta = \frac{1}{2} \arcsin\left(\frac{2I_{\zeta\gamma}}{I_{\varsigma\varsigma}}\right)\,; \tag{8.36}$$

the sine inverse function is defined only for arguments in the interval $[-1, 1]$, but it is easy to show that

$$\left|\frac{2I_{\zeta\gamma}}{I_{\varsigma\varsigma}}\right| \leq 1 \Leftrightarrow I_{\varsigma\varsigma} \geq \pm 2 I_{\zeta\gamma} \Leftrightarrow \sum_{i=1}^{N} \omega_i(\zeta_i^2 + \gamma_i^2) \pm 2 \sum_{i=1}^{N} \omega_i \zeta_i \gamma_i \geq 0 \Leftrightarrow$$

$$\Leftrightarrow \sum_{i=1}^{N} \omega_i (\zeta_i \pm \gamma_i)^2 \geq 0$$

is always true for each (ζ_i, γ_i) being a summation of squared terms. Moreover, the angle given by the sine inverse function is inside the interval $[-\pi/2, \pi/2]$ that implies $\vartheta \in [-\pi/4, \pi/4]$.

8.A.3 The inertia main reference analogy

For a system of two particles, the obtained value of ϑ corresponds to the reference rotation angle which gives the main inertia axis. In general, this doesn't coincide with the reference rotation angle of the initial system containing N particles. The main reference is, indeed, defined as that reference in which the centrifugal inertia moment $I_{\zeta\gamma} = I_{\gamma\zeta}$ is zero; in the rotated reference, the new coordinates are given by

$$\begin{pmatrix} \zeta^* \\ \gamma^* \end{pmatrix} = \begin{pmatrix} \cos\vartheta & \sin\vartheta \\ -\sin\vartheta & \cos\vartheta \end{pmatrix} \begin{pmatrix} \zeta \\ \gamma \end{pmatrix} \qquad \text{with} \qquad \vec{\vec{N}} = \begin{pmatrix} \cos\vartheta & \sin\vartheta \\ -\sin\vartheta & \cos\vartheta \end{pmatrix},$$

and, consequently, the characteristic tensor transformation is

$$\vec{\vec{I}}^* = \vec{\vec{N}}\,\vec{\vec{I}}\,\vec{\vec{N}}^T,$$

which leads to

$$\begin{aligned} I_{\zeta^*\zeta^*} &= \frac{I_{\zeta\zeta} + I_{\gamma\gamma}}{2} + \frac{I_{\zeta\zeta} - I_{\gamma\gamma}}{2} - I_{\zeta\gamma}\sin(2\vartheta) \\ I_{\gamma^*\gamma^*} &= \frac{I_{\zeta\zeta} + I_{\gamma\gamma}}{2} - \frac{I_{\zeta\zeta} - I_{\gamma\gamma}}{2} + I_{\zeta\gamma}\sin(2\vartheta) \\ I_{\zeta^*\gamma^*} &= \frac{I_{\zeta\zeta} - I_{\gamma\gamma}}{2}\sin(2\vartheta) + I_{\zeta\gamma}\cos(2\vartheta). \end{aligned}$$

Note that again $I_{\gamma^*\gamma^*} + I_{\zeta^*\zeta^*} = I_{\gamma\gamma} + I_{\zeta\zeta} = I_{\varsigma\varsigma}$, the polar moment being an invariant of the system. The main reference is obtained by imposing $I_{\zeta^*\gamma^*} = 0$, this condition giving

$$\tan(2\vartheta) = -\frac{2I_{\zeta\gamma}}{I_{\zeta\zeta} - I_{\gamma\gamma}}, \tag{8.38}$$

which defines the rotation angle ϑ that nullify the centrifugal moment $I_{\zeta^*\gamma^*}$ and maximize the axial ones $I_{\zeta^*\zeta^*}$ and $I_{\gamma^*\gamma^*}$. It was shown that equation (8.32) is always true for a system of 2 particles; then, from equation (8.35), applying $\cos(2\vartheta) = \sqrt{1 - \sin^2(2\vartheta)}$, it follows that

$$\tan(2\vartheta) = \frac{\sin(2\vartheta)}{\cos(2\vartheta)} = \frac{2I_{\zeta\gamma}}{\sqrt{I_{\varsigma\varsigma}^2 - 4I_{\zeta\gamma}}},$$

which results equal to equation (8.38) if and only if

$$I_{\gamma\gamma} - I_{\zeta\zeta} = \sqrt{I_{\varsigma\varsigma}^2 - 4I_{\zeta\gamma}^2} = \sqrt{I_{\gamma\gamma}^2 + 2I_{\gamma\gamma}I_{\zeta\zeta} + I_{\zeta\zeta}^2 - 4I_{\zeta\gamma}^2} \Leftrightarrow I_{\gamma\gamma}I_{\zeta\zeta} = I_{\zeta\gamma}^2,$$

as previously stated. The conclusion must not surprise, since the main reference for a system of two particles is identified by the axis coincident with the line connecting the particles: in this case, it results $I_{\gamma^*\gamma^*} = I_{\zeta^*\gamma^*} = 0$ and only $I_{\zeta^*\zeta^*} \neq 0$ (maximized), while for a system of more than 2 particles the inertia ellipses has two main axes

with both $I_{\gamma^*\gamma^*} \neq 0$ and $I_{\zeta^*\zeta^*} \neq 0$. Moreover, it can be noted from equation (8.38) that, since the tangent function has a periodicity of π, both ϑ and $\vartheta + \pi/2$ would lead to the same main reference with an inversion of ζ^* and γ^*. In the particular case of two particles, a rotation of $\pi/2$ would nullify the main inertia moment $I_{\zeta^*\zeta^*}$ and maximize $I_{\gamma^*\gamma^*}$.

8.A.4 The merged particles coordinates

The distances $\varrho_{1'}$ and $\varrho_{2'}$ of the two particles along the main axis are still unknown and strictly dependent on their weights $\omega_{1'}$ and $\omega_{2'}$. Due to the arbitrariness of particles labeling, one can ask the first particle to fall in positive ζ half plane. Paying much attention to the signs, one obtains

$$\begin{aligned}\zeta_{1'} &= \varrho_{1'}\cos\vartheta = \varrho_{1'}\sqrt{1-\sin^2\vartheta}\\ \gamma_{1'} &= \varrho_{1'}\sin\vartheta = \pm\varrho_{1'}\sqrt{1-\cos^2\vartheta}\,,\end{aligned}$$

$\cos\vartheta$ being always positive for each $\vartheta \in [-\pi/2, \pi/2]$ and $\sin\vartheta \geq 0$ only for $\vartheta \in [0, \pi/2]$. Then, working on the squares of sine and cosine, it follows

$$\begin{aligned}\sin^2\vartheta &= \frac{1-\cos(2\vartheta)}{2} \;\Rightarrow\; \cos\vartheta = \sqrt{\frac{1}{2}(1+\cos(2\vartheta))}\\ \cos^2\vartheta &= \frac{1+\cos(2\vartheta)}{2} \;\Rightarrow\; \sin\vartheta = \sqrt{\frac{1}{2}(1-\cos(2\vartheta))}\,.\end{aligned}$$

In order to use equation (8.35), the $\cos(2\vartheta)$ has to be converted in $\pm\sqrt{1-\sin^2(2\vartheta)}$ where the positive sign is obtained for $\vartheta \in [-\pi/4, \pi/4]$ and the negative one outside. By substitution, the two coordinates of the first merging particle are

$$\zeta_{1'} = \varrho_{1'}\sqrt{\frac{1}{2}\left(1 \pm \sqrt{1-\sin^2(2\vartheta)}\right)} = \sqrt{\omega_{\mathrm{r}}\frac{I_{\varsigma\varsigma} + \chi\sqrt{I_{\varsigma\varsigma}^2 - 4I_{\zeta\gamma}^2}}{2}} \tag{8.39a}$$

$$\gamma_{1'} = \pm\varrho_{1'}\sqrt{\frac{1}{2}\left(1 \mp \sqrt{1-\sin^2(2\vartheta)}\right)} = \kappa\sqrt{\omega_{\mathrm{r}}\frac{I_{\varsigma\varsigma} - \chi\sqrt{I_{\varsigma\varsigma}^2 - 4I_{\zeta\gamma}^2}}{2}}\,, \tag{8.39b}$$

where χ and κ depends on ϑ and modifies only the signs in the expressions as given in the following scheme

$\vartheta \in$	$[-\pi/2, -\pi/4]$	$[-\pi/4, 0]$	$[0, \pi/4]$	$[\pi/4, \pi/2]$
χ	$-$	$+$	$+$	$-$
κ	$-$	$-$	$+$	$+$

The position of the second particle is immediately obtained by equations (8.34).

It arises evident that the coordinates expressions are in the form of solutions of an equation of the fourth order directly obtainable from the system of Section 8.A.2.

Looking at the table summarizing the signs of χ and κ, one could complain that the interval for ϑ as obtained from equation (8.36) must be $[-\pi/4, \pi/4]$ due to the invertibility of sine function. The ϑ interval of variability can, indeed, be limited to

$[-\pi/4, \pi/4]$ without lack of generality: the complementary interval over $[-\pi/2, \pi/2]$ is completely equivalent. In both cases, $|I_{\zeta\gamma}|$ and $I_{\varsigma\varsigma}$ are still conserved. Obviously, inverting the ζ and γ coordinates produces an inversion of $I_{\zeta\zeta}$ and $I_{\gamma\gamma}$, which are not included in the considered system of equations.

8.A.5 Unique choice of the rotation angle

The $I_{\gamma\gamma}$ axial moment can be used to determine univocally the rotation angle in $[-\pi/2, \pi/2]$ rather than in $[-\pi/4, \pi/4]$. From equation (8.31a) it follows that

$$\omega_{1'}\zeta_{1'} + \omega_{2'}\zeta_{2'} = I_{\gamma\gamma} \qquad \Rightarrow \qquad \zeta_{1'} = \varrho_{1'}^2 \cos^2\vartheta = \omega_{\mathrm{r}} I_{\gamma\gamma}\,;$$

an expression for $\cos\vartheta$ can be immediately derived:

$$\cos\vartheta = \sqrt{\frac{I_{\gamma\gamma}}{I_{\varsigma\varsigma}}}\,. \tag{8.40}$$

The assumption $\zeta_{1'} > 0$ implies $\cos\vartheta > 0$, which means $\vartheta \in [-\pi/2, \pi/2]$. Therefore, it's enough to evaluate if

$$\cos\vartheta \gtrless \frac{\sqrt{2}}{2}$$

to know if $\vartheta \in [-\pi/4, \pi/4]$ or $\vartheta \in [-\pi/2, -\pi/4[\cup]\pi/4, \pi/2]$ respectively; the sign of $\sin(2\vartheta)$ will then allow to discriminate $\vartheta \gtrless 0$.

Practically speaking, if $\cos\vartheta < \sqrt{2}/2$, then $\sin\vartheta$ and $\cos\vartheta$ has o be exchanges. If $\sin(2\vartheta) < 0$ the new angle is given by $\vartheta' = -\pi/2 + \vartheta < 0$ and, then, also the signs must be inverted; in the opposite case, the new angle is $\vartheta' = \pi/2 - \vartheta > 0$ and no sign exchange is needed. Remembering that $\mathrm{sign}(\sin(2\vartheta)) = \mathrm{sign}(I_{\zeta\gamma})$, it can be synthetically written

$$\sin\vartheta' = \frac{I_{\zeta\gamma}}{|I_{\zeta\gamma}|}\cos\vartheta \qquad \text{and} \qquad \cos\vartheta' = \frac{I_{\zeta\gamma}}{|I_{\zeta\gamma}|}\sin\vartheta\,.$$

The reader should observe that the exact conservation of $I_{\gamma\gamma}$ (or $I_{\zeta\zeta}$) wouldn't supply any additional information on the particles weights or on their distances from the charge centroid. Moreover, the two angle obtained by conservation of axial moments or centrifugal and polar moments are generally different for a system of more than two particles.

Anyway, the condition on $I_{\gamma\gamma}$ allows to fix univocally th rotation angle ϑ, that, in the case of two starting particles, means to identify exactly their orientation in the cell. The arbitrariness on weights still remains.

8.A.6 Cell coordinates limits

Working in the local reference centered in G, each particle position strictly depends on the direction on which it lies, as defined by ϑ. The bounds for $(\zeta_{1'}, \gamma_{1'})$ and $(\zeta_{2'}, \gamma_{2'})$ are summarized in the following table:

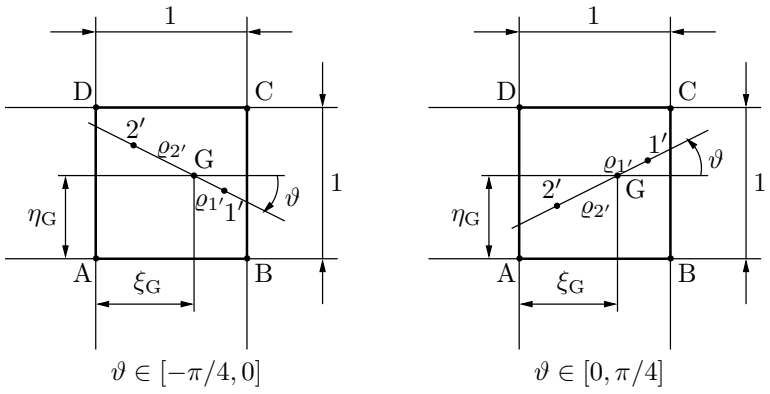

Figure 8.7: Coordinates limits depending on ϑ and centroid position.

$\vartheta \in$	$[-\pi/2, 0]$ $(I_{\zeta\gamma} < 0)$	$[0, \pi/2]$ $(I_{\zeta\gamma} > 0)$
$\zeta_{1'}^{\lim}$	$\min\{1-\xi_G, \eta_G \cot\vartheta\}$	$\min\{1-\xi_G, (1-\eta_G)\cot\vartheta\}$
$\gamma_{1'}^{\lim}$	$\max\{-\eta_G, (1-\xi_G)\tan\vartheta\}$	$\min\{1-\eta_G, (1-\xi_G)\tan\vartheta\}$
$\zeta_{2'}^{\lim}$	$\max\{-\xi_G, -(1-\eta_G)\tan\vartheta\}$	$\max\{-\xi_G, -\eta_G\cot\vartheta\}$
$\gamma_{2'}^{\lim}$	$\min\{1-\eta_G, \xi_G\cot\vartheta\}$	$\max\{-\eta_G, -\xi_G\tan\vartheta\}$

(refer to Figure 8.7 and remember the assumption $\zeta_{1'} > 0$).

Moving from the cartesian (ζ, γ) reference system to the polar (ϱ, ϑ) one with origin in G, the mentioned bounds reflects on $\varrho_{1'}$ and $\varrho_{2'}$, being ϑ fixed by the conservation of centrifugal and polar inertia moments (refer to equation (8.35)). The previous summarizing table can, then, be compressed in the following one:

$\vartheta \in$	$[-\pi/2, 0]$ $(I_{\zeta\gamma} < 0)$	$[0, \pi/2]$ $(I_{\zeta\gamma} > 0)$
$\varrho_{1'}^{\lim}$	$\min\left\{\dfrac{1-\xi_G}{\cos\vartheta}, -\dfrac{\eta_G}{\sin\vartheta}\right\}$	$\min\left\{\dfrac{1-\xi_G}{\cos\vartheta}, \dfrac{1-\eta_G}{\sin\vartheta}\right\}$
$\varrho_{2'}^{\lim}$	$\min\left\{\dfrac{\xi_G}{\cos\vartheta}, -\dfrac{1-\eta_G}{\sin\vartheta}\right\}$	$\min\left\{\dfrac{\xi_G}{\cos\vartheta}, \dfrac{\eta_G}{\sin\vartheta}\right\}$

(the minus signs is due to $\sin\vartheta < 0$ for $\vartheta < 0$).

In Section 8.A.4 the coordinates of the system of new particles $\{1', 2'\}$ were derived by conservation of centrifugal and polar inertia moments, for weights $\omega_{1'}$ and $\omega_{2'}$ treated as parameters.

It was stated in Section 8.2 that the assumption of equal weighted merging particles appears a wise decision: unfortunately, this condition is not sufficient to assure both particles fall inside the cell of interest. The conservation laws for $I_{\zeta\gamma}$ and $I_{\varsigma\varsigma}$ fix the rotation angle ϑ; then, the just derived bounding limits on $\varrho_{1'}$ and $\varrho_{2'}$ define a limited interval for the weights of the two particles. These conditions must be observed in order to place both of them inside the cell.

The system of conservation equations (8.13) initially considered can be rewritten in terms of distances from the barycenter

$$\omega_{1'} + \omega_{2'} = 1 \tag{8.41a}$$

$$\varrho_{2'} = \frac{1}{\omega_{\mathrm{r}}}\varrho_{1'} \tag{8.41b}$$

$$\varrho_{1'}^2 = \omega_{\mathrm{r}} I_{\varsigma\varsigma}\,. \tag{8.41c}$$

The two distances are easily derivable from the polar inertia moment and particles weights as

$$\varrho_{1'} = \sqrt{\omega_{\mathrm{r}} I_{\varsigma\varsigma}} \qquad \text{and} \qquad \varrho_{2'} = \sqrt{\frac{1}{\omega_{\mathrm{r}}} I_{\varsigma\varsigma}}\,.$$

Since

$$0 < \varrho_{1'} < \varrho_{1'}^{\lim} \qquad \text{and} \qquad 0 < \varrho_{2'} < \varrho_{2'}^{\lim}\,,$$

equation (8.41c) allows to write two conditions for the weights ratio which can be merged in the following one:

$$\frac{I_{\varsigma\varsigma}}{(\varrho_{1'}^{\lim})^2} < \frac{1}{\omega_{\mathrm{r}}} < \frac{(\varrho_{2'}^{\lim})^2}{I_{\varsigma\varsigma}}\,,$$

and, by substituting ω_{r} with $\omega_{2'}/\omega_{1'} = (1-\omega_{1'})/\omega_{1'}$, it follows that

$$\omega_{1'}^{\min} = \frac{I_{\varsigma\varsigma}}{(\varrho_{1'}^{\lim})^2 + I_{\varsigma\varsigma}} < \omega_{1'} < \frac{(\varrho_{2'}^{\lim})^2}{(\varrho_{2'}^{\lim})^2 + I_{\varsigma\varsigma}} = \omega_{1'}^{\max}\,. \tag{8.42}$$

The rightmost-hand of the disequation is not always greater than the leftmost one. In few cases, the weight interval $[\omega_{1'}^{\min}, \omega_{1'}^{\max}]$ for $\omega_{1'}$ is void, i.e. it is not possible to obtain both the new particles inside the cell of interest and to conserve both the centrifugal and polar moment. A graphical interpretation of the imposed condition can help to find a starting set of particles which cannot be merged into two new particles belonging to the cell.

8.A.7 A graphical interpretation

As previously discussed in Section 8.2.6, the obtained results can be graphically represented in the cell domain. In the present case, the conservation of the polar inertia moment has allowed to define a circle on which each of the two new particles lies; moreover, even the centrifugal moment has still to be preserved impling that only the points of two hyperbola branches can be acceptable solutions. Therefore, the intersection of the two curves (characteristic of each new particle) leads to two possible solutions (only one in the case of tangency), as shown in Figure 8.8. This is the explanation of the two acceptable values for the rotation angle ϑ: it's now evident why they result symmetric with respect of the $\pi/4$ angle, corresponding to the circle-hyperbola tangency case; symmetric values of ϑ leads to not symmetric solutions since the cell bounds aren't symmetric in any way. Only the study of the

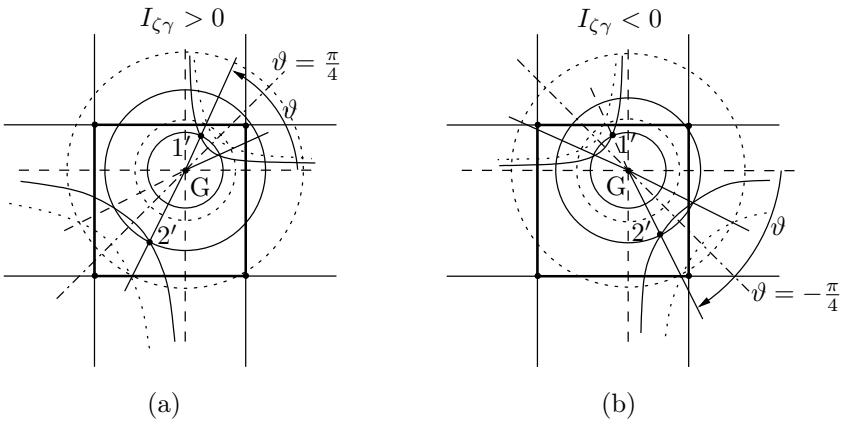

Figure 8.8: Graphical interpretation of the second spatial merging technique. Dotted lines represent the limiting curves on which the particles lie (depending on the fixed ϑ).

$I_{\gamma\gamma}$ inertia moment of the original particles system can add a simple condition to univocally fix the value of ϑ.

Weights variations modifies the curves parameters: concentric homothetic circles and coasinthotic hyperbola are obtained; their two intersections are preserved on the conjunction lines for ϑ and its symmetric $\pm(\pi/4 \pm \vartheta)$. This fact can be noticed in Figure 8.8, where the chosen curves and the limiting ones present the mentioned feature.

Even in this case, the equal-weighted particles are not always an acceptable choice. The limiting weights are those which allow the intersection between the corresponding circle and hyperbola to fall inside the cell. As shown in Section 8.2.6, particular configurations of starting particles could entirely push out of the cell one of the hyperbola branches, or give an intersection on one side and not on the other one: even thought still partially contained in the cell, at least one of the intersections between the hyperbola branches and the corresponding circle (or, equivalentely, with the ϑ conjunction line) does not fall inside the cell bounds, making the solution unacceptable.

8.A.8 Example of an unacceptable solution

Only a counter example is enough to show that the $\omega_{1'}$ variability interval of equation (8.42) can be void.

Let consider 4 starting particles equally weighted ($\omega_i = 1/4 \; \forall i = 1, \ldots, 4$) and

symmetrically positioned inside the cell:

$$(\xi_1, \eta_1) = (\varepsilon, \varepsilon) \qquad (\zeta_1, \gamma_1) = (-\frac{1}{2} + \varepsilon, -\frac{1}{2} + \varepsilon)$$
$$(\xi_2, \eta_2) = (1 - \varepsilon, \varepsilon) \qquad (\zeta_2, \gamma_2) = (\frac{1}{2} - \varepsilon, -\frac{1}{2} + \varepsilon)$$
$$(\xi_3, \eta_3) = (\varepsilon, 1 - \varepsilon) \qquad (\zeta_3, \gamma_3) = (-\frac{1}{2} + \varepsilon, \frac{1}{2} - \varepsilon)$$
$$(\xi_4, \eta_4) = (1 - \varepsilon, 1 - \varepsilon) \qquad (\zeta_4, \gamma_4) = (\frac{1}{2} - \varepsilon, \frac{1}{2} - \varepsilon)$$

being $(\xi_G, \eta_G) = (1/2, 1/2)$ the barycenter coordinates. The centrifugal and polar inertia moments are given by

$$I_{\zeta\gamma} = \sum_i \omega_i \zeta_i \gamma_i = 0\,,$$
$$I_{\varsigma\varsigma} = \sum_i \omega_i (\zeta_i^2 + \gamma_i^2) = 2\left(\frac{1}{2} - \varepsilon\right)^2 .$$

Solving the system of equations (8.14) and (8.11) directly, the two equations

$$\zeta_{1'}\gamma_{1'} = \omega_r I_{\zeta\gamma} = 0$$
$$\zeta_{1'}^2 + \gamma_{1'}^2 = \omega_r I_{\varsigma\varsigma} = 2\omega_r \left(\frac{1}{2} - \varepsilon\right)^2$$

are obtained. They represent respectively the equation of a degenerate hyperbola and that of a circle in the plane (ζ, γ). The possible solutions are

$$\left\{\zeta_{1'} = 0 \text{ and } \gamma_{1'} = \sqrt{2\omega_r}\left(\frac{1}{2} - \varepsilon\right)\right\} \quad \text{or} \quad \left\{\zeta_{1'} = \sqrt{2\omega_r}\left(\frac{1}{2} - \varepsilon\right) \text{ and } \gamma_{1'} = 0\right\} .$$

Since the centroid fall in the center of the cell, the coordinates bounds for the particle $1'$ are immediately deduced; the solution exists if and only if a weight ratio ω_r can satisfy the condition

$$\sqrt{2\omega_r}\left(\frac{1}{2} - \varepsilon\right) < \frac{1}{2}\,.$$

It can be easily shown that any value of $\omega_r < (8(1/2 - \varepsilon)^2)^{-1}$, for example $\omega_r = 1/2$, would lead to an unacceptable solution for the coordinate of the opposite particle $2'$. Intuitively, since the centroid is in $(1/2, 1/2)$, for symmetry reasons, equal weights ($\omega_r = 1$) must make both the particles falling inside the cell. Otherwise, it means that the problem does not have any solution: the choice $\omega_r \neq 1$ would bring one particle nearer to the centroid, but, at the same time, would push the other one far away from it. If for $\omega_r = 1$ both the particles fall outside the cell, then any value would satisfy the relation. In the present case, $\omega_r = 1$ leads to

$$\sqrt{2\omega_r}\left(\frac{1}{2} - \varepsilon\right) \lesssim \frac{\sqrt{2}}{2}$$

which[1] is fairly greater than the limiting value of 1/2.

The second alternative method here proposed has the main advantage to better represent the spatial distribution of the starting set of particles. When only two equally weighted particles are considered, the coordinates of the new particles exactly match those of the starting ones. Moreover, if equal weights are acceptable, no variable has to be chosen randomly. As seen, the main drawback is the incompatibility of the inertia moments conservation with the cell bounds: for those few cases, one could accept the induced perturbation of the charge on the nodes or go back to the procedure proposed in Section 8.2.

[1] The above condition is completely equivalent to that of equation (8.42), obtained as variability interval for $\omega_{1'}$, being $\rho_{1'}^{\lim} = \rho_{2'}^{\lim} = 1/2$.

CHAPTER 9

PF breakdown simulation

Abstract. The model described in Chapter 7, improved with the particle control techniques of Chapter 8, has been used to simulate the early stages of the electrical breakdown in a PF device. A reference case has been, firstly, considered and examined in details pointing out the physical results of interest. A numerical analysis of the implemented techniques for particle number control is then performed in order to show their essential role and effectiveness. At last, a sensitivity analysis will be proposed by varying few operating parameters.

9.1 Discharge evolution

The nature of particle codes allows to have a deeper insight into the microscopic behavior of the modeled system. Moreover, macroscopic quantities can be deduced by integration following the moment definition. The discharge formation and evolution in a PF device will be hereafter examined in details, pointing out the effectiveness of the model in reproducing the physical phenomena described in Chapter 6 and their role in the discharge [205].

9.1.1 Reference operative conditions

The geometric configuration and the operating conditions of the device slightly modifies the discharge formation and evolution, as far as they are in proper ranges (see Section 6.3.1). Any well-working device can then be chosen as reference case; a qualitative description of the phenomenon is provided by many authors [15, 18, 106, 107], while the only experimental data available (photographs, time delay, pressure dependence, ...) are referred to a Mather type PF operating in the Institute für Angewandte Physik (Technische Hochschule Darmstadt) in the early 1980s [19, 20], but, unfortunately, they are referred to an advanced temporal stage of the discharge (hundreds of nanoseconds) still far to be reached by present simulations. To allow a comparative analysis of the results, the geometry used in [41, 42, 117, 156] for hydrodynamic and particle simulations will be considered. Only two parameters will be here modified in order to simplify the analysis of the results and accelerate the simulation: Argon will be used as filling gas instead of Hydrogen, since it is characterized by a lower number of less complex collisions and the corresponding cross sections are commonly used in particle simulations (interpolation formulae are available); the insulator length will be halved, resulting still greater than the inter-electrode gap, allowing to deduce the total simulation domain length. A unitary pressure (in Torr) will be considered as reference, still being in the range of gliding discharge over the insulator and reducing the number of collisions to be simulated, as follows by definition from equation (7.10). A linear voltage ramp of 200 V/ns is applied between the electrodes, being in good agreement with experimental data (as stated in Section 6.3.1).

The geometry dimensions, operative conditions and simulation parameters are summarized in Table 9.1 for the case of reference.

9.1.2 Macroscopic quantities

As already stated in Chapter 6, the electrical breakdown in gases is characterized by an exponential growth in the particle number. This condition is purely ideal, since deduced for a gas in a uniform electric field and not interacting with the boundaries. In a real device like the PF, however, these conditions are not fully verified: as seen in Section 6.3.1, the electric field is neither uniform nor stationary but presents a more intense region just over the insulator sleeve near the cathode edge.

The charged particle densities over the whole domain are plotted in Figure 9.1, while Figure 9.2 and 9.3 contains the collisional fraction frequencies of electrons with the background gas and boundary surfaces respectively. During the first 1.5 ns, only elastic collisions take place since particles have not yet been accelerated by the

Parameter	Value
CE radius (r_{int})	5.0 cm
OE radius ($r_{\text{ext}} = r_{\text{ex,domain}}$)	7.5 cm
Insulator outer radius ($r_{\text{ins}} = r_{\text{int}}$)	5.0 cm
Insulator length (l_{ins})	5.0 cm
Insulator thickness (s_{ins})	0.5 cm
Simulation domain internal radius ($r_{\text{in,domain}}$)	4.5 cm
Simulation domain length (l_{domain})	10.0 cm
Dielectric material	Pyrex
Electrodes material	Copper
Filling gas pressure (p)	Ar at 1 Torr
Voltage ramp ($\mathrm{d}V/\mathrm{d}t$)	200 V/ns
Mesh spacing ($\Delta r = \Delta z$)	0.2 mm
Time step (Δt)	10^{-2} ns

Table 9.1: Simulation parameters for the reference case of interest. The reader is referred to Figure 7.8 for the geometry sketch of the simulation domain, and to Table 7.5 and 7.6 for material properties. The parameters of the clustering and merging procedures are collected in Table 8.1.

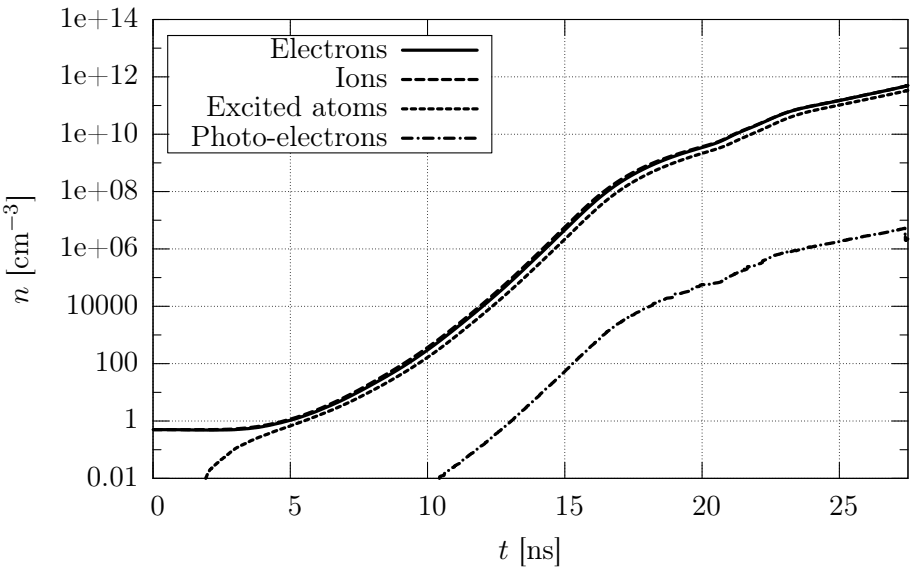

Figure 9.1: Growth of particle densities during the whole simulation; the density of excited states is monitored in total to deduce the number of electrons produced by photo-electric effect on the cathode backwall.

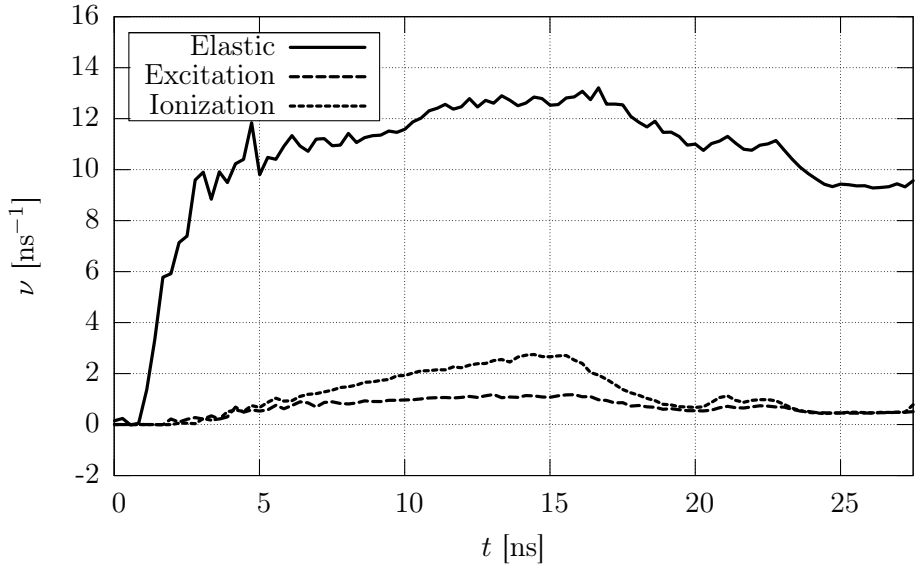

Figure 9.2: Fractional collisional frequency of electrons with the background gas.

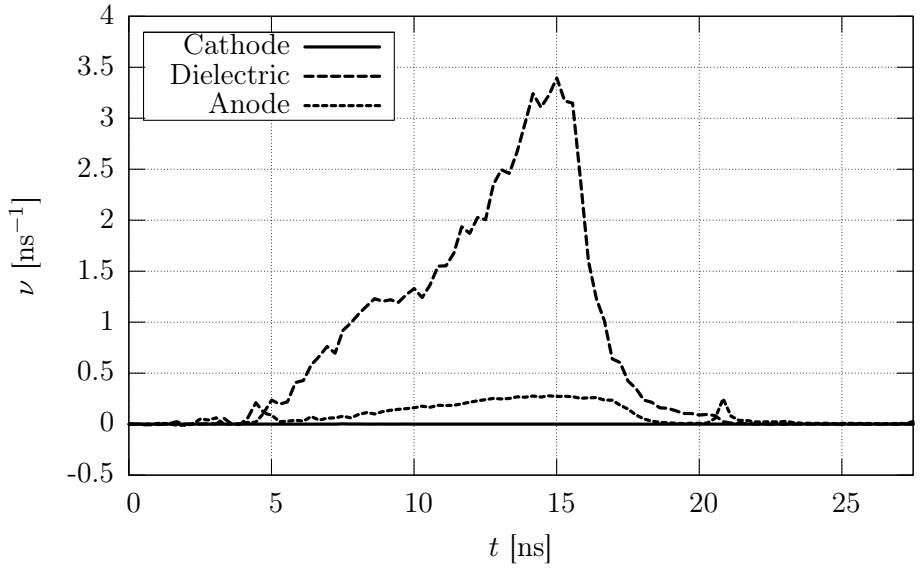

Figure 9.3: Fractional collisional frequency of electrons with the boundary surfaces of the simulation domain.

external field up to the threshold energies for inelastic collisions. Just before 1 ns the mean energy of the system reaches values corresponding to the Ramsauer minimum in elastic cross section (as described in Section 7.3.3 and evident in Figure 7.10): the collective behavior of the species in the first stages of the phenomenon makes this effect evident even over the average collisional rate frequency, which undergoes a slight drop when the mean energy reaches a value of about 0.2 eV. Isolated excitation or ionization processes are possible only for particles of the high energetic tail of the initial Maxwellian distribution, but just one collision would be sufficient to slow down the particle below the threshold. While the number of ions is perfectly constant, the higher mobility of electrons make them interact with the domain boundaries and a loss of about 2.5% is, consequently, observed. Notwithstanding the loss of energy per collision, the charged particles are accelerated by the increasing external field and, rapidly, some of them reach the ionization threshold energy: new electron-ion pairs are produced and 1.5 ns is enough to restore the initial condition on the electron number. The initial seed electrons induce a series of electron avalanches and the particle number rapidly grows with an exponential trend: the newborn particles are similarly accelerated and rapidly overcome the ionization energy, producing new charge-pairs.

As shown in Figure 9.2, the elastic collisional fraction increases steeply in the first instants of the discharge, because of the perturbation induced by the applied electric field; then, a change of derivative and statistical oscillations are observed. In the meanwhile, the inelastic collisional frequencies become not negligible: excitation processes are the first to appear, having a lower threshold energy(see Figure 7.10); the ionization collisional frequency soon overcomes the excitation rates (having a higher cross section at higher energies) and starts increasing almost linearly following the temporal derivative of the external electric field: the introduced energy is readily converted into particle kinetic energy, as shown in Figure 9.4.

The surface collisions are dominated by dielectric impact: as already highlighted, the electric field has its maximum intensity near the cathode edge, just over the insulator sleeve; this means the charged particles multiplication is localized in a small region close to the dielectric surface. The electrons are attracted by the driving electric potential of the anode; when hitting the dielectric surface, their electric charge is accumulated here as a surface negative charge density, which screens the anode positive potential below it. In the meanwhile, secondary avalanches develop in the interelectrode gap over the uncovered part of the anode, producing an increasing rate of electron impacts over it (see Figure 9.3, dotted line).

Even the mean electron velocity components confirm the macroscopic motion of the charge particles: as shown in Figure 9.5, the electrons are attracted from the anode, hence move in the positive axial direction and the negative radial one (see Figure 7.8 for a sketch of the simulation domain and reference system). In this first stage the mean energy is dominated by the radial velocity component, which is predominant over the axial one. The polar mean velocity component, as expected by the 2D-3V nature of the code, is slightly oscillating around the null value.

The highly energetic electrons, the so called runaway electrons, after having accelerated the ionization process, are no more slowed down, since the elastic scattering exhibits high anisotropy in the forward direction, thus with a negligible loss of energy (see Section 7.2.3 for more details), and the cross sections of inelastic processes

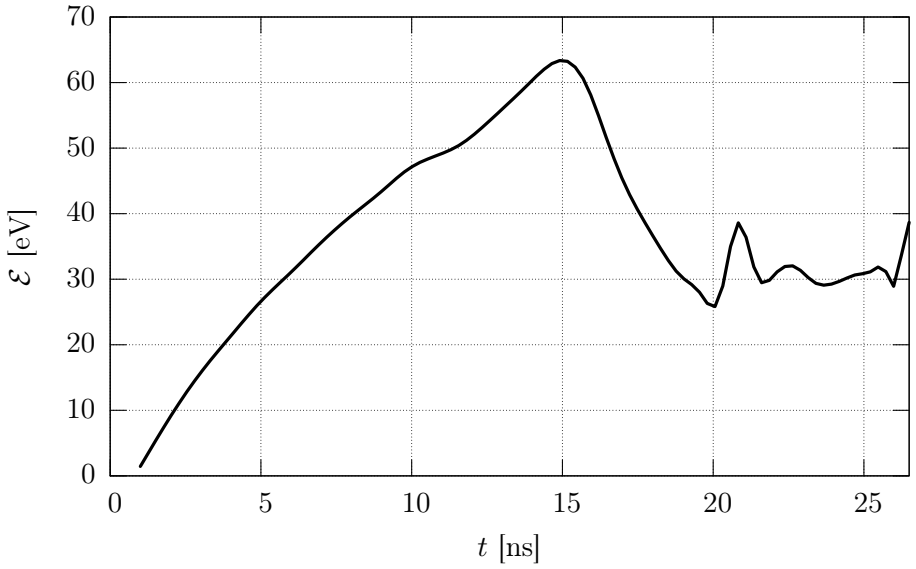

Figure 9.4: Electron mean energy evolution.

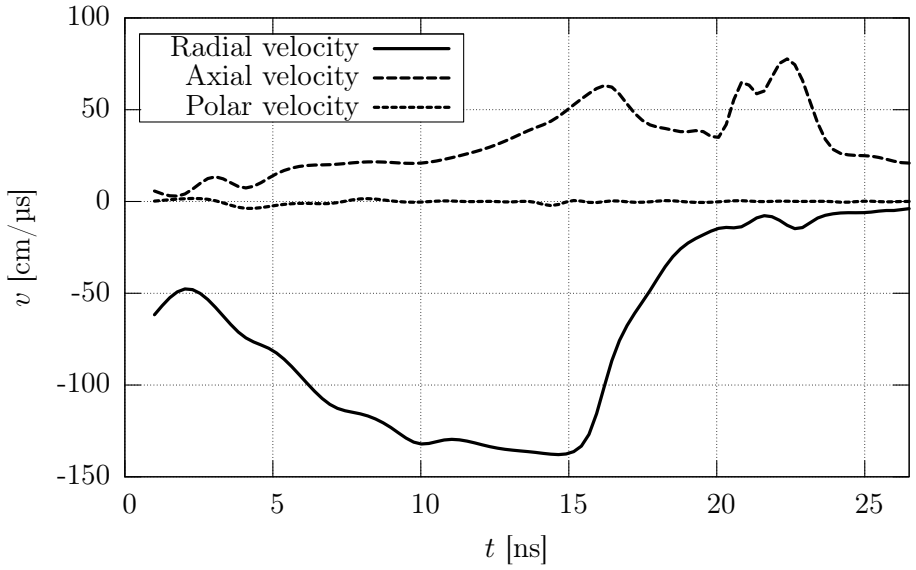

Figure 9.5: Electron mean velocity components versus time; the signs are preserved.

are monotonically decreasing at high energies (see Figure 7.10). The increase in the mean free path length promotes the interaction of the particles with the boundaries of the domain and reduces the exponential growth. Moreover, the space and surface charge become not negligible and the external electric field is locally modified: the slower ions, not following the highly mobile electrons, produce a positively charged sheath which compensates the negative surface charge density accumulated over the insulator sleeve. The net effect is a strong reduction of the mean electron energy, as shown in Figure 9.4; looking at Figure 9.5, the main velocity drop is observed in the radial component. The accumulated surface charge over the dielectric is the main cause of the potential screening: from this point (approximately 15 ns), the ionized gas spot won't move radially towards the insulator, but axially over it developing into a gliding discharge. The rapid drop in the mean electron energy worsen the ionization rate, which is lowered down to the level of the excitation one, in few nanoseconds. Even the dielectric and anode collisional rates suffer a steep fall reaching their minimum at about 20 ns: the deposited surface charge on the insulator opposes to new electron depositions, while the avalanches over the anode are vanishing; the positive space charge they leave at their back contributes in the axial attraction of the electrons located over the insulator sleeve.

Just after 15 ns, the number of fresh electrons produced by photoelectric effect on the cathode backwall becomes not negligible; the charged particles are axially accelerated and develop in new avalanches, which contribute to feed the discharge. The positive screening charge left by the slower ions expands towards the cathode edge increasing the axial electric field. In the meanwhile the discharge develops up to the end of the insulator sleeve approaching the uncovered part of the anode; the electrons are strongly accelerated by the positive potential, since they find a region of highly intense electric field due to the dielectric edge and material transition. These two contributions produce an increase in the particles growth; at the same time the mean energy presents a secondary peak, mainly due to the axial velocity component (see Figure 9.4 and 9.5). While the electron impact over the dielectric still maintains negligible, the electrons approaching the end of the insulator sleeve contributes to the charge deposition over the anode. Soon, this transient situation extinguishes and a more self-sustaining condition is reached.

A last macroscopic quantity of interest in the breakdown analysis is the current flowing between the electrodes. As discussed in Section 6.1.5, the charge deposited over the electrodes in the unit time is not fully representative of the flowing current if the system hasn't yet reached a stationary condition; the displacement current is a more reliable quantity, which is not affected by accumulated discrete pulses of charge deposition, but takes into account the charged particles motion and their interaction with the electric field. In Figure 9.6, the two quantities are compared: the integral over time is approximately comparable, while the deposited charge presents a strong instantaneous variability. Values of about ten amperes are reached when the simulation is stopped. At an advanced stage, other SEE processes have to be considered to feed the discharge with fresh electrons and increase the flowing current.

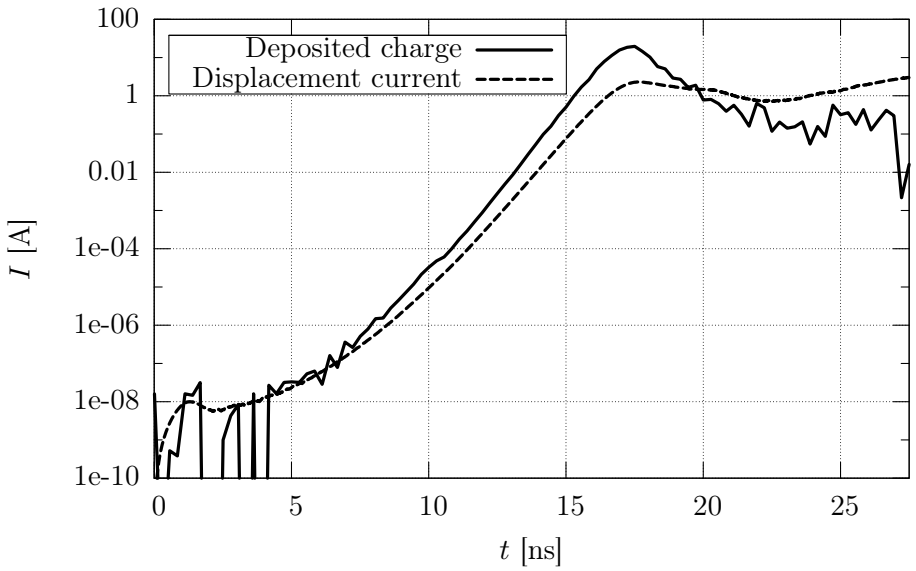

Figure 9.6: Deposited charge over the electrodes and displacement current.

9.1.3 Local quantities

A clearer picture of the discharge development, described in the previous section on the basis of average quantities and macroscopic quantities, can be obtained following the evolution of the charged particle density and electric potential profiles.

As shown in Figure 9.7-a, at about 7 ns, a first ionization process has started in the localized region of most intense electric field, i.e. where the isopotential lines are denser, near the cathode edge over the insulator sleeve. The position and the electric field configuration justify the observed collisional rates on the dielectric surface, as shown in Figure 9.3. The low electron densities (maximum values reach approximately $8 \cdot 10^3$ cm^{-3}) are not yet high enough to perturb the external applied electric field; the spatial derivative change at the insulator surface, due to the dielectric properties, can be appreciated.

After about ten nanoseconds (see Figure 9.7-b), the electron density reaches a maximum value of approximatively 10^{11} cm^{-3}. The surface charge deposited on the insulator surface and the net space charge over it become sufficiently high to perturb the electric field, which, in the meanwhile, has increased in magnitude because of the externally imposed voltage ramp (at a rate of 200 V/ns, a potential of more than 3 kV is reached on the driving electrode).

As shown in Figure 9.7-c), in a little more than 1 ns, the electron density approximately doubles, while the shape of the ionized gas spot develops towards the cathode backwall, being fed by fresh electrons produced by the photoelectric effect; the isopotential lines are expelled out of the spot, producing an increasing axial electric field at the cathode backwall, which rapidly accelerated the emitted electrons up to energies higher than the ionization threshold: the new electron avalanches reach

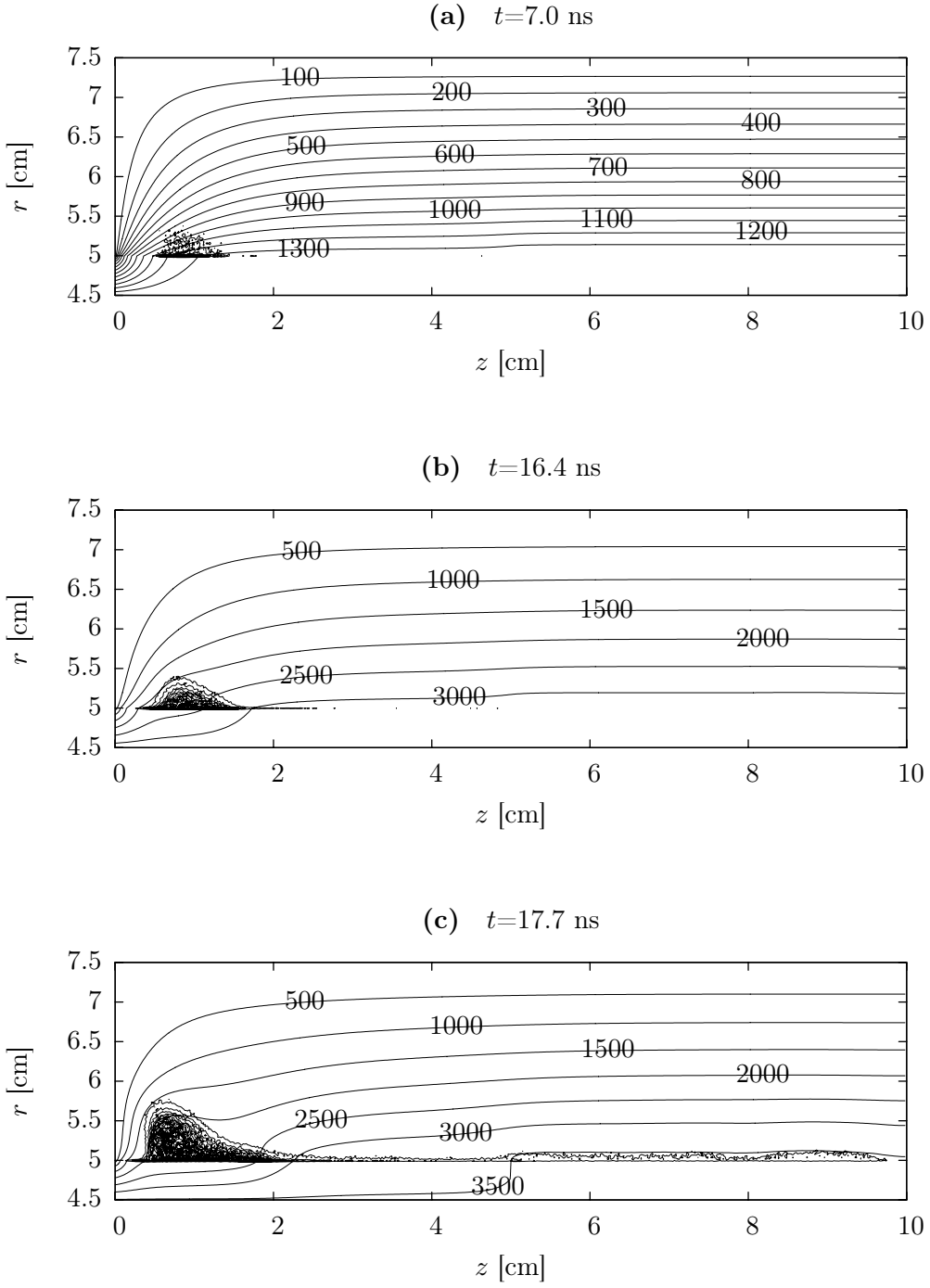

Figure 9.7: Density profiles and isopotential lines at fixed time instants during the first part of the simulation.

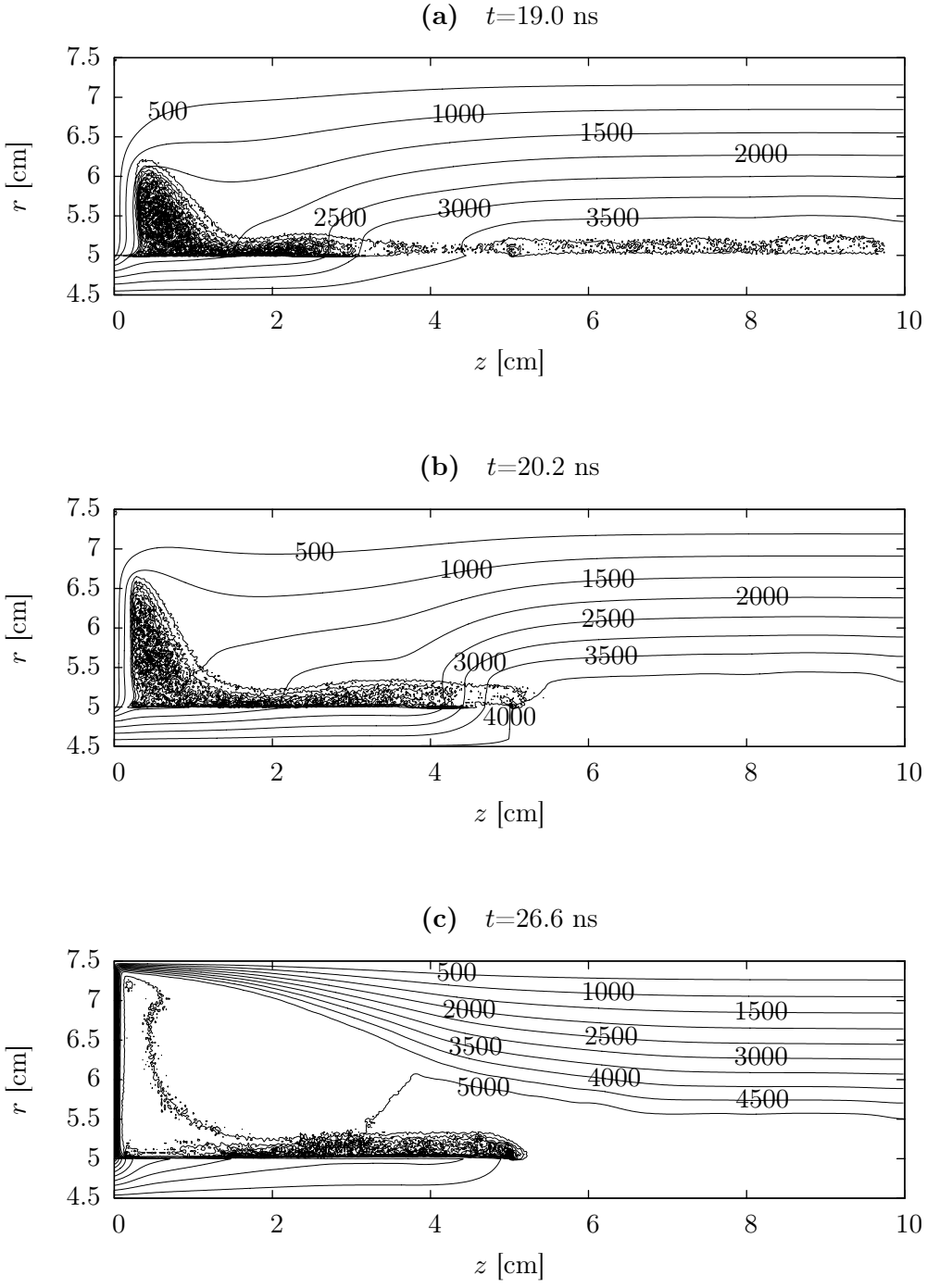

Figure 9.8: Density profiles and isopotential lines at fixed time instants during the second part of the simulation.

the plasma spot enlarging it towards the cathode, while the positive space charge left by the slower ions increments the effect. On the opposite side of the spot, the initial seed electrons uniformly distributed in the interelectrode gap are accelerated by the increasing electric field; when they overcome the ionization threshold energy, new avalanches are produced both on the insulator sleeve and on the uncovered part of the anode.

Again, in the following nanosecond, the discharge continues to expand both towards the cathode backwall and over the insulator sleeve, reaching densities of the order of $4 \cdot 10^{11}$ cm^{-3}. As shown in Figure 9.8-a, the external electric potential is further distorted by the space charge and by the surface charge density accumulated on the insulator sleeve; the net effect is an axial gradient (more intense in the region at lower density), which attracts the electrons towards the uncovered anode; here the electron density has increased to values of about one order of magnitude lower than those of the bulk spot, over the insulator sleeve.

After about 1 ns (see Figure 9.8-b), the expansion of the discharge, driven by the induced axial component of the electric field, reaches the end of the insulator sleeve, where the potential gradient is even more intense. The electron density increases at a lower rate reaching values of approximately $6 \cdot 10^{11}$ cm^{-3} as maximum in the discharge region; the ionized gas, produced over the anode by later avalanches, is no more fed by new electrons and the anode charge deposition makes negligible its density.

In the following 5 ns, the shape of the discharge doesn't undergo strong variations, while its density increases of about two order of magnitude (see Figure 9.8-c). The accumulated surface charge density on the insulator surface strongly modifies the electric potential, screening it in the whole region of the discharge. The axial gradient along the sheath over the insulator sleeve disappears, while the electric field is strongly enhanced in about $1 \div 2$ mm of the domain faced to the cathode backwall. At this stage the sheath appears about one order of magnitude denser at the end of the insulator sleeve, just over it, while it seems to undergo a gradual depletion in the first 2 cm.

This spurious effect, not consistent with the breakdown condition, could have two possible reasons still under investigation: the first, purely numerical, is the excessive increase in local densities and mean energies which would require a finer grid to correctly match the accuracy and stability conditions of PIC methods, as mentioned in Section 7.1.4; the second, more physical, could be the absence in the model of the field emission as additional source term of fresh electrons from the cathode edge over the insulator. Even if a value of about $5 \cdot 10^4$ V/cm, is still too low to sustain an electron current density, two aspects must be highlighted: the axial electric field in the emitting region is so high that few electrons extracted from the metal would generate a strong ionizing avalanche which would feed the discharge; the presence of an edge highly enhances the electric field and the field emission effect, through the β parameter of equation (6.7). Further analysis and tests are under investigation.

9.1.4 Energetic distribution functions

The EEDF evolution is plotted in Figures 9.9 to 9.12, for four different simulation time instants: the first corresponds to the first frame of Figure 9.7; the second is

representative of the particle exponential growth; while the third has been chosen at the maximum mean energy, the fourth, and last, corresponds to the following minimum. The EEDFs are built starting from the simulation particle properties and plotted in comparison with the Maxwell-Boltzmann ones at the same mean temperature.

It appears how the EEDF is characterized by an excess of slow and high energetic electrons, already in the first ten nanoseconds (Figures 9.9 and 9.10): the fresh electrons produced in the ionization processes are the first, followed by those accelerated by the electric field which reach energetic regions where the inelastic cross sections start to decrease allowing longer mean free path and, hence, further acceleration.

Moreover, at this stage, the photo-electrons starts to become not negligible. The electrons emitted from the cathode backwall are immediately accelerated by the intense electric field between the electrode and the positive space charge of the slower ions accumulated over the insulator sleeve (as evident from Figure 9.8-a). In addition, a bulk region of ionized gas is formed and partially self-screened by the ion positive charges. While the electrons emitted by the cathode feed the energetic tail of the distribution, the new ones in the bulk region are confined in an equipotential region and start to redistribute their energy by elastic and inelastic collisions, moving towards lower energies (Figure 9.11).

After approximately 15 ns, the average energy of the system reaches its maximum and starts to decrease as a consequence of the above described processes. The EEDF of Figure 9.12 can be seen as composition of two main contributions: a thermal component near the equilibrium and a high energetic one, located in the less dense electron avalanches which feed the discharge. This also explains the drops in inelastic collisional fractions and dielectric impacts observable in Figure 9.3.

9.2 Numerical analysis

The results discussed in the previous section were obtained making deep use of the particle control techniques presented in Chapter 8. Indeed, even accepting an extremely long computational time, the exponential growth of the simulation particle number, characteristic of electrical discharges, represents a tight bond on the simulated time-interval of the phenomenon, the finite amount of memory in modern workstations being the limit. The only way to deceive the obstacle is the use of a particle number control technique. The effectiveness of the implemented method is hereafter analyzed showing how the basic rules presented in Section 8.1.2 are satisfied and focusing on the induced perturbations.

9.2.1 Memory and time limits

As previously stated, particle simulations are affected by a main drawback: larger is the number of particles, necessary to avoid numerical noise and to obtain a sufficiently accurate statistical description, more memory- and time-consuming results the code.

The total computational time related to a PIC method is proportional to the sum of the number of particle N_p and $N_\mathrm{g}^D \log N_\mathrm{g}^D$, with N_g number of grid points in D dimensions [130, 129]; when variance reduction techniques are not employed, the

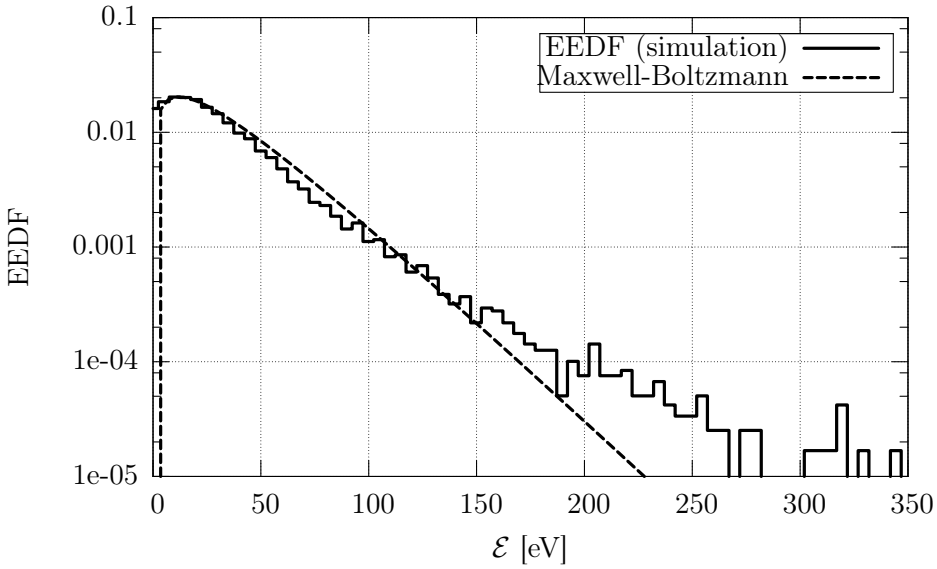

Figure 9.9: EEDF at $t = 7.0$ ns of the simulation time, compared with the Maxwell-Boltzmann distribution function at the same mean energy $\langle \mathcal{E} \rangle = 35.6$ eV.

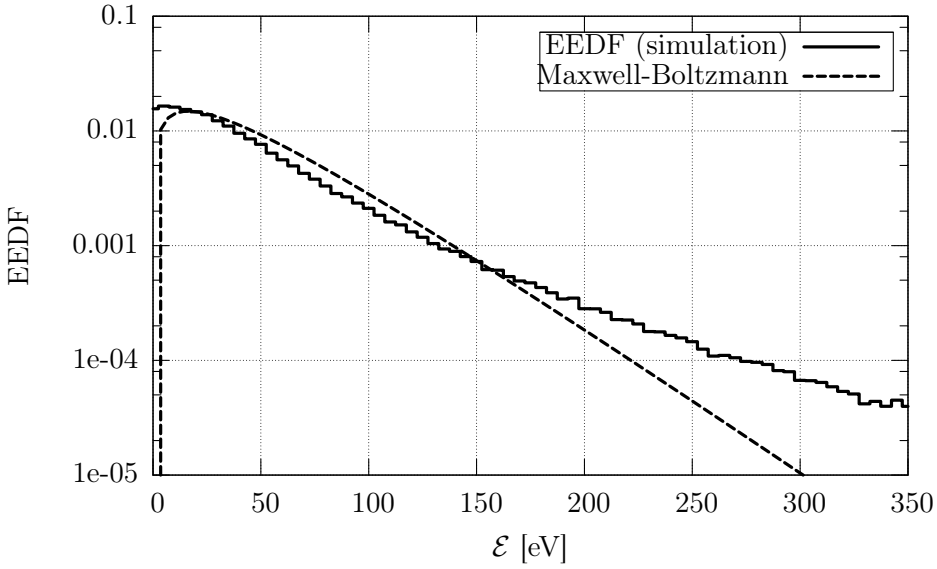

Figure 9.10: EEDF at $t = 10.8$ ns of the simulation time, compared with the Maxwell-Boltzmann distribution function at the same mean energy $\langle \mathcal{E} \rangle = 48.8$ eV.

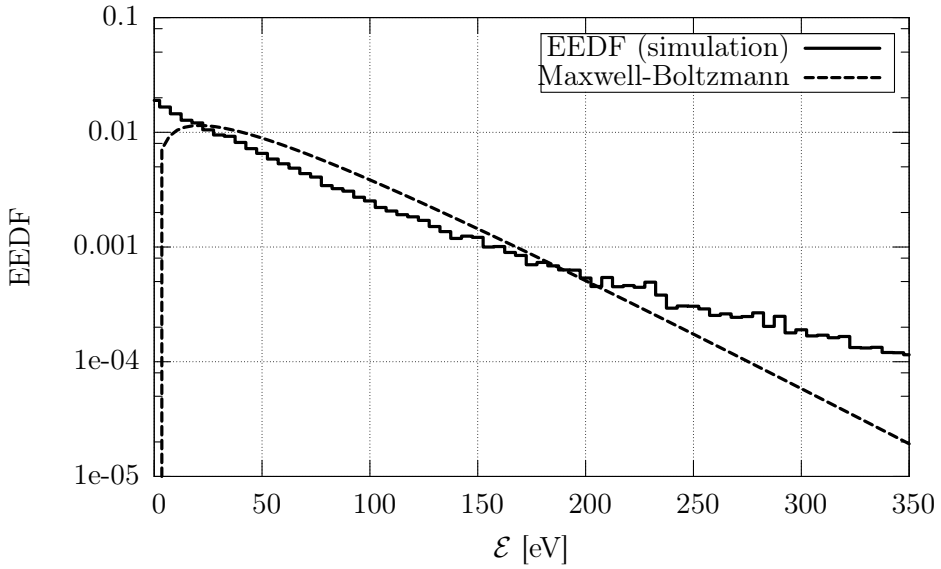

Figure 9.11: EEDF at $t = 15.1$ ns of the simulation time, compared with the Maxwell-Boltzmann distribution function at the same mean energy $\langle \mathcal{E} \rangle = 63.3$ eV.

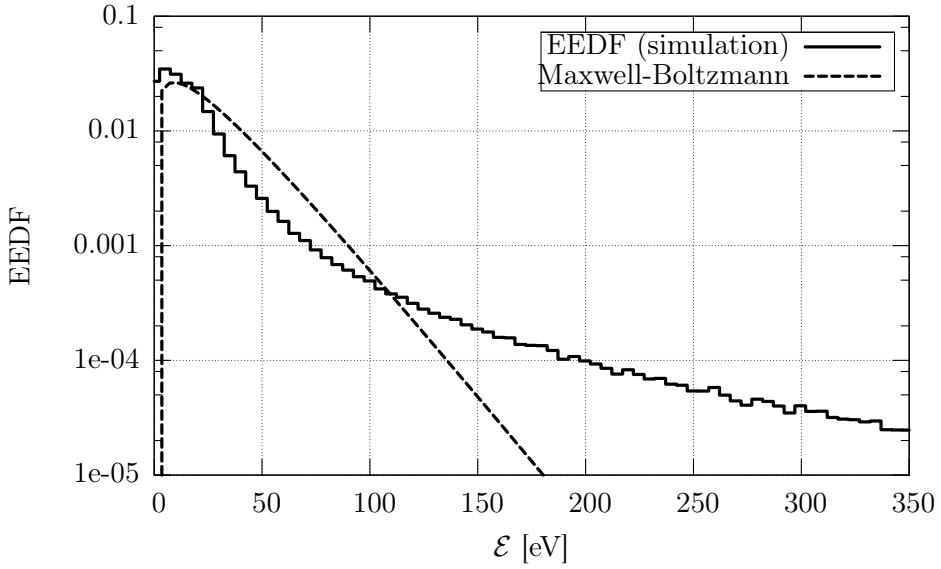

Figure 9.12: EEDF at $t = 20.0$ ns of the simulation time, compared with the Maxwell-Boltzmann distribution function at the same mean energy $\langle \mathcal{E} \rangle = 27.4$ eV.

MCC module contributes with an additional term proportional to N_p [145, 140]). Thus, the number of simulation particles doubly weigh upon the computational cost. On the other hand, the statistical error associated with any quantity deduced from a discrete set of elements can be assumed to be inversely proportional to the square root of their number. In a coupled PIC-MCC method, a numerical technique, which aims to reduce the computational time through an artificial control of the simulation particle number, cannot set aside the variance changes induced in the whole phase-space.

The computational time is not the only performance that affects particle simulations: the finite amount of memory sets a limit to the number of simulation particles. In a 2D-3V PIC-MCC code, as that here in use, each simulation particle requires at least 6 (weight, 2 spatial coordinates, 3 velocity components) real properties. If double precision is used, each stored variable occupies 8 bytes, hence, a modern commodity workstation with 4 GB (usually combined to obtain cluster PCs) can manage up to few tens million of simulation particles. The results presented in Section 9.1.2 makes evident that the time-interval which could be simulated with real particles is approximately of ten nanoseconds: the statistical weight associated with each simulation particle is of great importance and largely used since the first PIC-MCC simulations.

For better understanding, a comparative test can be performed running two simulations with identical input parameters. In the first case the simulation handles only real particles: the hybrid counting sort, the clustering procedure and the merging method are inhibited in order to maximize the available memory and the run is stopped by memory saturation. The second case exploits the clustering and merging techniques to reduce the number of simulation particles, while the number of real particles is deduced by the weight conservation law. The electron and ion density growths are plotted in Figure 9.13: the simulation of purely real particles ends when the limit of about $20 \cdot 10^6$ particles is reached, at less than 11.9 ns; the particle growth rate appears to be correctly preserved, while a small temporal shift can be observed, probably due to the different random number sampling already in the first stages of the simulation, the particle sorting being turned off in one case. On the other hand, the number of simulation particles settles down on a value in the range $2.5 \div 3.0 \cdot 10^6$ both for ions and electrons, not only allowing to go on with the simulation, but also strongly reducing its computational cost.

A parallel code could improve the computational time and slightly overcome memory costs, but it could not represent a totally effective solution. The developed merging technique fully exploits the simulation macro-particle concept and the statistical importance property allowing to extend the simulated time-interval up to tens of nanoseconds, where the stopping limit is purely numerical and under deeper investigation. The following sections will deal with the a numerical analysis of the results highlighting the effectiveness of the employed methods.

9.2.2 Merging analysis

The merging technique is based on two fundamental rules, as described in Section 8.1.2: the starting and final sets have to equally contribute to the grid moments and the to sample the same velocity distribution functions. These conservation

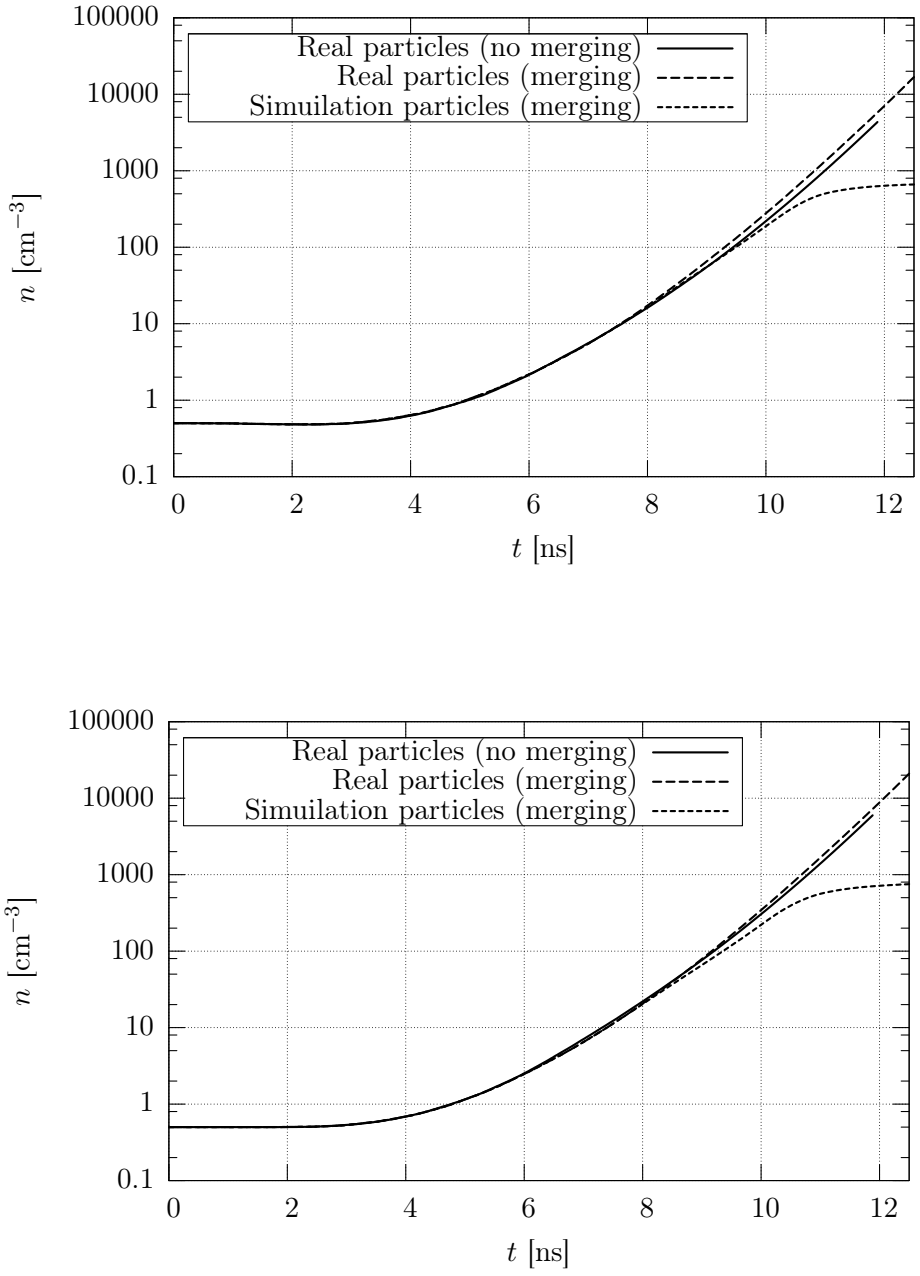

Figure 9.13: Charge particle densities growth for electrons (top) and ions (bottom); the case of simulations without the merging procedure is compared with that exploiting the particle number control, for which both the real and simulation particle curves are plotted.

rules can be checked for a typical case of interest: a simulation was run starting from equally weighted simulation particles and the merging routine was called as soon as $5 \cdot 10^5$ particles were reached. The population has been printed out just before and after the merging in order to make the starting and final sets fully comparable. The spatial coordinates are made dimensionless inside the corresponding cell; the planar velocity has been normalized with the maximum value of the two sets ($v_{12,\max} = 5.7 \cdot 10^6$ m/s), while the energy has been modified into lethargy, firstly dividing it by its maximum value ($E_{\max} = 105.1$ eV) and then operating on it with the log function.

Firstly, the clustering algorithm will be examined. The method works on the direction of flight, planar velocity and energy logarithm as explained in Section 8.6.1, making use of the threshold values summarized in Table 8.1. It will be referred the case of a typical cell, having a not too large number of particles (electrons) to make the data more readable. The staring set is compared with the final one in Figure 9.14, 9.15 and 9.16: the particles falling in the same cluster are depicted with the same symbol, which is unchanged between different graphs, and is maintained also for the two particles arising from the merging procedure, as described in Section 8.2 and 8.3. As can be seen in Figure 9.14, particles are collected in clusters independently from their spatial position, the only condition being to belong to the same cell. The polar plot of Figure 9.15, instead, highlight the proximity condition both on the planar velocity and on the direction of flight of the particles: the comparison between the starting and the final sets makes evident the effectiveness of the clustering and merging procedures both in the collection of "near" particles and in the conservation of the velocities between the two sets. Finally, in Figure 9.16 the weight modification and energy conservation are highlighted: the starting clusters of real particles ($w = 1$) are merged producing equally weighted pairs of new particles; in the specific case, the maximum number of particles in a cluster is 5, which leads to a weight of 2.5 per particle.

A three-dimensional representation of the particle sets separated in clusters by different symbols is proposed in Figure 9.17, where each point represents a particle in the velocity space; in particular, the poloidal component is here replaced by the third property of the clustering procedure, i.e. the particle lethargy, defined as $\log(E/E_{\max})$ for normalization reasons[1].

While the charge conservation on the grid nodes is checked inside the code "a posteriori" for each cell (only in this test case, the operation being as useless as time-consuming), the velocity distribution functions are built and plotted to make easier their comparison. The distribution functions are built using a uniformly meshed reference axis having characteristic spacing comparable with the threshold distances used in the clustering procedure; this allows a more intuitive interpretation of the plots, even if it could be a little misleading: the clustering method is mesh-free, that means it is independent from a discretization of the property of interest. Thus the proposed comparative graphs, and corresponding maximum relative errors, must be intended as purely indicative. Moreover, the distribution functions are normalized in order to give 1 as integral over the corresponding property range; the error-bars corresponds to the square root of simulation particles falling in the bin.

[1]The poloidal component of the particle velocity is of no matter in a 2D3V particle code: it contributes only to the total energy, of great importance in cross section evaluation.

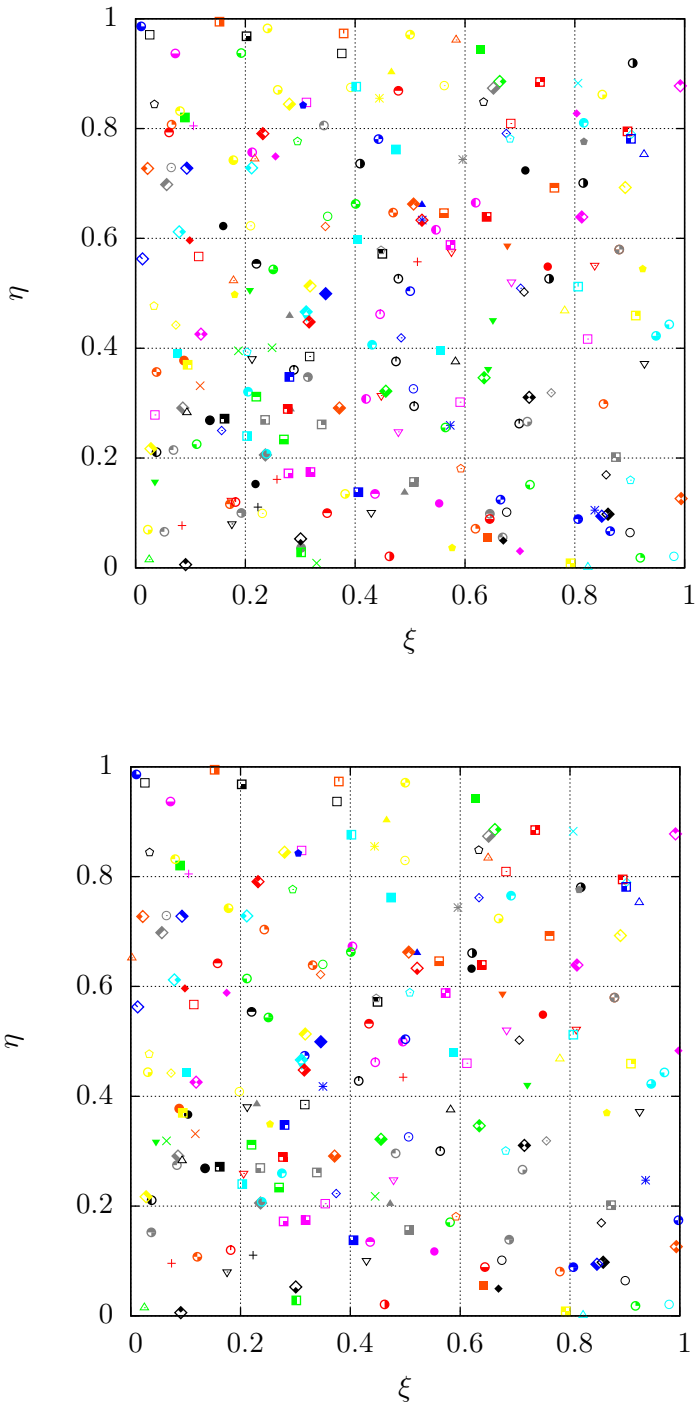

Figure 9.14: Starting (top) and final (bottom) sets of particles processed through the merging procedure. The coordinates are normalized on the cell width: the particles of the two sets uniformly fill the cell.

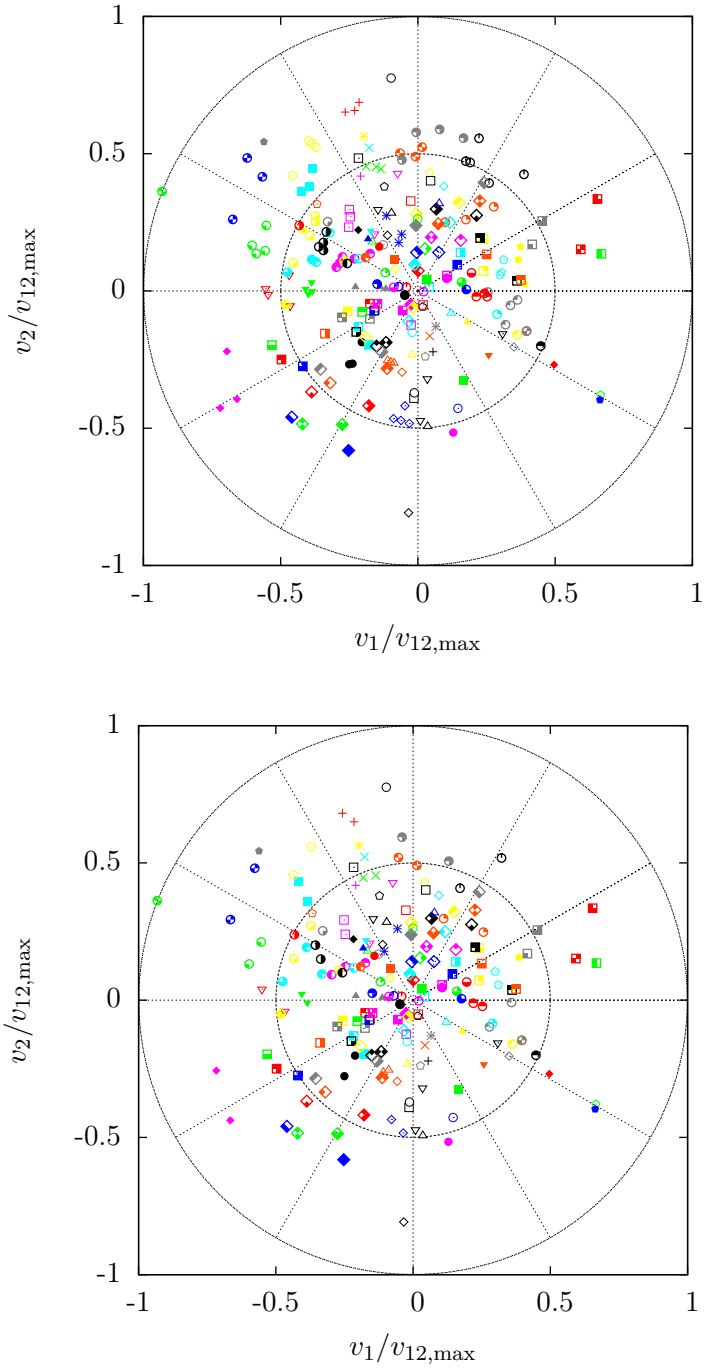

Figure 9.15: Starting (top) and final (bottom) sets of particles processed through the merging procedure. The particles are plotted on the (v_1, v_2) velocity plane. The polar grid, normalized to the maximum planar velocity of the two sets, makes clearer the clustering on the direction of flight and planar velocity.

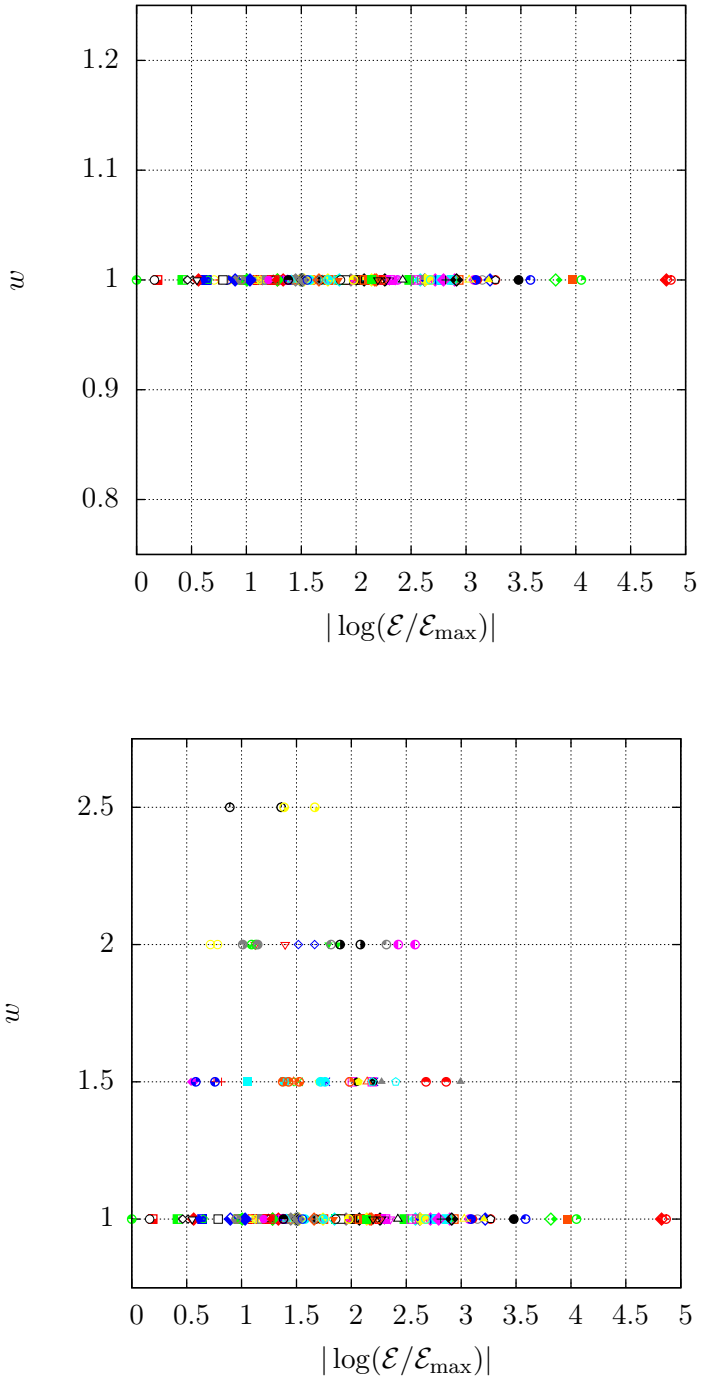

Figure 9.16: Starting (top) and final (bottom) sets of particles processed through the merging procedure. The lethargy, referred to the maximum energy of the two sets, is used in abscissas, being also a clustering property.

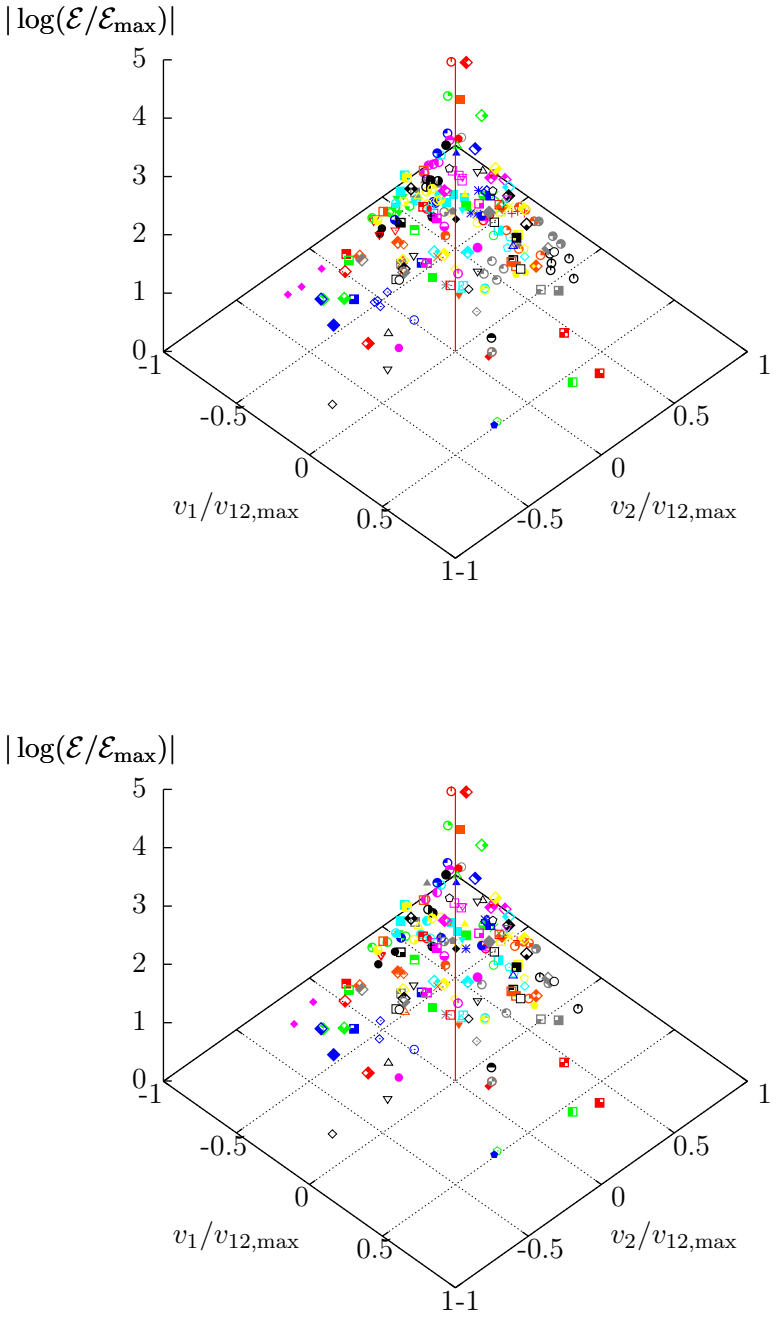

Figure 9.17: Starting (top) and final (bottom) sets of particles processed through the merging procedure. The points represent the particles in the 3D velocity space, where the poloidal velocity is replaced by the lethargy property.

The first property to be examined is the direction of flight ϑ_v: as proposed in Figure 9.18, the polar direction of velocities is correctly preserved with a maximum relative error of about 14% over a single bin. A good distribution preservation can be observed also for the planar velocity v_{12} property in Figure 9.19: the corresponding maximum relative error is less than 23%. Finally, the most delicate conservation rule is that based on the particle energy (or lethargy), this being strictly related with the gas cross sections. Even in this case (see Figure 9.20), the relative error is lower than 25%. A similar analysis could be extended to the two main velocity components v_1 and v_2, but it would not add much more information. In general, a good compensation of the discrepancies is observed for adjacent bins, as a confirmation of the mesh-free feature of the clustering method.

Globally, the starting set contains 237 particles, which are reduced to 197 after the merging procedure with an efficiency of about the 17%. About 170 clusters have been identified, many containing only 1 or 2 particles, on which the merging would not have any effect. Obviously, the increase of the chosen threshold distances would increase the efficiency in the particle number reduction with a lack of precision in distribution function conservation as main drawback. The thresholds in use have been tuned to find a good compromise between the efficiency and precision.

The above analysis has been entirely devoted to the electron species. Similar results can be obtained for ions, tuning the proper threshold values for the clustering procedure.

9.2.3 Merging effectiveness

In a typical simulation, the local number of particles per cell largely varies: the temporal growth of charged particles is governed by ionization, then localized in region with higher electric field. In the previous section, a low populated cell was chosen to make more readable the presented plots; if the whole domain is considered, the total number of simulation particles is reduced of about the 47% (from 50004 to 26382). In fact, higher local densities of particles per cell increase the method efficiency, producing better results where it is precisely needed, i.e. where a more intense charges multiplication takes place.

The analysis of the probability distribution functions, performed in the previous section for the single cell, can be extended to the whole spatial domain in order to obtain an estimate of their average deviations. Since the total number of particles is sufficiently high, the mesh on the three properties of interest can be strongly reduced. The comparison between the distribution functions of the three properties of interest is plotted in Figure 9.21-9.23. The local relative error is lower than 20%; the value could appear quite high but one must consider the finer meshing, which leads to a bin width quite lower than the threshold distances of the clustering method.

Since the number of particles per bin is much higher than in the case of the single cell examined in the previous section, the error-bars become so small that they are no more distinguishable. However, one should remember they are related to the number of simulation particles falling in the bin, independently from their weight. In Figure 9.24-9.26, the comparison between the distribution functions of the initial set, final set and final set for simulation particles is proposed. The distribution function on the direction of flight in Figure 9.24 shows a flattening over the whole axis:

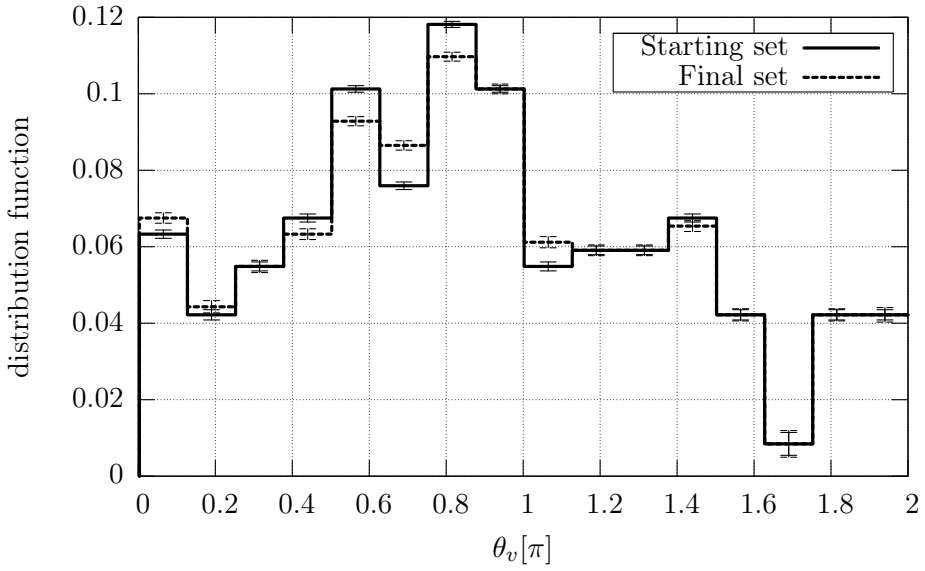

Figure 9.18: Distribution functions of the starting and final sets of particles, processed through the clustering and merging routines, with respect to the direction of flight (first property of interest). The angle ϑ_v is expressed in radiant, as fractions of π.

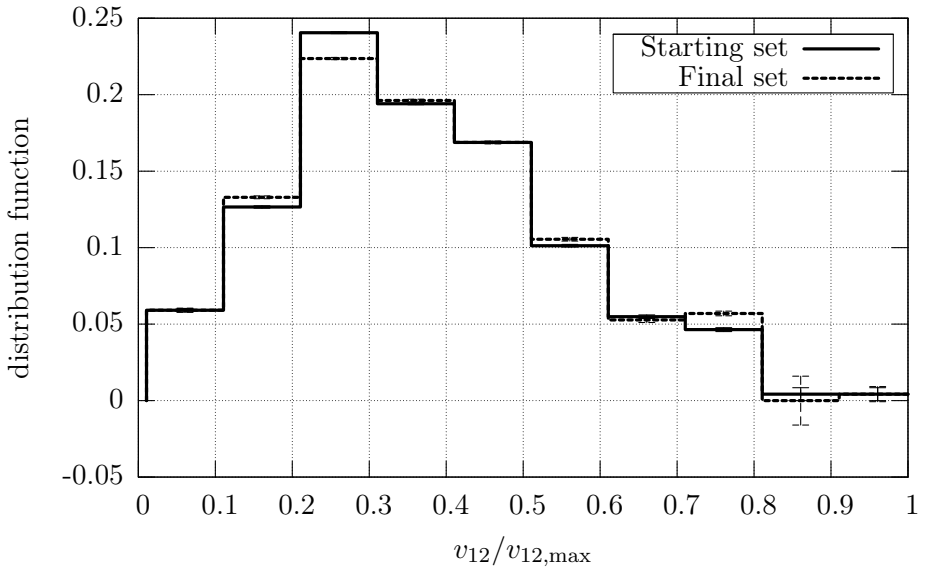

Figure 9.19: Distribution functions of the starting and final sets of particles, processed through the clustering and merging routines, with respect to the planar velocity (second property of interest).

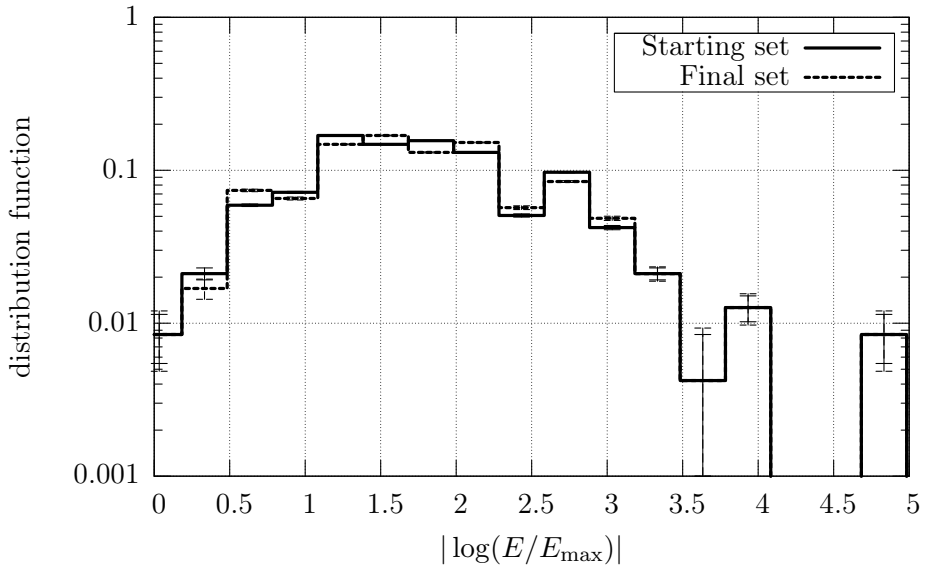

Figure 9.20: Distribution functions of the starting and final sets of particles, processed through the clustering and merging routines, with respect to the lethargy (third property of interest).

the clustering is more effective where the number of particles is higher, then peaks are lowered and valleys are increased. This makes the standard deviations more uniform over the whole distribution function. Looking at the distribution functions for the planar velocity property in Figure 9.25, one can observe a shift towards lower velocities of the curve for the simulation particles after merging. This can be interpreted also considering the third property on which the clustering is based: since the lethargy is used instead of the energy, the corresponding linear energetic bin has a lower width at lower energies; thus, the planar velocity being strictly related to the total energy, the lethargy clustering reflects on the efficiency at lower planar velocities. Despite the logarithmic mesh, the energetic distribution function of the particles of the starting set allows to obtain a higher efficiency at low energies where the number of particles is sensibly higher, and a lower efficiency on the low populated energetic tail. This result is of great importance: even if the total number of the simulation particles is reduced, the statistics of the collisional processes is not uniformly reduced, taking advantage of the redistribution of simulation particles at higher energies.

From the above considerations, it arises evident that the merging procedure not only reduces the number of simulation particles but also redistributes them over the spatial domain. The dependence of the effectiveness of the method on the number of particles per cell increases its performances where the particle densities are greater. In Figure 9.27, the number of particles per cell for the starting and final sets are presented for the spatial domain region of greatest interest: not only the maximum

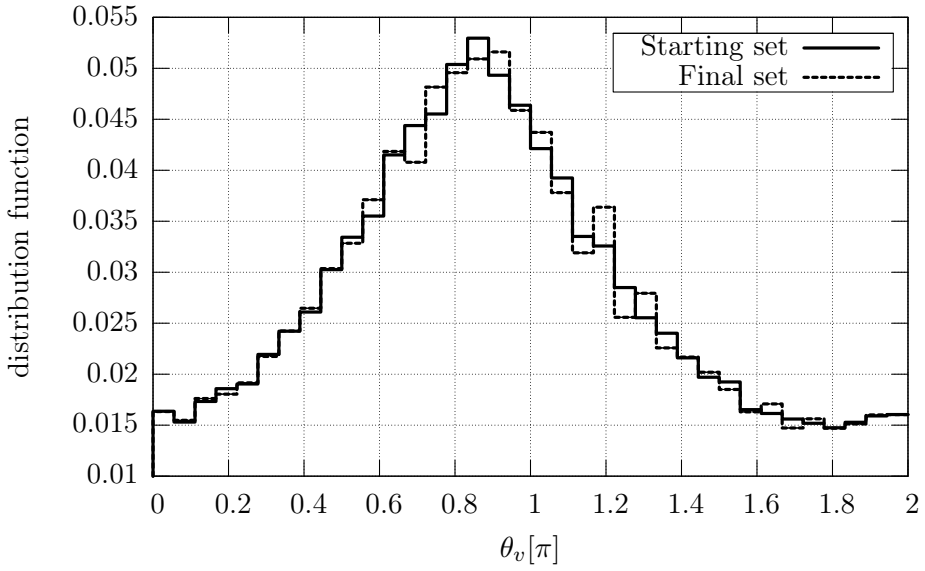

Figure 9.21: Distribution functions of the starting and final sets of particles on the whole domain, processed through the clustering and merging routines, with respect to the direction of flight (first property of interest).

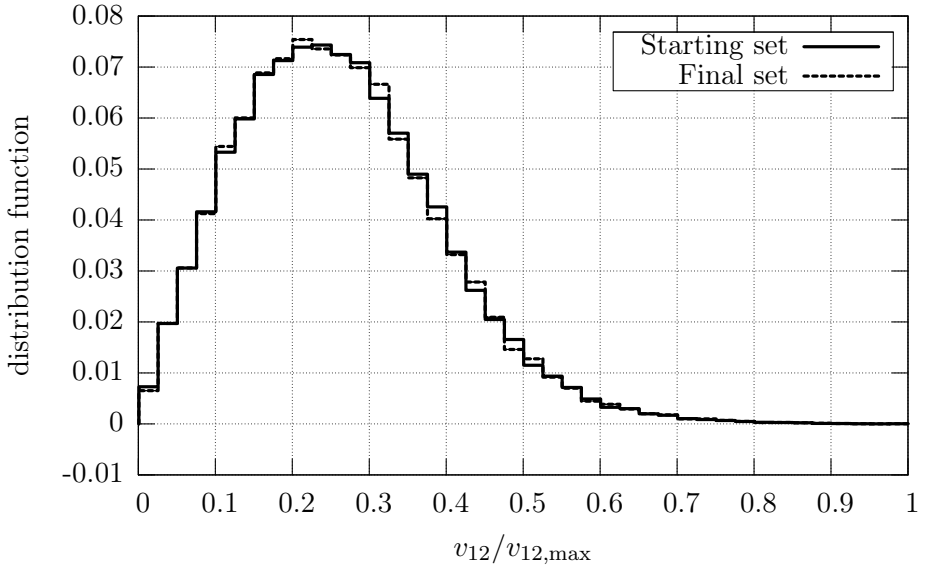

Figure 9.22: Distribution functions of the starting and final sets of particles on the whole domain, processed through the clustering and merging routines, with respect to the planar velocity (second property of interest).

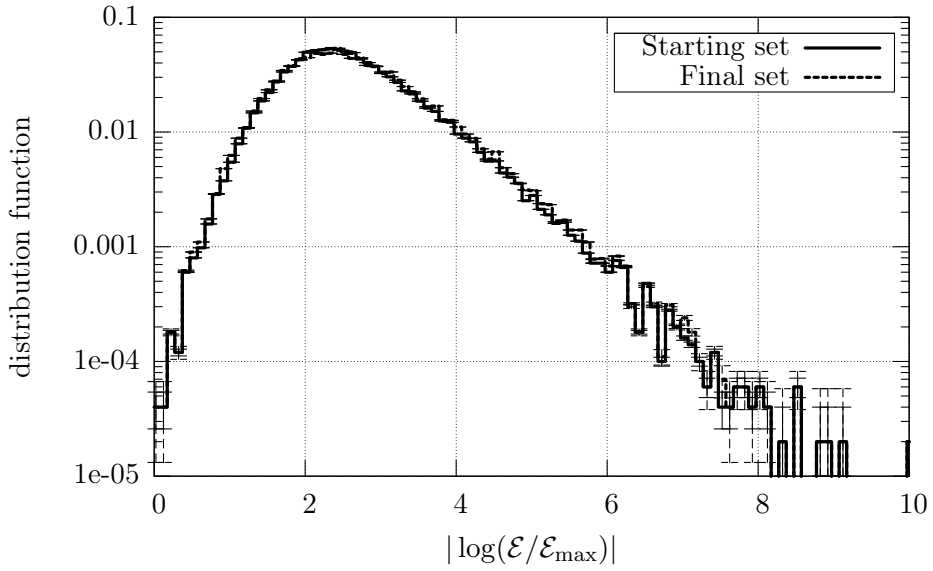

Figure 9.23: Distribution functions of the starting and final sets of particles on the whole domain, processed through the clustering and merging routines, with respect to the lethargy (third property of interest).

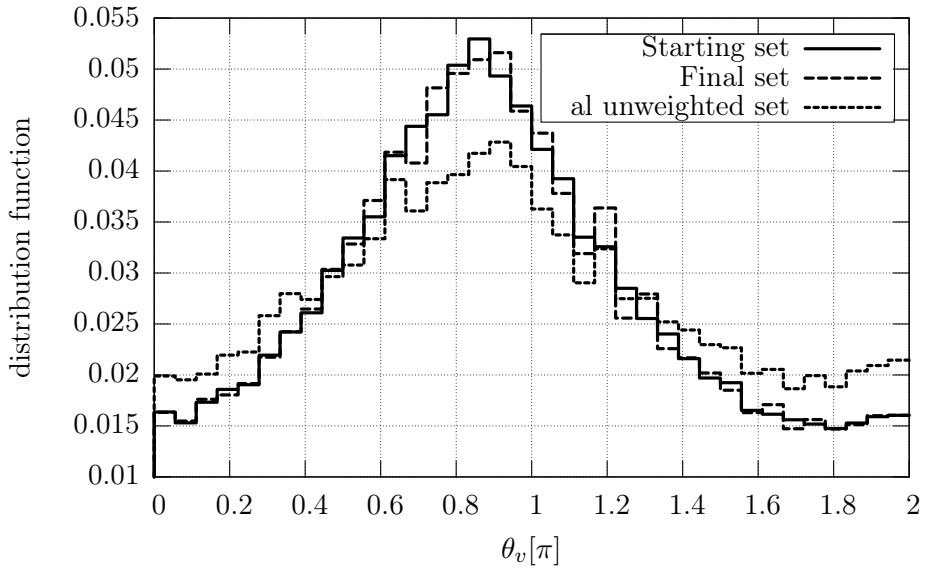

Figure 9.24: Distribution functions of the starting and final sets of particles on the whole domain with respect to the direction of flight; the distribution function of the simulation particles (not weighted) of the final set is also plotted.

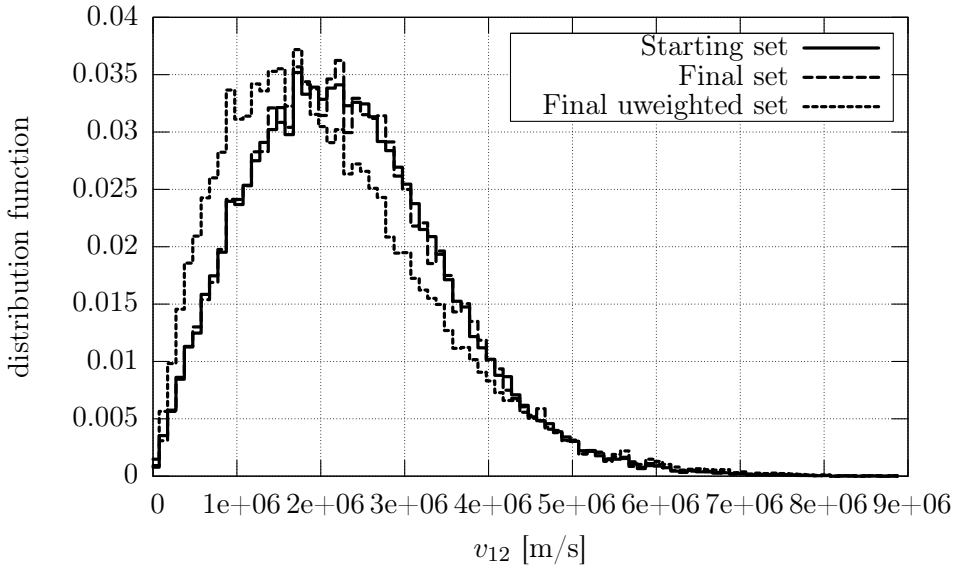

Figure 9.25: Distribution functions of the starting and final sets of particles on the whole domain with respect to the planar velocity; the distribution function of the simulation particles (not weighted) of the final set is also plotted.

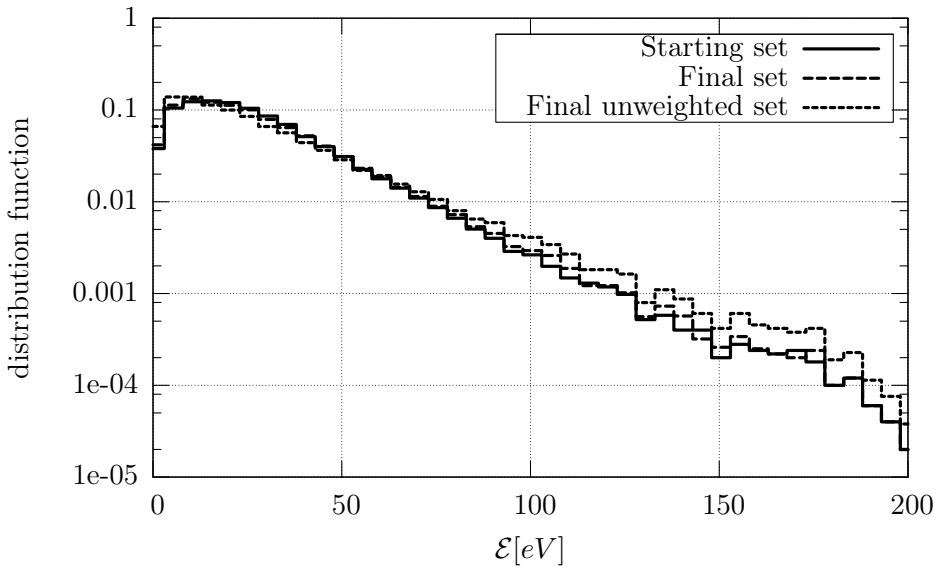

Figure 9.26: Distribution functions of the starting and final sets of particles on the whole domain with respect to the energy; the distribution function of the simulation particles (not weighted) of the final set is also plotted.

number of particles per cell is decreased (approximately from 10^3 down to 350), but also the number of particles is made more homogeneous over the spatial region.

9.2.4 A case of interest

To better understand the effectiveness of the method when applied multiple times, a short analysis of the simulation of Section 9.1 will be proposed.

The plot of Figure 9.13 is extended to the whole simulation time: even if the number of real particles would increase of many orders of magnitude, the number of simulation particles is preserved essentially constant. This prevents excessive memory consumption and reduces computational time, as already stated in Section 9.2.1.

The evolution of the particles number per cell is shown in Figure 9.29. For comparison of the first frame with that of Figure 9.7-a, a perfect correspondence between the number of simulation particle and the electron density is observed, being the merging not yet started at this temporal stage. The other two frames corresponds to the same simulation instants of the first and last ones of Figure 9.8: as evident, the number of simulation particles has been redistributed over the spatial domain with higher values in strongly unstationary regions; notwithstanding the local higher densities would help the clustering procedure increasing the number of treated particles per cell, the velocity distribution function plays an essential role, representing a limit to the clusters extension.

The comparison between the real EEDF and the numerical distribution function obtained assuming equally-weighted simulation particles, independently from their statistical importance, is proposed in Figure 9.30 and 9.31. The redistribution of the simulation particles over the energetic axis improves the representativeness of the sample used in the MCC module, reducing the variance associated to the simulated statistical events. The effect becomes more and more evident as the simulation time increases, the merging and clustering techniques being applied at each time iteration.

9.3 Sensitivity analysis

The simulation examined in Section 9.1 is here taken as reference case for a sensitivity analysis. One simulation parameter per time will be modified in order to show which role it plays in the discharge initiation and evolution. Particular attention will be drawn on the filling gas pressure, voltage ramp, insulator configuration and background gas; as last, the photo-electric effect will be turned off to show how the SEE process is fundamental in feeding the discharge.

9.3.1 Pressure and voltage ramp

As discussed in Section 6.1.1 for the particular case of parallel plane electrodes, the Townsend's ionization coefficient α strictly depends on the reduced electric field. Moreover, the coefficients A and B, which are present in equation (6.2) and concur in the deduction of the Paschen's law , can be considered constant on a limited range of E/p (see Table 6.1 and Figure 6.1). In order to better understand the role played

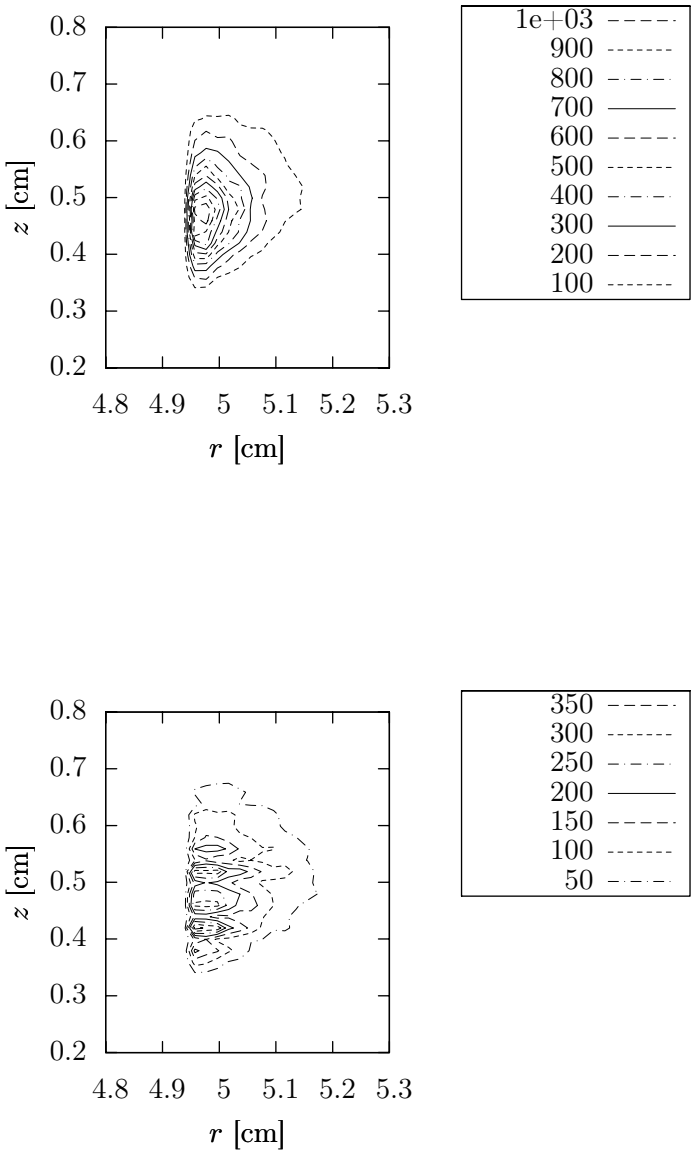

Figure 9.27: Contour lines of the number of particles per cell for the starting (top) and final (bottom) sets of simulation particles. Only the spatial region of interest has been analyzed. A reduction of the maximum number of particles per cell can be observed together with an homogeneization over the domain.

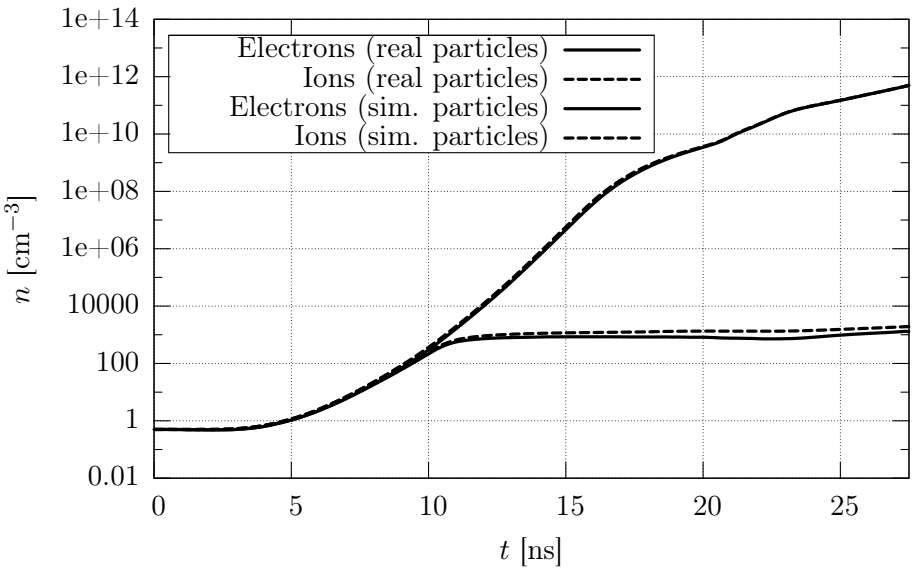

Figure 9.28: Charge particle densities growth for simulation and real particles and for both species, electrons and ions.

by the filling gas pressure and how the macroscopic quantities are influenced, three simulations have been performed at $p = 1, 3$ and 5 Torr respectively.

In Figure 9.32, the electron density growth is scaled over the gas pressure and plotted against time. What arises evident is the gradual temporal shift in the particles growth. This can be easily explained looking at the collisional fraction frequencies proposed in Figure 9.33 and 9.34 for the elastic and ionization processes respectively: since the collisional frequency is proportional to the neutral background density, at higher pressures the energy losses through elastic scattering is stronger and delays the acceleration of electrons to the threshold energy for ionization; even if starting at a more advanced temporal stage, the ionization collisional rate grows steeper for higher pressures and the three curves of Figure 9.34 are reversed after approximately 10 ns.

The growth in the particle densities presented in Figure 9.32 does not intersect their trend, as one could expect as a consequence of the ionization rate inversion, due to the impact with boundaries. Since the ionization process starts just over the insulator sleeve, the impact over the dielectric surface is predominant: as shown in Figure 9.35, a behavior similar to that of ionization rate is obtained even for the dielectric impinging. The two effects compensate producing a particle growth derivative approximately independent on the filling gas pressure.

More intuitive is the comparison between cases with different applied voltage ramps ($\mathrm{d}V/\mathrm{d}t = 100$, 200 and 300 V/ns respectively). The analysis allows to scale the value of the reduced electric E/p field at each instant, with any change in the background gas properties.

A higher time derivative of the applied electric field induces higher accelerations in the seed electrons already in the first instants of the discharge: as shown in

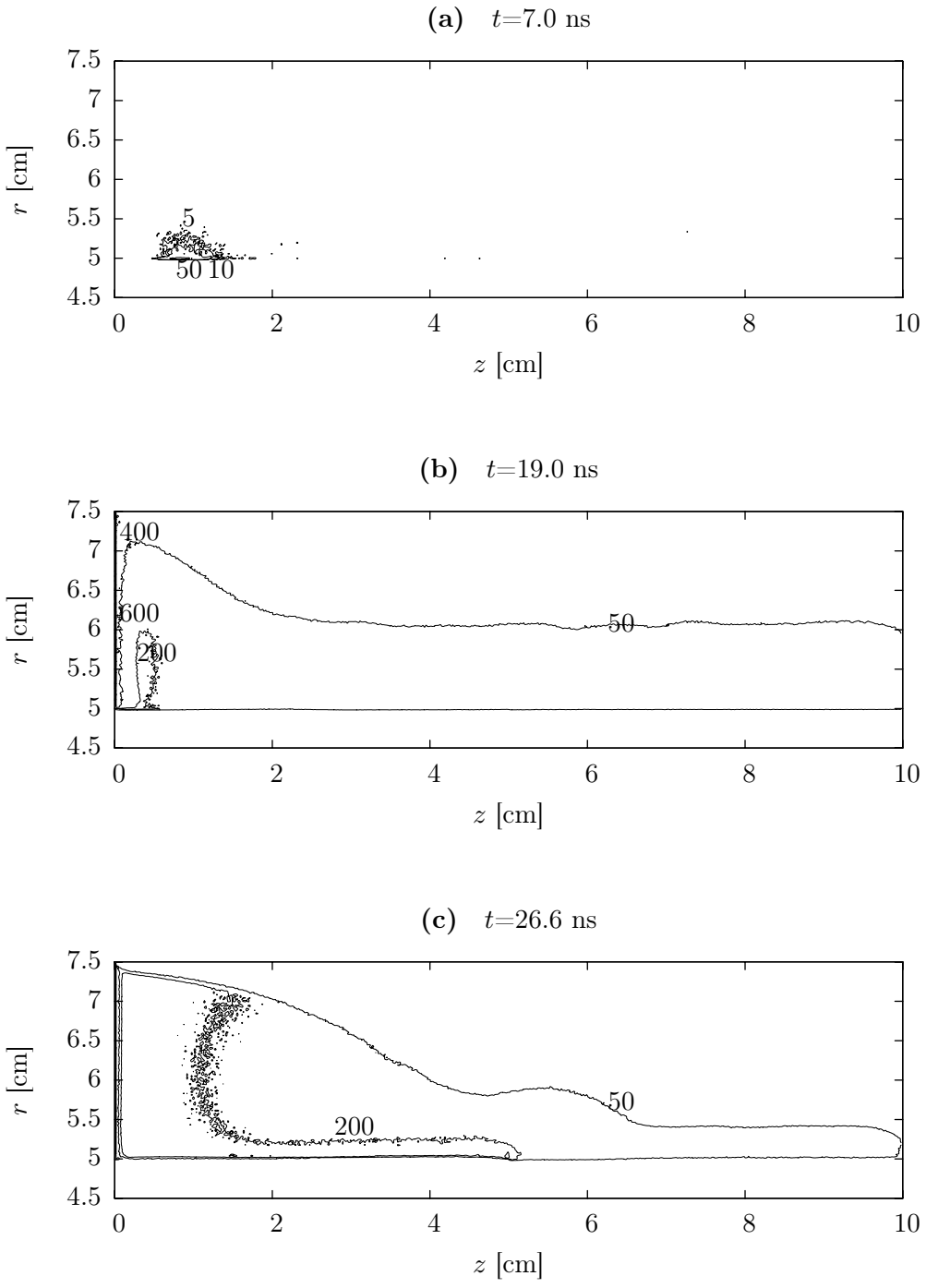

Figure 9.29: Particle number contour lines at fixed time instants during the simulation: the redistribution over the spatial domain obtained through the merging and clustering techniques is evident.

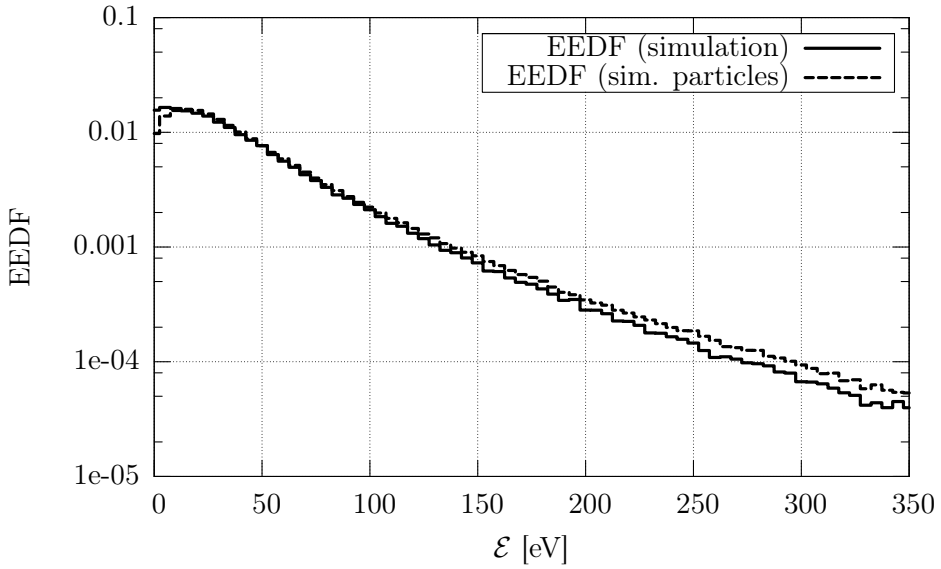

Figure 9.30: EEDF at $t = 10.8$ ns, compared with the distribution function of the simulation particles not weighted on their importance.

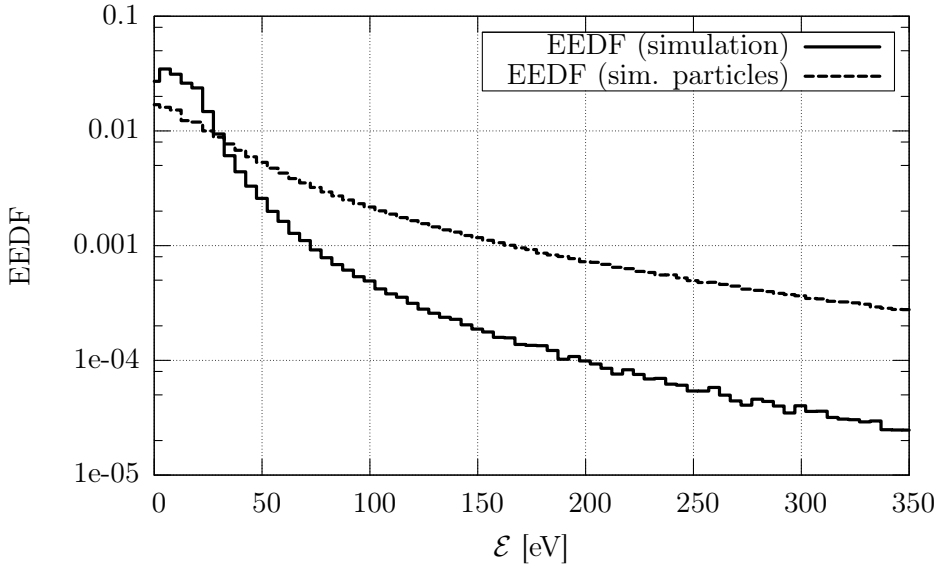

Figure 9.31: EEDF at $t = 20.0$ ns, compared with the distribution function of the simulation particles not weighted on their importance.

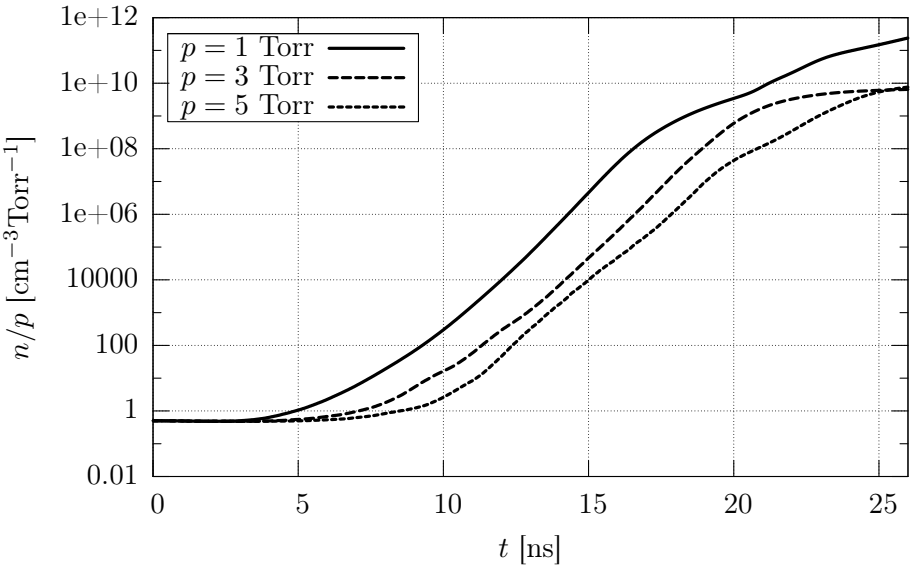

Figure 9.32: Electron density growth scaled over pressure of the filling gas, for three different values.

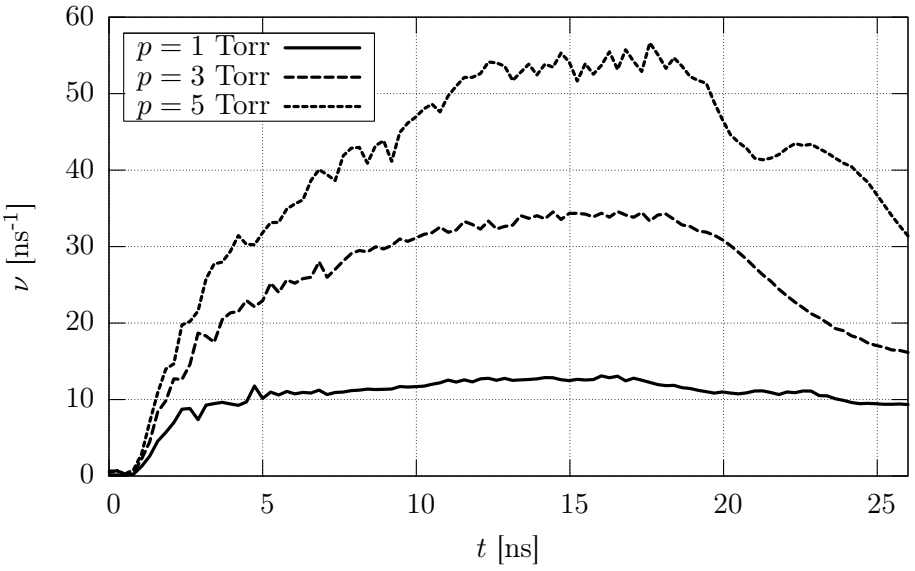

Figure 9.33: Elastic collisional fractions frequencies for the electrons at three different pressure values of the filling gas.

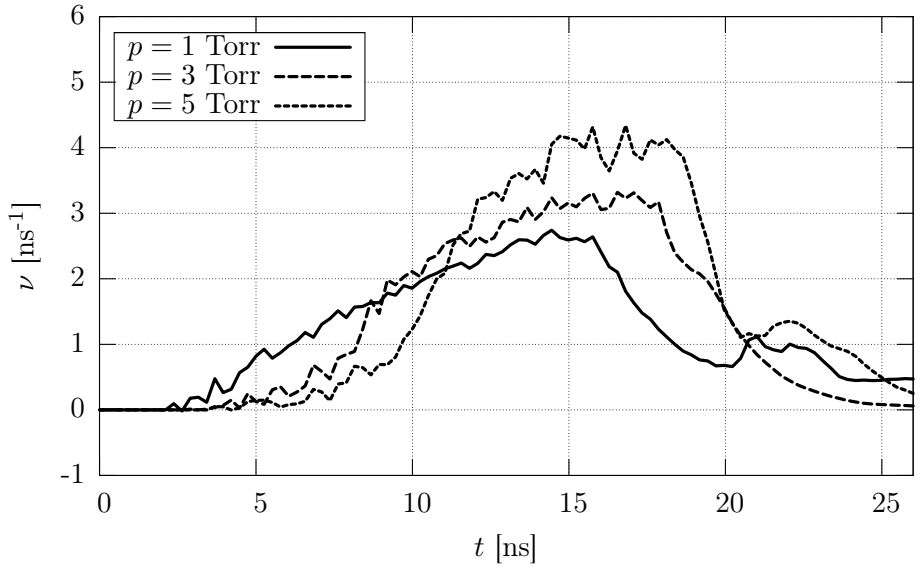

Figure 9.34: Ionization collisional fractions frequencies for the electrons at three different pressure values of the filling gas.

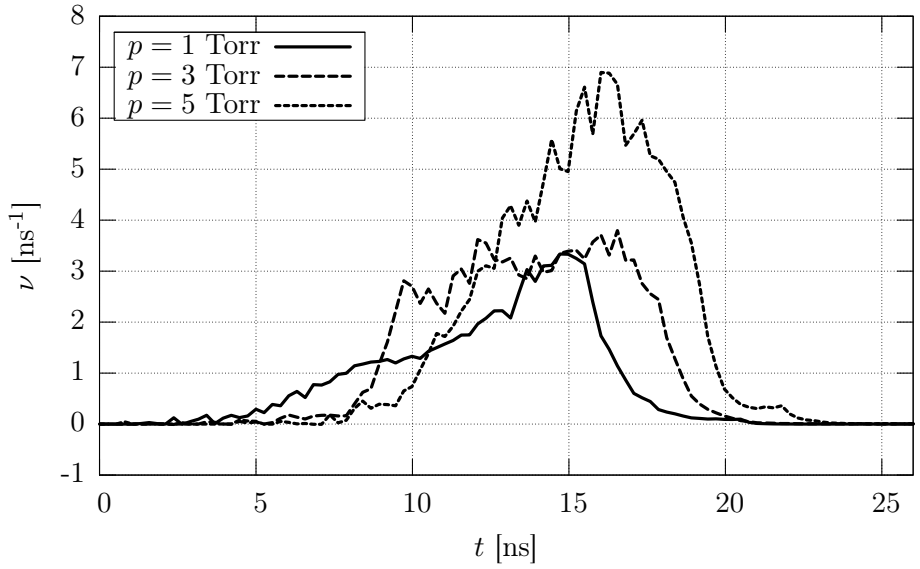

Figure 9.35: Electron impact frequency over the surface of the insulator sleeve at three different pressure values of the filling gas.

$\mathrm{d}V/\mathrm{d}t$ [V/ns]	Time range [ns]	Voltage range [kV]	α_t [ns^{-1}]
100	$15.0 \div 20.0$	$1.5 \div 2.0$	1.59
200	$11.0 \div 17.5$	$2.2 \div 3.5$	1.77
300	$7.5 \div 13.7$	$2.3 \div 4.1$	2.23

Table 9.2: Ionization growth rate corresponding to the exponential growth of the particle densities for three different values of the externally applied linear voltage ramp.

Figure 9.36, the particle densities rise more rapidly for higher voltage ramps, until the interaction with the boundaries limits the ionization growth. A rough estimate of α for an exponential growth rate of the type $n = n_0 \exp(\alpha_t t)$ is proposed in Table 9.2 for the three cases of interest.

Unlike the above case, since the pressure is unchanged in the three simulations, the elastic collisional rates, plotted in Figure 9.37, are of the same order, but shifted in time, due to the different growth of the mean kinetic energy of the colliding particles. On the other hand, the ionization collisional frequencies are affected by the boundary interaction (see both Figures 9.38 and 9.39): the more energetic particles, which are scattered mainly in the forward direction with a limited loss of energy, will be the first to reach the insulator sleeve, being eliminated from the system; higher is the voltage ramp, higher will be the mean energy reached by the system and, consequently, the ionization collisional rate. The dielectric impact frequency is only shifted in time, similarly to the elastic collision rate.

9.3.2 Insulator configuration

In order to examine how the geometry of the insulator influences the discharge development, the reference input geometrical parameters collected in Table 9.1 have been modified moving the insulator over the anode: while the radius of the CE r_{int} and the insulator thickness s_{ins} have been maintained, its outer radius has been increased to $r_{\mathrm{ins}} = 5.5$ cm. The obtained geometrical configuration is widely used in many PF designs, the manufacturing and maintenance operations being easier.

Comparing the growth of particle densities over the whole domain, in the first stage of the discharge, the multiplication rate results slightly increased in the alternative insulator configuration, due to the higher enhancing of the electric field at the closed end of the electrodes, near the cathode edge. At approximately 14 ns the trend is inverted and, while in the reference case the particle number continues to grow, in that under consideration the particles multiplication slows down. The fact is confirmed by the comparison between the electron mean energy evolution: while in the first case it grows up to 63.3 eV at about 15 ns, in the insulator alternative configuration, $\langle \mathcal{E} \rangle$ presents a plateau at about 49 eV between 10 and 16 ns and drops down to 15 eV in less than 5 ns. This reflects on the ionization collisional rate which does not reach the values observed in Figure 9.2 with a reduction of about 30% on

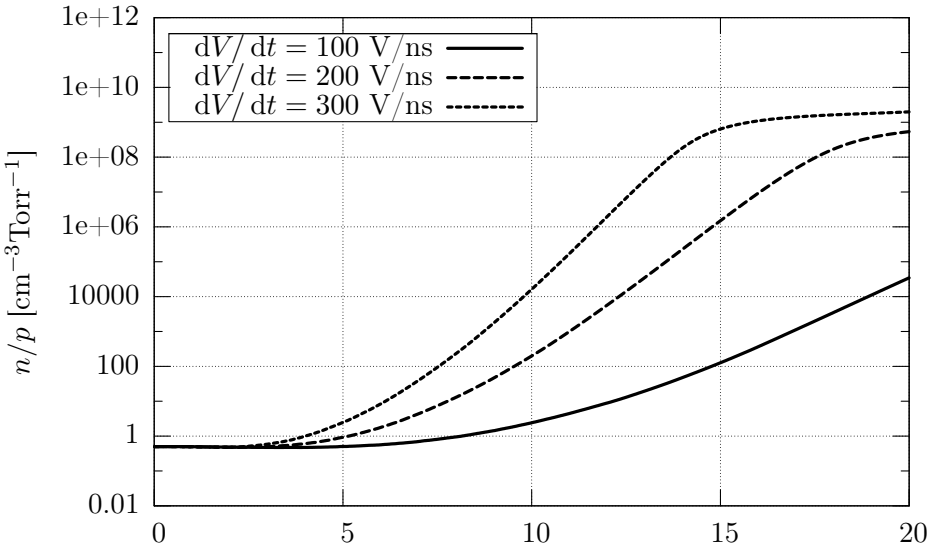

Figure 9.36: Electron density growth, for three different values of the imposed voltage ramp.

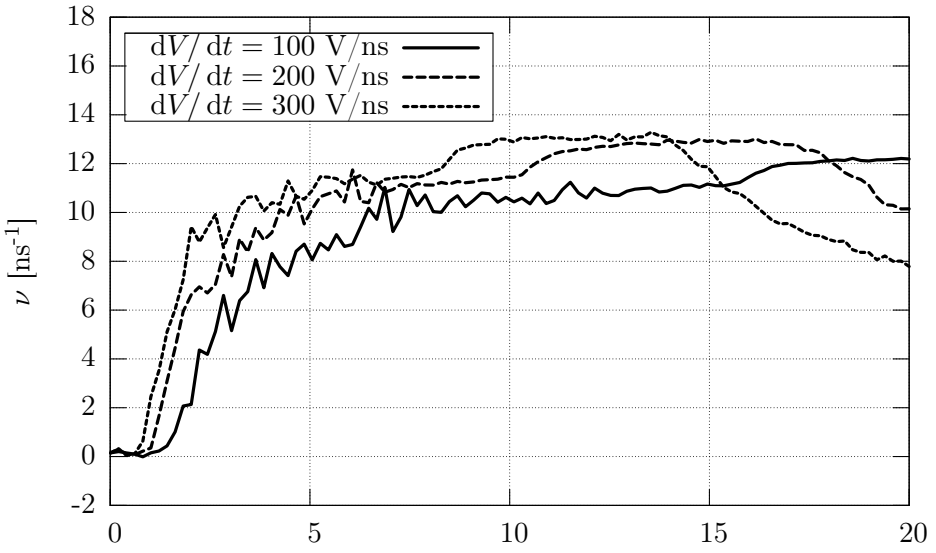

Figure 9.37: Elastic collisional fractions frequencies for the electrons at three different values of the imposed voltage ramp.

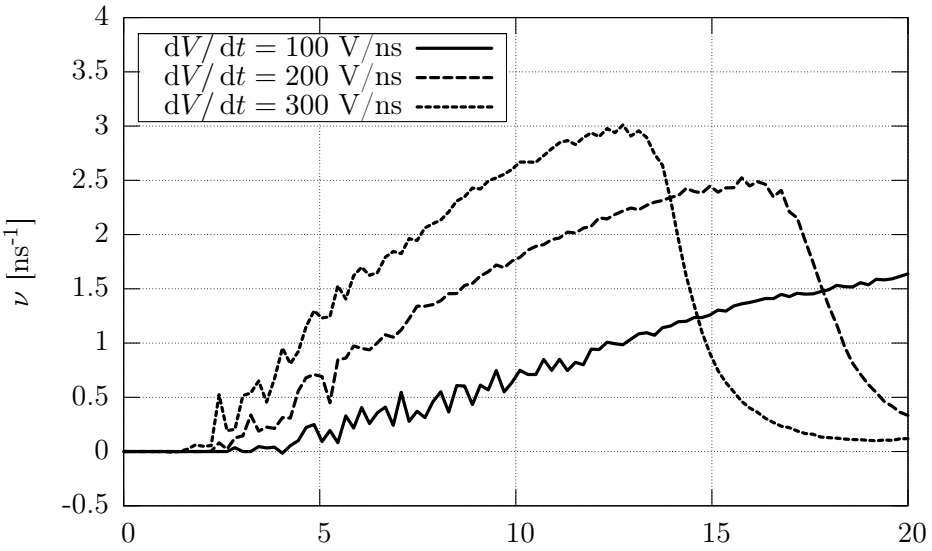

Figure 9.38: Ionization collisional fractions frequencies for the electrons at three different values of the imposed voltage ramp.

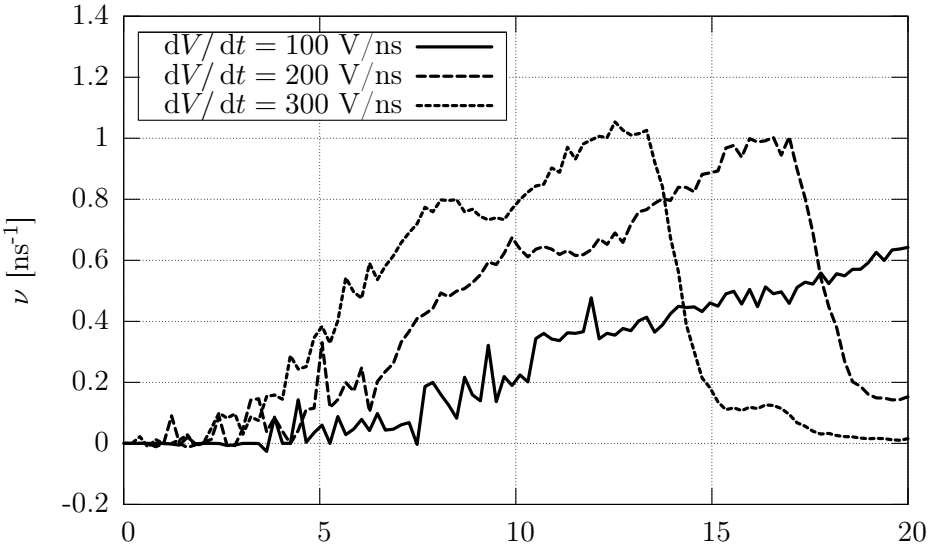

Figure 9.39: Electron impact frequency over the surface of the insulator sleeve at three different values of the voltage ramp.

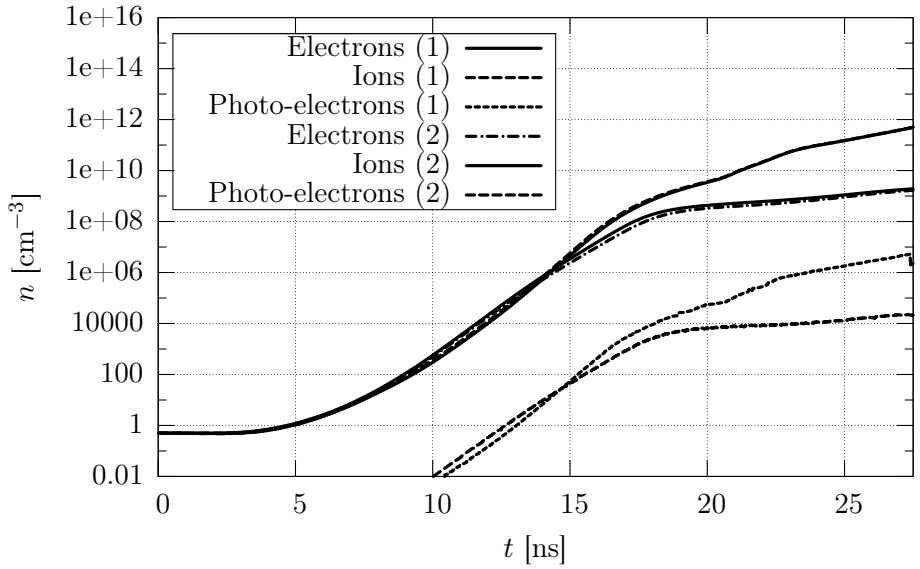

Figure 9.40: Comparison between the growth of particle densities during the whole simulation for the reference case (1) and the alternative insulator configuration (2).

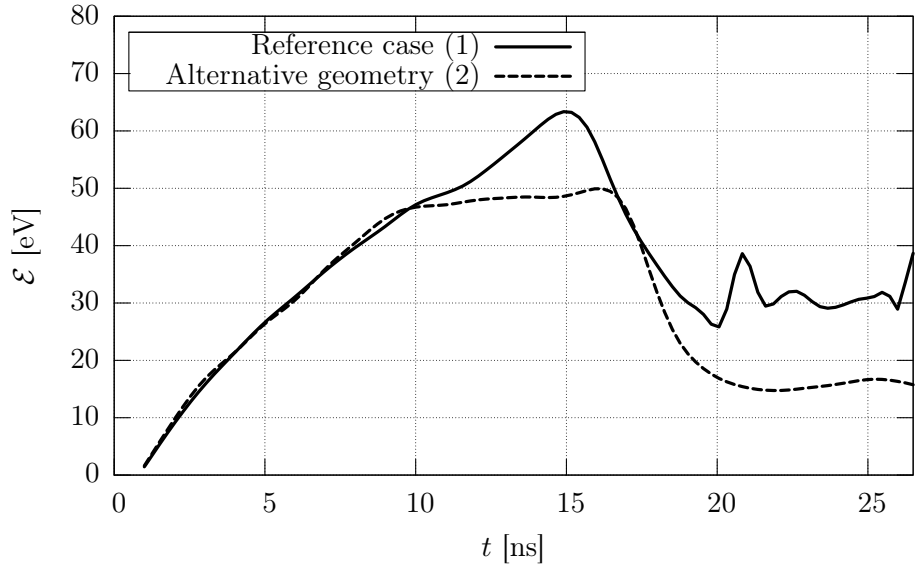

Figure 9.41: Comparison between the electron mean energy evolution for the reference case (1) and the alternative insulator configuration (2).

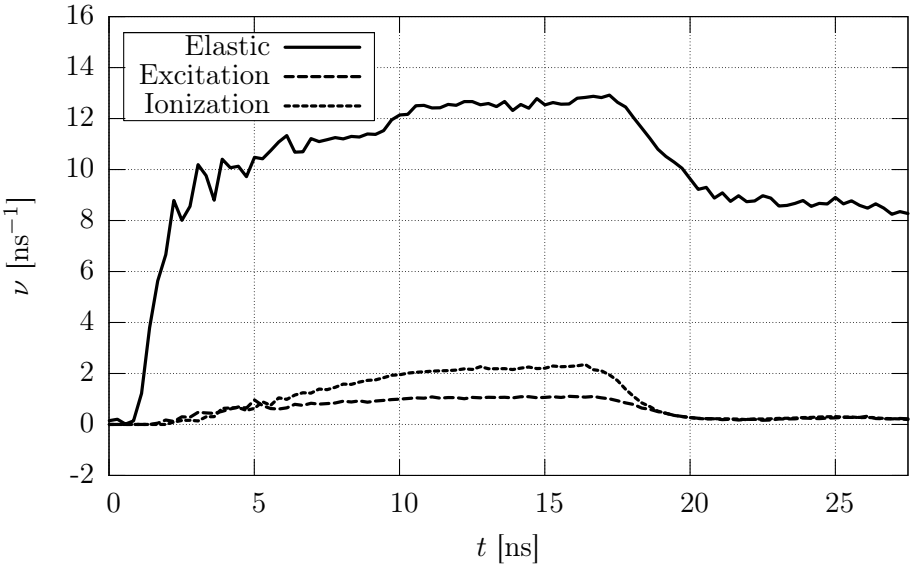

Figure 9.42: Fractional collisional frequency of electrons with the background gas, in the alternative insulator configuration.

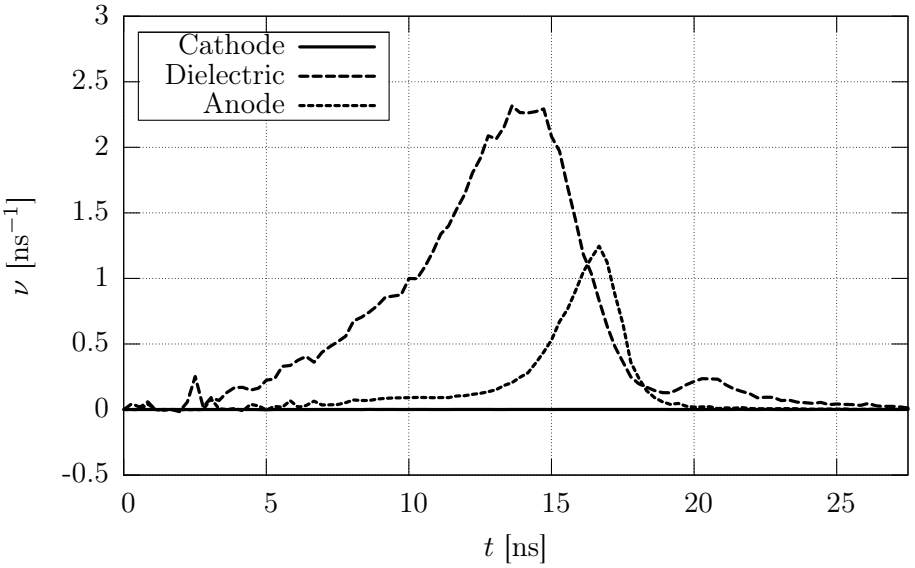

Figure 9.43: Fractional collisional frequency of electrons with the boundary surfaces of the simulation domain, in the alternative insulator configuration.

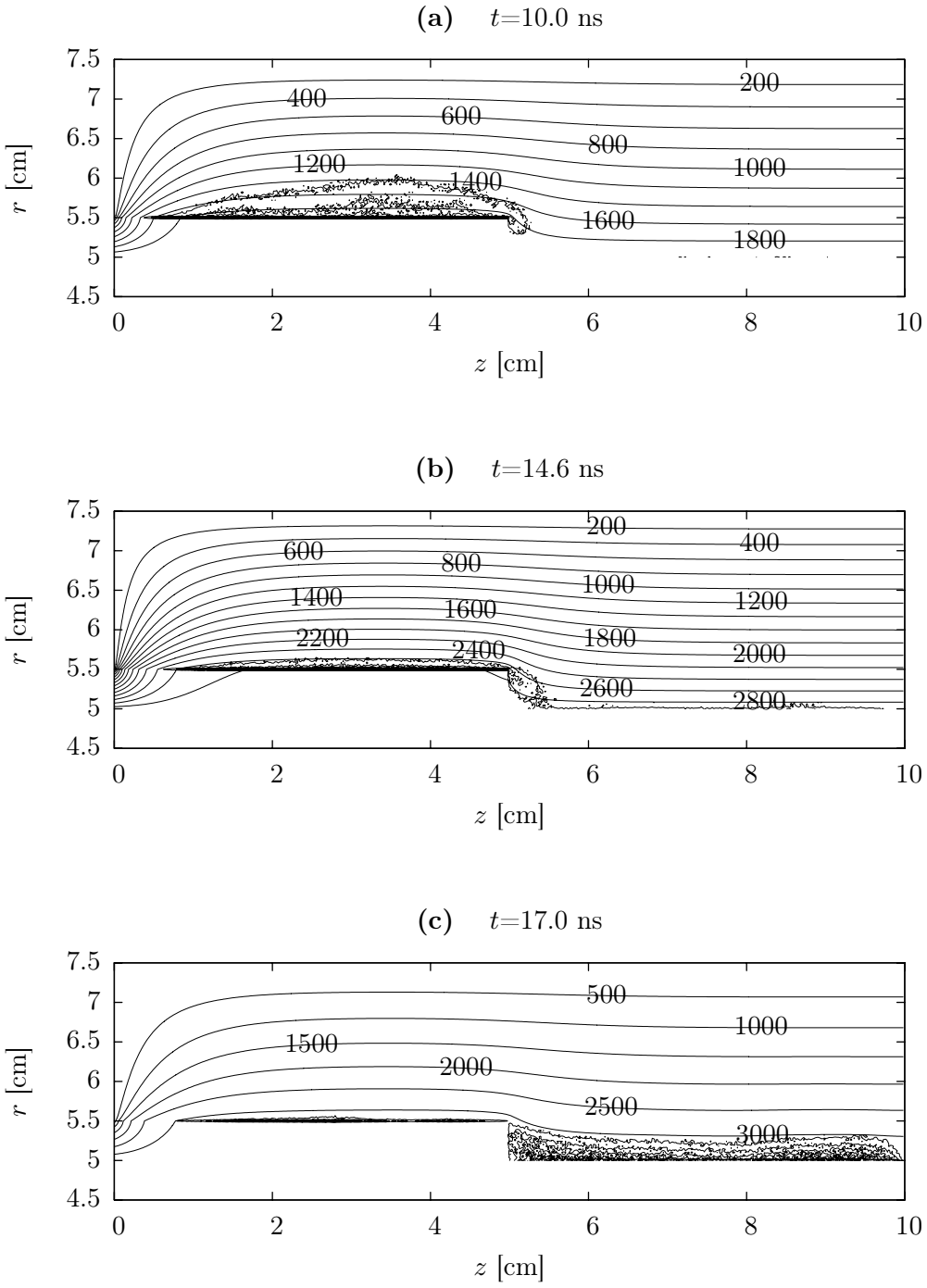

Figure 9.44: Density profiles and isopotential lines at fixed time instants during the first part of the simulation; the alternative insulator configuration is evident.

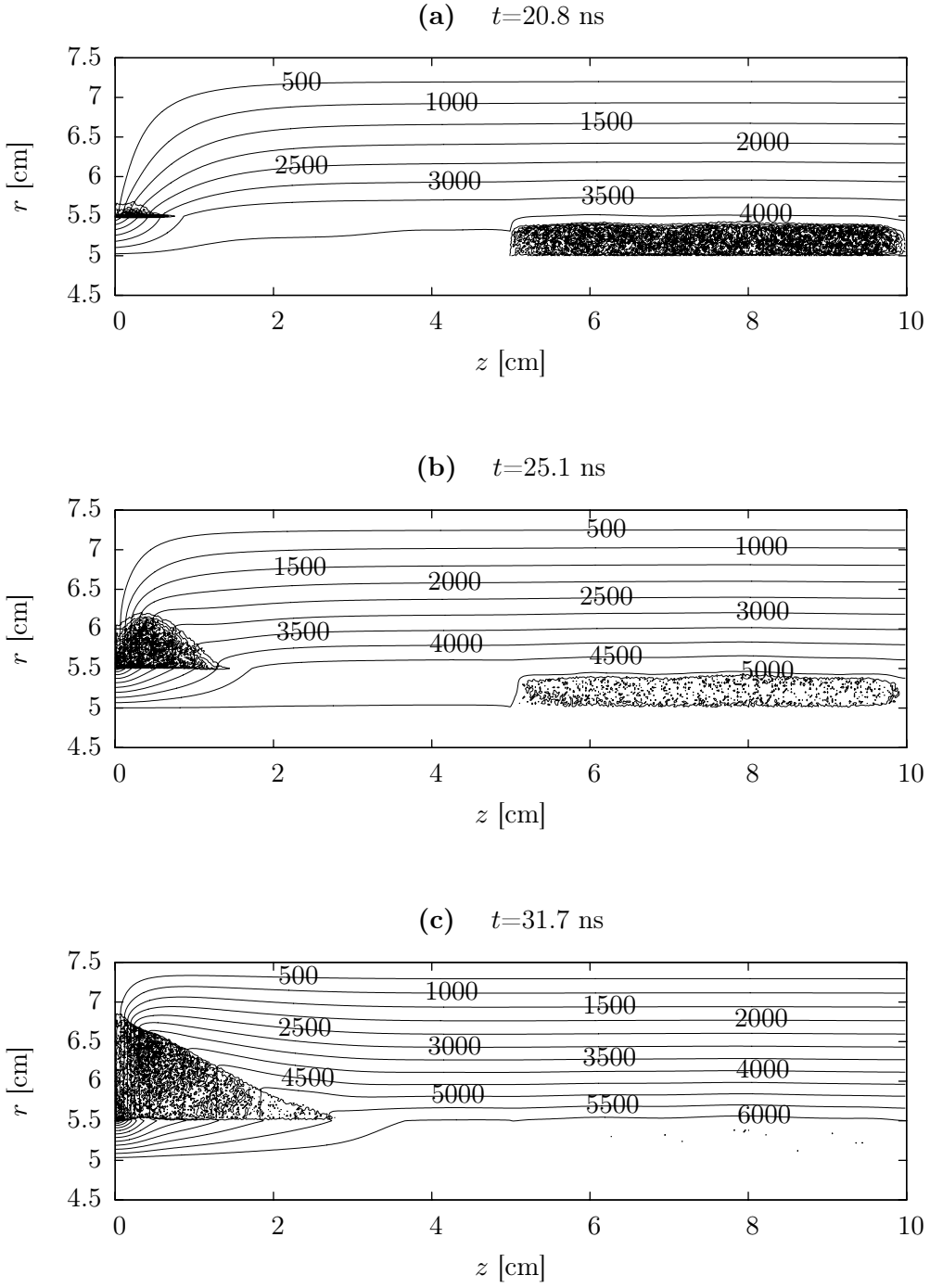

Figure 9.45: Density profiles and isopotential lines at fixed time instants during the second part of the simulation.

the maximum. A similar reduction is observed even on the dielectric impact events, while the negative charge deposition over the anode is increased of about four times.

A better interpretation of the phenomenon is made easier if the evolution of the electric field and of the density profiles is examined over the whole domain. The isopotential lines of Figure 9.44, not yet modified by the space charge and the surface charge deposited over the dielectric, show the differences in the spatial dependence of the external electric field, $\vec{E}(\vec{r})$: due to the dielectric properties, the thickness of the insulator sleeve substantially reduces the interelectrode gap to 2.0 cm over the first 5.0 cm in the axial direction inducing thickening of the isopotential lines (increased electric field along the radial direction); on the residual part of the uncovered anode, the gap is restored to 2.5 cm, with a consequently less intense electric field. The first ionization events occur diffusely over the whole insulator sleeve, and not concentrated near the cathode edge, producing a first layer of ionized gas with densities in the range $2 \div 12 \cdot 10^4$ cm^{-3}. At a time instant corresponding with the maximum of the dielectric collisional rate frequency (Figure 9.44-b), the density of the layer results increased up to $7 \cdot 10^8$ cm^{-3}, with a very low thickness of few mm. In few ns, the electric field reaches sufficiently high values to induce electron avalanches over the uncovered part of the anode: the charge particles, attracted towards the positive electrode, produce a second layer of ionized gas over it with densities of the order of $5 \cdot 10^9$ cm^{-3}, comparable with those of the residual part over the insulator, in great measure deposited over its surface. The positive space charge, left by ionization and surface impact events, becomes soon high enough ($3 \cdot 10^{10}$ cm^{-3} in Figure 9.45-a) to modify the electric field: in particular, the interelectrode gap over the uncovered part of the anode is actually reduced to 2.0 cm, with a net effect similar to the presence of the insulator. In the meantime, a new ionization avalanche is started at the cathode edge and rapidly reaches densities $2 \cdot 10^{11}$ cm^{-3}, overcoming the densities over the uncovered anode; the time instant corresponds to the secondary peak in the electron collisional frequency over the dielectric, observable in Figure 9.43. Hereafter, the ionized gas will develop into a discharge over the insulator surface with a lower density growth rate: the axial potential gradient, produced by the space charge and the deposited one over the insulator, pushes the charged particles along the insulator sleeve towards the perturbed region of the uncovered anode, where density becomes negligible if compared to those of the evolving discharge.

9.3.3 Background gas

As shown in Section 7.3.3 on page 163, many possible excitation processes have been considered for hydrogen.

What arises evident from the evolution of particle densities plotted in Figure 9.46 is a much less growth rate than in the case of argon as background gas. Even if the ionization threshold energies of the ionization process are comparable for argon and hydrogen, as well as their energy dependence (see Figure 7.10 and 7.12), the maximum value for H_2 is 3 times lower than that of Ar. Moreover, the Ramsauer-Townsend effect, characteristic of noble gases, is completely absent in the case of interest: the progressively accelerated electrons never see an almost transparent background medium when they move in an hydrogen gas, in spite of the electrons in an Argon gas (whose elastic scattering cross section is almost zero at approximately

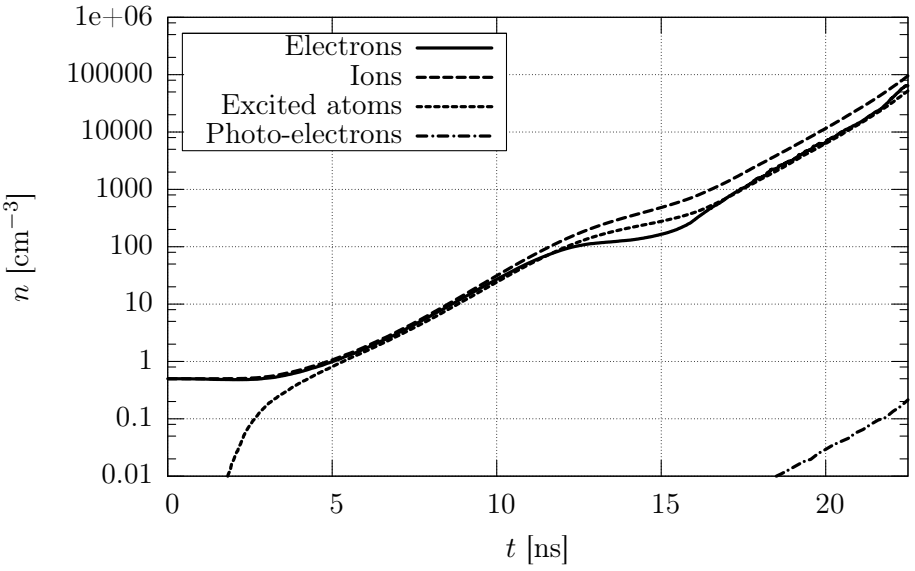

Figure 9.46: Growth of particle densities during the whole simulation, in the case of H_2 as background gas; the density of excited states is monitored in total to deduce the number of electrons produced by photo-electric effect on the cathode backwall.

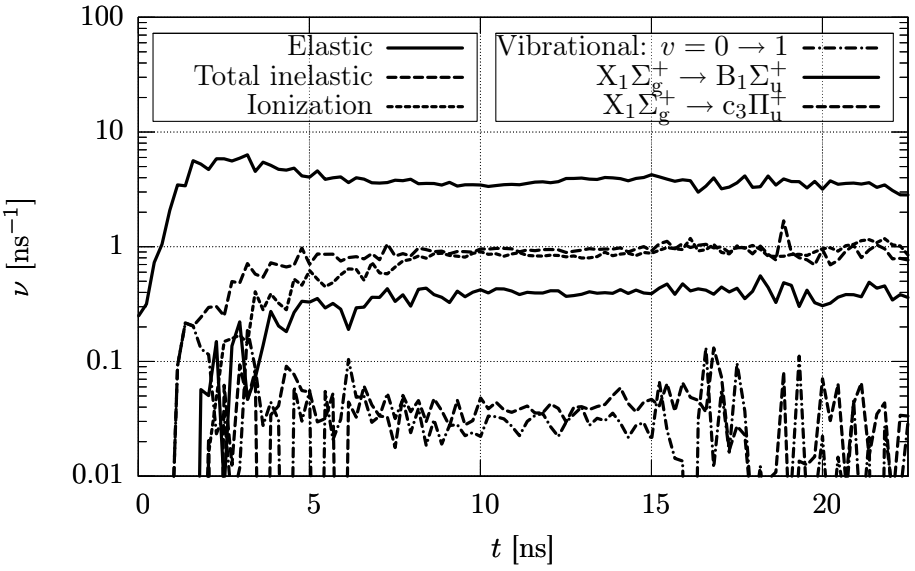

Figure 9.47: Fractional collisional frequency of electrons with the background gas, in the case of H_2 as background gas for a selection of reaction types.

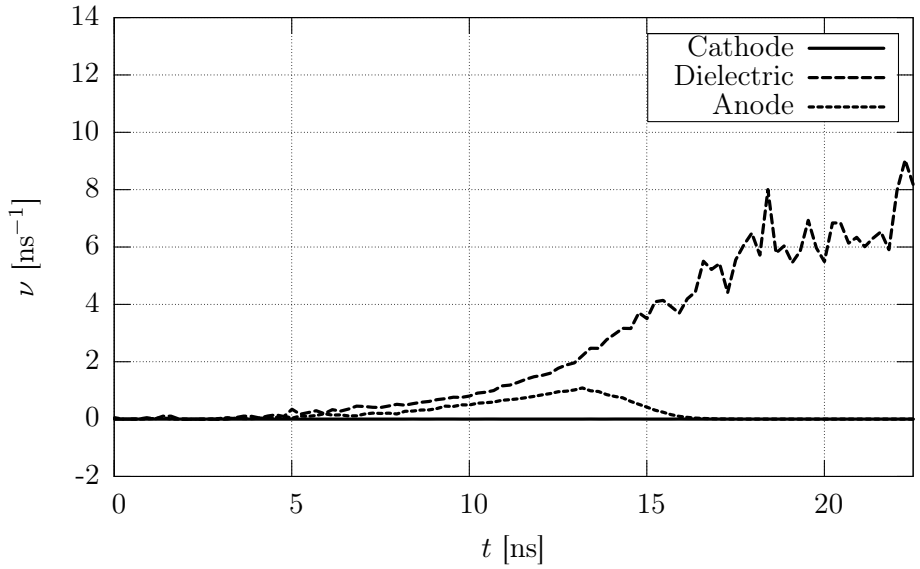

Figure 9.48: Fractional collisional frequency of electrons with the boundary surfaces of the simulation domain, in the case of H_2 as background gas..

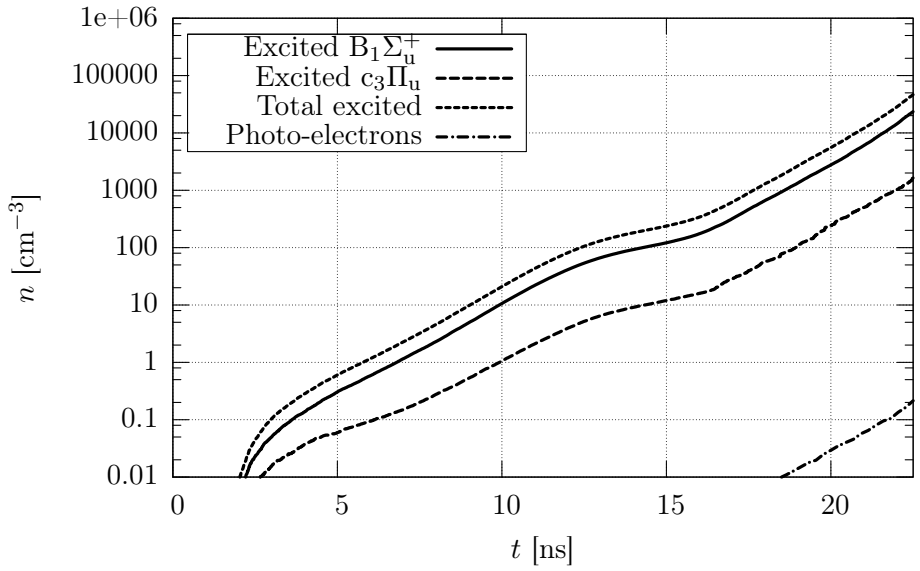

Figure 9.49: Time evolution of the densities of excited species and of the produced photo-electrons, in the case of H_2 as background gas.

0.2 eV). This is evident comparing the very first instants of the elastic scattering collisional fractions plotted in Figure 9.2 and 9.47, for argon and hydrogen respectively: no decreasing slope is observed in the second case. The large number of inelastic cross sections is another reason of the lower growth rate: the contribution due to all the inelastic scattering processes is comparable with the that corresponding to ionization, resulting even greater collisional up to 10 ns (Figure 9.47).

The strong variation in the slope of densities growth between 10 and 15 ns is related to the loss of a large number of particles at the anode surface; while the dielectric impacts are monotonically increasing in time, as shown in Figure 9.48, the anode collisional fraction frequency reach its maximum at about 13 ns; this is due to an homogeneous ionization even in the region above the CE: the increasing applied potential attracts the negative charges so rapidly that losses are not compensated by ionizations. The effect was present even in the case of argon, but the higher ionization rate mitigated it.

A larger number of possible decay channels corresponds to the larger number of excitation processes; the time evolution of three excited species is plotted in Figure 9.49 and compared with the total number of emitted photo-electrons. In particular, it arises evident the difference between the evolution of the $B_1\Sigma_u^+$ and $c^3\Pi_u$ species due to their completely different characteristic decay times (see Table 7.4).

9.3.4 Photoemission

As stated in Section 6.1, the SEE plays a fundamental role in the breakdown development and, in particular, in the discharge maintainance. In Section 6.2.3, many processes are considered for the interaction of both electrons and ions on the cathode, anode and dielectric surfaces. Due to the low mobility of ions, most of all in the first stages of the PF breakdown, when the voltage applied between the electrodes is lower than 10 kV, the SEE by ion impact on the cathode surface can be neglected: as shown in Figure 9.50, only sporadic events are detected. At about 25 ns, the evolution of the space charge has drastically modified the electric field near the cathode back-wall (see Figure 9.8-c) and electrons emitted by photo-electric effect, are rapidly accelerated to energies over the ionization threshold; as a consequence, the ions, produced near the cathode, are accelerated by a very high electric field (approximately 45 kV/cm) and impact on the cathode back-wall with an increasing frequency.

On the contrary, the SEE by photo-electric effect induced by photons produced inside the system by decay of exited states plays a fundamental role feeding the discharge with fresh electrons from the cathode back-wall. In Figure 9.51, the density of excited states and produced photo-electrons is plotted at 1 Torr in Argon (the comparison with the total density of ions and electrons was proposed in Figure 9.1, for the same input parameters). The photon and photo-electron densities are also compared to show the effect of the sight factor and of the secondary emission coefficient; the number of emitted simulation particles, which follows the basic principles explained in Section 8.5.5, is also plotted.

To fully understand the role of photo-electrons, a simulation with the same operational parameters of that proposed in Section 9.1 was run deactivating the call to the photo-emission routine. The particle density growth is the first representa-

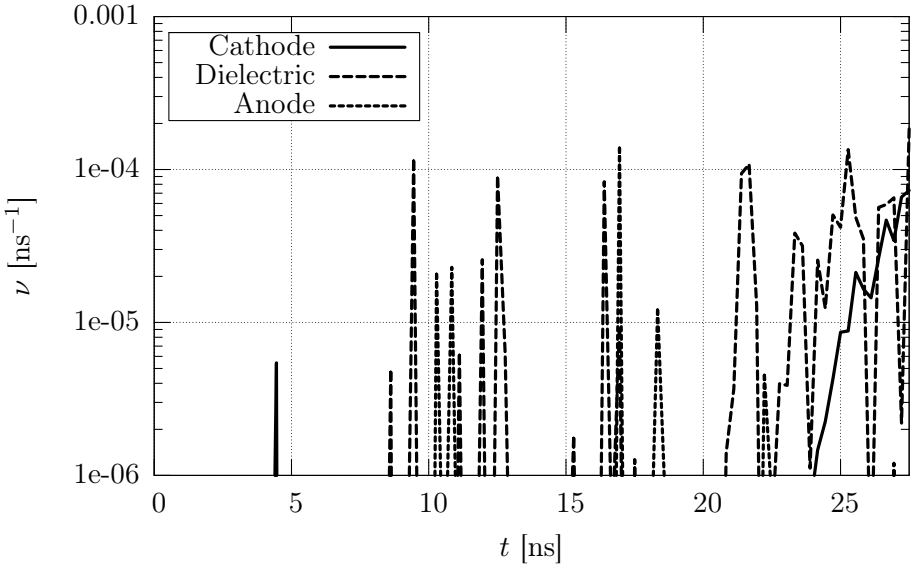

Figure 9.50: Ion collisional rate frequencies with the domain boundaries; the sporadic events are due to the low mobility of heavy particles.

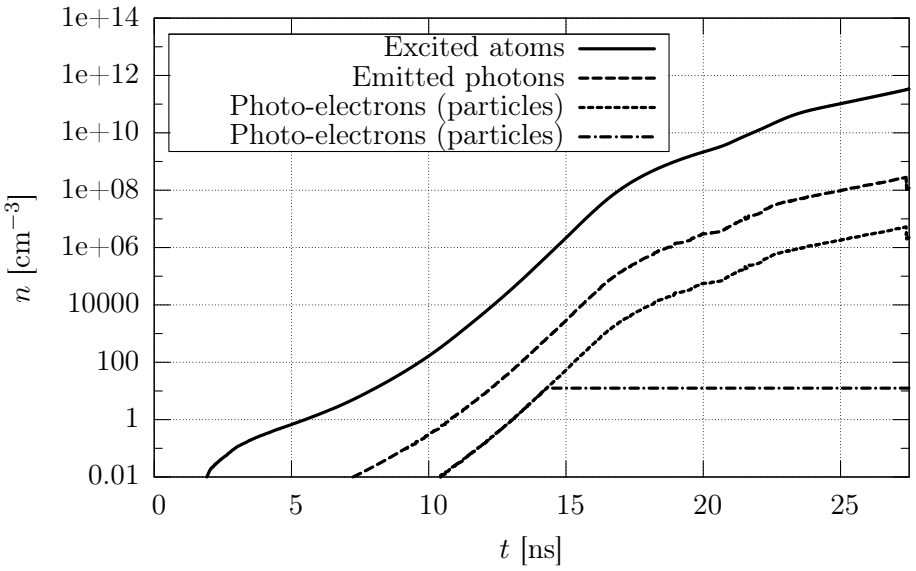

Figure 9.51: Temporal growth of excited atoms and photo-electron total densities, compared with the density of simulation particles effectively emitted from the cathode back-wall.

tive macroscopic quantity of interest: in Figure 9.52, the time when photo-emission starts to become not negligible is evident by comparison. Other quantity of interest, about which the effects of the photo-emission were discussed, is the time-evolution of mean energy for the electron species: in Figure 9.53, a steeper decrease with no oscillation is observed when photo-electrons don't perturb the system.

As far as the fractional collisional frequencies of the electrons with the background gas are compared, it appears clear the similarity between the two cases and their dependence on the mean energy of the species: the only appreciable difference between Figure 9.2 and Figure 9.54 lies beyond the threshold of 20 ns, where the little peaks of ionization, observed in the first case with photo-emission, disappear in the present one. More differences characterize the collisional frequencies with the domain boundaries: as evident comparing Figure 9.3 and Figure 9.55 (please note the different scales in ordinates), the impacts over the dielectric are strongly enhanced when photo-electrons are emitted from the cathode back-wall (a factor 3 separates the two cases at about 15 ns). The differences between the negative charges impinging on the anode (a factor 2 higher in the case without the photo-emission at about 5 ns) have to be interpreted in relative terms, the collisional fractions frequencies being calculated as the ratio between the colliding particles and the total number of particles; this means that, when the photo-electric effect is absent, the discharge develops more uniformly over the whole electrode length, both on the dielectric and on the anode.

The fact becomes more evident if the sheath density profiles and isopotential lines are examined (Figure 9.56) and compared with the corresponding time-instant of Figure 9.7 and 9.8. It is evident how the absence of electrons emitted from the cathode back-wall modify the sheath development: the connection with the cathode edge is completely lost.

The absence of photo-electrons modifies also the EEDF, as shown in Figure 9.57-9.60, at time instants corresponding to those of Figure 9.9-9.12. While at a first stage the distribution functions perfectly correspond (as deducible by above considerations), the EEDFs corresponding to the maximum of the mean energy, at approximately 15 ns, and after the consequent rapid decrease, deviates from those obtained in the reference case with photo-emission. The deviation from the Boltzmann-Maxwell distribution function at the same mean energy is still evident, but the contribution at low energies (few eV) and high energies (more than 150 eV) is slightly lower, due to the decrease in particles multiplication and in their acceleration by the electric field, modified by the spatial charge density.

The role of the photo-electrons in sustaining the breakdown and in connecting the discharge to the cathode edge is now more evident, but it merits further deeper investigations.

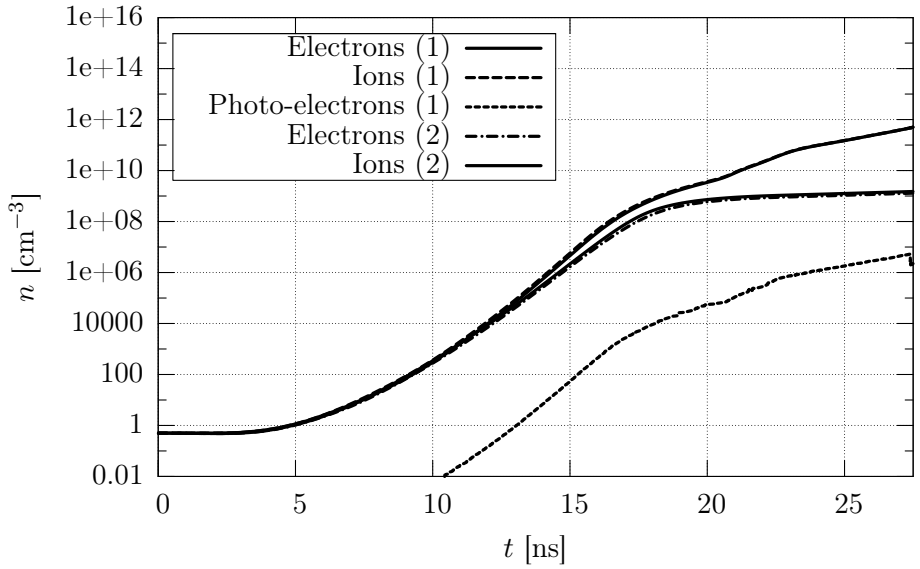

Figure 9.52: Growth of the ion and electron densities in the two cases with photo-emission (1) and without it (2); the density of photo-electrons emitted in the first case is also reported.

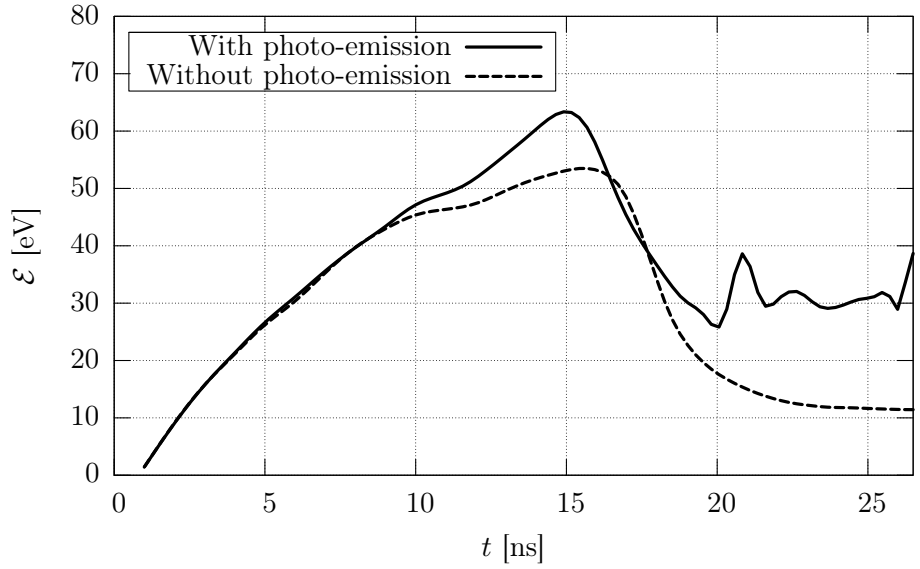

Figure 9.53: Mean energy evolution in the two cases with and without photo-emission.

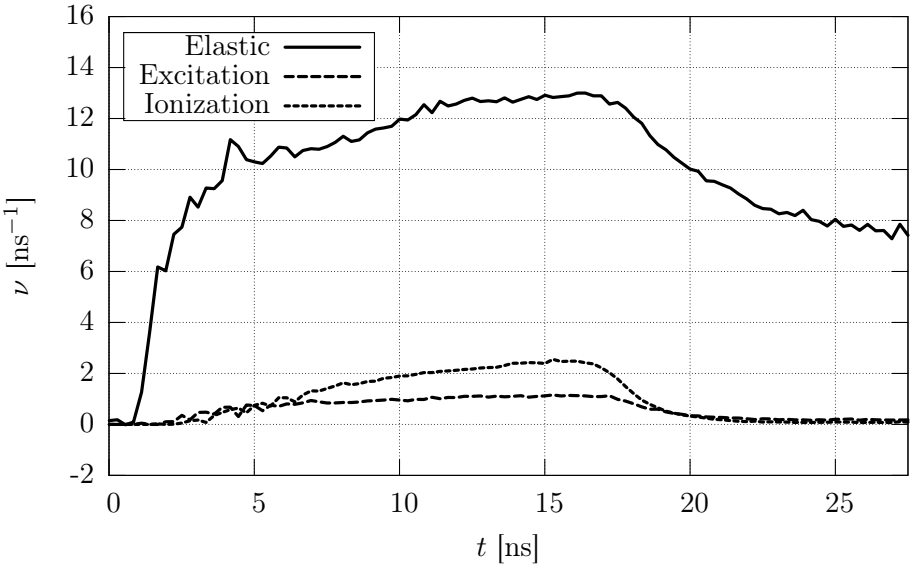

Figure 9.54: Fractional collisional frequency of electrons with the background gas, when photo-emission is turned off (compare it with Figure 9.2).

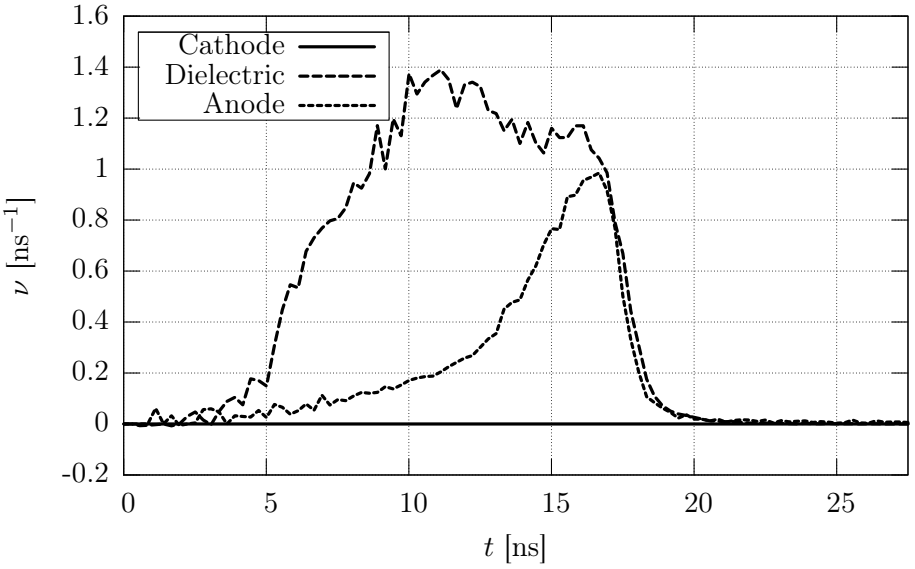

Figure 9.55: Fractional collisional frequency of electrons with the boundary surfaces of the simulation domain, when the photo-emission is turned off (compare it with Figure 9.3).

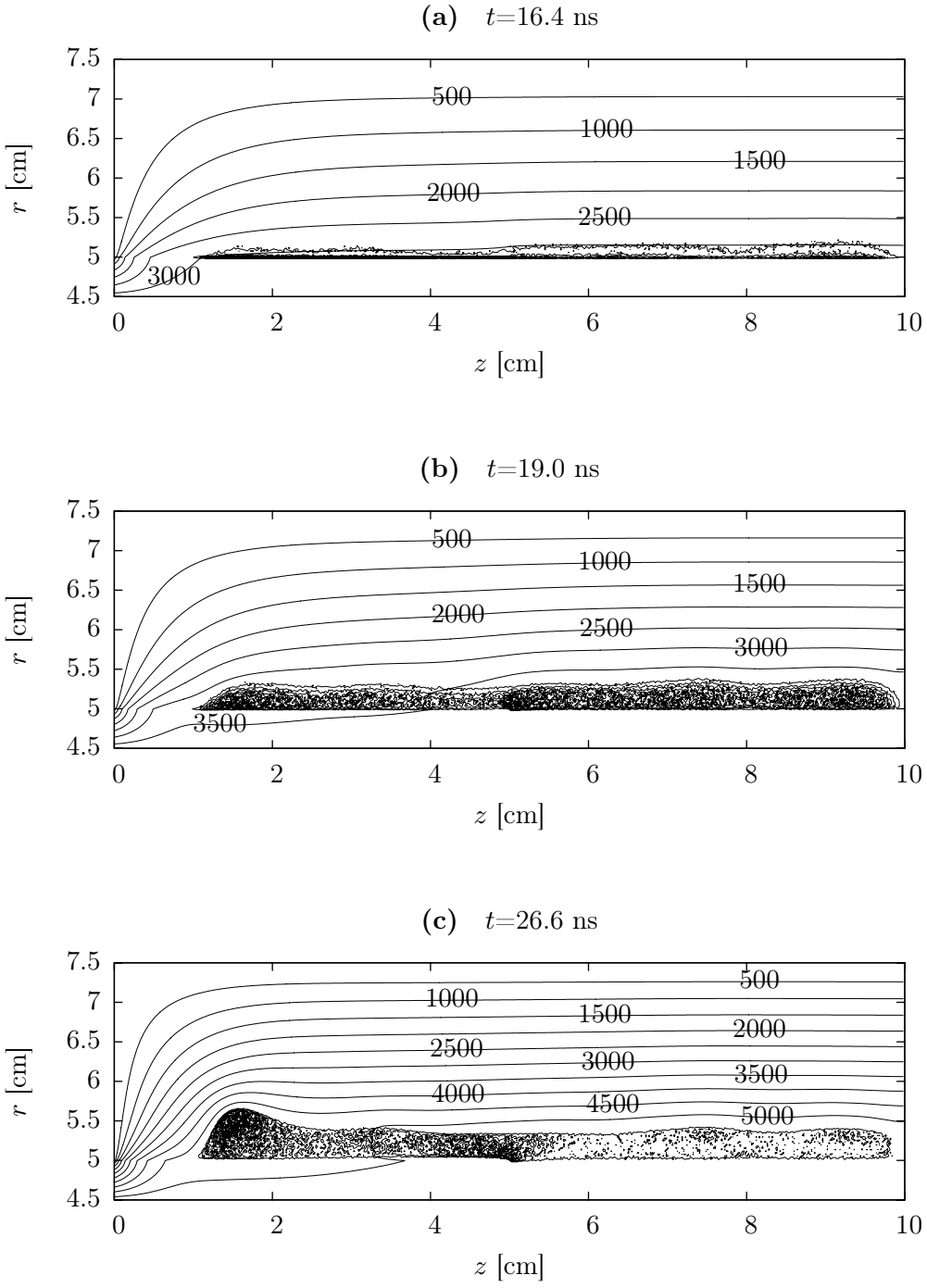

Figure 9.56: Density profiles and isopotential lines at fixed time instants during the first part of the simulation, when the photo-emission is turned off (compare it with Figure 9.7 and 9.8).

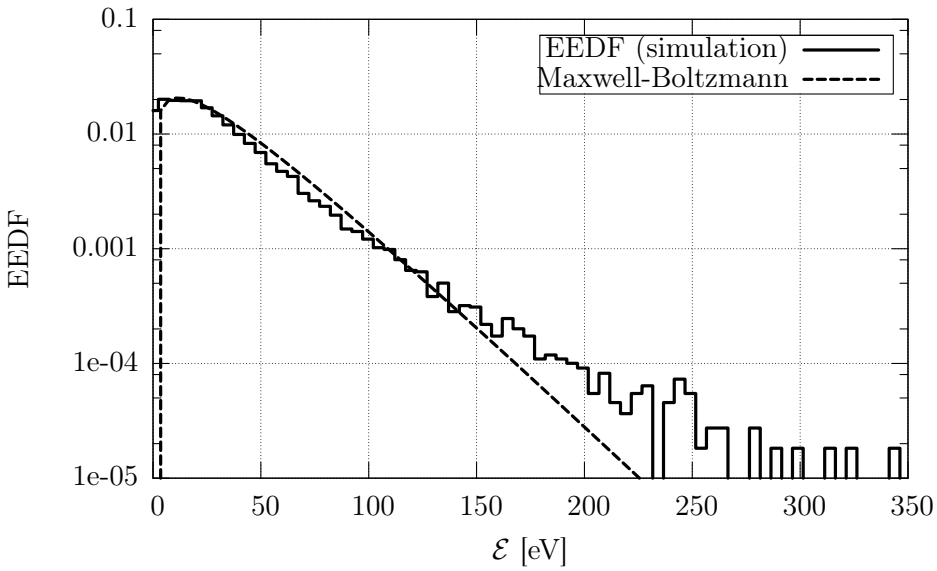

Figure 9.57: EEDF at $t = 7.0$ ns of the simulation time, compared with the Maxwell-Boltzmann distribution function at the same mean energy $\langle\mathcal{E}\rangle = 35.2$ eV (compare it with Figure 9.9).

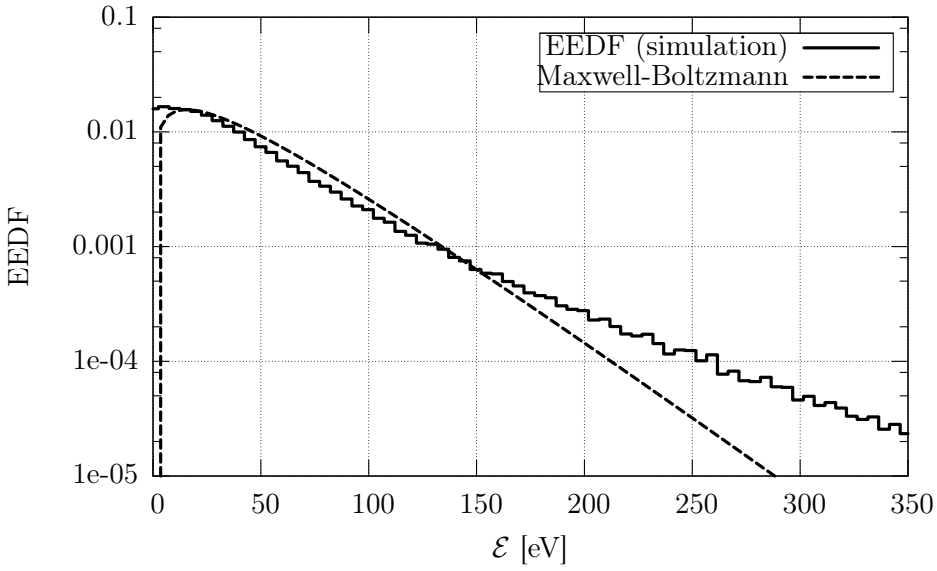

Figure 9.58: EEDF at $t = 10.8$ ns of the simulation time, compared with the Maxwell-Boltzmann distribution function at the same mean energy $\langle\mathcal{E}\rangle = 46.4$ eV (compare it with Figure 9.10).

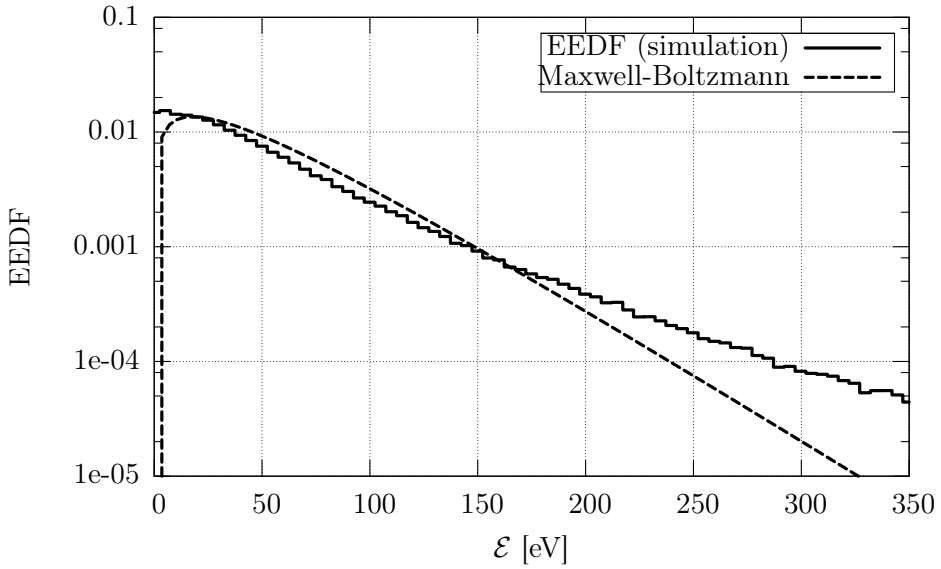

Figure 9.59: EEDF at $t = 15.1$ ns of the simulation time, compared with the Maxwell-Boltzmann distribution function at the same mean energy $\langle \mathcal{E} \rangle = 53.4$ eV (compare it with Figure 9.11).

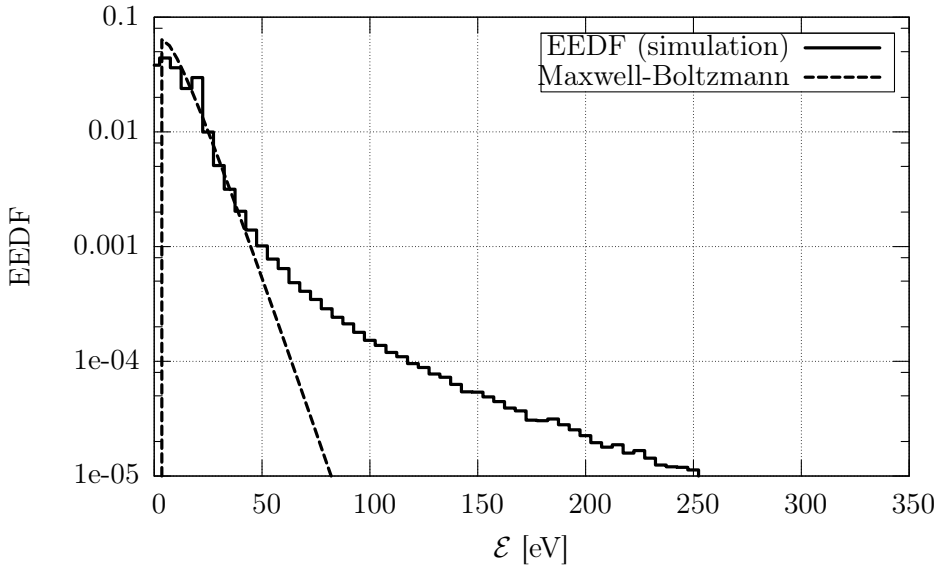

Figure 9.60: EEDF at $t = 20.0$ ns of the simulation time, compared with the Maxwell-Boltzmann distribution function at the same mean energy $\langle \mathcal{E} \rangle = 11.4$ eV (compare it with Figure 9.12).

Concluding remarks

A Dense Plasma Focus (DPF or, simply, PF) is a compact device in which the energy stored in a capacitor bank is discharged through gas mixtures inside a vacuum chamber in order to ignite, accelerate and then radially collapse a plasma sheath through self-induced electromagnetic forces. The short-lived pinched plasma is sufficiently hot and dense to enhance nuclear fusion reactions, even with high threshold energies. The multiplicity of possible reactions and secondary effects make the PF an efficient multi-radiation source, mostly when operated in a repetitive regime (thanks to the very short time-duration of the whole discharge).

In spite of all the accumulated research related to PFs, there are several questions still waiting for answers. Two of these subjects are deeply investigated in the present work. The first, more practical, is the optimization analysis of powerful devices: a numerical tool has been developed to simulate the macroscopic dynamics of the discharge and its coupling with the external electric circuit; tuning the input parameters makes the optimization of the device possible, in order to maximize the transfer of energy in the pinch phase; many related subjects are touched, describing the preliminary design of a PF for the production of short-lived radioisotopes for medical applications. The second, more theoretical, is the investigation of the microscopic phenomena governing the gas breakdown and its development into a plasma discharge; the well-suited and tested Particle-In-Cell Monte-Carlo-Collisional (PIC-MCC) numerical method has been successfully applied to the physical problem of interest. The non-standard problem under investigation has required the development of innovative techniques to control the simulation particle number, during the exponential growth characteristic of breakdown phenomena.

For each of the discussed topic, the main results obtained through computer simulations and their comparison with available data will be hereafter summarized.

Macroscopic simulation and design optimization

In high power apparatus, low inductance, minimum jitter, fast spark-gap switches are needed to transfer currents of hundreds of kA to the electrodes inside the vacuum chamber. When the switch is triggered a potential surge charges the central electrode so that in some hundreds of nanoseconds the full breakdown of the filling gas develops

on the insulator sleeve. As the plasma sheath is formed, the self-induced magnetic pressure forces its detachment from the insulator, then drives it axially toward the open end of the electrodes. As long as it runs, the ionized gas sweeps the neutral gas on its path, ionizing and incorporating it in a sort of snowplow effect.

Once the external circuit electrical parameters have been established, the optimization of electrodes design can be performed. This task consists in finding the right length to synchronize the pinch with the maximum current. The problem is highly non linear since during the plasma motion the total inductance varies with the sheath position. A numerical code was developed to model the 2-D axial-symmetric problem of the sheath motion coupled with external circuit equations. Plasma motion is modeled through snowplow approximation, starting from the initial condition of sheath formation upon the insulator sleeve as given by a macroscopic breakdown model. Circuit equation is solved globally, while equations of motion and mass continuity allow to obtain the shape of the plasma sheath driven by the magnetic pressure; at each iteration, the inductance of the coaxial gun, short-circuited by the current sheath, is recomputed and substituted into the circuit equation closing the time loop. Feeding in the external circuit parameters and following few simple rules of thumb, the optimum configuration can be found. Electrical parameters and sheath evolution are given as output data and can be easily plotted through a dedicated graphical user interface. The physical, mathematical and numerical models have been described in details, as well as the code structure, in order to facilitate future maintenance.

Preliminary tests are proposed: a real device, operated at the Nuclear Engineering Laboratory of Montecuccolino (University of Bologna) for neutron production through D-D nuclear fusion reactions, has been performed. Good results have been obtained both for the measured maximum peak current and global discharge timings. In particular, the developed code reveals itself more accurate than concurrent ones, thanks to the additional modeling of the gas breakdown, two-dimensional current sheath motion and gas sweeping, electrodes round-going and geometrical description. The comparison with analytical simplified models gives a good agreement and allow to numerically estimate a figure of merit for the device performances.

The promising developed tool has been employed for the design of a 150 kJ repetitive at 1 Hz PF device for the production of short-lived radioisotopes for medical applications. A first preliminary set of operating parameters, obtained through commonly used practical rules, revealed itself quite distant from the optimal condition: the input data have been tuned by successive iterations up to the proposed configuration. A peak current of 1.5 MA is expected, while the total inductance rapidly grows up from 20 to about 75 nH.

Several arduous tasks are involved in trying to enhance the energy that can be transferred to the load in a single PF shot; these concern the control of thermal and mechanical stresses, the prevention from surface currents at so high voltages and the reduction of electrodes material ablation strongly affecting the production efficiency. Similarly the accumulation of thermal energy from resistive dissipation on structural parts poses limits on the maximum repetition frequency. To obtain a maximum stored energy of 150 kJ, assuming to work at a 30 kV, a total capacity of 350 µF (composed by 32 modules of 11.1 µF each, parallel connected) is required. A total of 128 HV coaxial cables connect the capacitor bank to the plasma focus load

through a collector assembly. Very strong, pulsed, electro-dynamical forces arise at each shot producing remarkable stresses. Finite elements numerical simulations have been performed to study the mechanical response of the collector. The current densities involved, enhanced by fast transient skin depth phenomena, produce strongly localized heat generation able to melt the interested materials. To solve all these demanding issues, a stainless steel assembly was designed. The most demanding issue is very demanding limit of the external circuit inductance (assumed not greater than 40 nH) which is strongly affected by the collector contribution and shall be kept as low as possible in order to obtain high pulsed currents. Analytical and numerical analysis have been performed and compared; preliminary experimental data have confirmed the design values. The high pulsed currents arising during each discharge requires the use of current gasketing techniques. Special care was also devoted to the electrical insulation between high voltage and grounded elements as well as the prevention of current tracking along insulator surfaces. To allow electrodes dimensions fine tuning through experimental tests, great care has been devoted to maximize the flexibility of the central core.

The designed device has been realized and set up thanks to an ongoing, joint collaboration between the University of Bologna and the University of Ferrara. Preliminary tests have shown a good agreement with the here presented design data (peak current, pinch time, collector inductance, ...). Experiments for the production of sort-lived radioisotopes at full power are programmed for the next future.

Microscopic simulation: the gas breakdown

To better understand the underlying physics of plasma discharge in a PF device, the breakdown phase has been investigated, being a not yet completely understood phenomenon, even if widely known to be of great importance in the subsequent evolution of the discharge. A PIC method coupled with a MCC module has been used to study the time evolution of electron density and Electron Energy Distribution Function (EEDF) up to few tens of nanoseconds.

At the breakdown of the filling gas a plasma layer is formed on the insulator sleeve, short-circuiting the electrodes; high current densities (of the order of hundreds of kA/cm^2) are reached before the sheath detachment from the insulator sleeve and its acceleration along the focus tube. The available experimental data describe the feature of this phase mainly at an advanced temporal stage (hundred of nanoseconds), when the plasma sheath is well-formed. Due to the nonlinearity of the equations, analytical solutions of discharge breakdown cannot be faced, if not in the simplest 1D case.

Many numerical fluid models have been developed for discharge simulations. The main drawback of fluid codes is the assumption of a Maxwellian EEDF, while it's widely known that, in presence of strong electric fields, the electronic species cannot be considered at the thermodynamic equilibrium. Moreover, at high E/p values, the first Townsend ionization coefficient shows a decreasing behavior, due to the "runaway effect". A kinetic approach, able to describe a generic local non-stationary EEDF, appears more suited for the breakdown modeling of the very early stage of gas discharge development, dominated firstly by elastic collisions and then by electron impact ionizations.

Among all the kinetic numerical models, the PIC-MCC one has been chosen due to its high suitability in plasma discharge simulations. Many of the problems to be faced are connected to the efficiency and reliability of the method. In breakdown evolution, the total number of simulation particles grows exponentially when the ionization threshold energy is reached by the electronic species. Moreover, the cathode-fall region quickly undergoes a depletion due to the macroscopic motion of the electrons towards the anode. Therefore, a method to dynamically control the number of particles must be implemented, assuring a sufficiently high local accuracy and representativeness of the stochastic events.

Rough methods based on russian-roulette or splitting in the whole domain of interest are known to introduce numerical noise and to worsen the statistics in depleted regions. In the past, few authors developed techniques for particles splitting and sifting in one-dimensional domains; virtual interfaces were used to separate the spatial domain (for example the cathode-fall and the bulk regions in glow discharges) and two additional species (large- and low-weighted) were used in the two regions to control the number of particles. Recently, new techniques have been proposed for PIC codes. Their main drawbacks are the stiffness in the choice of a fixed number of equally-weighted particles; moreover and the absence of a thorough analysis on the MCC module statistics. An innovative dynamic control on the simulation particles number is developed.

A merging technique based on a Sorted Hierarchical Agglomerative Sub-Clustering is performed to collapse clusters of particles in the phase space. Great care must be paid to the equivalence of the starting and final sets of particles, which is based on two conditions: the two ensembles have to equally contribute to the grid moments (charge densities on the grid nodes for an electrostatic code) and to sample the same velocity distribution function. As far as merging with linear interpolation weighting in two dimensions is concerned, the spatial grid is used to separate particles into local ensembles by means of a hybrid counting sort algorithm, which is also known to increase performances avoiding cache trashing. Once a cell containing a too-high number of particles is found, a mesh-free complete linkage hierarchical agglomerative clustering is used to select the closest sets of particles in the velocity space. Properly choosing the maximum acceptable distances, a more severe condition can be used to avoid merging in the low populated high energy tail of the energy distribution function. At least two particles are required to merge a set of N particles lying in the same cell in order to exactly preserve the charge fractions on the grid nodes. The new particles coordinates and weights are derived and an interesting analogy with well-know mechanical properties of substitutional mass systems is presented. Secondly momentum and energy conservation laws are imposed between the starting and final sets in order to obtain the new velocity components.

Moreover, in order to avoid particles depletion in the cathode-fall region, a splitting procedure is proposed to preserve a sufficiently high sample representativeness for the stochastic secondary emission events and to limit local fluctuations in the electric field solution. Virtual temporal interfaces, provided by the simulation time-step, give a global breakpoint to check the number of particles per cell. If it is lower than a threshold, each single particle in the cell is split into N' new particles perfectly identical to the starting one, with no perturbation on the distribution function in the phase-space nor on the grid moments. The collisional events will

randomly spread them in time-of-flight, direction and energy. Depleted regions can be artificially populated with no addition of numerical noise. Since Secondary Electron Emission (SEE) is a fundamental aspect of Townsend discharges, the splitting technique is useful to enhance the related statistics. Moreover, the technique can be improved choosing an energy dependent splitting factor and adding a forced or multiple generation at ion-cathode interactions.

The large external voltage pulse applied between the electrodes accelerates the seed electrons of the filling gas mixture; once reached a sufficiently high energy, they induce ionization events of the neutral particles leading to a series of electron avalanches. Since the phenomenon is enhanced by the electric field strength, the initially weakly-ionized gas rapidly develops at the closed end of the electrodes, near the insulator-cathode edge, then spreading in a plasma sheath over the insulator sleeve. A prominent role is played the photo-electrons: the photons emitted by decay of excited atoms of the background gas produce fresh electrons by photo-electric effect on the cathode back-wall, feeding the discharge and connecting it to the grounded electrode.

The EEDF evolution is analyzed in conjunction with collision cross sections. The electron density increases exponentially in the first stages of the breakdown. As soon as threshold energies of inelastic reactions are reached, it appears clear the deviation of the EEDF from the Maxwellian distribution. Comparisons with hydrodynamic codes show a faster breakdown development than the expected one, followed by a relaxation of the Townsend avalanche due primarily to runaway electrons of the high energetic tail. The results confirm those obtained with similar kinetic simulations.

Additionally, the proposed techniques improve performances of the numerical code. The local control on the number of particles and the improved statistics on SEE allow to overcome not-physical discharge extinction. A sensitivity study on the PF working parameters (filling gas type and pressure, electrodes geometry, external voltage ramp, photoelectric effect, ...) is proposed to show their role in the discharge development. Improvements on both the numerical (adaptive mesh refinement, parallelization, ...) and the physical model (field emission, excited species evolution, space dependent sight factor, ...) are under deeper investigation, being aimed to give even better results and to push the simulation towards time comparable with experimental results.

Acronyms

AC	Alternate Current
AMR	Adaptive Mesh Refinement
AWG	American Wire Gauge
CIC	Cloud In Cell
CS	Current Sheath
DB	Distribution Box
DC	Direct Current
DM	Discharge Module
(D)PF	(Dense) Plasma Focus
EDF	Energy Distribution Function
EEDF	Electron Energy Distribution Function
EPDF	Electron Probability Distribution Function
ESL	Equivalent Series Inductance
EVDF	Electron Velocity Distribution Function
FEM	Finite Element Method
FFT	Fast Fourier Transform
FOM	Figure Of Merit
GPL	General Purpose License
(G)UI	(Graphical) User Interface
HIPGD	High Intensity Plasma Gun Device
HV	High Voltage
IE	Inner Electrode
LBE	Linear Boltzmann Equation
MC	Monte Carlo
MCC	Monte Carlo Collisional
MHD	Magneto-Hydro-Dynamics
MP	Magnetic Piston
NGP	Nearest Grid Point
OE	Outer Electrode

PDE	Partial Differential Equation
PET	Positron Emitting Tomography
PIC	Particle In Cell
(P)RNG	(Pseudo)Random Number Generator
PS	Power Supply
RF	Radio Frequency
SG	Spark Gap
SEE	Secondary Electron Emission
SHASC	Sorted Hierarchical Agglomerative Sub-Clustering
SLR	Short Lived Radioisotopes
SMP	Symmetric Multi Processor
SOR	Successive Over Relaxation
SPRNG	Scalable Parallel Random Number Generator
TU	Trigger Unit
UV	Ultra Violet

BIBLIOGRAPHY

[1] J W Mather. *Plasma Physics, Part B*, volume 9, chapter Densa Plasma Focus, pages 187–249. Academiic Press, New York, 1971.

[2] N V Filippov, T I Filippova, and V P Vinogradov. Dense, high-temperature plasma in a noncylindrical 2-pinch compression. *Nuclear Fusion Supplement*, 2:577, 1962.

[3] A H Robbins and W Miller. *Circuit Analysis: Theory and Practice*. Delmar Thomson Learning, 2nd edition, 1999.

[4] S Lee, B C Tan, C S Wong, and A C Chew. *Laser and Plasma Technology*. World Scientific, 1985.

[5] M Mathuthu, T G Zengeni, and A V Gholap. The three-phase teory for Plasma Focus devices. *IEEE Transaction on Plasma Science*, 25:1382–88, 1997.

[6] Benzi V, Mezzetti F, Rocchi F, and Sumini M. Feasibility analysis of a Plasma Focus neutron source for BNCT treatment of transplanted human liver. *Nuclear Instruments and Methods in Physics Research B*, 213:611–5, 2004.

[7] A Tartari, A Da Re, F Mezzetti, E Angeli, and P De Chiara. Feasibility of X-ray interstitial radiosurgery based on Plasma Focus device. *Nuclear Instruments and Methods in Physics Research B*, 213:607–10, 2004.

[8] K Takao, T Honda, I Kitamaura, and K Masugata. Purity of nitrogen ion beams produced in a Plasma Focus. *Plasma Sources and Science Technology*, pages 407–11, 2003.

[9] L Sing, P Lee, Z Guixin, F Xianping, V A Gribkov, L Mathe, A Serban, and T S Wong. High rep rate high performance Plasma Focus as a powerful radiation source. *IEEE Transactions on Plasma Science*, 26:1119–26, 1998.

[10] E Angeli, C Bonifazzi, A Da Re, M Marziani, A Tartari, M Frignani, S Mannucci, D Mostacci, F Rocchi, and M Sumini. Development of diagnostic tools for Plasma Focus derived X-ray source. *Nukleonika*, 51:5–20, 2006.

[11] E Angeli, A Tartari, M Frignani, V Molinari, D Mostacci, F Rocchi, and M Sumini. Production of radioisotopes within a Plasma Focus Device. *Nuclear Technology & Radiation Protection*, 1:33–7, 2005.

[12] E Angeli, A Tartari, M Frignani, D Mostacci, F Rocchi, and M Sumini. Preliminary results on the production of Short Lived Radioisotopes with a Plasma Focus Device. *Applied Radiation and Isotopes*, 63:545–51, 2005.

[13] E Angeli, M Frignani, S Mannucci, F Rocchi, M Sumini, and A Tartari. The heating of Plasma Focus electrodes. *Plasma Sources Science and Technology*, 15:91–8, 2006.

[14] M Sumini, D Mostacci, F Rocchi, M Frignani, A Tartari, E Angeli, D Galaverni, U Coli, B Ascione, and G Cucchi. Preliminary design of a 150 kJ repetitive Plasma Focus for the production of 18-F. *Nuclear Instruments and Methods in Physics Research Section A*, 562:1068–71, 2006.

[15] H Bruzzone and R Vieytes. The initial phase in Plasma Focus devices. *Plasma Physics and Controlled Fusion*, 35:1745–54, 1993.

[16] J N Feugeas. The influence of the insulator surface in the Plasma Focus behaviour. *Journal of Applied Physics*, 66:3467–71, 1989.

[17] W Kies. Power limits for dynamical pinch discharges? *Plasma Physics and Controlled Fusion*, 28:1645–57, 1986.

[18] A Donges, G Herziger, H Krompholz, F Ruhl, and K Schonbach. The breakdown phase in a coaxial plasma gun. *Physics Letters A*, 76:391–2, 1980.

[19] H Krompholz, W Neff, F Rull, K Schonbach, and G Herziger. Formation of the plasma layer in a Plasma Focus device. *Phys. Lett.*, 77A:246–8, 1980.

[20] M Lu, M Han, T Yang, C Luo, and T Miyamoto. A simple knife-edge design for initial phase optimization in Plasma Focus. *IEEE Transactions on Plasma Science*, 29:973–6, 2001.

[21] J W Mather and A H Williams. Image converter observations of the development of the dense Plasma Focus discharge. *Physics of Fluids*, 9:2080–1, 1966.

[22] W H Bostik, W Prior, L Grunberger, and G Emmert. Pair production of plasma vortices. *Physics of Fluids*, 9:2078–80, 1966.

[23] M J Sadowski and A Malinowska. Formation and role of filaments in high-current discharges of the pinch type. *Czechoslovak Journal of Physics, Suppl. B*, 56:364–70, 2006.

[24] J S Brzosko and V Nardi. High yield of 12C(d,n)13N and 14N(d,n)15O reactions in the Plasma Focus pinch. *Physics Letters A*, 155:162–8, 1991.

[25] J S Brozsko, K Melzacki, C Powell, M Gai, R H France III, J E McDonald, G D Alton, F E Bertrand, and J R Beene. Breeding of 10^{10}/s radioactive nuclei in a compact Plasma Focus device. In J L Dugganand and AIP I L Morgan, editors, *Application of Accelerators in Research and Industry, 16th International Conference*, pages 277–80, 2001.

[26] J S Brzosko, V Nardi, J R Brzosko, and D Goldstein. Observation of plasma domains with fast ions and enhanced fusion in plasma-focus discharges. *Physics Letters A*, 192:250–7, 1994.

[27] J S Brzosko, J R Brzosko, B V Robouch, and L Ingrosso. Triton burnup in Plasma Focus plasmas. *Physics of Plasmas*, 2:1259–69, 1995.

[28] M Favre, P Silve, P Choi, H Chuaqui, C Dumitrescu-Zoita, and E S Wyndham. Experimental investigations of hotspots in a low energy Plasma Focus operating in hydrogen-argon mixtures. *IEEE Transactions on Plasma Science*, 26:1154–61, 1998.

[29] J D Cobine. *Gaseous Conductors*. McGraw-Hill, New York, 1941.

[30] A Von Engel. *Ionized Gases*. Clarendon Press, Oxford, 1955.

[31] H Alfven and C G Falthammar. *Cosmic electrodynamics*. Clarendon press, Oxford, 1963.

[32] A A Kondratyev. 2D numerical modeling of pulsed plasma acceleration by a magnetic field. *Laser and Particle Beams*, 18:269–73, 2000.

[33] G Herziger, H Krompholz, W Schneider, and K Schonbach. A steady state fluid model of the coaxial plasma gun. *Physics Letters*, 71A:54–6, 1979.

[34] D E Potter. Numerical studies of the Plasma Focus. *Physics of Fluids*, 14:1911–24, 1971.

[35] M Trunk. Numerical parameter studies for the dense Plasma Focus. *Plasma Physics*, 17:237–48, 1975.

[36] D Potter. The formation of high density z-pinches. *Nuclear Fusion*, 18:813–23, 1978.

[37] S Maxon and J Eddleman. Two-dimensional magnetohydrodynamic calculations of the Plasma Focus. *Physics of Fluids*, 21:1856–65, 1978.

[38] K Behler and H Bruhns. Three-fluid magnetohydrodynamical simulation of Plasma Focus discharges. *Physics of Fluids*, 30:3767–76, 1987.

[39] M Scholz, W Stepniewski, B Bienkowska, I Ivanova-Stanik, R Miklaszewski, M Paduch, Sadowski, and K Tomaszewski. Progress in numerical modeling of Plasma-Focus discharge. In M. J. Sadowski, M. Dudek, H.-J. Hartfuss, and E. Pawelec, editors, *AIP Conference Proceedings 812: PLASMA-2005 Conference on Research and Application of Plasmas*, pages 57–63, 2006.

[40] W Stepniewski. MHD numerical modelling of the Plasma Focus phenomena. *Vacuum*, 76:51–5, 2004.

[41] M Scholz and I Ivanova-Stanik. Initial phase in a Plasma Focus device – model and computer simulation. *Vacuum*, pages 287–93, 2000.

[42] V Yordanov, D Genov, I Ivanova-Stanik, and A Blagoev. Ionization growth in the breakdown of Plasma Focus discharge. *Vacuum*, 76:365–8, 2004.

[43] C K Birdsall. Particle-In-Cell charged-particle simulations, plus Monte Carlo Collisions with neutral atoms, PIC-MCC. *IEEE Transactions on Plasma Science*, 19:65–85, 1991.

[44] J P Verboncoeur. Particle simulation of plasmas: review and advances. *Plasma Physics and Controlled Fusion*, 47A:231–60, 2005.

[45] A Serban and S Lee. Experiments on speed-enhanced neutron yield from a small Plasma Focus. *Journal of Plasma Physics*, 60:1, 1998.

[46] C Moreno, F Casanova, V Correa, and A Clausse. Experimental study and two-dimensional modelling of the plasma dynamics of magnetically driven shock waves in a coaxial tube. *Plasma Physics and Controlled Fusion*, 45:1989–99, 2003.

[47] Ya B Zel'dovich and Yu P Raizer. *Physics of Shock Waves and High-Temperature Hydrodynamic Phenomena*, volume 1. Academic Press, 1966.

[48] M A Libermann and A L Velikovich. *Physics of Shock Waves in Gases and Plasmas*. Springer Series in Electronics and Photonics. Springer, 1986.

[49] S J Chapman. *FORTRAN 90/95 for Scientists and Engineers*. McGraw-Hill series in general engineerig, 2nd edition, 1998.

[50] E Akin. *Object-Oriented Programming Via Fortran 90/95*. Cambridge University Press, 2003.

[51] Yu D Korolev and G A Mesyats. *Physics of Pulsed Breakdown in Gases*. URO-PRESS, 1998.

[52] J M Meek and J D Craggs. *Electrical Breakdown in Gases*. Wiley, New York, 1978.

[53] D Montanari. Valutazione dello yield neutronico del Plasma-Focus di Montecuccolino tramite detector a bolle. Master's thesis, University of Bologna, 2003–04. Supervisor: M Sumini.

[54] S Mannucci. Realizzazione di un software di controllo per una macchina Plasma Focus. Master's thesis, University of Bologna, 2003–04. Supervisor: M Sumini.

[55] S Lee. Scaling of the Plasma Focus – Viewpoint from dynamics. Invited paper International Workshop on Plasma Focus Research, Kudowa, Poland, 1998.

[56] J C Keck. Current distribution in a magnetic annular shock tube. *Physics of Fluids*, 5:630–2, 1962.

[57] F J Fishman and H Petschek. Flow model for large radius-ratio magnetic annular shock-tube operation. *Physics of Fluids*, 5:632–3, 1962.

[58] M Favre, P Silva, H Chuaqui, E Wyndham, and P Choi. Current sheath studies in a small Plasma Focus operating in hydrogen-argon mixtures. *Astrophysics and Space Science*, 256:485–90, 1997.

[59] M Frignani, S Mannucci, D Mostacci, F Rocchi, M Sumini, and L Karpinski. Short circuit tests on a 150 kJ, 1 hz repetitive Plasma Focus. *Czechoslovak Journal of Physics, Suppl. D*, 56, 2006.

[60] H Knoepfel. *Pulsed High Magnetic Fields*. North Holland Publishing Company, Amsterdam, 1970.

[61] *Fusion Plasma Analysis*. J Wiley (New York), 1981.

[62] *Conduction of heat in solids*. Oxford University Press (London), 1959.

[63] C B Wheeler. Calculation of wall heating for pinched discharges. *Journal of Physics D*, 7:546–50, 1974.

[64] B Feinberg. An experimental study of hot plasma in contact with a cold wall. *Plasma Physics*, 18:265–75, 1976.

[65] O Belluzzi. *Scienza delle costruzioni*. 5 vol.s.

[66] M A Liebermann and A J Lichtenberg. *Principles of plasma discharges for materials processing*. Wiley, New York, 1994.

[67] J S Townsend. *Electrons in gases*. Hutchinson, 1947.

[68] J S Townsend. *Electricity in gases*. Oxford, 1914.

[69] L B Loeb. *Fundamental processes on electrical discharges in gases*. Wiley, New York, 1939.

[70] E W McDaniel. *Collision phenomena in ionized gases*. Wiley, New York, 1964.

[71] Yu P Raizer. *Gas discharge pysics*. Springer, Berlin, 1991.

[72] L B Loeb and J M Meek. *The mechanism of the electrical spark*. Clarendon Press, Oxford, 1941.

[73] A N Lagarkov and I M Rutkevich. *Ionization waves in electrical breakdown of gases*. Springer, Berlin, 1994.

[74] K U Riemann. Theory of the electron distribution function in a lorentz gas at high E/n. *Physical Review A*, 46:4716–28, 1992.

[75] H Dreicer. *Physical Review*, 115:283, 1959.

[76] P Langevin. *Ann. Chim. Phys.*, 28:289, 1903.

[77] M J Druyvesteyn. *Physica*, 10:61, 1930.

[78] M J Druyvesteyn and F M PEnning. The mechanism of electrical discharges in gases of low pressure. *Review on Modern Physics*, 12:87–176, 1940.

[79] H Margenau. Conduction and dispersion of ionized gases at high frequencies. *Physical Review*, 69:508–13, 1946.

[80] G Ecker and K G Muller. *Z. Naturforsch. Teil A*, 16:246, 1961.

[81] R Goldston and P H Rutherford. *Introduction to plasma physics*. Institute of Physics Publishing, Philadelphia, 1995.

[82] U Kortshagen, C Busch, and L D Tsendin. On simplifying approaches to the solution of the boltzmann equation in spatially inhomogeneous plasmas. *Plasma Sources Science Technology*, 9:1–17, 1996.

[83] P T Matthews. *Introduction to quantum mechanics*. McGraw Hill, 1968.

[84] C B Opal, W K Peterson, and E C Beaty. Measurement of secondary electron spectra produced by electron impact ionization of a number of simple gases. *The Journal of Chemical Physics*, 55:4100–6, 1971.

[85] N St J Braithwaite. Introduction to gas discharges. *Plasma Sources Science Technologies*, 9:517–27, 2000.

[86] C Kittel. *Introduction to solid state physics*. Wiley, New York, 1956.

[87] R R Newton. Transients in Townsend discharges. *Physical Review*, 73:570–83, 1948.

[88] V Kudrle. Monte-Carlo simulation of the initial stage of the DC electrical breakdown of a gas. In *25th EPS Conference on Controlled Fusion and Plasma Physics*, volume 22C, pages 225–8, 1998.

[89] A Einstein. *Ann. Phys.*, 17:132, 1905.

[90] A Einstein. *Ann. Phys.*, 20:199, 1906.

[91] L A DuBridge and R C Hergenrother. The effect of temperature on the energy distribution of photoelectrons. I- Normal energies. *Physical Review*, 44:861–5, 1933.

[92] W W Roehr. The effect of temperature on the energy distribution of photoelectrons. II- Total energies. *Physical Review*, 44:866–71, 1933.

[93] C N Berglund and W E Spicer. Photoemission studies of copper and silver: experiment. *Physical Review A*, 136:1044–64, 1964.

[94] H Bruining. *Physics and applications of secondary electron emission*. Pergamon, London, 1954.

[95] O Hackenberg and W Brauer. *Secondary electron emission from Solids*, volume XI of *Advances in electronics and electron physics*. Academic, New York, 1959.

[96] A J Dekker. *Secondary electron emission*, volume 6 of *Solid state physics*. Academic, New York, 1958.

[97] F Taccogna, S Longo, and M Capitelli. Plasma-surface interaction model with secondary electron emission effects. *Physics of Plasmas*, 11(3), 2004.

[98] J R M Vaughan. A new formula for secondary emission yield. *IEEE Transactions on Electron Devices*, 36:1963–7, 1989.

[99] A Shih and C Hor. Secondary emission properties as a function of the electron incidence angle. *IEEE Transactions on Electron Devices*, 40:824–9, 1993.

[100] C W Mueller. The secondary electron emission of pyrex glass. *Journal of Applied Physics D*, 16:453–8, 1945.

[101] O W Richardson. *The emission of electricity from hot bodies*. Longman-Green, London, 1921.

[102] W B Nottingham. *Thermioni emission*, volume XXI of *Handuch der Physik*. Springer-Verlag, Berlin, 1956.

[103] R H Fowler and L Nordheim. *Proceedings of the Royal Society*, 119:173, 1928.

[104] M Lenzlinger and E H Snow. Fowler-Nordheim tunneling into thermally grown SiO_2. *Journal of Applied Physics*, 40:278–83, 1969.

[105] W Byszewski, M Enright, and J Proud. Transient development of nanosecond gas discharges. *IEEE Transactions on Plasma Science*, 10:281–5, 1983.

[106] H Bruzzone and H Acuna. The breakdown stage in long laser tubes and Plasma Focus devices. *Plasma Sources and Science Technologies*, 15:489–94, 2006.

[107] M Sadowski. Breakdown and initial ionization in high-current carrying discharges. In *Proceedings of the ICPPIG XX*, pages 274–83, 1991.

[108] H Bruzzone and D Grondona. Magnetic probe measurement of the initial phase of Plasma Focus device. *Plasma Physics and Controlled Fusion*, 39:1315–26, 1997.

[109] J N Feugeas and O von Pamel. Current distribution during the breakdown in a coaxial electrode system. *Journal of Applied Physics*, 66:1080–3, 1989.

[110] H Herold, A Jerzykiewicz, M Sadowski, and H Schmidt. *Nulear Fusion*, 29:1255, 1989.

[111] A J Davies, C J Evans, P Townsend, and P M Woodison. The numerical simulation of axially symmetric discharges between plane parallel electrodes. In *4th International Conference on Gas Discharges*, pages 141–4, 1976.

[112] R Morrow. Space-charge effects in high-density plasmas. *Journal of Computational Physics*, 46:454–61, 1982.

[113] J P Boris and D L Book. Flux-corrected transport. III. Minimal-error FCT algorithms. *Journal of Computational Physics*, 20:397–431, 1976.

[114] B E McDonald and J Ambrosiano. High-order upwind flux correction methods for hyperbolic conservation laws. *Journal of Computational Physics*, 56:448–60, 1984.

[115] J P Novak and R Bartnikas. Early stages of channel formation in a short-gap breakdown. *Journal of Applied Physics*, 64:1767–74, 1982.

[116] A J Davies. Discharge simulation. In *IEE Proceedings A (Physical Science, Measurement and Instrumentation, Management and Education, Reviews)*, volume 133, pages 217–40, 1986.

[117] I M Scholz and M Ivanova-Stanik. Effect of the insulator dielectric constant on the breakdown in Plasma Focus device computer simulation. *Journal of Technical Physics*, 40:145–8, 1999.

[118] P Meyer and G Wunner. Unified particle simulation technique for the plasma bulk and the cathode sheath of a DC glow discharge. *Journal of Applied Physics*, 77:992–1000, 1995.

[119] M Surendra, D B Graves, and G M Jellum. Self-consistent model of a direct-current glow discharge: treatment of fast electrons. *Physical Review A*, 41:1112–25, 1990.

[120] V Vahedi, G DiPeso, C K Birdsall, and M A Lieberman. Capacitive RF discharges modelled by particle-in-cell Monte Carlo simulation. I: analysis of numerical techniques. *Plasma Sources Science Technolog*, 2:261–72, 1993.

[121] V Vahedi, C K Birdsall, M A Lieberman, G DiPeso, and T D Rognlien. Capacitive RF discharges modelled by particle-in-cell Monte Carlo simulation. II: comparison with laboratory measurements of electron energy distribution functions. *Plasma Sources Science Technolog*, 2:273–78, 1993.

[122] S Longo and I D Boyd. Nonequilibrium dissociation of hydrogen in parallel-plate radio frequency discharge. *Chemical Physics*, 238:445–53, 1998.

[123] E E Kunhardt, Y Tzeng, and J P Boeuf. Stochastic development of an electron avalanche. *Physical Review A*, 34:440–9, 1986.

[124] E E Kunhardt and Y Tzeng. Development of an electron avalanche and its transition into streamers. *Physical Review A*, 38:1410–21, 1988.

[125] E E Kunhardt and Y Tzeng. Monte Carlo technique for simulating the evolution of an assembly of particles increasing in number. *Journal of Computational Physics*, 67:279–89, 1986.

[126] L E Kline and J G Siambis. Computer simulation of electrical breakdown in gases: avalanche and streamer formation. *Physical Review A*, 5:794–804, 1972.

[127] S M Starikovskaia, N B Anikin, S V Pancheshnyi, D V Zatsepin, and A Yu Starikovskii. Pulsed breakdown at high overvoltage: development, propagation and energy branching. *Plasma Sources Science and Technologies*, 10:344–55, 2001.

[128] S M Starikovskaia and A Yu Starikovskii. Numerical modeling of the electron energy distribution function in the electric field of a nanosecond pulsed discharge. *Journal of Physics D: Applied Physics*, 34:3391–99, 2001.

[129] R W Hockney and J W Eastwood. *Computer simulation using particles*. Adam Hilger, 1988.

[130] C K Birdsall and A B Langdon. *Plasma Physics via computer simulation*. McGraw-Hill, 1976.

[131] J P Verboncoeur. Symmetric spline weighting for charge and current density in particle simulation. *Journal of Computational Physics*, 174:421–7, 2001.

[132] C K Birdsall, A B Langdon, and H Okuda. Finite-size particle physics applied to plasma simulation. *Methods of Computational Physics*, 9:241, 1970.

[133] A B Langdon. Clouds-In-Clouds, Clouds-In-Cells physics for many-body simulation. *Journal of Computational Physics*, 135:139–40, 1997.

[134] V Vahedi and G DiPeso. Simultaneous potential and circuit solution for two-dimensional bounded plasma simulation codes. UCB/ERL m95/95, EECS Department University of California, 1995.

[135] G Grasso. Applicazione di metodi Particle In Cell alla modellizzazione della dinamica del plasma in dispositivi Plasma Focus. Master's thesis, University of Bologna, 2005–06. Supervisor: M Sumini.

[136] J P Boris. Relativistic plasma simulation-optimization of a hybrid code. In DC Washington, editor, *Proceedings of the 4th Conference on Numerical Simulation of Plasmas*, pages 3–67, 1970.

[137] A B Langdon. Nonphysical modifications to oscillations, fluctuations, and collisions due to space-time differencing. In DC Washington, editor, *Proceedings of the 4th Conference on Numerical Simulation of Plasmas*, pages 467–95, 1970.

[138] A B Langdon. Effect of spatial grid in simulation plasmas. *Journal of Computational Physics*, 6:247–67, 1970.

[139] A B Langdon. Kinetic theory of fluctuations and noise in computer simulation of plasma. *Physics of Fluids*, 22:163–71, 1979.

[140] L L Carter and E D Cashwell. *Particle transport simulation with the Monte Carlo method*. Los Alamos Laboratory, 1975.

[141] X-5 Monte Carlo Team. *MCNP, A General Monte Carlo N-Particle Transport Code system, Version 5.* Oak Ridge National Laboratory, 2003. managed by UT-BATELLE, LLC for the U.S. DEPARTMENT OF ENERGY (RSICC computer code collection).

[142] F Salvat J M Fernandez-Varea and J Sempau. *PENELOPE – A Code System for Monte Carlo Simulation of Electron and Photon Transport.* Facultat de Fisica (ECM), Universitat de Barcelona, Spain, 2003.

[143] I Kawrakow and D W O Rogers. *The EGSnrc Code System: Monte Carlo Simulation of Electron and Photon Transport.* Ionizing Radiation Standards – National Research Council of Canada.

[144] S Longo. Monte Carlo models of electron and ion transport in non-equilibrium plasmas. *Plasma Sources and Science Technologies*, 9:468–76, 2000.

[145] A F Bielajew. *Fundamentals of the Monte Carlo method for neutral and charged particle transport.* The University of Michigan, 2001.

[146] *The theory of atomic collisions.* Oxford University Press, 1965.

[147] M Surendra, D B Graves, and G M Jellum. Self-consistent model of a direct-current glow discharge: treatment of fast electrons. *Physical Review A*, 41:1112–25, 1990.

[148] A Okhrimovskyy, A Bogaerts, and R Gijbels. Electron anisotropic scattering in gases: a formula for Monte Carlo simulations. *Physical Review E*, 65(037402), 2002.

[149] R Kinder and M J Kushner. Non-collisional heating and electron energy distributions in magnetically enhanced inductively coupled and helicon plasma sources. *Journal of Applied Physics*, 55:4100–6, 1971.

[150] V Vahedi and M Surendra. A Monte Carlo collision model for the particle-in-cell method: applications to argon and oxygen discharges. *Computer Physics Communications*, 87:178–98, 1995.

[151] J P Boeuf and E Marode. A Monte Carlo analysis of an electron swarm in a non-uniform field: the cathode region of a glow discharge. *Journal of Physics D: Applied Physics*, 15:2169–87, 1982.

[152] M S Chung and T E Everhart. Simple calculation of energy distribution of low-energy secondary electrons emitted from metals under electron bombardment. *Joutnal of Applied Physics*, 45:707–9, 1974.

[153] V Yordanov, I Ivanova-Stanik, and A Blagoev. The role of photoelectrical effect in propagation of electron avalanche in Plasma Focus device. *Journal of Physics: Conference Series*, 2007. Under Press.

[154] M Zakaullah, K Alamgir, M Shafiq, M Sharif, and A Waheed. Scope of Plasma Focus with argon as a soft x-ray source. *IEEE transactions on plasma science*, 30:2089–94, 2002.

[155] V A Gribkov, A Srivastava, C P K Lee, V Kudryashov, and S Lee. Operation of nx2 dense Plasma Focus device with argon filling as a possible radiation source for micro-machining. *IEEE transactions on plasma science*, 30:1331–8, 2002.

[156] V Yordanov, I Ivanova-Stanik, and A Blagoev. PIC-MCC method with finite element solver for poisson equation used in simulation of the breakdown phase in dense Plasma Focus devices. *Journal of Physics: Conference Series*, 44:215–220, 2006.

[157] M Frignani and G Grasso. Argon cross sections for PIC-MCC codes. Technical report, LIN, 2006.

[158] L R Peterson and J E Allen Jr. Electron impact cross sections for argon. *Journal of Chemical Physics*, 56:6068–76, 1971.

[159] E Eggarter. Comprehensive optical and collision data radiation action. II. Ar^+. *Journal of Chemical Physics*, 62:833–47, 1975.

[160] Plasma Theory and Simulation Group of Berkeley University. Xoopic code. `http://ptsg.eecs.berkeley.edu/pub/codes/xoopic/`.

[161] A V Phelps and Z Lj Petrovic. Cold-cathode discharges and breakdown in argon: surface and gas phase production of secondary electrons. *Plasma Sources Science Technology*, 8:R21–44, 1999.

[162] W Y Baek and B Grosswendt. Total electron scattering cross sections of He, Ne and Ar, in the energy range 4 eV – 2 keV. *Journal of Physics B*, 36:731–53, 2003.

[163] A Williart and G Garcia. Analytical formulae for total cross sections for electron scattering by atoms (N, O, F, Ne, P, S, Cl, Ar, As, Se, Br, Kr) between 0.5 nad 10 keV. *Phys. Scr.*, 64:343–5, 2001.

[164] J C Gibson, R J Gulley, J P Sullivan, S J Buckman, V Chan, and P D Burrow. Elastic electron scattering from argon at low incident energies. *Journal of Physics B*, 29:3177, 1996.

[165] W M Ariyasinghe, C Goains, D Powers, T Wijeratne, and P Palihawadana. Total electron scattering cross sections of He, Ne and Ar at intermediate electron energies. *Nuclear Instruments and Methods in Physics Research B*, 225:191, 2004.

[166] K Tachibana. Excitation of the 1s5,1s4, 1s3, and 1s2 levels of argon by low-energy electrons. *Physical Review A*, 34:1007–15, 1986.

[167] W H Cramer. Elastic and inelastic scattering of low-velocity ions: Ne^+ in Ar, Ar^+ in Ne, and Ar^+ in Ar. *Journal Chemical Physics*, 30:641–2, 1959.

[168] IAEA Nuclear Data Section/Atomic and Molecular Data Unit. Aladdin v3.0. `www-admis.iaea.org/cgi_bin/ALADDIN/`.

[169] A V Phelps. Cross sections and swarm coefficients for H^+, H_2^+, H_3^+, H, H_2 and H^- in H_2 for energies from 0.1 ev to 10 kev. *Journal of Physical and Chemical Reference Data*, 19:653–75, 1990.

[170] M J Brunger and S J Buckman. Electron-molecule scattering cross-sections. I. Experimental techniques and data for diatomic molecules. *Physics Report*, 357:215–458, 2002.

[171] K L Bell, H B Gilboy, J G Hughes, A E Kingston, and F J Smith. Reccomended data on the electron impact ionization of light atoms and ions. *Journal of Physical and Chemical Reference Data*, 12:891–916, 1983.

[172] H Tawara, Y Itikawa, H Nishimura, and M Yoshino. Cross sections and related data for electron collisions with hydrogen molecules and molecular ions. *Journal of Physical and Chemical Reference Data*, 19:617–63, 1990.

[173] T W Shyn, W E Sharp, and Y K Kim. Doubly differential cross sections of secondary electrons ejected from gases by electron impact: 25-250 eV on H_2. *Physical Review A*, 24:79–88, 1981.

[174] V Dose, P Pecher, and R Preuss. Formulas for cross sections and rate coefficients for partial electron impact ionization of CH_4 and H_2. *Journal of Chemical Reference Data*, 29:1157–64, 2000.

[175] R Celiberto, R K Janev, A Laricchiuta, M Capitelli, J M Wadehra, and D E Atems. Cross section data for electron-impact inelastic processes of vibrationally excited molecules of hydrogen and its isotopes. *Atomic Data and Nuclear Data Tables*, 77:161–213, 2001.

[176] M Capitelli R Celiberto and A Laricchiuta. Towards a cross section database of excited atomic and molecular hydrogen. *Physica Scripta*, T96:32–44, 2002.

[177] K P Subramanian and V Kumar. Total electron scattering cross section for molecula hydrogen at low electron energies. *Journal of Physics B: Atomic and Molecular Optical Physics*, 22:2387–92, 1989.

[178] CPAT and Kinema Software. The siglo data base. `http://www.siglo-kinema.com`.

[179] T N Rescigno, C W McCurdy, and V McKoy. Low-energy excitation of the hydrogen molecule. *Physical Review A*, 13:216–23, 1976.

[180] S E Branchett, J Tennyson, and L A Morgan. Differential cross sections for electronic excitation of molecular hydrogen using the r-matrix method. *Journal of Physics B: Atomic and Molecular Optical Physics*, 24:3479–90, 1991.

[181] J N Bardsley and J M Wadehra. Dissociative and vibrational excitation in low-energy collisions of electrons with H_2 and D_2. *Physical Review A*, 20:1398–405, 1979.

[182] J P Verboncouer, M V Alves, V Vahedi, and C K Birdsall. Simultaneous potential and circuit solution for 1d bounded plasma particle simulation codes. *Journal of Computational Physics*, 104:321–8, 1993.

[183] R W Boswell and I J Morey. Self-consistent simulation of a parallel-plate RF discharge. *Applied Physics Letters*, 52:21–3, 1988.

[184] H J Lee and J P Verboncouer. A radiation transport coupled to particle-in-cell simulation: Part I. Description of the model. *Physics of Plasmas*, 8:3077–88, 2001.

[185] J E Lawler, G J Parker, and W N G Hitchon. Radiation trapping simulations using the propagator function method. *Journal of Quantum Spectroscopy and Radiation Transport*, 49:627–38, 1993.

[186] P MacNiece, K M Olson, C Monbarry, R de Fainchtein, and C Parker. Paramesh: a parallel adaptive mesh refinement community toolkit. Technical report, NASA Center for AeroSpace Information, 1999.

[187] T H Cormen, C E Leiserson, and R L Rivest. *Introduction to Algorithms*. MIT Press, Cambridge, MA, 1990.

[188] J K Bowers. Accelerating a Particle-In-Cell simulation using a hybrid counting sort. *Journal of Computational Physics*, 173:393–411, 2001.

[189] M Frignani. Memory occupation and linked lists effectiveness in scientific programming. Technical report, LIN, 2006.

[190] Intel Software Development Products. *Quick reference guide to optimization with intel compilers*. available online: `www.intel.com/software/products/compilers`.

[191] Intel Software Development Products. *Intel Fortran Compiler optimizing applications*.

[192] M Matsumoto and T Nishimura. Marsenne twister homepage. `www.math.sci.hiroshima-u.ac.jp/~m-mat/MT/emt.html`.

[193] M Matsumoto and T Nishimura. Marsenne Twister: a 623-dimensinally equidistributed uniform pseudorandom number generator. *ACM Transactions on Modeling and Computer Simulations*, 8:3–30, 1998.

[194] M Matsumoto and T Nishimura. Sum-discrepancy test on pseudorandom number generators. *Mathematics and Computers in Simulation*, 62:431–42, 2003.

[195] W H Press, S A Teukolsky, W T Vetterling, and B P Flannery. *Numerical Recipes in Fortran 90: The Art of Parallel Scientific Computing*. Cambridge University Press, 1996.

[196] A Srinivasan, M Mascagni, and D Ceperley. Testing parallel random number generators. *Parallel Computing*, 26:69–94, 2003.

[197] M Mascagni and A Srinivasan. Algorithm 806: SPRNG: A scalable library for pseudorandom number generation. *ACM Transactions on Mathematical Software*, 26:436–61, 2000.

[198] V Scot. *1D multilayer and 3D "voxel model" Monte Carlo codes for simulation of photon-matter interactions taking into accoun the evolution of the polarization state*. PhD thesis, Bologna University, 2006.

[199] M Cooper. Advanced bash-scripting guide, an in-depth exploration of the art of shell scripting, 2006.

[200] Gnuplot homepage. `www.gnuplot.info`.

[201] P Meyer and G Wunner. Asynchronous cycling as a convergence acceleration method in particle simulation of direct current glow discharges. *Physics of Plasmas*, 4:3152–62, 1997.

[202] C H Shon, H J Lee, and J K Lee. Method to increase the simulation speed of particle-in-cell (PIC) code. *Computer Physics Communications*, 141:322–329, 2001.

[203] G Lapenta. Particle rezoning for multidimensional kinetic Particle-In-Cell simulations. *Journal of Computational Physics*, 181:317–37, 2002.

[204] A K Jains and R C Dubes. *Algorithms for clustering data*. Prentice Hall, 1988.

[205] M Frignani, G Grasso, F Rocchi, and M Sumini. PIC-MCC simulation of the electrical breakdown in a Plasma Focus device. In *Joint International Topical Meeting on Mathematics and Computation and Supercomputing in Nuclear Applications (M&C + SNA 2007)*. American Nuclear Society, 2007. (on CD-ROM).

Acknowledgments

A special thank is addressed to Prof. M. Sumini who patiently allowed me to mature a critical conscientiousness in the field of research activity. I have greatly profited from hints, generously lavished by my colleague F. Rocchi who introduced me to the complex phenomenology of Plasma Focus devices. My coridal thanks to Prof. Tartari and Mr. Angeli who welcomed me to the world of experimental physics, as well as to Mr. Venturi for his precious help and practical viewpoint. A final thank to the IFPiLM for its hospitality and, in particular, to Prof. Miklazewski and Prof. Karpinski, for the usefull brain-storming on plasma physics and PF devices during my staying at the institute.

A conclusione di questo lavoro, che mi ha occupato, più che a tempo pieno, durante tutto l'ultimo anno, non posso che ringraziare tutti coloro che mi sono stati vicini e mi hanno dato sostegno.

Un ringraziamento particolare va a tutti i "colleghi" e amici del Laboratorio di Montecuccolino tra cui, in particolare, ricorderò sempre con affetto: Simone, un grande amico e filosofo di vita, che mi ha aperto gli occhi salvandomi da un sacco di errori; Viviana, sempre presente quando si trattava di uscire a bere qualcosa, ma anche quando, dopo una serie `cicli` ed `if` concatenati, una pausa alle macchinette si rendeva necessaria; Lanfranco, che, sebbene mi abbia lasciato sul più bello, ha contribuito a farmi maturare una visione più ampia della vita e della ricerca; Giacomo, compagno di pomeriggi e nottate (mattinate ne ricordo poche!) a Montecuccolino, quando tra gesso consumato con lavagnate di conti e occhi che si intrecciavano a fissare guaine in evoluzione, l'unica soluzione rimaneva quella di tornarsene a casa e dormirci su.

Ringrazio anche tutti gli altri, da Claudia, e i suoi non-so-quanti-kg che non ci sono più, a Teo, e il suo perenne buonumore; da Sandro, e i suoi "balotti cosati", a Barbara, e il suo fantastico bimbo che ho avuto il piacere di conoscere; da Amanda, e le storie grottesche che iniziano a girare sul suo conto, ad Amadesi, e il suo spirito di inventore e/o comico; da Salvo, e i suoi infallibili metodi pratici, a Lucia, e il suo tanto promesso macrobiotico al quale devo ancora andare; da Fabrizio, e la sua

disponibilità nei miei confronti, a Francesca, che ora concorderà con me nel dire la felicità sta in cose ben più importanti ...

Ringrazio anche tutti i professori del Laboratorio che mi hanno supportato, fornendomi preziosi spunti di riflessione.

Un ringraziamento anche a tutti coloro che mi sono stati vicini in questo ultimo perido, durante il quale, mi rendo conto, sono stato poco presente e spesso alquanto suscettibile. Un grosso bacio e abbraccio a tutta la mia famiglia alla quale dedico queste 300 pagine di fatica e soddisfazioni, e, in particolare, al piccolo Andrea che, con un semplice sorriso, è in grado di far svanire la stanchezza di una intera giornata di intenso lavoro.

Curriculum Vitæ

Education

- 1997/98 – 2003/04: Master Degree in Nuclear Engineering (maximum cum laude), Engineering Faculty – University of Bologna (Italy), July 23rd 2003. Degree Thesis: "Ionic bounding energy in an iperdense quantistic plasma spot" (in italian) – Advisor: Prof. F. Premuda, Advanced Nuclear Reactors.

- 1992/93 – 1996/97: Italian secondary school in scientific studies, "Liceo Scientifico Wiligelmo" in Modena (Italy).

Schools

- October 24th–28th, 2005: First Specialistic School in Parallel Computing – CINECA, Bologna (Italy).

- August 21st–30th, 2002: Frederic Joliot & Otto Hann Summer School in Reactor Physics: "Nuclear Waste Transmutation and Related Innovative Technologies" – Cadarache (France).

Ph.D courses and seminars, International conferences

- "Distributed computing and coordination environments" (in italian) – A. Messina, 2004 – Bologna.
- "Solid state electronics" (in italian) – M. Rudan, 2004 – Bologna.
- "From the radio-nuclide to the radio-medicine" (in italian) – A. Fini, May 17th, 2004 – Bologna.
- "Numerical simulation of the automation of liquid jets" – S. Zaleski, May 21st, 2004 – Bologna.
- "Visit to the Podgorica and Krsko nuclear power plants (SLO)" – May 25th–26th, 2004 – Bologna.
- "Introduction to FEMLab 3.0" – D. Ericsson, F. Lucca, May 27th, 2004.
- "National Instruments solutions for Linux OS" (in italian) – R. Foddis, June 30th, 2004.

- "Workshop on Plasma Physics" – IFPiLM, November 27th/December 2nd, 2004 – Warsaw.
- "Enhancing security and safety using nuclear methods" – G. Vourvopoulos, January 25th, 2005.
- "ACCAPP05" – August 8th/September 9th, 2005 – Venice.
- "FEMLab Conference 2005" – G. L. Zanotelli, D. Ericsson, October 11th, 2005 – Milan.
- "Comsol Multiphysics workshop" – G. L. Zanotelli, D. Ericsson, October 19th, 2005 – Bologna.
- "Parallel computing introduction with MPI" (in italian)- S. Manservisi, October 20th, 2005 – Bologna.
- "The Bohm potential" (in italian) – V. G. Molinari, February 10th, 2006 – Bologna.
- "ENHS neutronic design evaluation" (in italian) – L. Monti, April 4th, 2006 – Bologna.
- "T.A.Or.M.I.N.A.: From the research to the first applications" (in italian) – T. Pinelli, May 12th, 2006 – Bologna.
- "Ludwig Boltzmann: The kinetic theory and the H-theorem" (in italian) – V. G. Molinari, May 7th, 2006 – Bologna.
- "The MonteCarlo modeling role in internal and external dosimetry" (in italian) – G. Gualdrini, June 9th, 2006 – Bologna.
- "Scintillation crystal based gamma detectors for imaging" (in italian) – R. Piani, June 15th, 2006 – Bologna.
- "22nd Symposium on Plasma Physics and Technology" – June 26th/29th, 2006 – Prague.
- "Numerical methods for CFD of two-phase flow" – D. Schmidt, October 10th, 2006 – Bologna.
- "Future energetic strategies: Nuclear energy and Renewable sources" (in italian) – Physics Department of the University of Milan, November 8th, 2006 – Milan.

Publications

- M. Frignani, D. Mostacci, F. Rocchi, and M. Sumini. Montecarlo simulation of neutron backscattering from concrete walls in the Dense Plasma Focus Laboratory of Bologna University. *Radiation Protection Dosimetry*, **115**:380–385, 2005.

- E. Angeli, A. Tartari, M. Frignani, D. Mostacci, F. Rocchi, and M. Sumini. Preliminary results on the production of Short Lived Radioisotopes with a Plasma Focus Device. *Applied Radiation and Isotopes*, **63**:545–51, 2005.

- E. Angeli, A. Tartari, M. Frignani, V. Molinari, D. Mostacci, F. Rocchi, and M. Sumini. Production of radioisotopes within a Plasma Focus Device. *Nuclear Technology & Radiation Protection*, **1**:33–7, 2005.

- E. Angeli, M. Frignani, S. Mannucci, F. Rocchi, M. Sumini, and A. Tartari. The heating of Plasma Focus electrodes. *Plasma Sources Science and Technology*, **15**:91–8, 2006.

- M. Sumini, D. Mostacci, F. Rocchi, M. Frignani, A. Tartari, E. Angeli, D. Galaverni, U. Coli, B. Ascione, and G. Cucchi. Preliminary design of a 150 kJ repetitive Plasma Focus for the production of 18-F. *Nuclear Instruments and Methods in Physics Research Section A*, **562**:1068–71, 2006.

- E. Angeli, C. Bonifazzi, A. Da Re, M. Marziani, A. Tartari, M. Frignani, S. Mannucci, D. Mostacci, F. Rocchi, M. Sumini, and L. Karpinski. *Development of diagnostic tools for plasma focus derived X-ray source.* Nukleonika, **51**:5–20, 2006.

- M. Frignani, S. Mannucci, D. Mostacci, F. Rocchi, and M. Sumini. Short circuit tests on a 150 kJ, 1 Hz repetitive Plasma Focus. *Czechoslovak Journal of Physics, Suppl. D*, **56**, 2006.

- M. Frignani, G. Grasso, F. Rocchi, and M. Sumini. PIC-MCC simulation of the electrical breakdown in a Plasma Focus device. In *Joint International Topical Meeting on Mathematics and Computation and Supercomputing in Nuclear Applications (M&C + SNA 2007).* American Nuclear Society, 2007.

- M. Frignani, F. Premuda. New Mott density values for degenerate plasma spots in Hydrogen/Deuterium loaded metals. *International Society for Condensed Matter Nuclear Science* – Asti, March 2004.

- E. Angeli, A. Tartari, M. Frignani, D. Mostacci, F. Rocchi and M. Sumini. Short lived radioisotopes beams with a Plasma Focus device. *Workshop on Plasma Physics* – Warsaw, December 2004.

Teaching experiences

- Students Tutor of *Fundamentals of Computer Science*, Prof. R. Scardovelli – Mechanical Engineering, University of Bologna – 2004/05, 2005/06.

- Support teaching, training and students examination for the courses of *Neutronics and Plasmas*, *Advanced Nuclear Reactors*, *Numerical Methods for Advanced Nuclear Reactors* – 2004/05, 2005/06.